Observations of the Sunyaev-Zel'dovich Effect using the Cosmic Background Imager 2

James Richard Allison

Physics Department and Jesus College, Oxford

A thesis submitted for the degree of Doctor of Philosophy
in the University of Oxford.

Michaelmas Term 2009

To Sheena, Robert, Harriet and Sarah.

Declaration

I declare that no part of this thesis has been accepted, or is currently being submitted, for any degree or diploma or certificate or any other qualification in this University or elsewhere. Except where explicit reference is made to the work of others, the work contained in this thesis is my own, and is not the outcome of work done in collaboration.

James R. Allison

(December 2009)

Acknowledgements

The Cosmic Background Imager 2 is a collaboration between the institutions of the Strategic Alliance for the Implementation of New Technologies (SAINT). I am indebted to a number of people within the collaboration and I would like to thank them all for their wisdom and advice on the analysis of CBI data, especially Jonathan Sievers, Brian Mason and Steve Myers. Thanks also to Clive Dickinson for introducing me to CBI observing all those years ago as an undergraduate student. A huge thank you to all of the CBI2 and Astro-Norte staff in Chile, including Rodrigo Reeves, Ricardo Bustos, Nolberto Oyarce, Martin Shepherd, Lorena Toro, Jose Cortes, Wilson Araya and Javiera Vergara, for kindly putting up with my inexperience and being such great hosts. Many thanks to Scott Kay and Yu-Ying Zhang for generously providing the simulated and X-ray data required for this work.

Within the group at Oxford I would like to give a huge thank you to both my supervisor Mike Jones, and Angela Taylor, for all these years of guidance and tutoring. A special thank you also to Steve Rawlings for his support and input in my work. Thanks to Paul Grimes and Jamie Leech for so generously giving their time to teach me the subtleties of UNIX computing.

Thanks to all my graduate friends in Oxford Astrophysics. Thank you so much for all the memories, from great times as 1st year graduate students in room 512, to all the moral support and welcomed distraction you provided during writing up.

Finally I would like to thank my wonderful parents, Sheena and Robert, for their invaluable support throughout my whole education. Many thanks to my lovely sister Harriet, fiancé Sarah and future parents-in-law Sue and Dave, for all their constant support during my DPhil study.

Abstract

This thesis describes the analysis of pointed thermal Sunyaev-Zel'dovich (SZ) effect data from observations using the Cosmic Background Imager 2 (CBI2). CBI2 is an upgrade to the original Cosmic Background Imager, with antennas that have twice the effective collecting area, and hence provide greater sensitivity on longer baselines. Observations of the thermal SZ effect constrain the line-of-sight integrated gas pressure within clusters of galaxies and, when combined with X-ray data, provide an excellent tool for deriving the physical properties of these large structures.

The CBI2 SZ data combine relatively low-resolution with a large field-of-view, and can therefore be used to constrain the gas properties of medium-redshift clusters out to the virial radius. By jointly fitting a suitable analytical model to SZ data and X-ray surface brightness data, it is possible to obtain constraints on the temperature and total mass of the cluster. For the analysis work presented in this thesis I choose to parametrise the gas based upon the known behaviour of the entropy, and the total mass by the Navarro, Frenk and White (NFW) prescription. This model is tested against Hydrodynamic/N-body simulations and is found to reproduce the radial behaviour of key cluster properties.

The CBI2 observations presented in this work focus on the REFLEX-DXL clusters, an X-ray luminous sub-sample of the REFLEX survey at $z \sim 0.3$, which have previously published X-ray surface brightness data. The Bullet Cluster, a significant merger system, is a member of this sample and is presented here as a case study for use of the entropy-based model. The derived total mass and gas mass fraction of this cluster are found to be consistent with results from previous X-ray observations. The derived properties from the REFLEX-DXL sample are used to construct a preliminary set of SZ scaling relations out to r_{200}, and are found to be consistent with the self-similar model for massive clusters.

Contents

Chapter 1

Introduction

The Cosmic Microwave Background (CMB) is a relic radiation from the origins of the Universe, that is almost completely isotropic across the whole sky, and is thought to originate 100,000 years after the Big Bang with a temperature of 3000 K. This radiation has since cooled to 2.728 K as the Universe has expanded, and is an almost perfect example of naturally occurring black body radiation. The characteristic temperature of the CMB produces a peak in the frequency spectrum suitable for observation at centimetre and millimetre wavelengths. In this thesis I will describe the observation and analysis of the interaction between the CMB radiation and the ionised gas located within massive clusters of galaxies, known as the intra-cluster medium (ICM). This interaction is called the Sunyaev-Zel'dovich (SZ) effect and is important not only in our understanding of cosmology but in providing a powerful tool with which to probe the astrophysics of the largest gravitationally bound structures in the Universe.

1.1 The Cosmic Microwave Background

The CMB was detected in 1965 by Arno Penzias and Robert Wilson, reporting an excess antenna temperature equal to 3.5 ± 1.0 K at 4.08 GHz (Penzias & Wilson, 1965). Other groups, including Peebles, Dicke and Wilkinson at Princeton, had been looking for a universal microwave background after its predicted existence by Ralph Alpher and Robert Herman (Alpher & Herman, 1948). The discovery of the CMB provided the 'smoking gun' evidence for the Big Bang model of the Universe proposed by George Gamow (Gamow, 1942, 1946). The Big Bang model states that the early Universe was very dense and hot, which then ex-

panded and cooled to form the structure seen at the present epoch. Gamow used this model to explain the relative abundances of the chemical elements seen today, created in a process known as nucleosynthesis. In nucleosynthesis the rates at which reactions occur between the nuclear particles are eventually dominated by the expansion rate of the Universe, causing the abundances of different nuclei to freeze-out at fixed values. Most of the Universe observed at the present epoch consists of Hydrogen and Helium, with trace amounts of Lithium and various isotopes thereof; the heavier elements are generally believed to have formed much later during the supernova deaths of stars. For the first 100,000 years following the Big Bang, radiation and matter formed an opaque primordial plasma, within which the photons and unbound electrons interacted via Compton scattering. As this plasma expanded and cooled below the binding energy of the lightest atoms, the number of unbound electrons reduced considerably, causing the radiation and matter in the universal plasma to de-couple and evolve separately. The CMB that is observed today is an image of the Universe during this epoch of re-combination, propagating through the now transparent Universe. The spherical shell surrounding the observer, from which the CMB radiation originated, is known as the surface of last scattering.

1.1.1 Anisotropies in the CMB

Following the discovery of the CMB in 1965, a number of complimentary experiments were carried out to determine both the spectral and isotropic properties of the radiation. Spectral measurements were carried out in the 1970s and 1980s on ground based, aircraft and balloon borne experiments across a range of frequencies. They showed that the background radiation behaves very similarly to the expected black body curve and measured the average temperature to be $\sim 3\,\mathrm{K}$ (see e.g. Richards & Woody, 1980). The high degree of smoothness in the CMB was consistent with the cosmological principle that the Universe is both isotropic and homogeneous on the largest scales. However it was also expected that the CMB should be anisotropic at some level, since the radiation had once been tightly coupled to matter, which has now formed distinctly anisotropic complex structures under the action of gravity. A number of experiments before the 1990s had observed the dipole anisotropy at a level of 1 part in 10^3 (see e.g. Smoot et al., 1977; Cheng et al., 1979), caused by the relative motion of the observer and CMB. However the primordial anisotropies were not detected until the advent of the COsmic Background Explorer (COBE), a satellite that was launched in 1989

Figure contents property of Third Party. Removed from online version of Thesis.

Figure 1.1: *Left*: The CMB all-sky map from COBE observations by Bennett et al. (1996). The grey region in the centre represents the mask for the galactic foreground emission. *Right*: The CMB all-sky map from WMAP five year observations by Hinshaw et al. (2009). In this case a model template has been used to remove the galactic foreground emission, using spectral information from all frequency bands of the instrument.

and designed specifically to measure the CMB spectrum and anisotropy to unprecedented accuracy (Boggess et al., 1992). COBE carried three instruments, the Far Infrared Absolute Spectrophotometer (FIRAS), the Differential Microwave Radiometer (DMR) and the Diffuse Infra-Red Background Experiment (DIRBE). The FIRAS instrument found that the frequency spectrum is within 0.03 % of the equivalent theoretical Planck curve and hence the CMB radiation is a good example of a naturally occurring black body (Fixsen et al., 1996). The DMR instrument detected the first examples of the CMB primordial anisotropy, at the level of one part in 10^5, on angular scales greater than 7 degrees (Smoot et al., 1992). Figure 1.1 shows the all-sky map of the CMB observations from the DMR instrument, demonstrating the resolution achieved. An equivalent map is also shown for the most recent data set from the Wilkinson Microwave Anisotropy Probe (WMAP, Hinshaw et al., 2009), which is the successor satellite experiment to COBE.

Following on from the results of COBE a number of balloon-borne and ground-based experiments were built to concentrate on determining the behaviour of the anisotropy at angular scales less than 1 degree (see e.g. Wollack et al., 1995; Scott et al., 1996; Miller et al., 1999; Lange et al., 2001; Halverson et al., 2002; Scott et al., 2003; Mason et al., 2003). In order to analyse the CMB temperature as a function of angular scale the anisotropy is normally given in terms of its power spectrum. The angular power spectrum is derived

from expressing the fractional temperature difference as a sum of the spherical harmonics ($Y_{\ell,m}$) as follows

$$\frac{\Delta T}{T}(\theta,\phi) = \sum_{\ell=2}^{\infty} \sum_{m=-\ell}^{\ell} a_{\ell,m} Y_{\ell,m}(\theta,\phi), \tag{1.1}$$

where the polar coordinates θ and ϕ represent positions on the sky. The quantity ℓ is known as the multipole and is essentially a measure of the angular scale under consideration, with $\theta \sim 2\pi/\ell$ for large values of ℓ. The coefficients $a_{\ell,m}$ determine the contribution of each spherical harmonic to the temperature anisotropy. The number of possible independent anisotropy measurements for each angular scale are limited by the fact that there are $2\ell+1$ values of $a_{\ell,m}$. By calculating the mean value of $a_{\ell,m}a^*_{\ell,m}$ as a function of ℓ one can ascertain the degree of anisotropy over each angular scale. The CMB temperature power spectrum is thus given by the following expression

$$\begin{aligned} C_\ell &= \frac{1}{2\ell+1} \sum_{m=-\ell}^{\ell} a_{\ell,m} a^*_{\ell,m} \\ &= \langle |a_{\ell,m}|^2 \rangle, \end{aligned} \tag{1.2}$$

where the power spectrum is typically plotted against $\log(l)$, with $(2\ell+1)C_\ell/2\pi$ on the ordinate, so as to give equal power per ℓ interval. Figure 1.2 shows a theoretical power spectrum predicted from the current cosmological model, alongside the measured version from a selection of the most recent experiments.

1.1.2 Physical interpretation of the CMB power spectrum

The shape of the CMB power spectrum is dominated by a series of peaks that decrease in magnitude towards the high ℓ region. The peaks are associated with the acoustic oscillations that occurred within the primordial plasma, with the largest peak located at $\ell \sim 200$ or equivalently on angular scales of ~ 1 degree. Acoustic oscillations arose in the plasma as a result of the competing processes of gravity and radiation pressure. The peaks in CMB anisotropy are located at those angular scales on which the oscillations were at their extrema, captured at the epoch of re-combination. Once radiation and matter had de-coupled, the gravitation and radiation pressure were no longer competing processes and so the shape of the CMB primordial power spectrum became frozen into what we observe today.

The main features of the current version of the CMB power spectrum are labelled in Figure 1.2. On

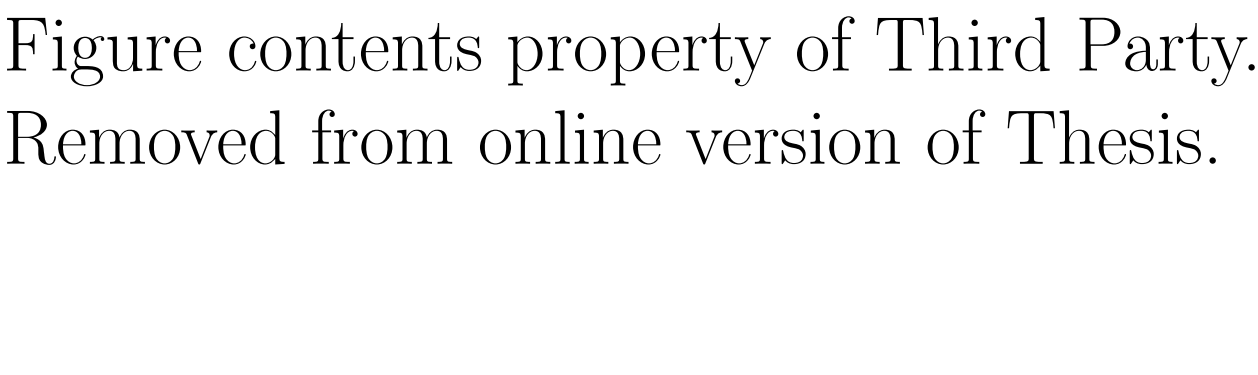

Figure 1.2: *Left*: The CMB angular power spectrum predicted by the ΛCDM cosmological model. The labelled features correspond to the following aspects of cosmology; (a) the Sachs-Wolfe effect, (b) universal geometry, (c) the baryon fraction, (d) Silk damping and (e) the CBI excess power. *Right*: The measured power spectrum from a selection of recent CMB experiments by Sievers et al. (2009). In this version the multipole axis has been plotted linearly in order for the high ℓ behaviour to be clearly seen.

scales larger than 10 degrees, the anisotropy is dominated by the Sachs-Wolfe effect, where the photons of background radiation are gravitationally redshifted by the potential wells (Sachs & Wolfe, 1967). The non-integrated Sachs-Wolfe effect is a primordial (primary) anisotropy resulting from the distribution of regions of over-density and under-density in the mass distribution of the Universe at the epoch of re-combination. Since this anisotropy occurs on scales larger than the plasma oscillations, the non-integrated Sachs-Wolfe effect encodes the original fluctuations in matter and radiation that have not changed since the Big Bang. Therefore it is this region of the power-spectrum that can constrain the value of n_s, which represents the initial power-law spectrum of scalar perturbations. The integrated Sachs-Wolfe effect is a non-primordial (secondary) anisotropy resulting from the evolution of the very large-scale distribution of gravitational potential wells between the epoch of re-combination and the present. The anisotropy due to the integrated effect will evolve with time as the large-scale mass distribution changes.

The first peak in the power spectrum represents the oscillation mode in the primordial fluid that has been captured in its first compression phase before re-combination. The position of this peak therefore gives the angular scale upon which information could have travelled across the primordial fluid up to that epoch. The particle horizon is strongly dependent upon the universal geometry and therefore the curvature

of space-time can be constrained by the first peak. All current measurements of this feature are consistent with the Universe being spatially flat (see e.g. Sievers et al., 2009, and references therein), which indicates that the sum of the energy density from the baryonic, cold dark matter and dark energy component is very close to unity. Subsequent anisotropy peaks alternately represent extrema in rarefaction (even peaks) and compression (odd peaks). Since the compression due to gravity is strongly dependent upon the number of baryons in the fluid, the relative height of the odd to the even peaks in the power spectrum constrains the Universal baryon fraction. The over-all scaling of the heights of the peaks is dependent upon the initial size of the gravitational potential wells which the baryon-photon fluid falls into. The energy density of the cold dark matter component is therefore independently constrained by the over-all amplitude of the peaks in the power spectrum.

At the high ℓ end of the spectrum the amplitude of the primordial anisotropies is seen to decrease considerably. This result is due to the effect of two physical processes. Firstly the time period over which re-combination occurred was clearly not instantaneous, and so oscillations in the fluid that happened on time scales smaller than this period will have reduced amplitude. The factor in amplitude reduction due to this effect is equal to N^{-2}, where N is the number of oscillations that could occur during re-combination. The second effect is known as Silk damping (Silk, 1968) whereby, on angular scales equal to the distance that photons can travel during the period of re-combination, the hot and cold regions in the primordial fluid mix and are cancelled out. The amplitudes of the acoustic peaks on these scales drop off exponentially with ℓ as a result of this effect.

At the highest ℓ values there have been recent concerted efforts to ascertain the possible onset of a secondary anisotropy component in the power spectrum due to the integrated effect of the large scale Sunyaev-Zel'dovich effect (see Section 1.2). The CBI experiment observed what is believed to be excess power at $\ell \sim 3500$, at a level above that predicted from the primordial anisotropy (Sievers et al., 2009). However the interpretation of this result is controversial (see e.g. Sharp et al., 2010) and it is not clear yet if this is due to the SZ effect or contaminating emission from an unknown population of radio point sources at 30 GHz. The resolution of this problem will have implications for the value of σ_8, the cosmological parameter that represents the amplitude of matter fluctuations on a physical scale of $8h^{-1}$ Mpc.

Figure contents property of Third Party. Removed from online version of Thesis.

Figure 1.3: Diffuse galactic foreground components in CMB observations as a function of frequency by Bennett et al. (2003).

1.1.3 Galactic Foregrounds

Between the surface of last scattering and the observer there are a number of astronomical sources that contaminate the observed CMB signal. Diffuse sources of radio emission are typically galactic in origin, and therefore small-scale ground-based experiments concentrate on observing the CMB away from the galactic plane to avoid the most significant parts of this contamination. All-sky observations of the CMB by satellites, such as WMAP, use a technique that separates the components based on the difference in frequency behaviour between the CMB and the foregrounds. The following is a brief summary of the main contributions to the diffuse foreground contamination from the galaxy. For a more in-depth discussion of the diffuse contaminants of total intensity CMB observations the reader should refer to the work by Bennett et al. (2003). Figure 1.3 gives a pictorial summary of the relative amplitudes as a function of frequency.

Free-Free emission arises from unbound electrons that scatter off charged ions in an ionised hydrogen cloud. This mechanism is similar to the bremsstrahlung process that produces X-rays in the intra-cluster medium of galaxy clusters, which is discussed later in this chapter and throughout this thesis. At frequencies greater than 10 GHz the free-free flux density spectrum has a negative spectral index

with $\alpha = -0.15$, and at lower frequencies it has a steeply rising spectrum with $\alpha = 4$, where $S_\nu \propto \nu^\alpha$. The cut-off in flux density at low frequencies is due to self-absorption where the electron population re-absorbs the high energy radiation.

Synchrotron emission occurs when relativistic cosmic-ray electrons are accelerated in a strong magnetic field. In the case of diffuse galactic emission the acceleration occurs in the remnants of Type Ib and Type II supernovae. Synchrotron emission is classified as non-thermal because its frequency spectrum is distinct from that of a black-body or bremsstrahlung. The behaviour of the galactic synchrotron signal is incredibly complex, with a wide range of spectral indices arising from two distinct types of relativistic electrons, namely those confined to the magnetic fields of discrete supernova remnants and those that have escaped into the wider Galaxy. The high frequency behaviour is dependent upon the rate of energy loss of the electrons as well as their state of confinement. Typically higher energy loss and confinement will produce a steeper spectral index, while low confinement electrons will produce a flatter spectrum. The synchroton spectrum is seen to steepen away from the disk in both observations of the Milky Way and external galaxies, suggesting that energy loss is significant for high energy electrons in galactic haloes (see Lisenfeld & Völk, 2000). For example, Hummel et al. (1991) find that the edge-on spiral galaxy NGC 891 has a spectral index (over the frequency range 610 MHz to 1.49 GHz) which changes between $\alpha = -0.6$ in the galactic plane to $\alpha = -1.1$ in the halo. At higher frequencies a flatter spectral index from the galactic plane is expected to dominate over the observed emission. The synchrotron spectrum cuts-off at low frequencies due to self-absorption; varying between ∼MHz to ∼GHz depending on the source.

Dust emission arises from grains of molecular material (such as SiO_2 and MgO) that emit thermal radiation in the infra-red. Thermal dust emission dominates over other components of the diffuse foreground at frequencies greater than 100 GHz with a steeply rising spectrum of $\alpha \sim 4$. In addition microwave radiation can be emitted from both spinning and thermally fluctuating dust grains that generate electric and magnetic dipole radiation respectively. Spinning dust is expected to be a significant source of radiation at $\nu \sim 30$ GHz (see e.g. Draine & Lazarian, 1998a,b), and has possibly been detected in CBI2 and VSA observations of the RCW175 HII region by Dickinson et al. (2009).

1.1.4 Extragalactic foregrounds

Extragalactic foreground contamination of the CMB signal comes from two distinctly different sources that dominate observations away from the plane of the galaxy; namely active galactic nuclei and the Sunyaev-Zel'dovich effect. In the case of the former, microwave emission arises from the active centres of radio-galaxies and quasars due to the acceleration of relativistic electrons in the magnetic fields. This is the same process that produces the diffuse galactic synchrotron radiation described in the previous section, and as such has a similar complex behaviour with frequency. These sources can have a highly variable brightness due to the significant variation in the accretion rate of matter onto a central black hole. They typically appear point-like at the resolution of CMB experiments and can be identified separately by using long-baseline interferometric arrays. While substantial blind surveys of radio point sources have been conducted at frequencies lower than 10 GHz (see e.g Condon et al., 1998; Mauch et al., 2003) our knowledge of the population at higher frequencies is limited. It is very important to understand the behaviour of these sources at higher frequencies for interpreting the results of high-ℓ power spectrum measurements, and there has recently been some work in this area (see e.g Taylor et al., 2001; Waldram et al., 2003; Mason et al., 2009; Murphy et al., 2010).

An additional extragalactic foreground originates from the SZ effect in galaxy clusters. This process is the main focus of this thesis and will be discussed in detail throughout the rest of the this chapter and those following. The spectrum of the SZ effect is complex at frequencies higher than ~ 30 GHz, however at frequencies in the Rayleigh-Jeans regime it has a spectral index $\alpha \approx 2$. The relative contribution of the SZ effect and radio point sources to the high-ℓ region of the CMB power spectrum is a subject of some debate, and requires a better understanding of the number of sources of both types at higher frequencies.

1.2 The Sunyaev-Zel'dovich Effect

The Sunyaev-Zel'dovich effect refers to the perturbation of the CMB temperature on angular scales $\lesssim$ 10 arcminutes from the interaction between CMB photons and hot electrons along the line-of-sight. This effect predominantly arises in the context of galaxy clusters, in which the interacting electrons reside within the hot virialised gas of the intra-cluster medium. From an astrophysical perspective the SZ effect provides a powerful tool for probing the physics of galaxy clusters, and in combination with other wavelengths can

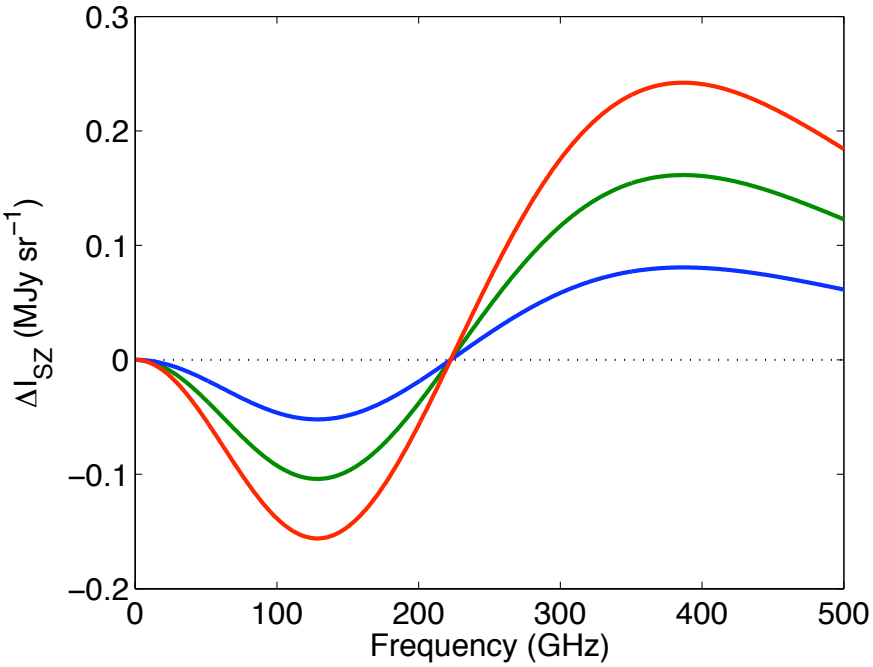

Figure 1.4: The change in CMB brightness due to the non-relativistic thermal SZ effect, as a function of frequency. Cluster properties include comptonisation parameters equal to 5×10^{-5} (*blue line*), 10×10^{-5} (*green line*) and 15×10^{-5} (*red line*) and an electron temperature of 10 keV.

be used to estimate their total mass. In terms of cosmological application it provides a means of conducting cluster surveys over a broad redshift range, thereby providing a strong constraint on the universal mass distribution and evolution. I give here a brief theoretical outline of the SZ effect, and the reader should refer to reviews by Birkinshaw (1999) and Carlstrom et al. (2002) for further details.

1.2.1 The Thermal SZ Effect

The SZ effect was predicted theoretically in the early 1970s (Sunyaev & Zel'dovich, 1970), based on earlier work by Kompaneets (1956); Dreicer (1964); Weymann (1965). The SZ effect arises from the scattering between relatively low energy photons and mildly relativistic and non-relativistic electrons. Since the photon energy is much less than $m_e c^2$, the interaction (known as inverse-Compton scattering) is almost elastic, and can simply be represented by the classical Thomson cross-section formula (σ_T). In the limit that the electrons are non-relativistic ($k_B T_e \ll m_e c^2$) the scattering process simplifies further and the change in occupation

number n for the CMB photons is given by the Kompaneets (1956) equation

$$\frac{\partial n}{\partial y} = \frac{1}{x_e^2}\frac{\partial}{\partial x_e} x_e^4 \left(\frac{\partial n}{\partial x_e} + n + n^2 \right), \tag{1.3}$$

where $x_e = h\nu/k_B T_e$ and T_e is the electron temperature. The parameter y, known as the comptonization parameter, is a dimensionless measure of the total time spent by the photons in the electron distribution and is given by

$$y = \frac{k_B T_e}{m_e c^2}\frac{ct}{\lambda_e} = \int \frac{k_B T_e}{m_e c^2} n_e \sigma_T \mathrm{d}l, \tag{1.4}$$

where the scattering mean free path $\lambda_e = (n_e \sigma_T)^{-1}$. The comptonization parameter is proportional to the product of the electron density and temperature, integrated along the line-of-sight, and is therefore a very important quantity in relating the observable thermal SZ effect and physical properties of the cluster. In the limit that $T_e \gg T_{rad}$, which is true of the scattering between CMB photons and hot electrons, the first term in the Kompaneet's equation dominates and so simplifies to

$$\frac{\partial n}{\partial y} = \frac{1}{x_e^2}\frac{\partial}{\partial x_e} x_e^4 \frac{\partial n}{\partial x_e}. \tag{1.5}$$

If we assume further that the incident CMB photons have a spectrum given by a black body, and that the ICM is optically thin, then the change in occupation number is given by

$$\Delta n = y \frac{x e^x}{(e^x - 1)^2} \left(x \frac{e^x + 1}{e^x - 1} - 4 \right), \tag{1.6}$$

where $x = h\nu/k_B T_{CMB}$. The change in CMB brightness due to the thermal SZ is then given by the following expression

$$\frac{\Delta I_{SZ,Therm}}{I_0} = x^3 \Delta n = y \frac{x^4 e^x}{(e^x - 1)^2} \left(x \frac{e^x + 1}{e^x - 1} - 4 \right), \tag{1.7}$$

where $I_0 = \frac{2h}{c^2}\left(\frac{k_B T_{CMB}}{h}\right)^3$. Figure 1.4 shows $\Delta I_{SZ,Therm}$ as a function of frequency for three different typical values of the comptonization parameter. The net effect of the scattering process is to increase the frequency of the overall CMB spectrum, and thereby produce a brightness decrement at frequencies less than 220 GHz, and an increment at higher frequencies. The position where the thermal SZ spectrum changes between these two brightness regimes is known as the null and is fixed in the non-relativistic limit. The change in CMB

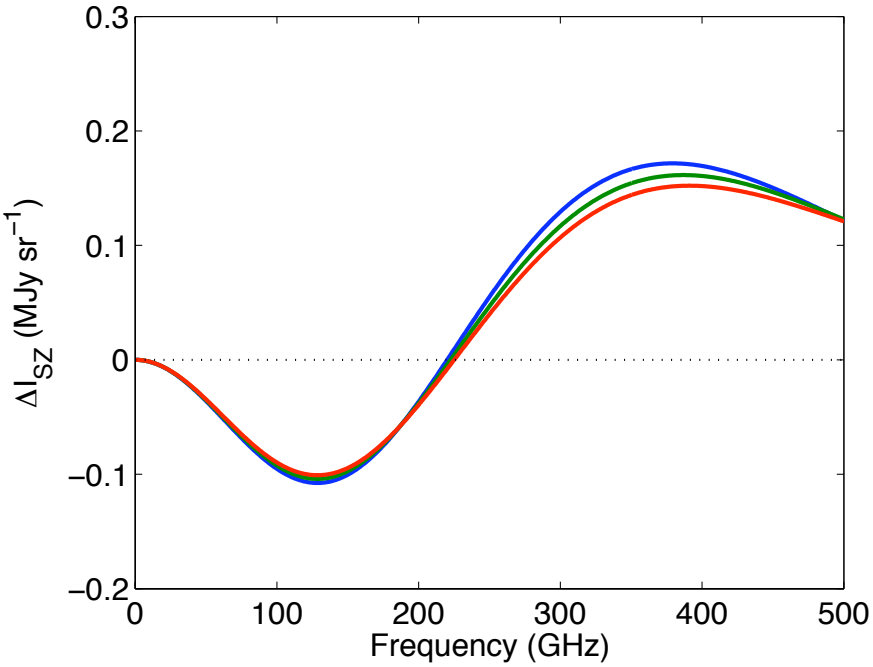

Figure 1.5: The thermal SZ effect as a function of frequency, demonstrating the correction due to relativistic electrons in the cluster gas. Cluster properties include a comptonisation parameter of 10×10^{-5} and electron temperatures equal to 5 keV (*blue line*), 10 keV (*green line*) and 15 keV (*red line*).

brightness is independent of redshift and hence the SZ effect is a very useful tool for mapping the distribution and evolution of large-scale structure.

1.2.2 The Relativistic Correction

The Kompaneet's equation, used in the previous section to derive the change in CMB brightness due to the thermal SZ effect, is based upon the assumption that the electrons in the ICM are non-relativistic. However it is known from observations of X-ray bremsstrahlung emission that the electrons in galaxy clusters are extremely hot ($T_e \sim 10^7 - 10^8$ K) and are therefore not completely non-relativistic. The correction due to the relativistic nature of the electrons can be constructed from a more general version of the Kompaneet's equation and leads to the change in brightness being expressed as a series of increasing powers of T_e. In general the change in brightness due to the thermal SZ effect is given by

$$\frac{\Delta I_{\mathrm{SZ,Therm}}}{I_0} = y \frac{x^4 e^x}{(e^x-1)^2} \left(x \frac{e^x+1}{e^x-1} - 4 \right) (1 + \Delta(x, T_e)), \tag{1.8}$$

where $\Delta(x, T_e)$ is the relativistic correction. Challinor & Lasenby (1998) derive a numerical expression for $\Delta(x, T_e)$ that is accurate to $O(T_e^3)$ and Itoh et al. (1998) go further, giving an expression that is accurate to $O(T_e^5)$. These power-series are approximations to the true relativistic SZ effect and are reliable only for limited ranges of frequency and electron temperature. For example the expression given by Itoh et al. (1998) is reliable for electron temperatures less than 50 keV in the Rayleigh-Jeans region, and less than 15 keV for higher frequencies. The corrections are still based upon the original assumptions that the electrons are described by a relativistic Maxwellian distribution (i.e. a single temperature gas) and that the cluster is optically thin, so these expressions must be used with caution in cases where very high accuracy is required. Figure 1.5 shows the relativistic correction given by Itoh et al. (1998) for three different temperatures. For typical cluster gas temperatures and observing frequencies the relativistic correction is only a few percent of the total thermal SZ effect. From this plot it can be seen that the null frequency is a function of the relativistic correction, and therefore an experiment that could accurately measure the position could produce an independent estimate of T_e.

1.2.3 The Kinematic SZ Effect

In general clusters have a motion that is non-zero relative to the background radiation. The effect of this peculiar velocity is to add a Doppler shift to the frequency of the scattered CMB photons. In the non-relativistic and thermal approximation the change in CMB brightness due to this effect is given by

$$\frac{\Delta I_{\mathrm{SZ,Kin}}}{I_0} = \frac{x^4 e^x}{(e^x - 1)^2} \left(-\tau_e \frac{v_{\mathrm{pec}}}{c} \right), \tag{1.9}$$

where τ_e is the optical depth and v_{pec} is the bulk peculiar velocity of the cluster (Sunyaev & Zel'dovich, 1972; Phillips, 1995). In the case of the kinematic SZ effect the resulting brightness spectrum for the scattered CMB is still described by a Planck curve, but with a different thermodynamic temperature. Figure 1.6 demonstrates the correction to the observed SZ signal due to the non-relativistic kinematic SZ effect as a function of frequency. It is clear from this plot that the kinematic SZ effect is most significant at frequencies near to the null position, where the thermal SZ signal is very weak. Observations at frequencies in this region have been used to provide estimates of cluster peculiar velocities (see e.g. Benson et al., 2003; Nord et al., 2009) and future spectral experiments, with significantly broader bandwidth, should improve upon

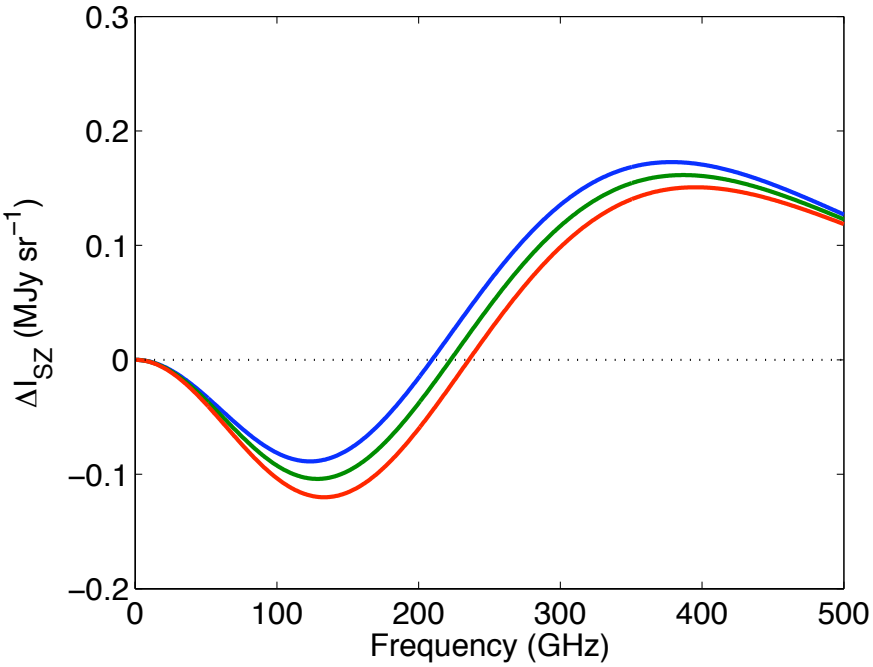

Figure 1.6: The SZ effect as a function of frequency, demonstrating the non-relativistic kinematic correction due to the peculiar motion of the galaxy cluster. Cluster properties include a comptonisation parameter of 10×10^{-5}, an electron temperature of 10 keV, and peculiar velocities equal to $-1000\,\mathrm{kms}^{-1}$ (*blue line*), $0\,\mathrm{kms}^{-1}$ (*green line*) and $+1000\,\mathrm{kms}^{-1}$ (*red line*).

these estimates.

The above expression is a first order approximation, and there are higher order corrections that take into account both the relativistic nature of the electrons and the relativistic peculiar velocity (see e.g. Nozawa et al., 1998). For a cluster with a peculiar velocity of $c/300$ and an electron temperature of 10 keV, the corrections to the non-relativistic kinematic SZ effect are at the level of -8.2 %, +1.3 % and +0.2 % for the $\mathrm{O}(v_{\mathrm{pec}}T_{\mathrm{e}})$, $\mathrm{O}(v_{\mathrm{pec}}T_{\mathrm{e}}^2)$ and $\mathrm{O}(v_{\mathrm{pec}}^2)$ terms respectively.

1.2.4 Observations and Motivation

Following the theoretical foundation laid down in 1970 by Sunyaev and Zel'dovich, attempts were made in the subsequent two decades to provide a reliable detection of the thermal SZ effect. These first observations used single radio dish experiments that employed the beam switching technique to remove systematics from the atmosphere and ground spill-over. Beam-switching is based upon measuring the difference between two

signals, on and off the source, and assuming that the atmosphere and ground signal vary slowly with pointing position. However this method can introduce additional systematic effects, for example if the beam shapes are different, or if the source is extended over the two positions. The first reliable single dish detections were achieved by Birkinshaw et al. (1984) using the OVRO 40 m telescope and Uson (1986) using the Greenbank 140 foot telescope. Later radio interferometers were built that could simultaneously observe the microwave background on a range of angular scales, with the first interferometric SZ image by Jones et al. (1993). These instruments measure the correlated signal between pairs of antennas, and so any uncorrelated signals from the atmosphere and ground are removed from the data, significantly reducing the systematic error. An additional advantage of interferometry is that one can easily select a range of angular scales and therefore monitor and remove contamination from bright radio point sources.

The SZ effect is proportional to the integrated line-of-sight pressure of the intra-cluster medium, and therefore provides a constraint on the product of the electron temperature and density. By combining the SZ effect with data from other wavelengths it is possible to break the electron density and temperature degeneracy, particularly using X-ray surface brightness data, and thereby provide constraints on other cluster properties. Following the early detections of the 80s and 90s, a number of ground based CMB experiments have been used to observe the SZ effect, and in the following section I will discuss the motivation for these observations.

The Hubble Constant

The SZ effect and X-ray surface brightness have different dependencies on the line-of-sight integration of the electron density and temperature, given by the following expressions

$$\Delta T_{\rm SZ} \propto \int f(x,T_{\rm e}) n_{\rm e} T_{\rm e} D_{\rm A} {\rm d}\zeta \tag{1.10}$$

$$S_{\rm X} \propto \frac{1}{(1+z)^4} \int n_{\rm e}^2 \Lambda(T_{\rm e}) D_{\rm A} {\rm d}\zeta, \tag{1.11}$$

where $\Lambda(T_{\rm e})$ is the emissivity over the appropriate X-ray energy band and $D_{\rm A}$ is the angular diameter distance. In this notation the line-of-sight distance in physical units is given by $l = D_{\rm A}\zeta$. By eliminating the electron density from both of these expressions a relationship can be obtained between the angular diameter distance and the observables. The exact form of this expression depends upon the analytical model that is

adopted for the cluster gas, however the approximate dependencies are given by

$$D_{\rm A} \propto \frac{1}{\theta_{\rm c}(1+z)^4}\left(\frac{\Delta T^2_{\rm SZ,0}}{S_{\rm X,0}}\right)\frac{\Lambda(T_{\rm e})}{f(x,T_{\rm e})T_{\rm e}^2}, \tag{1.12}$$

where $\theta_{\rm c}$ is a characteristic scale radius, equal to the angular size of the cluster (along the line-of-sight), and $\Delta T_{\rm SZ,0}$ and $S_{\rm X,0}$ are the values of the SZ temperature and X-ray surface brightness at the cluster centroid. In deriving this simple expression the ICM is assumed to be isothermal, which is not generally true of most clusters observed out to large radii. The Hubble constant (H_0), a cosmological parameter that represents the rate of expansion of the Universe, can therefore be obtained by combining the cluster angular diameter distance with the redshift and universal geometry. There are two main assumptions made about the sample that can lead to sytematic error in the estimate of H_0 (in addition to any systematics due to the calibration). Firstly it is assumed that on average the value of $\theta_{\rm c}$ is equal to the angular size of the cluster in the plane of the sky (i.e. that clusters are spherical), which is true for a large enough sample. However cluster samples are typically selected based upon their known X-ray flux measurements, which for a given electron density will be brighter if the cluster is extended along the line-of-sight. Hence for clusters that are close to the sample flux limit one will preferentially choose those that are extended along the line-of-sight. Since this could systematically shift the value of H_0 to low values, the SZ cluster sample must be selected from those clusters with total X-ray fluxes significantly greater than the flux limit given for that survey (see e.g. Jones et al., 2005). A second systematic error can arise from the assumption that clusters have low substructure, so that $\langle n_{\rm e}^2\rangle^{1/2} = \langle n_{\rm e}\rangle$. If significant substructure does exist on a global scale in galaxy clusters then the H_0 estimate will be overestimated by a factor of C^2, where

$$C \equiv \frac{\langle n_{\rm e}^2\rangle^{1/2}}{\langle n_{\rm e}\rangle}. \tag{1.13}$$

Therefore, in order to obtain reliable estimates of H_0 from clusters of galaxies, these systematic errors must be addressed by a proper understanding of the selection effects of the sample and the physical processes that produce significant substructure. Recent measurements of the Hubble constant from cluster SZ samples that were selected based on removing the orientation-systematic include Udomprasert et al. (2004) and Jones et al. (2005). With the commencement of dedicated SZ surveys and subsequent follow-up observations at X-

ray and optical wavelengths, a strong independent estimate of the Hubble Constant should be obtainable. For the work described in this thesis the value of H_0 is assumed to be equal to a fixed value of $70\,\mathrm{kms}^{-1}\mathrm{Mpc}^{-1}$ that is consistent with estimates from the Hubble Space Telescope (HST) Key project (Freedman et al., 2001), the SZ effect from OVRO/BIMA results (Reese et al., 2002) and the WMAP 5-year result (Dunkley et al., 2009).

The gas mass fraction

If instead the angular diameter distance is eliminated in Equations 1.10 and 1.11, then both the electron density and temperature can be estimated from joint SZ effect and X-ray surface brightness observations. The gas mass can then be calculated by integrating the electron density over a spherical volume within a fixed radius and assuming a reasonable value for the number of baryons per electron in the intra-cluster medium. If it is assumed that the cluster gas is also in hydrostatic equilibrium, then an estimate can be made of the total cluster mass, and hence the fraction of mass that is contained within the intra-cluster medium (f_{gas}). The gas mass fraction provides a lower-limit estimate of the enclosed baryonic mass fraction of the cluster, since a small, but finite baryonic mass will be contained within the galaxies. It is also thought that mass segregation does not occur between dark and baryonic matter on the scales from which massive galaxy clusters form. Therefore one would expect that measurements of the average gas mass fraction from a sample of galaxy clusters would be a reasonable lower-limit constraint on the universal baryonic mass fraction (f_{B}). The relationship between the various quantities is given by

$$f_{\mathrm{gas}} \lesssim f_{\mathrm{B}} \equiv \frac{\Omega_{\mathrm{B}}}{\Omega_{\mathrm{M}}}, \tag{1.14}$$

where Ω_{B} and Ω_{M} are the universal density parameters for baryons and matter respectively. If the value of the universal baryonic density parameter is known from primordial CMB observations, as well as the Hubble constant and universal geometry, then a reasonable independent estimate can be made of the matter density parameter (Grego et al., 2001). Recent observations of the SZ effect using the OVRO/BIMA radio interferometers, and X-ray data from the Chandra satellite, have been used to measure the gas mass fraction within r_{2500}. By studying the redshift evolution of the gas mass fraction they find that their results are consistent with the standard ΛCDM cosmological model, and rule out a Universe with $\Omega_{\mathrm{M}} = 1$ and $\Omega_{\Lambda} = 0$

Figure contents property of Third Party. Removed from online version of Thesis.

Figure 1.7: *Left*: The co-moving number density, given by the Press-Schechter formalism, for clusters with masses greater than $10^{14}h^{-1}M_{\odot}$ (upper lines) and $10^{15}h^{-1}M_{\odot}$ (lower lines). The solid and dashed lines represent cosmologies with ($\Omega_{\rm M} = 0.3$, $\Omega_{\Lambda} = 0.7$) and ($\Omega_{\rm M} = 0.5$, $\Omega_{\Lambda} = 0.5$) respectively, with σ_8 fixed at a value of 0.9. This plot was taken from Carlstrom et al. (2002). *Right*: The measured scaling relation between the integrated SZ effect and the hydrostatic total mass within a radius of r_{2500}, using the OVRO and BIMA interferometric arrays and the Chandra X-ray satellite (Bonamente et al., 2008).

(LaRoque et al., 2006). Constraining the gas and total mass of clusters out to larger radii will provide a better estimate of the global value of gas mass fraction and hence a lower-limit to $\Omega_{\rm M}$. The gas mass fraction is also an important indicator of the distribution of baryons in the cluster and hence will be strongly dependent upon its thermal history. Results from X-ray observations by Pratt et al. (2010) find that the intrinsic scatter in the observed entropy profiles of clusters appears to be significantly reduced when scaled by the gas mass fraction at each radius.

Cluster Surveys and the SZ Scaling Relations

Until recently most cluster surveys were conducted almost exclusively at optical and X-ray wavelengths, with follow up observations using the SZ effect. However a number of recent CMB experiments have been constructed that make use of the fact that the SZ surface brightness is independent of redshift, and therefore a powerful method for cluster surveys. These include large bolometer arrays, such as the Atacama Cosmology Telescope (Kosowsky, 2003) and the South Pole Telescope (Ruhl et al., 2004), as well as interferometers such as the Sunyaev-Zel'dovich Array (Muchovej et al., 2007) and the Arcminute Micro-kelvin Imager

(Kneissl et al., 2001). One of the key science goals of these surveys is to provide a constraint on the number of clusters as a function of both mass and redshift, since the behaviour of this quantity is strongly dependent upon cosmology, providing constraints on the values of $\Omega_{\rm M}$, Ω_Λ and σ_8 (see e.g. Carlstrom et al., 2002). The standard Press-Schechter mass function (Press & Schechter, 1974) gives the co-moving number density per unit mass as

$$\frac{{\rm d}n(M,z)}{{\rm d}M} = -\sqrt{\frac{2}{\pi}}\frac{\bar{\rho}}{M^2}\frac{{\rm d}\ln\sigma(M,z)}{{\rm d}\ln M}\frac{\delta_{\rm c}}{\sigma(M,z)}\exp\left[\frac{-\delta_{\rm c}^2}{2\sigma^2(M,z)}\right], \tag{1.15}$$

where $\bar{\rho}$ is the mean background density of the universal at the present epoch, $\sigma^2(M,z)$ is the density field variance when smoothed on a mass scale M, and $\delta_{\rm c}$ is the critical density contrast for spherical gravitational collapse. The density field variance can be separated into the product of functions of mass and redshift as follows

$$\sigma^2(M,z) \equiv \sigma^2(M)D^2(z), \tag{1.16}$$

where $\sigma^2(M)$ is the variance in the initial density field and $D(z)$ is the linear growth function that dictates how the amplitude of the density field grows with redshift (and hence time). This formalism explicitly shows that the abundance of clusters is exponentially suppressed as a function of redshift, dependent upon the behaviour of linear growth function. Since $D(z)$ is sensitive to the cosmological parameters, the exponential suppression of the massive cluster abundance makes surveys using the SZ effect a very powerful tool for cosmology. Figure 1.7 shows the co-moving number density as a function of redshift, for two different mass regimes, highlighting the sensitivity to the values of the matter and dark energy density parameters. The South Pole Telescope has recently reported the detection of three previously unknown clusters (Staniszewski et al., 2009) and it is expected that more clusters will be detected using the SZ effect by both this survey and others.

Current SZ surveys will measure the integrated SZ effect (Y) of a number of previously undetected clusters in an attempt to provide an empirical measurement of the co-moving number density. However, in order to determine the behaviour of the function ${\rm d}n/{\rm d}M$, we require an empirical relationship between Y and the total mass. Hence there is strong motivation for SZ experiments to provide good pointed measurements of known clusters with previous X-ray and weak lensing detections. There have been a number of recent measurements of the scaling between the integrated SZ effect and the total mass, from both hydrostatic

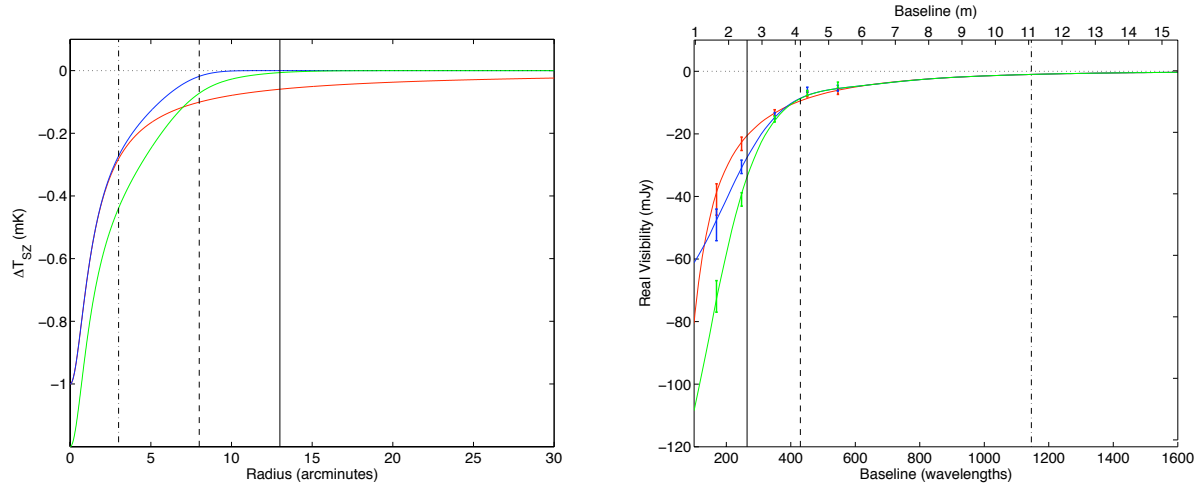

Figure 1.8: *Left:* The change in CMB temperature due to the thermal SZ effect from three clusters, at $z = 0.15$, with different large-scale properties. The vertical lines represent typical radii at r_{2500} (*dashed-dotted*), r_{500} (*dashed*) and r_{200} (*solid*). *Right:* The corresponding real visibility as a function of baseline distance, at $\nu = 31\,\mathrm{GHz}$. The vertical lines represent angular scales corresponding to the three radii. The error bars represent typical data from the CBI2 experiment, including both thermal noise and intrinsic CMB components.

(Benson et al., 2004; Bonamente et al., 2008) and weak lensing (Marrone et al., 2009) estimates. However these relationships were only obtained out to relatively small radii ($\sim 200 - 400\,\mathrm{kpc}$) and observations with experiments such as CBI2, APEX-SZ (Schwan et al., 2003) and AMIBA (Ho et al., 2009) are expected to provide constraints out to a few Mpc ($\sim r_{200}$). Figure 1.8 shows the change in CMB temperature due to the thermal SZ effect, from three clusters at $z = 0.15$, with different large-scale properties. The blue and red profiles have similar radial behaviours within the cluster centre but then diverge at $r \gtrsim r_{2500}$. The green profile has a similar radial behaviour to the blue, but with an additional additive component that produces a larger over-all value for the SZ. The corresponding real visibility profiles show that interferometric experiments can only distinguish between these SZ profiles if one observes on the shortest baselines. In the case of observing at frequencies $\sim 30\,\mathrm{GHz}$, we require an interferometer with baselines smaller than 6 m, making the CBI2 array a perfect instrument for observing the SZ. If instead one were to use an interferometer with baselines longer than this, then it would be difficult to obtain the correct SZ profile at $r \gtrsim r_{2500}$, and to correctly measure the central SZ value. Figure 1.8 also displays the expected data that would be obtained from CBI2 observations of these three SZ profiles. The error-bars include both a thermal noise component

and the intrinsic CMB anisotropy, the latter being significant on baselines shorter than 2.5 m. The error due to the noise will integrate down with the square-root of the observing time whereas the primordial CMB will not. Therefore the sensitivity of radio interferometers to the large-scale SZ effect is ultimately limited by the primordial CMB, and this is discussed further in Chapter 3.

1.3 Cluster properties at other wavelengths

Galaxy clusters emit radiation at a variety of wavelengths and observations of each regime provide an insight into the underlying processes that govern the physical state of the cluster. In the following discussion I give a brief summary of three principal wavelength ranges used to observe galaxy clusters and the information they provide to constrain cluster properties.

1.3.1 Radio

The predominant component of radio emission in clusters originates from radio-loud member galaxies (see Section 1.1.4), and which appear as point sources in relatively low-resolution observations of the CMB. However extended radio sources have also been observed in about 10 % of known galaxy clusters at a range of frequencies from 100 MHz to a few GHz (see e.g. Bacchi et al., 2003; Venturi et al., 2007). These sources are diffuse and hence are associated with the ICM rather than individual galaxies. Their spectra are indicative of non-thermal synchrotron radiation and therefore provide strong evidence for the existence of a diffuse population of relativistic electrons and magnetic fields in some clusters. These sources commonly have steeply declining spectral indices ($\alpha \sim -1$) suggesting an ageing population of relativistic electrons in a strong magnetic field. They are divided into three different observable classes which are briefly discussed here. The reader should refer to the review by Ferrari et al. (2008) for further details.

Halos are extended sources at the centre of clusters with fairly regular morphologies and radii greater than 1 Mpc. The emission from radio halos is typically polarized by a few percent and has a spectral index that steepens with radius. All radio halos observed at present are associated with clusters that have disturbed dynamical states and do not contain cool cores; however not all clusters with these properties contain radio halos. There is observational evidence to suggest a correlation between the radio power of these halos and the luminosity and spectral temperature from X-ray emission. Hence

there may well be a relationship between the distribution of magnetic fields and relativistic electrons and the mass of the host cluster.

Mini halos have a regular morphology that is similar to their giant counter-parts, but are typically much smaller, with radii $\sim 10^2$ kpc. They are found at the centres of cooling clusters where they surround a powerful radio galaxy and their size is similar to that of the cluster cool core region. Since they are associated with cool cores they are usually found in clusters with little evidence of recent merger activity. Less than ten radio mini halos have been observed so far and hence the understanding of the origin of these sources is still fairly limited.

Relics are extended sources with a typically filamentary morphology and steep radio spectra with $\alpha \lesssim -1$. They can roughly be divided further into three types dependent on their size and location in the host cluster. The first group includes small relics of several 10 kpc in size and polarized emission of less than 20 %. These sources are situated near to the central cD galaxy and are typically anti-correlated with the density of the ICM, suggesting they are related to past active galactic nuclei activity from a parent galaxy. The other two groups consist of 10^2 and 10^3 kpc relics that are typically found in the periphery of clusters and have polarized emissions at the level of 10-30 %. Unlike the first group these relic sources are not associated with a parent radio galaxy.

1.3.2 Optical

Optical (and infrared) emission from clusters is dominated by both the member galaxies and those in the background field. While the baryonic mass fraction predominantly consists of the intra-cluster medium, the properties of the galaxy content are still indicative of the global properties of the cluster. The following is a brief discussion of various aspects of the use of optical data, and the reader should refer to the review by Biviano (2008) for further details.

Redshifts can be obtained from both spectral and photometric observations of member galaxies. Spectral redshifts are obtained from strong emission and absorption lines of elements (such as hydrogen, carbon, silicon and iron) by comparing the redshifted lines with their known positions in the rest-frame (see e.g. Broadhurst et al., 2000; Halliday et al., 2004). Photometric redshifts are obtained by

comparing the expected photometric brightness from a template spectrum, with that observed due to redshifting of the spectrum, for a range of wavelength filters. Traditionally spectral line measurements have been a more reliable estimate of redshift and typically have lower associated errors. Recently more precise methods have been developed for use in photometric redshift estimation and, with the onset of large cluster surveys (see e.g. Pelló et al., 2009), the technique has become more popular. Accurately constrained optical redshifts are invaluable for inferring the physical properties of clusters from their observable properties at other wavelengths (such as thermal X-ray emission and the SZ effect) and are used in the work in this thesis.

Richness is essentially a measure of the number of member galaxies contained within a fixed radius of the cluster centre. This characteristic was first used by Abell in 1958 to identify over 2712 clusters from the Palomar Observatory Sky Survey (Abell, 1958). The richness (N), and for that matter the total optical luminosity ($L_{\rm opt}$), can be used as a proxy for the total cluster mass using well calibrated empirical scaling relations. Since there may be many faint galaxies in the cluster, to determine the total cluster N or $L_{\rm opt}$, one must extrapolate a known magnitude distribution function to the these sources. An example of a suitable function is the Schechter luminosity function (Schechter, 1976).

Velocity Dispersion refers to the distribution of galactic velocities that are measured using the Doppler shifts of known spectral lines. The velocity dispersion can be used in conjunction with the virial theorem to produce an estimate of the total cluster mass. Under the assumptions that the cluster is spherical and in virial equilibrium, the total mass is given by

$$M = \frac{3\pi K}{G} R_{\rm h} \sigma_v^2, \tag{1.17}$$

where σ_v^2 is the velocity dispersion, $R_{\rm h}$ is the harmonic mean of the projection spatial distributions of the galaxies (equal to half the viral radius) and K is a correction term to account for not including the whole cluster in the calculation (usually $\sim 0.8 - 0.9$).

Gravitational Lensing is a technique used to directly measure the surface mass distribution in clusters, based on the lensing effect of the gravitational potential on background galaxies. Lensing is divided into two classes based on the relative strength of the deflection. In the case of strong lensing, back-

ground sources will form multiple images, and if the source is extended it will even form arcs. Weak lensing is a more subtle effect that produces an increase in the ellipticity of background sources in a direction tangential to the cluster. Since galaxies are typically elliptical in their nature, weak lensing is a statistical technique that requires averaging over multiple background galaxies in order to produce a reconstructed map of the surface mass distribution. The fractional error associated with the surface mass density will decrease with the number of density of galaxies in the background field. Typically strong lensing occurs within a critical region of the lensing cluster, approximately equal to the central 10 - 100 kpc, while weak lensing can be used to constrain the mass distribution to larger radii. Gravitational lensing produces the most direct estimate of the cluster mass available, but in the absence of adequate redshift information it can suffer from degeneracy of the constrained surface mass distribution. The combination of strong and weak lensing, as well as using background sources at a range of redshifts, is a powerful tool for direct cluster mass estimation (see e.g. Bradač et al., 2005).

1.3.3 X-rays

Continuum X-ray emission in the intra-cluster medium is generated via bremsstrahlung radiation from hot electrons as they scatter off atomic nuclei. In addition to the continuum emission there exist some spectral line features that are generated from the inner shell transitions of heavy elements such as iron. The X-ray spectra from cluster observations are typically well fitted by that of a plasma in collisional equilibrium, with temperatures of $10^7 - 10^8$ K and metallicities approximately equal to 1/3 of the solar abundance. Fitting templates to X-ray spectra, extracted from annuli at increasing radii from the cluster centroid, have successfully allowed astronomers to obtain temperature profiles of the cluster gas out to radii $\sim r_{500}$ (see e.g. Vikhlinin et al., 2006; Pratt et al., 2007; Zhang et al., 2008). The surface brightness of the thermal X-ray emission for a given energy band is related to the physical properties of the cluster gas by the following expression

$$S_{\rm X} = \frac{1}{4\pi(1+z)^4} \int n_{\rm e}^2 \Lambda(T_{\rm e}) {\rm d}l, \tag{1.18}$$

where $\Lambda(T_{\rm e})$ is the emissivity. The emissivity is typically only weakly dependent on the electron temperature ($\Lambda \propto T_{\rm e}^{1/2}$ for pure bremsstrahlung) and so surface brightness measurements provide a strong constraint on the gas density. The combination of fitting joint electron temperature and density models to the X-ray

spectral and surface brightness data allows an estimation of the cluster total mass to be made based on the assumption of hydrostatic equilibrium. However obtaining significant signal-to-noise spectral measurements at large radii is difficult and so enclosed hydrostatic mass estimates can only be obtained for $r \lesssim r_{500}$ with X-ray data alone. The combination of X-ray and weak lensing data uniquely provides us with a tool to probe the relationship between the cluster gas and underlying mass halo, and was successfully used by Clowe et al. (2006) to provide compelling direct evidence for the existence of dark matter.

There is considerable current effort within the community to study the relationship between the X-ray properties of the cluster gas and the total mass; thereby providing a set of well calibrated scaling relations for use in future X-ray surveys (see e.g. Zhang et al., 2008; Pratt et al., 2009). In carrying out studies of these representative cluster samples the understanding of the underlying gas physics has been greatly improved, and it is becoming clear that much of the seemingly complex behaviour in the cluster cores is due to the presence of non-gravitational processes and merger histories. It is hoped that by fully understanding these processes, and their effect on the observable quantities, a better understanding of the intrinsic scatter in the X-ray scaling relations will be obtained.

In addition to the thermal X-ray emission described above, there is some evidence for the existence of non-thermal emission from Compton scattering of relativistic electrons by the CMB radiation. If this non-thermal component can be separated from the thermal emission at energies $\gtrsim 20\,\mathrm{keV}$ then estimates can be made of the magnetic field strength and relativistic electron density in clusters of galaxies. At present limited evidence for non-thermal X-ray emission has been obtained from observations of a few clusters, however the observational and systematic uncertainties, as well as a lack of spatial information, still dominate these observations. It is not clear yet whether the measured excess of hard X-ray emission in a few clusters, above that from thermal Bremsstrahlung, is the result of Compton scattering or perhaps due to other sources such as the energetic jets of active galactic nuclei and binary systems (see e.g. Rephaeli et al., 2008).

1.4 Adopted Cosmology

The following parameters define the adopted cosmological model used throughout this thesis, unless otherwise indicated. In all calculations a flat ΛCDM cosmology is assumed with the following relevant parameters:

Figure contents property of Third Party. Removed from online version of Thesis.

Figure 1.9: *Left*: An X-ray observation of 1E 0657-558 "The Bullet Cluster" by Markevitch et al. (2002) using the Chandra satellite. *Right*: An observation at optical wavelengths of the lensing cluster Abell 1689 by Broadhurst et al. (2005) using the Advanced Camera for Surveys (ACS) on the Hubble Space Telescope.

- $h = 0.7$, where h is the Hubble constant scaled to $100\,\mathrm{kms}^{-1}\mathrm{Mpc}^{-1}$.

- $\Omega_\mathrm{M} = 0.3$, where Ω_M is the matter energy density fraction at the present epoch.

- $\Omega_\Lambda = 0.7$, where Ω_Λ is the dark energy density fraction at the present epoch.

- $\Omega_\mathrm{k} = 0$, where Ω_k is the curvature energy density fraction at the present epoch.

1.5 Thesis Summary

This thesis describes the observation, reduction and analysis of data from pointed observations of the thermal SZ effect using the Cosmic Background Imager 2. The following is a summary of the content of each chapter:

Chapter 2 gives a brief overview of aperture synthesis in the context of observing the Cosmic Microwave Background. The CBI2 array is described in detail, including both the predicted and measured sensitivity from blank field CMB observations.

Chapter 3 describes in detail the observation and subsequent reduction of data taken with the CBI2 array. This includes selection of the cluster sample, scheduling the observations, flagging and calibration of

the raw data, and stacking and gridding the data into a form suitable for analysis.

Chapter 4 presents a parametric model designed for use in returning estimates of physical properties of the galaxy clusters from low-resolution pointed SZ observations and X-ray surface brightness data. The model is tested against mock data created from realistic hydrodynamic/N-body simulations.

Chapter 5 describes CBI2 observations of the Bullet Cluster, a massive cluster that has recently undergone a merger with a smaller sub-cluster. An analysis of the global mass and temperature of the system is performed using joint fits with published X-ray surface brightness data.

Chapter 6 describes the calibration of the thermal SZ scaling relations, from CBI2 observations of the REFLEX-DXL cluster sample at $z \sim 0.3$. Masses and temperatures are estimated from a joint fit with X-ray surface brightness data, and power-law fits are conducted to estimate the relationship between the SZ effect and these quantities.

Chapter 7 concludes this thesis with a summary of the work that is currently being undertaken and that will form the basis of future SZ analysis. In particular there is a wealth of more CBI2 data to be examined, and can be used in a combined analysis with other complimentary SZ experiments.

Chapter 2

The Cosmic Background Imager 2

The Cosmic Background Imager 2 (CBI2) consists of a compact radio interferometer on a single mount, designed specifically for observations of the cosmic microwave background at 26-36 GHz. The CBI2 array is an upgrade to the original CBI experiment (Padin et al., 2002), with a larger antenna collecting area, and is optimised for measuring the SZ effect on angular scales that are not dominated by the intrinsic CMB anisotropies at 31 GHz. Observations involve using aperture synthesis, a technique where the instrument samples a discrete set of angular scales over a source field. The angular scales to which CBI2 is sensitive are ideal for observing the high-ℓ region of the CMB power spectrum, and for measuring the global SZ effect of bright, moderate redshift galaxy clusters.

2.1 Overview of Aperture Synthesis Imaging

Aperture synthesis refers to the technique of measuring the sky brightness distribution by correlating pairs of signals from an array of radio telescopes. The term arises from the fact that the array synthesises an aperture of size equal to the longest baseline, defining the effective resolution of the instrument. The resulting data are not in the form of an image, but rather a discrete sampling of the Fourier transform of the sky brightness, convolved with the aperture response of the antennas. Hence synthesis imaging is a naturally suitable technique for measuring the CMB, where often the quantity of interest is the angular power spectrum. In the following discussion I give a brief overview of aperture synthesis imaging, and derive the equations that are used to relate the data measured by CBI2 to the thermal SZ effect.

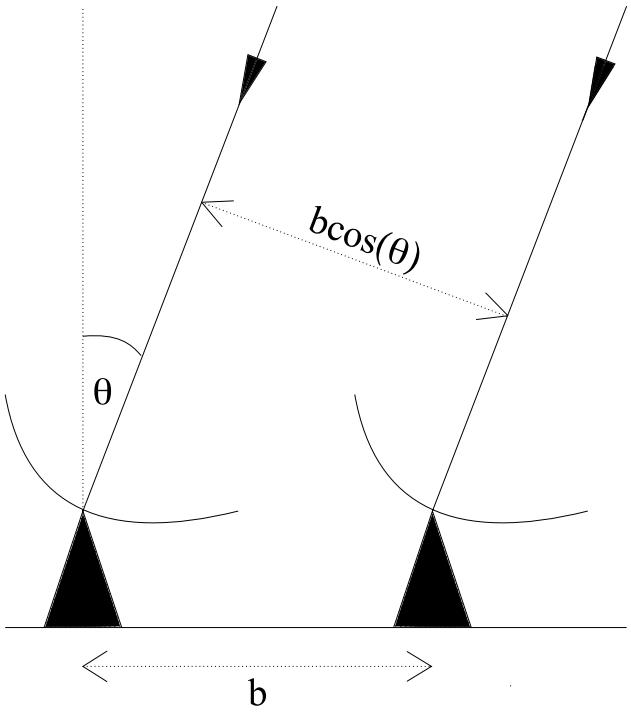

Figure 2.1: A single baseline interferometer, where b is the baseline distance.

2.1.1 The response of a single-baseline interferometer

Consider a far-field signal from a point-like source, arriving at two radio antennas that are both receiving at the same frequency ν and separated by a baseline distance b (see Figure 2.1). The projected baseline is equal to $b\cos(\theta)$, and the time delay between the signals arriving at each antenna is given by $\tau_g = (b/c)\sin(\theta)$. The voltage signals from each receiver, as a function of time and frequency, are then proportional to

$$\begin{aligned} V_1 &\propto \sin(2\pi\nu t) \\ V_2 &\propto \sin(2\pi\nu(t-\tau_g)). \end{aligned} \tag{2.1}$$

For an interferometer like CBI2, the signals from pairs of antennas are combined at a correlator, where they are multiplied together and integrated over time. If for now the effect of finite bandwidth is ignored, then

the product of the above two voltage signals is given by

$$V_1 \times V_2 \propto \sin(2\pi\nu t)\sin(2\pi\nu(t-\tau_g) \tag{2.2}$$

$$\propto \cos(2\pi\nu\tau_g) - \cos(4\pi\nu t)\cos(2\pi\nu\tau_g) - \sin(4\pi\nu t)\sin(2\pi\nu\tau_g). \tag{2.3}$$

The value of $\nu\tau_g$ is much less than that of νt, and so the rapidly-varying latter terms in Equation 2.3 are easily filtered out, leaving the correlator output given by

$$r \propto \cos\left(\frac{2\pi b\sin(\theta)}{\lambda}\right). \tag{2.4}$$

So as the antennas track the source, the angle θ changes with time, and a sinusoidal fringe pattern is generated at the correlator. The correlator integrates the voltage product over a finite time τ_{acc} and this is set to be much less than the period of the fringe rate.

Now consider that the single baseline interferometer is observing a source of finite extent with brightness I, distributed in a direction represented by the unit vector $\hat{\mathbf{s}}$. Note that in the following discussion it is assumed that the spatial components of the source are uncorrelated and that the wave-fronts are planar i.e. the source is in the far-field. The responses of the antennas to the signal power are assumed to be equal (true for arrays with identical antennas) and are expressed as a function of the source direction by $A(\hat{\mathbf{s}})$. Hence, if the gain factors from amplification are ignored, the correlator output for a signal from an element of solid angle of the sky $d\Omega$, over a finite bandwidth $\Delta\nu$, is given by

$$dr = A(\hat{\mathbf{s}})I(\hat{\mathbf{s}})\cos\left(\frac{2\pi}{\lambda}\mathbf{b}\cdot\hat{\mathbf{s}}\right)\Delta\nu d\Omega, \tag{2.5}$$

where $\mathbf{b}$ is a vector with magnitude b and in the direction of the antenna baseline. In the case of pointed observations the interferometer tracks a particular field in the sky, and therefore it is more suitable to take a reference position at the centre of the field-of-view, known as the phase tracking centre. If the direction to the phase tracking centre is represented by the unit vector $\hat{\mathbf{s}}_0$, the direction to a given source element is then given by $\hat{\mathbf{s}} = \hat{\mathbf{s}}_0 + \hat{\sigma}$, where $\hat{\sigma}$ is the direction of the element with respect to the phase tracking centre. The source brightness and antenna response are now re-defined so that they are centred in the direction $\hat{\mathbf{s}}_0$, and

hence the correlator output from a solid angle element is given by

$$\mathrm{d}r = A(\hat{\boldsymbol{\sigma}})I(\hat{\boldsymbol{\sigma}})\left[\cos\left(\frac{2\pi}{\lambda}\mathbf{b}\cdot\hat{\mathbf{s}}_0\right)\cos\left(\frac{2\pi}{\lambda}\mathbf{b}\cdot\hat{\boldsymbol{\sigma}}\right) - \sin\left(\frac{2\pi}{\lambda}\mathbf{b}\cdot\hat{\mathbf{s}}_0\right)\sin\left(\frac{2\pi}{\lambda}\mathbf{b}\cdot\hat{\boldsymbol{\sigma}}\right)\right]\Delta\nu\mathrm{d}\Omega. \tag{2.6}$$

This expression is integrated over the solid angle of the sky to obtain the total correlator output, noting that in practice the response of an antenna is zero over most of the sky,

$$\begin{aligned} r &= \Delta\nu\cos\left(\frac{2\pi}{\lambda}\mathbf{b}\cdot\hat{\mathbf{s}}_0\right)\int_{\mathrm{sky}} A(\hat{\boldsymbol{\sigma}})I(\hat{\boldsymbol{\sigma}})\cos\left(\frac{2\pi}{\lambda}\mathbf{b}\cdot\hat{\boldsymbol{\sigma}}\right)\mathrm{d}\Omega \\ &- \Delta\nu\sin\left(\frac{2\pi}{\lambda}\mathbf{b}\cdot\hat{\mathbf{s}}_0\right)\int_{\mathrm{sky}} A(\hat{\boldsymbol{\sigma}})I(\hat{\boldsymbol{\sigma}})\sin\left(\frac{2\pi}{\lambda}\mathbf{b}\cdot\hat{\boldsymbol{\sigma}}\right)\mathrm{d}\Omega. \end{aligned} \tag{2.7}$$

The *visibility*, a complex quantity that is essentially a measure of the coherence of the electric field modified by the principle characteristics of the interferometer, is now defined by the following expression

$$\mathscr{V} \equiv |\mathscr{V}|\mathrm{e}^{\mathrm{i}\phi_{\mathscr{V}}} = \int_{\mathrm{sky}} \mathscr{A}(\hat{\boldsymbol{\sigma}})I(\hat{\boldsymbol{\sigma}})\mathrm{e}^{-2\pi\mathrm{i}\mathbf{b}\cdot\hat{\boldsymbol{\sigma}}/\lambda}\mathrm{d}\Omega, \tag{2.8}$$

where $\mathscr{A}(\hat{\boldsymbol{\sigma}}) = A(\hat{\boldsymbol{\sigma}})/A_0$ is the antenna response normalised by the central value A_0. Substituting this expression into Equation 2.7 gives

$$r = A_0\Delta\nu|\mathscr{V}|\cos\left(\frac{2\pi}{\lambda}\mathbf{b}\cdot\hat{\mathbf{s}}_0 - \phi_{\mathscr{V}}\right). \tag{2.9}$$

The aim of observation is to produce a measurement of the source brightness, $I(\hat{\mathbf{s}})$, and this can be done by performing the inverse of the transformation given in Equation 2.8. By correctly calibrating the amplitude and phase of the correlator output (remembering that the input voltage signals will include gain factors due to amplification) we can obtain a measurement of the amplitude and phase of $\mathscr{V}$. In order to generate a good reconstruction of the source brightness, the complex visibility has to be measured over a sufficiently wide range of $\mathbf{b}\cdot\hat{\mathbf{s}}/\lambda$. This is the component of the baseline normal to the source direction, measured in units of wavelengths. Therefore in most applications interferometry is performed with an array of radio telescopes, rather than a single baseline, so as to produce a wide range of $\mathbf{b}$ and therefore adequately sample the visibility function. In the next few sections I will move the discussion away from single-frequency and single-baseline to a real multi-antenna, finite bandwidth interferometer.

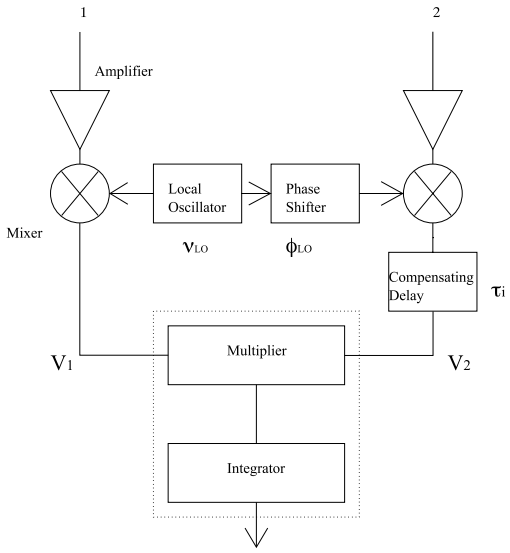

Figure 2.2: A simple two element interferometer showing the basic components required to process the voltage signal.

2.1.2 Bandwidth and frequency conversion

Consider a two element interferometer as shown in Figure 2.2 with input sky signals 1 and 2. The input radio frequency (RF) signal is amplified by a gain factor that is later calibrated-out by observing a bright astronomical source of known brightness. The amplifier response has a characteristic passband as a function of frequency, which ideally will be a rectangular function (the CBI2 bandwidth for each frequency channel is nominally 1 GHz). To derive the correct correlator response for a rectangular pass-band, centred on a frequency ν_0, the expression given in Equation 2.9 must be integrated over frequency as follows

$$\begin{aligned} r &= A_0|\mathscr{V}|\int_{\nu_0-\Delta\nu/2}^{\nu_0+\Delta\nu/2}\cos(2\pi\nu\tau_g-\phi_{\mathscr{V}})\mathrm{d}\nu \\ &= A_0|\mathscr{V}|\Delta\nu\frac{\sin(\pi\Delta\nu\tau_g)}{\pi\Delta\nu\tau_g}\cos(2\pi\nu\tau_g-\phi_{\mathscr{V}}). \end{aligned} \tag{2.10}$$

where $\tau_g = \mathbf{b}\cdot\hat{\mathbf{s}}_0/c$. Therefore the effect of the finite receiver passband is to generate a modulating envelope over the fringe pattern in the correlator output, as a function of the geometric time delay between the pair of antennas. In order to observe at a wide range of hour angles, and also compensate for τ_g, an additional instrumental time delay (τ_i) is often introduced in one of the input signals.

The processes of amplification, delaying and cross-correlation, mentioned above, are technically dif-

ficult to perform at radio frequencies and so the two input signals are usually down-converted to a lower intermediate frequency (IF). This is performed by combining the RF signal with a local oscillator signal at a single frequency $\nu_{\rm LO}$, using a component called a mixer. Mixers have a non-linear response, and combine the signal frequencies as follows

$$\nu_{\rm RF} = \nu_{\rm LO} \pm \nu_{\rm IF}. \tag{2.11}$$

So a mixer responds to two pass-bands (known as the upper and lower sidebands). Usually only one sideband is used, the other being filtered out before the signal reaches the mixer. If the relative phases are considered for the two correlator inputs, as a result of the geometrical delay and the signal processing (see Figure 2.2), in the case of a lower sideband system we have

$$\phi_1 = -2\pi(\nu_{\rm LO} - \nu_{\rm IF})\tau_{\rm g} \tag{2.12}$$

$$\phi_2 = 2\pi\nu_{\rm IF}\tau_{\rm i} - \phi_{\rm LO}, \tag{2.13}$$

where $\phi_{\rm LO}$ is the relative phase difference introduced between the local oscillator signals injected into the two mixer inputs. Hence the response of the correlator in a lower sideband system, again ignoring the gain factor from amplification, is given by

$$r = A_0 \Delta\nu |\mathscr{V}| \frac{\sin(\pi\Delta\nu\Delta\tau)}{\pi\Delta\nu\Delta\tau} \cos\left(2\pi(\nu_{\rm LO}\tau_{\rm g} - \nu_{\rm IF0}\Delta\tau) - \phi_{\mathscr{V}} - \phi_{\rm LO}\right), \tag{2.14}$$

where $\nu_{\rm IF0}$ is the centre frequency of the IF band and $\Delta\tau = \tau_{\rm g} - \tau_{\rm i}$. The amplitude and phase of the visibility for the baseline can be reproduced by calibrating the various instrumental components. Many interferometers in practice use a complex correlator, which has two outputs for every baseline. One output produces the cosine response as described above, however the second output has the form of a sine response, where a $\pi/2$ phase difference has been added between the input signals. Therefore the calibrated response of these two outputs is essentially equal to the real and imaginary components of the complex visibility.

2.1.3 Re-constructing the source brightness

In order to reconstruct the source brightness from the measured visibility, one can perform the inverse transformation of that stated in Equation 2.8. Coordinate systems are chosen at the aperture and source

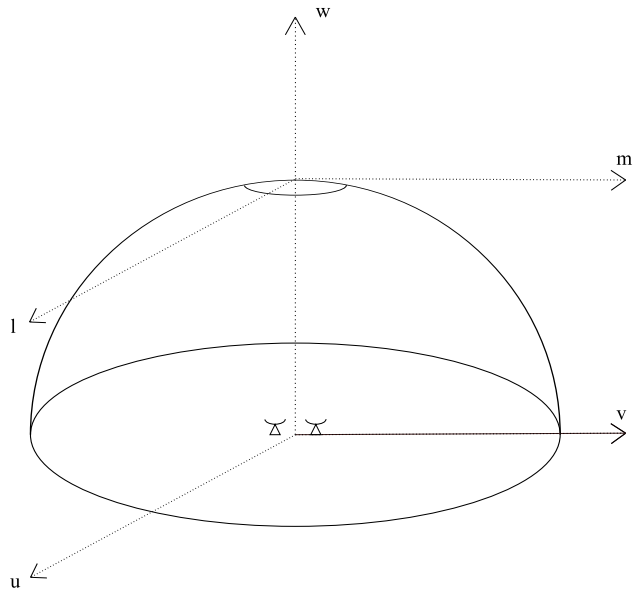

Figure 2.3: The coordinate system used in interferometry where the w axis in this case lies along the direction to the centre of the source field. If the field-of-view is considered to be small enough, then when projected from the celestial sphere onto the (l,m) plane, the (u,v) plane defines the coordinate system for the Fourier transform of the source.

positions in order to make this inverse transformation practicable. The coordinate system at the aperture is defined by the components of the baseline vector, (u,v,w), where w is the component in the direction of the phase tracking centre and u and v are in the plane perpendicular to this direction, and are defined in units of wavelengths. The position on the sky is given by (l,m,n), where l and m are the direction cosines measured with respect to the u and v axes, and (l,m) is the projection of the celestial sphere onto the tangent plane (see Figure 2.3). Hence the projected baselines and the solid angle used in the expression for the visibility are now given by

$$\frac{\mathbf{b}\cdot\hat{\mathbf{s}}}{\lambda} = ul+vm+wn \tag{2.15}$$

$$\frac{\mathbf{b}\cdot\hat{\mathbf{s}}_0}{\lambda} = w \tag{2.16}$$

$$d\Omega = \frac{\mathrm{d}l\mathrm{d}m}{n}, \tag{2.17}$$

where $n = \sqrt{1-l^2-m^2}$. The visibility in terms of the normalised aperture response and source brightness now becomes

$$\mathscr{V}(u,v,w) = \iint \mathscr{A}(l,m) I(l,m) \mathrm{e}^{-2\pi \mathrm{i}(ul+vm+w(n-1))} \frac{\mathrm{d}l\mathrm{d}m}{n}. \tag{2.18}$$

This expression simplifies to a two dimensional Fourier transform for small fields (i.e. l and m are small) where $\sqrt{1-l^2-m^2} \approx 1$. In this case the visibility and the sky brightness are given by

$$\mathscr{V}(u,v) = \iint \mathscr{A}(l,m) I(l,m) \mathrm{e}^{-2\pi \mathrm{i}(ul+vm)} \mathrm{d}l\mathrm{d}m \tag{2.19}$$

$$I(l,m) = \frac{1}{\mathscr{A}(l,m)} \iint \mathscr{V}(u,v) \mathrm{e}^{2\pi \mathrm{i}(ul+vm)} \mathrm{d}u\mathrm{d}v, \tag{2.20}$$

where u and v now define spatial frequencies in the source brightness distribution. However in practice it is not possible for an array of discrete radio antennas to continuously sample the aperture plane, and therefore the inverse transform of the measured visibility does not reproduce an exact copy of the true source brightness. The actual image reconstructed from an interferometer is equal to the true sky image, multiplied by the normalised antenna response and convolved with the inverse Fourier transform of the visibility sampling function $S(u,v)$, known as the synthesised or 'dirty' beam. Hence the 'dirty' image is related to the complex visibility function by the following expression

$$\begin{aligned} I_{\mathrm{dirty}}(l,m) &= [\mathscr{A}(l,m) I(l,m)] \star \mathrm{FT}^{-1}(S(u,v)) \\ &= \iint \mathscr{V}(u,v) S(u,v) \mathrm{e}^{2\pi \mathrm{i}(ul+vm)} \mathrm{d}u\mathrm{d}v. \end{aligned} \tag{2.21}$$

Figure 2.4 demonstrates the effect of discrete sampling in the (u,v) plane on a typical source brightness distribution from the thermal SZ effect. The effect of sampling a finite baseline distance is to not resolve the source on small scales. The finite size of the antennas also prevents sampling at the zero baseline spacing and hence the interferometer cannot directly measure the total source brightness. The exact geometry of the sampling function will also generate features (known as side-lobes) in the synthesised beam and hence these will be present in the reconstructed dirty image. It is often desirable to remove side-lobes from the image in order to make obscured source features clearer. This can be done using the CLEAN algorithm (Högbom, 1974), which is used throughout this thesis when presenting maps from CMB observations.

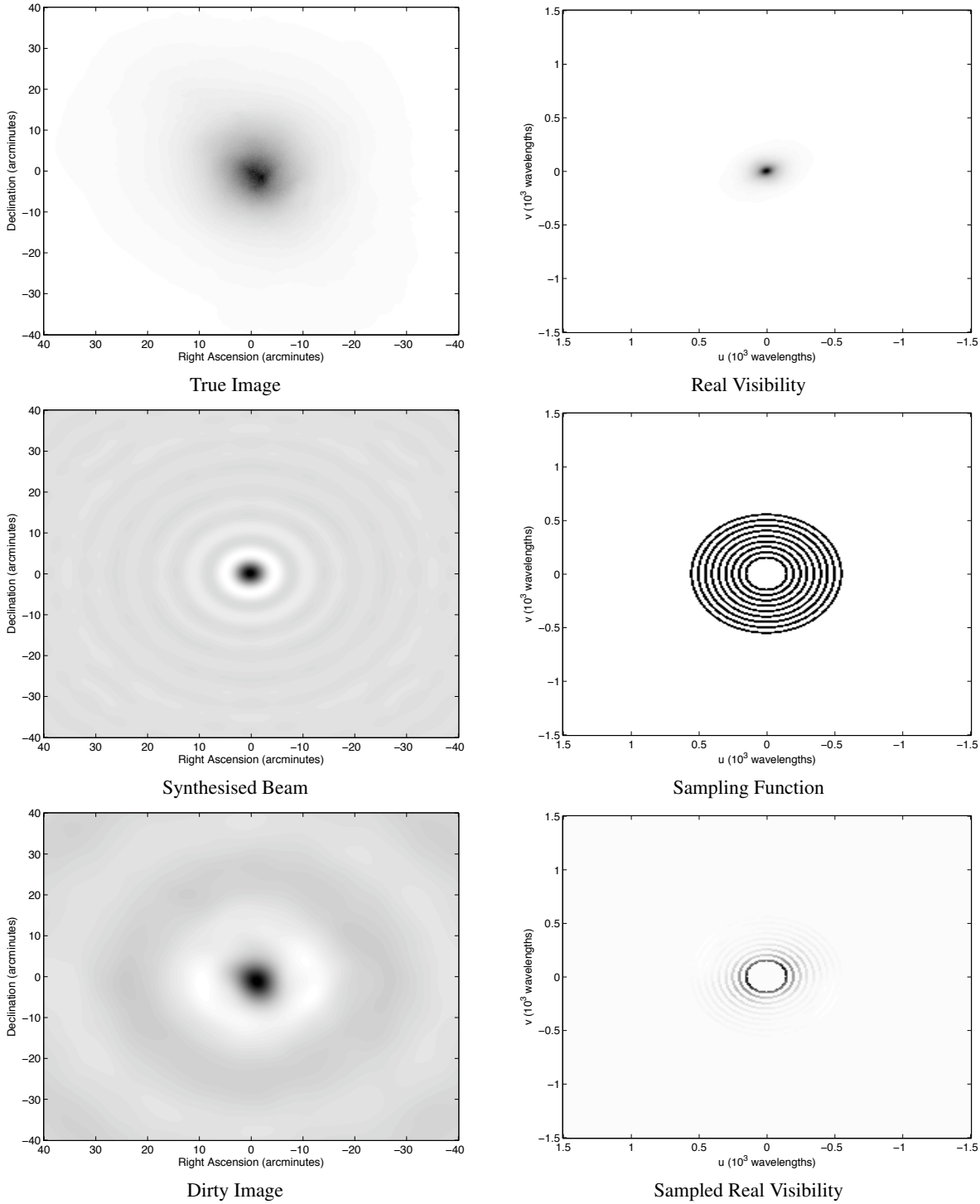

Figure 2.4: A demonstration of the effect of finite sampling on the reconstructed source image from interferometric data. The true source brightness distribution is the SZ effect from a simulated galaxy cluster. The sampling function covers an area of the (u,v) plane similar to that of the baseline range available to CBI2, and is constructed from loci spaced at 50 wavelength intervals. The frames on the right are the Fourier transforms of those adjacent on the left.

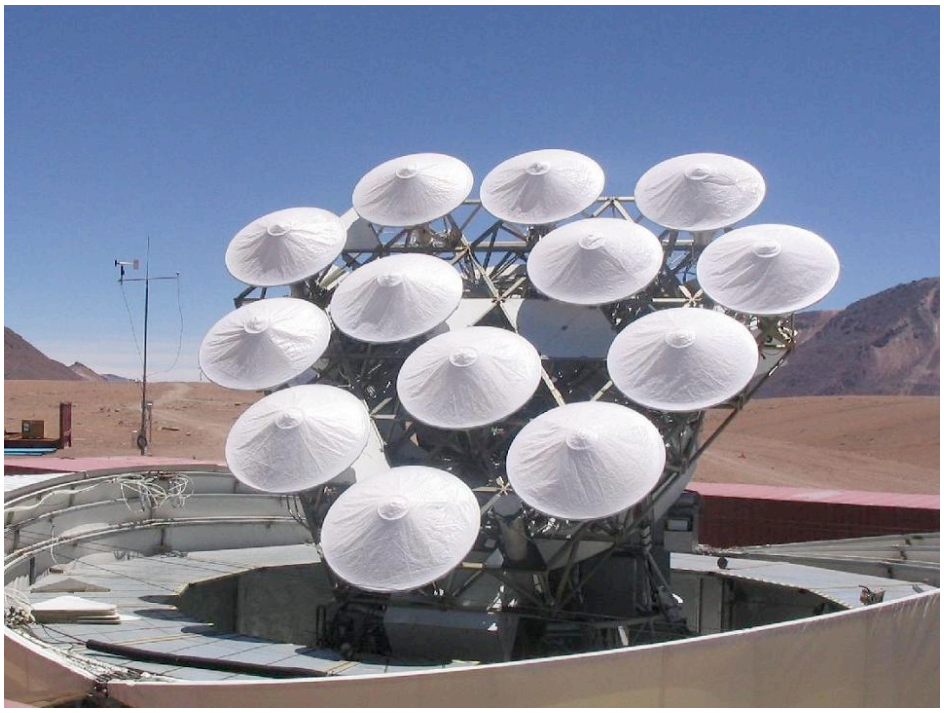

Figure 2.5: A photograph of the CBI2 array at the Chajnantor Observatory in Chile, showing the 1.4 m antennas mounted on the 6 m rotatable deck. The dishes are covered by fabric tarpaulins to prevent exposure to the extremes of weather on the Chajnantor Plateau.

2.2 Interferometry with CBI2

CBI2 is a 13 element interferometer observing at frequencies in the range 26-36 GHz, separated into ten 1 GHz channels. The field-of-view is dictated by the antenna size of 1.4 m, which at 31 GHz corresponds to a full-width at half-maximum (FWHM) of 28.2 arcminutes. The longest possible baseline distance in the array is 5.5 m ($\approx$ 550 wavelengths), which corresponds to a synthesised beam width of 6 arcminutes at 31 GHz.

2.2.1 The mount and tracking platform

The CBI2 experiment is an unusual interferometer because the antennas are co-mounted and so the projected baseline distances are equal to the corresponding antenna spacings. Hence there is no geometrical time delay τ_g between pairs of antennas and so there is no requirement to introduce an instrumental delay in order to compensate for this effect. The CBI2 mount consists of a basic azimuth and elevation axis, with an additional

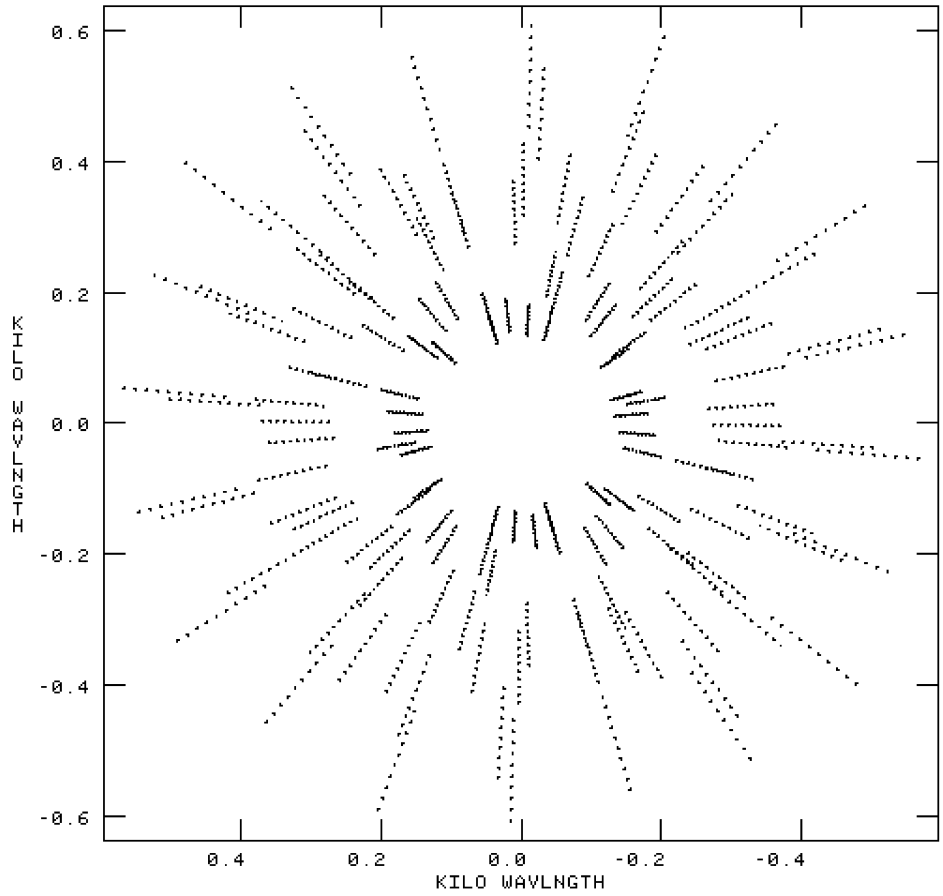

Figure 2.6: A snapshot of the instantaneous (u,v) coverage for the CBI2 array (13 antennas, 10 frequency channels).

third axis provided by a rotatable tracking platform (deck), upon which the antennas are mounted. The deck motion allows rotation of the antenna baselines in the aperture plane, providing the (u,v) coverage usually obtained in a larger interferometer by the Earth's rotation. During an observing run the deck is rotated every few minutes through a discrete set of offset angles, so as to sample a wide range of (u,v) coordinates.

Continuous deck rotation would also allow one to measure spurious signals from ground emission or antenna cross-talk. The spurious signal would rotate with the array while the source would not, allowing the unwanted signal to be filtered out. However in practice any spurious signals were removed after observation by subtraction of the signal in 'blank' reference fields separated from the source field in right ascension (see Chapter 3).

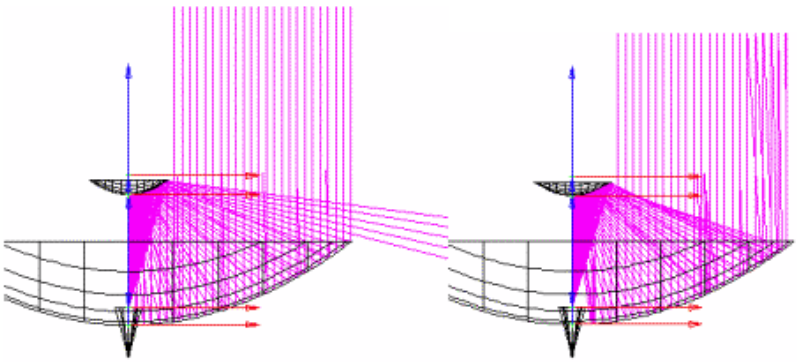

Figure 2.7: Ray trace diagram of a CBI2 antenna showing the effect of an over-sized hyperbolic secondary mirror (left) and the effect of re-shaping the edge of the secondary mirror (right).

2.2.2 The antennas and array

For the CBI2 experiment the original Cosmic Background Imager was upgraded from 0.9 to 1.4 m antennas in order to make full use of the the physical size of the tracking platform. The aim of the upgrade was to have an instrument with twice the effective collecting area, greatly improving the sensitivity on the longest baselines (especially on angular scales in the range 4-15 arcminutes). For moderately massive clusters the virial radii typically have values ~ 2 Mpc, which at a redshift of 0.15 correspond to an angular size of 12 arcminutes. Therefore the new array improves the sensitivity of the instrument for probing the cluster gas right to the outskirts. On these scales the intrinsic CMB anisotropies are also significantly smaller than the noise and hence the sensitivity of the instrument to the thermal SZ is greatly improved in this regime.

The new antennas are an on-axis Cassegrain design, where the hyperboloid secondary mirror is supported by a Zotefoam cone that is transparent to radiation at the frequencies observed by CBI2. In both the original and new antenna designs the secondary mirrors were over-sized in order to increase the illumination of the aperture. While this improves the efficiency of the aperture it means that the ray paths from the secondary extend over the edge of the primary mirror. The array is relatively compact (the shortest baseline is 1.4 m) and so cross-talk can arise between adjacent antennas, whereby the secondary mirror of one antenna is coupled to the feed of the other. Any signal that enters the antenna feed from the spill-over side-lobe will be present in the correlator output and will generate a spurious signal in the data. As well as cross-talk between adjacent antennas, spurious signals can arise from ground emission and are especially strong when

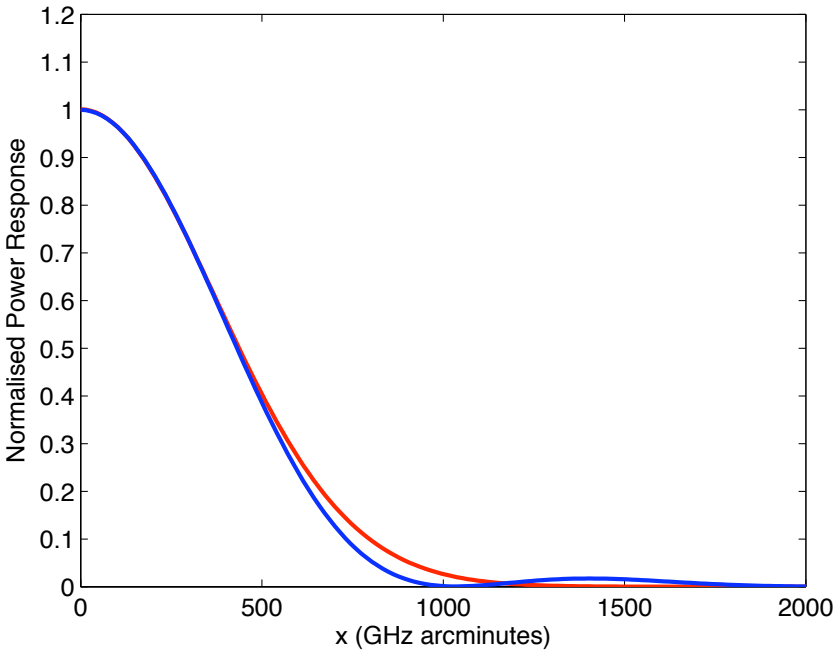

Figure 2.8: The CBI2 primary beam (blue) and fitted Gaussian model (red) with a 28.2 arcminute FWHM at 31 GHz. Assuming a Gaussian model for the primary beam at radii greater than FWHM/2 will therefore lead to a systematic error in the estimated source brightness in this region of the field.

the array is observing at low elevations. In order to reduce both these spurious signals in the original array, the antennas were encased in a metal can extending above the primary mirror rim by 40 cm. The cans were designed to reflect the spill-over to wide angles of the sky and were found to reduce the amplitude of the spill-over side-lobes by 30 dB (Padin et al., 2002). For the CBI2 upgrade the spill-over was reduced by re-shaping the outer part of the secondary mirrors and so re-directing the spill-over pattern onto the primary (see Figure 2.7). GRASP[1] simulations of the beam pattern for the new antennas show that re-shaping the secondary mirrors reduces the side-lobes by a further 20 dB on top of that obtained by the cans in the original design. Figure 2.8 shows the calculated primary beam response as a result of these simulations, along with a fitted Gaussian model with a FWHM of 28.2 arcminutes at 31 GHz. This plot shows that the Gaussian model is a good description of the primary beam out to the half-power, however if one wishes to re-construct the source image at larger radii then a more accurate model is required.

[1] http://www.ticra.com/

Figure contents property of Third Party. Removed from online version of Thesis.

Figure 2.9: The system diagram for CBI2, showing the receiver details for two antennas, and hence the correlator readout for one baseline in band 0 (Padin et al., 2002).

2.2.3 Signal Processing

Figure 2.9 shows the diagram for the receiver and correlator readout system in CBI2. Each antenna in the CBI2 array is connected to a heterodyne receiver with a 26-36 GHz high electron mobility transistor (HEMT) amplifier, a Shottky Mixer and a 2-12 GHz IF amplifier. A two stage refrigerator is used to cool the components of the receiver down to 8 K, with compressed helium being supplied by compressors mounted around the azimuth axis of the telescope. The antenna signal is passed from the HEMT amplifier, through a low-pass filter and mixed with a 38 GHz signal from a local oscillator. The down-converted 2-12 GHz IF signal is then passed through a filter bank where it is split into ten channels. Each channel is then further down-converted to generate the 1-2 GHz input band at which the correlator multipliers operate. For each band, the 13 signal inputs to the correlator require 156 multipliers to measure the real and imaginary parts of the visibility. The complex correlator produces 780 baseline-channel visibility outputs sampled every 4.2 s and has an efficiency in the range 0.9-1. Measurements of the correlated signal from a noise source generator by Padin et al. (2002) found the total system efficiency to be in the range 0.8-1, dependent upon

the passband errors for each channel.

2.3 Sensitivity

The noise in CBI2 data is generated by a number of independent sources, including the receiving electronics of the instrument, the antennas, the ground surrounding the telescope, the atmosphere at the site and the source signal. The following discussion describes these various components in the noise, derives the expected level and compares this with the measured value from CBI2 observations.

2.3.1 Receiver Noise

The sensitivity of CBI2 is predominantly set by the Johnson-Nyquist noise generated in the receiving electronics, and principally the HEMT amplifiers (Padin et al., 2002). The charge carriers within the instrument move randomly at finite temperatures producing an oscillating voltage within the conducting medium (Johnson, 1928). The RMS voltage at a finite system temperature $T_{\rm n}$ and bandwidth $\Delta\nu$ is given by the Nyquist relation (Nyquist, 1928)

$$v_{\rm n} = \sqrt{4Rk_{\rm B}T_{\rm n}\Delta\nu}, \tag{2.22}$$

where R is the resistance of the conducting medium. If the noisy resistive system is modelled as a voltage source and an ideal resistor R, matched by a resistance load, then the effective noise power available is given by

$$P_{\rm n} = k_{\rm B}T_{\rm n}\Delta\nu. \tag{2.23}$$

Note that the noise power is independent of both the resistance and the frequency, and depends only the system temperature and the bandwidth.

For a single radio antenna observing the sky with total flux density $S_{\rm T}$, the antenna power is given by the Rayleigh-Jeans approximation as follows

$$P_{\rm a} = \frac{1}{2}g^2\eta_{\rm a}AS_{\rm T}\Delta\nu, \tag{2.24}$$

where A is the effective collecting area, $\eta_{\rm a}$ is the antenna efficiency and g is the amplifier gain. The factor of

two arises in Equation 2.24 because a single channel receiver can only measure half the total radiation from an unpolarized source. The antenna temperature $T_{\rm a}$ is then related to the total flux density by

$$T_{\rm a} = S_{\rm T}\left(\frac{\eta_{\rm a} A}{2k_{\rm B}}\right). \tag{2.25}$$

Hence, under the assumption that the source and noise voltages are uncorrelated, the expected total power from a single antenna is given by the sum of the source and noise components respectively

$$\begin{aligned} \langle P_{\rm i} \rangle &= P_{\rm ai} + P_{\rm ni} \\ &= g_{\rm i}^2 k_{\rm B} (T_{\rm ai} + T_{\rm ni}) \Delta\nu. \end{aligned} \tag{2.26}$$

In the case of interferometric data we are interested in calculating the power of the correlated product of voltage signals from pairs of antennas. The following is a very brief derivation of the expected noise level in the correlated output from an interferometer, and for more detail the reader should refer to the review by Wrobel & Walker (1999). For an interferometer with antennas of equal collecting area, the expected power after cross-multiplication is given by

$$\left\langle P_{\rm ij} \right\rangle = g_{\rm i} g_{\rm j} \left(\frac{\sqrt{\eta_{\rm ai}\eta_{\rm aj}}}{2\eta_{\rm s}}\right) A S_{\rm c} \Delta\nu, \tag{2.27}$$

where $S_{\rm c}$ is the correlated flux density and $\eta_{\rm s}$ is the system efficiency factor. The noise level in the correlator output can be calculated by taking the root mean square (RMS) of the correlated product of the antenna voltages given by

$$\sigma(P_{\rm ij}) = \sqrt{\left\langle P_{\rm ij}^2 \right\rangle - \left\langle P_{\rm ij} \right\rangle^2}, \tag{2.28}$$

where $\left\langle P_{\rm ij}^2 \right\rangle$ is the expectation value of the square of the correlated product. This quantity is given in terms of the total incident flux density ($S_{\rm T}$), the correlated flux density ($S_{\rm c}$) and system temperature for each antenna ($T_{\rm ni}$) by the following expression

$$\left\langle P_{\rm ij}^2 \right\rangle = g_{\rm i}^2 g_{\rm j}^2 \left(\frac{\eta_{\rm ai}\eta_{\rm aj}}{4\eta_{\rm s}^2}\right) A^2 \left[2S_{\rm c}^2 + \left(S_{\rm T} + \frac{2k_{\rm B}T_{\rm ni}}{\eta_{\rm ai}A}\right)\left(S_{\rm T} + \frac{2k_{\rm B}T_{\rm nj}}{\eta_{\rm aj}A}\right)\right] \Delta\nu^2. \tag{2.29}$$

For a correlator with accumulation time $\tau_{\rm acc}$, the noise level per visibility sample is calculated by dividing $\sigma(P_{\rm ij})$ by the product $g_{\rm i}g_{\rm j}\sqrt{\eta_{\rm ai}\eta_{\rm aj}}A\Delta\nu/2$, in order to convert the cross-correlated power into source flux density units, and by the square root of the number of independent correlator samples $\sqrt{2\Delta\nu\tau_{\rm acc}}$. In which case the noise level in each of the real and imaginary correlator outputs is then given by

$$\Delta S_{\rm ij} = \frac{1}{\eta_{\rm s}\sqrt{2\Delta\nu\tau_{\rm acc}}}\sqrt{S_{\rm c}^2 + S_{\rm T}^2 + 2S_{\rm T}\left(\frac{2k_{\rm B}T_{\rm n}}{\eta_{\rm a}A}\right) + \left(\frac{2k_{\rm B}T_{\rm n}}{\eta_{\rm a}A}\right)^2}, \tag{2.30}$$

where for simplicity it is assumed that the antennas on CBI2 have identical system temperatures $T_{\rm n}$ and efficiencies $\eta_{\rm a}$. For CMB observations the astronomical source signal contributes a tiny fraction of the noise and so the last term in the above expression dominates. Hence in this limit the noise is given by

$$\Delta S_{\rm ij} = \frac{1}{\eta_{\rm s}\sqrt{2\Delta\nu\tau_{\rm acc}}}\left(\frac{2k_{\rm B}T_{\rm n}}{\eta_{\rm a}A}\right). \tag{2.31}$$

In the absence of other contributions to the noise power, the antenna and receiving electronics contribute a system temperature of $T_{\rm n} \sim 30\,{\rm K}$ (Padin et al., 2002). Typical values for the CBI2 array include an effective antenna collecting area of $0.8\,{\rm m}^2$, effective bandwidth of $\sim 0.85\,{\rm GHz}$, correlator accumulation time of $4.2\,{\rm s}$ and a system efficiency of $\sim 90\%$. Hence one would expect the CBI2 RMS noise level (in the absence of the atmospheric, CMB and ground contributions) to be approximately equal to $1.4\,{\rm Jy}$ per sample.

2.3.2 The Atmosphere

In addition to the electronics of the instrument, the atmosphere also contributes to the overall system temperature of the instrument. The atmosphere acts as an absorbing medium, which is assumed to be in local thermodynamic equilibrium with a temperature $T_{\rm atm}$. In the case of a neutral absorbing medium the intensity of the signal I_ν passing through the atmosphere obeys the equation of radiative transfer

$$\frac{{\rm d}I_\nu}{{\rm d}h} = -\alpha(I_\nu - B_\nu(T_{\rm atm})), \tag{2.32}$$

where α is the absorption coefficient, B_ν is the black body intensity at temperature $T_{\rm atm}$ and dh is the change in height. In the Rayleigh-Jeans approximation this equation can be re-written in terms of the Rayleigh-Jeans

brightness temperature $T_{\rm a}$ (Rybicki & Lightman, 1979)

$$\frac{{\rm d}T_{\rm a}}{{\rm d}h} = -\alpha(T_{\rm a} - T_{\rm atm}). \tag{2.33}$$

Integrating the above equation over the height, and assuming a constant value for $T_{\rm atm}$, one obtains the following expression for the brightness temperature at the antenna

$$T_{\rm a}(\nu) = T_{\rm a,0}(\nu){\rm e}^{-\tau_\nu} + T_{\rm atm}(1 - {\rm e}^{-\tau_\nu}), \tag{2.34}$$

where τ_ν (the optical depth) is equal to the integral of the absorption coefficient from the instrument to infinity. The optical depth is proportional to the path length through the atmosphere and hence varies approximately as $\sec(z)$, where z is the zenith angle. The first term in Equation 2.34 represents the attenuation of the source signal ($T_{\rm a,0}$) due to absorption, while the second term corresponds to the emission due to the finite temperature of the atmosphere, acting as an effective extra noise temperature component in the signal. At 31 GHz the astronomical signal is attenuated mainly by absorption due to the presence of the 22 GHz water vapour transition line (Waters, 1976). Hence the dry site at the Chajnantor observatory is a good choice for CMB observations at this frequency, with the atmospheric contribution to the noise varying from $\sim$ 1-5 K (equivalent to a noise level of $\sim$ 0.05-0.2 Jy per sample). Therefore at the CBI2 site the atmosphere is not the dominant factor for sensitivity.

2.3.3 Other contributions to the noise

Any other finite signal will also contribute to the overall system temperature of the instrument and hence act to increase the noise level in the correlator output. When observing the CMB, the sky has a temperature of 2.728 K (Fixsen et al., 1996) and hence this will generate noise $\sim$ 0.1 Jy per sample. Emission from the ground can also leak into the antennas and is especially strong when CBI2 is observing at low elevations where the signal can reflect off the sides of the antenna and enter the receiver. At lower elevations the ground spill-over contribution is estimated to be $\sim$ 5 K, degrading the system sensitivity by up to $\sim$ 0.2 Jy. While these extra contributions to the noise are individually much less than the receiver noise, when combined they do contribute a significant fraction of the noise level.

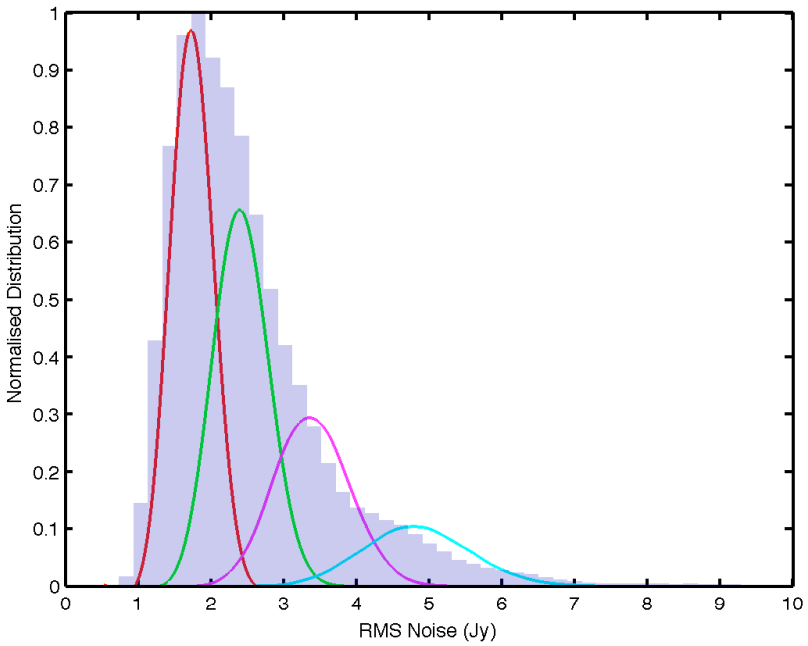

Figure 2.10: A histogram of the RMS noise per sample, normalised to unity, from CBI2 intrinsic CMB observations. The CMB fields are considered not to contain any significant source of 31 GHz radiation in addition to the cosmic microwave background. They are therefore chosen to characterise the instrument's noise level. The coloured solid lines demonstrate that the overall RMS noise is a superposition of individual Rician distributions (Rice, 1945).

2.3.4 The measured sensitivity

The sensitivity of CBI2 is expected to be in the range of ∼1.4-2 Jy per correlator sample, based on the above contributions to the total system temperature. Figure 2.10 shows the noise from CBI2 observations of CMB fields over the period 1st April 2007 to 10th May 2008. The RMS noise was calculated using the match_ha command in CBICAL[2] and is based on the mean RMS of the real and imaginary visibilities after subtraction of the time-average sky signal. Each datum is generated from approximately 23 samples of the correlator output. The distribution of RMS noise values is expected to be given by a Rician distribution that peaks at the square-root of the variance in the visibilities (Rice, 1945). The measured peak in the RMS noise histogram lies within the expected range for CBI2, but with a tail in the distribution to larger noise values. This high-noise tail originates from baselines that contain warmer than average receivers, i.e. those having higher system temperatures. The measured distribution of RMS values contains contributions from data with

[2]T. J. Pearson, http://www.astro.caltech.edu/∼tjp/CBI/

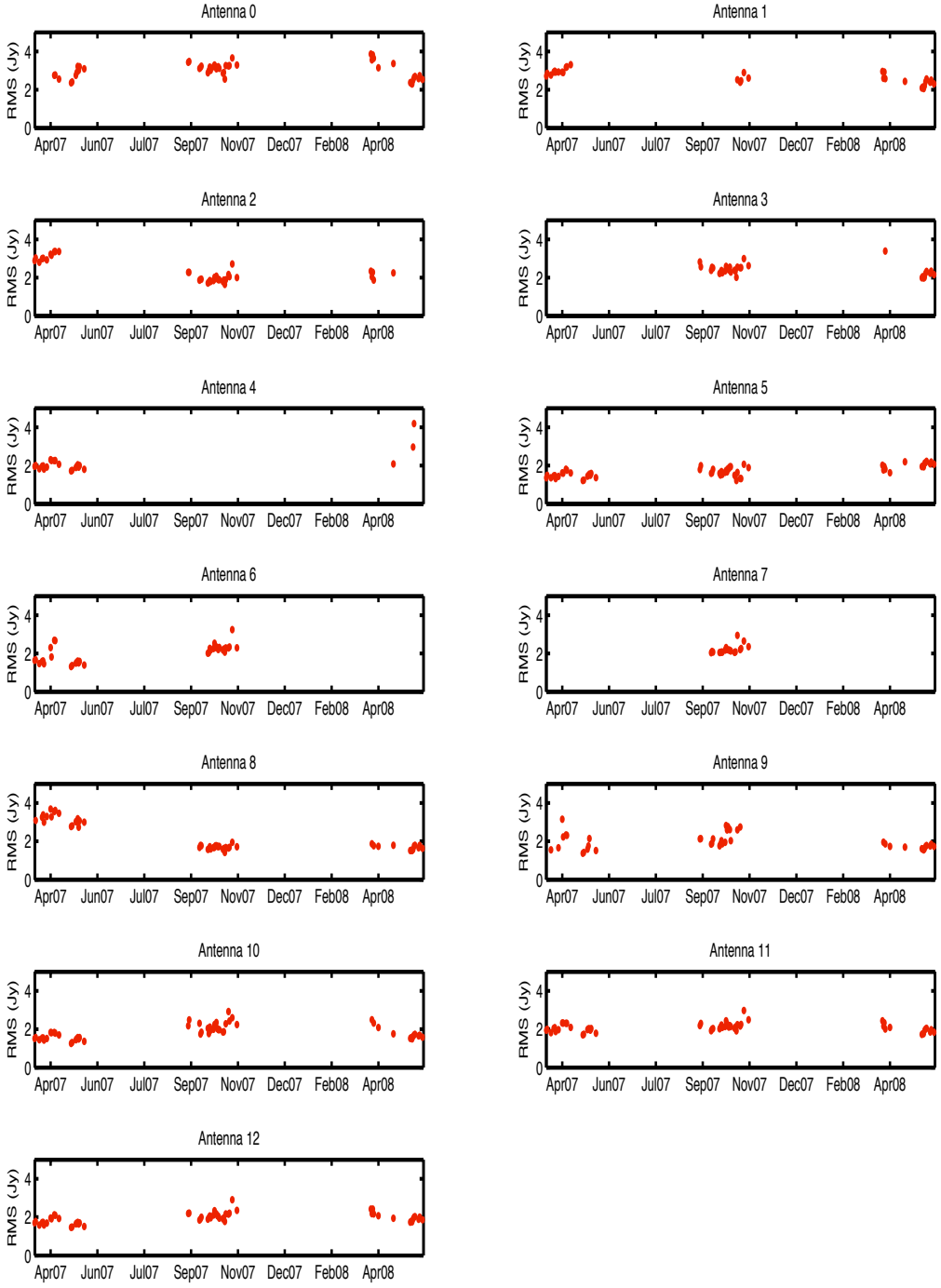

Figure 2.11: The mean RMS noise per day for each CBI2 antenna, for the period 1st April 2007 to 10th May 2008. The noise level is calculated based on observations of CMB fields, and so the time coverage in these plots reflects the availability of the 3 fields observed as part of the CMB program.

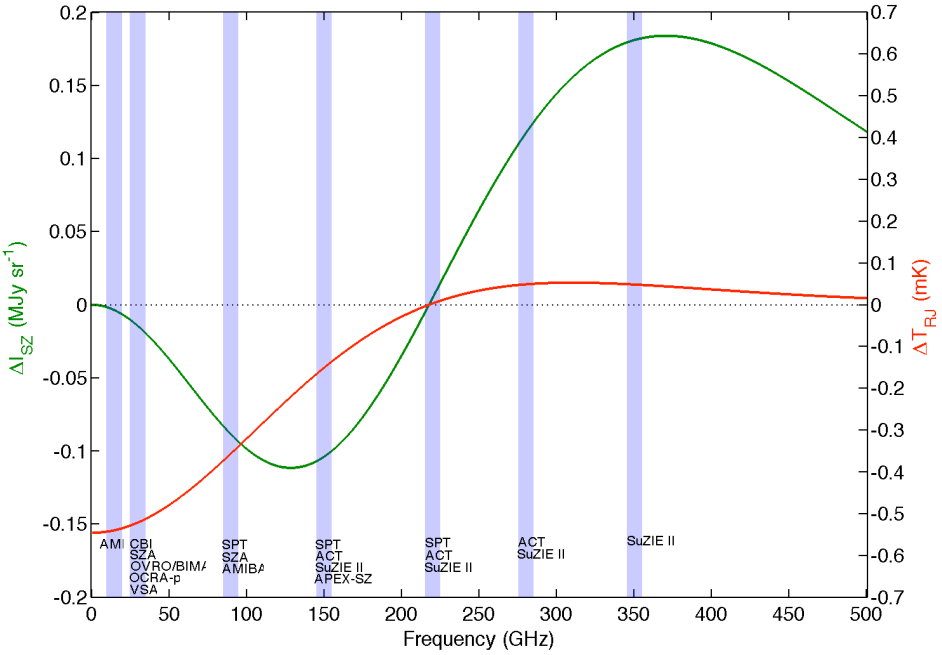

Figure 2.12: A summary of recent and current SZ experiments as a function of frequency. The change in CMB intensity (*green line*) and Rayleigh-Jeans brightness temperature (*red line*) are also plotted as a function of frequency, for a typical cluster with $y = 10^{-4}$. Note that the blue bars are purely for illustrative purposes and do not accurately represent the bandwidths of the instruments indicated.

a range of noise values, and so the true distribution is constructed from a superposition of multiple Ricians, all peaking at slightly different values. Fitting four separate Rician distributions to the data presented in Figure 2.10 shows that $\sim 70\%$ of the data is distributed by the predicted RMS noise. Figure 2.11 also shows the RMS noise values per day for each antenna. Fluctuations in the antenna noise occur on a day-by-day basis as a result of an increase in the system temperature, either due to bad weather or loss of vacuum in the cryostat, therefore generating the long tail in the RMS noise distribution.

2.4 Comparison with other SZ experiments

The CBI2 instrument is one of a number of current experiments used to observe clusters of galaxies via the SZ effect. With the exception of the Planck Satellite (launched 14$^{\text{th}}$ May 2009), all SZ experiments are ground-based, and are therefore restricted to observing at frequencies at which the atmospheric absorption is comparatively low. Therefore many telescopes are located at high altitude, dry sites where the water vapour

content is relatively low. For example CBI2, APEX-SZ (Schwan et al., 2003) and the Atacama Cosmology Telescope (ACT, Kosowsky, 2003) are located at the Chajnantor Observatory, Chile; AMIBA (Ho et al., 2009) and SuZIE II (Benson et al., 2003) are on Mauna Loa and Mauna Kea, Hawaii; and the South Pole Telescope (SPT, Ruhl et al., 2004) is in Antarctica. Figure 2.12 gives a summary of current SZ experiments and their observing frequencies.

The current technologies in use separate the SZ experiments into two categories; the radio interferometers and the single dish bolometer arrays, with the exception of OCRA-P, a prototype single dish radiometer (Lancaster et al., 2007; Lowe et al., 2007). Interferometric experiments measure the pair-wise correlation between signals received at the antennas, while bolometer arrays are used to produce a direct image of the sky via a scanning strategy. Two of the principal survey instruments, ACT and SPT, consist of arrays of bolometer detectors that are designed to scan large patches of sky in order to detect new clusters via the SZ effect. Both of these instruments operate at three different frequency bands and have sensitivity to angular scales between 1 arcminute and 1 degree. ACT has the highest frequency band so that it can observe the increments in CMB temperature at 270 GHz. Other bolometers include APEX-SZ, a 150 GHz single dish instrument with a bolometeric receiver designed for mapping known clusters, and SuZIE II, a multi-frequency infrared receiver that is used for measuring the peculiar velocities of bright clusters.

Radio interferometers are typically used for pointed observations of the SZ effect, where one can target known clusters and integrate for extended periods of time. Unlike a single dish experiment, a radio interferometer can stay on a single pointing position for a very long time, since the instrument is insensitive to any time-varying signal that is constant across the field-of-view. Single dish experiments either have to employ a special beam-switching or scanning strategy in order to remove any systematic error that might be introduced from time-varying signals. Two interferometers, the Arcminute Micro-kelvin Imager (AMI, Kneissl et al., 2001) and the Sunyaev-Zel'dovich Array (SZA, Muchovej et al., 2007) have also conducted surveys in addition to pointed SZ observations. Radio interferometers for use in observations of the CMB typically operate at lower frequencies to the bolometer arrays, in the range 15-90 GHz, with the majority at 30 GHz. Of these instruments CBI2 has a relatively wide field-of-view and medium resolution, and is therefore used to constrain the properties of the intra-cluster medium out to the virial radius. The CBI2 array is an atypical interferometer because all of its 13 antennas are co-mounted on a single rotatable platform. Therefore the

system is much simpler because there is no compensating delay required in order to remove the effect of the geometrical delay between antennas. However this means that the fringe rate filtering method, implemented by experiments such as the Very Small Array (VSA, Watson et al., 2003), cannot be used for CBI2 data to remove spurious signals from ground spill-over and from the Sun and Moon. Instead the ground signal must be removed by subtracting reference fields, that are separated by $\sim$10 minutes in right ascension from the field of interest. Therefore the observing efficiency for CBI2 and other co-mounted arrays, such as AMIBA, is comparatively low.

2.5 Summary

The CBI2 experiment is a 26-36 GHz interferometer, designed specifically to observe primary and secondary anisotropies in the Cosmic Microwave background. There are two major benefits of using an interferometer for this purpose. Firstly a radio interferometer is insensitive to any spatially constant, time-varying signal from sources such as the atmosphere, and hence no beam-switching or scanning strategy is required (Lay & Halverson, 2000). Secondly the instrument directly samples the Fourier transform of the sky brightness, and hence requires very little manipulation to get the data into a usable form for power spectrum analysis. The CBI2 array is an upgrade to the original CBI experiment with larger antennas and hence improved sensitivity on longer baselines. Therefore with this instrument one can potentially measure the high-ℓ CMB with better precision, and also observe clusters of galaxies via the SZ effect with lower contamination from intrinsic CMB anisotropies.

Chapter 3

Observations and Data Reduction

Observations of the thermal SZ effect using CBI2 were conducted from June 2006 until July 2008, during which data was accumulated from 40 galaxy clusters. These clusters were selected based either on their expected SZ brightness from X-ray data (in the case of the scaling relations sample) or for their interesting astrophysical properties (for example the Bullet Cluster and the Shapley Supercluster). In this chapter I discuss in detail both the preparation for SZ observations and the reduction of the data.

3.1 Cluster Selection

Galaxy clusters were selected for observation with CBI2 based on a number of key science projects. One of the principal science goals of the experiment is to obtain calibrated empirical scaling relations between the SZ effect and other cluster properties, such as the total mass and characteristic temperature, out to the viral radius. These scaling relations are important for inferring both the intrinsic physical properties of clusters for which only an SZ detection has been obtained, and specifically in the case of the current SZ surveys. A number of other interesting SZ clusters and samples are included in the CBI2 observations, and these will help to provide an understanding of the physics of the intra-cluster medium out to the largest cluster radii. In this section I give a brief description of each of the cluster samples, and then later the expected observable limit placed on the cluster mass by the sensitivity of CBI2 to the SZ effect.

3.1.1 The Cluster samples

SZ Scaling Relations: Two X-ray samples were chosen to study the scaling relations between the SZ, X-ray and physical properties of galaxy clusters at two different redshifts. The REFLEX-DXL sample is a distant (z = 0.27-0.31) and luminous ($L_X \geq 10^{45}\,\mathrm{ergs}^{-1}$, 0.1-2.4 keV) sub-sample of the ROSAT-ESO flux limited X-ray survey (Böhringer et al., 2001), that has existing detailed XMM-Newton observations (Zhang et al., 2006). This sample contains 13 clusters, 11 of which were observed with CBI2 and form the basis for the analysis work described in this thesis. The clusters have X-ray constrained total masses and temperatures ranging from $5-11\times10^{14}\,\mathrm{M}_{\odot}$ (at r_{500}) and $5.1-10.6\,\mathrm{keV}$. Of the two un-observed clusters, one has a declination lower than the observable limit for the CBI2 site and the other was missed due to technical problems with the telescope.

The second sample is taken from XMM-Newton observations of the REXCESS clusters, a low redshift ($z \leq 0.2$) sub-sample of the REFLEX survey, with X-ray luminosities in the range $0.407-20\times10^{44}\,h_{50}^{-2}\mathrm{ergs}^{-1}$ in the 0.1-2.4 keV rest frame band (Böhringer et al., 2007). In total there are 33 REXCESS clusters and only the most X-ray luminous were selected for CBI2 observations, down to a limit based on the predicted observing times from the relations between L_X and ΔT_{SZ} given by Cooray (1999). The 10 most luminous REXCESS clusters were observed with CBI2 and the sub-sample is morphologically unbiased, based purely on the X-ray luminosity in the 0.1-2.4 keV rest frame band.

High-redshift Sample: Four massive and X-ray luminous clusters were selected for observation, located at $z \sim 0.5$. These clusters were included in the total sample because they were expected to give a significant detection and hence would provide a constraint on cluster properties at higher redshifts. The high-redshift sample comprises of the galaxy clusters RXJ1347-1145, RXJ1206-0848, MS0015.9+1609 and MS0451.6-0305.

The SuZIE Sample: In order to perform a joint spectral analysis with the SuZIE experiment, ten clusters from the sample analysed by Benson et al. (2004) were observed with CBI2. These observations will provide a constraint on the low-frequency end of the SZ spectrum for these clusters and hence a stronger derivation of the peculiar velocities.

Figure 3.1: Mosaic of the Shapley Supercluster core region from ROSAT PSPC observations by Ettori et al. (1997). SZ observations by CBI1 and CBI2 were carried out as a mosaic of five fields across this region.

The Shapley Supercluster: The core region of the Shapley Supercluster has previously been observed with the CBI experiment as a mosaic of four galaxy clusters: A3558, SC1329-313, SC1327-312 and A3562. Observations of this region were continued with CBI2, which has greater sensitivity on the longer baselines i.e. on the smaller angular scales. The CBI1 and CBI2 data will be jointly analysed with existing X-ray surface brightness data, with the aim of trying to detect the existence of an intra-supercluster medium.

3.1.2 The expected sensitivity of CBI2 to the thermal SZ effect

In order to select those clusters that are likely to be detected with the instrument, within a reasonable integration time, an estimate must be made of the sensitivity of CBI2 to the thermal SZ effect. As was shown in Chapter 1, the thermal SZ effect is proportional to the ICM gas pressure integrated along the line-of-sight (Sunyaev & Zel'dovich, 1970), and hence the signal is strongest for clusters with high masses and temperatures. The uncertainty in the SZ signal at 26-36 GHz is dominated by both the thermal noise in the

instrument and the intrinsic CMB anisotropy. Since the thermal noise decreases as the square-root of the integration time, if the observation is reasonably long, then the CMB component (which is independent of the integration time) will limit the cluster mass that can be detected with CBI2. A reasonable estimate of the sensitivity of CBI2 for different cluster masses can be obtained by first assuming a simple cluster model and cosmology, and then simulating observations with the instrument. The thermal SZ effect can be modelled for a given enclosed total mass (M) by assuming that the cluster is in hydrostatic equilibrium, has a typical gas mass fraction $f_{\rm gas} = 0.120$ (LaRoque et al., 2006), and that the ICM gas is well described by an isothermal β model (Cavaliere & Fusco-Femiano, 1976, 1978). Under these assumptions the electron density ($n_{\rm e}$) and temperature ($T_{\rm e}$) are given by

$$n_{\rm e}(r) = n_{\rm e0}\left(1+\left(\frac{r}{r_{\rm core}}\right)\right)^{-3\beta/2} \quad (3.1)$$

$$T_{\rm e}(r) = \frac{GM\mu m_{\rm p}}{3\beta}\frac{(r_{\rm core}^2+r^2)}{r^3}, \quad (3.2)$$

where the shape parameter, β, and core radius, $r_{\rm core}$, are fixed at 2/3 and 0.3 Mpc respectively. The mean hydrogen mass per gas particle μ is assumed to be constant throughout the gas and equal to 0.6 (Kay et al., 2004). The central electron density can be determined from the total mass and gas mass fraction by the following relation

$$n_{\rm e0} = \frac{Mf_{\rm gas}}{4\pi\mu_{\rm e}m_{\rm p}}\left[\int_0^r r'^2\left(1+\left(\frac{r'}{r_{\rm core}}\right)^2\right)^{-3\beta/2}{\rm d}r'\right]^{-1}, \quad (3.3)$$

where $\mu_{\rm e}$ is the mean hydrogen mass per electron and is equal to 1.16 (Grego et al., 2001). The thermal SZ effect as a function of projected radius can now be estimated for clusters of different masses by integrating the product of the electron density and temperature along the line-of-sight,

$$\Delta T_{\rm SZ} \propto \int n_{\rm e}T_{\rm e}{\rm d}l. \quad (3.4)$$

CBI2 observations were simulated for three different enclosed masses ($5, 10$ and $20\times10^{14}\,{\rm M}_\odot$) at a radius of 2 Mpc and two redshifts (0.15 and 0.3), using the procedure outlined in Chapter 4. The resulting mock visibilities are a combination of the simulated thermal SZ signal, realisations of the primordial CMB and the estimated thermal noise. In order to have a figure of merit for the SZ sensitivity, the signal-to-noise ratio

(SNR) for each mock observation is calculated as follows

$$\mathrm{SNR} \equiv \frac{\bar{d}}{\sigma_{\bar{d}}}, \tag{3.5}$$

where $\bar{d}$ and $\sigma_{\bar{d}}$ are the mean and the standard deviation in the mean respectively. In the case where weights are applied to each of the visibilities, these quantities are given by

$$\bar{d} = \frac{\sum_{i=1}^{N} w_i d_i}{\sum_{i=1}^{N} w_i} \tag{3.6}$$

$$\sigma_{\bar{d}}^2 = \frac{1}{N} \frac{\sum_{i=1}^{N} w_i \sigma_i^2}{\sum_{i=1}^{N} w_i}, \tag{3.7}$$

where N is the number of visibilities, and w_i is the weight applied to the ith visibility. Typically data that are distributed normally should be weighted by the inverse of the variance. However since the simulated SZ signal varies considerably as a function of baseline distance and we know its expected value, the weights should also include the expected signal. Therefore each weight is given by the form

$$w_i = \frac{s_i}{\sigma_i^2}, \tag{3.8}$$

where s_i is the expected value for the visibility when no noise or intrinsic CMB component is present. This is a fairer representation of the signal-to-noise ratio since those visibilities with an expected low signal will be appropriately down-weighted.

Figure 3.2 shows the SNR as a function of the total integration time for a typical CBI2 observation. As expected, the most massive clusters ($M \sim 20 \times 10^{14}\,\mathrm{M}_{\odot}$, $r = 2\,\mathrm{Mpc}$) are easily detectable for reasonable integration times, while intermediate masses ($M \sim 10 \times 10^{14}\,\mathrm{M}_{\odot}$, $r = 2\,\mathrm{Mpc}$) require slightly longer observing. It is not possible to detect clusters with virial masses $M \lesssim 5 \times 10^{14}\,\mathrm{M}_{\odot}$, since the signal is strongly dominated by the intrinsic CMB anisotropies, and therefore increasing the total integration time makes no improvement. For the most massive clusters the SNR statistic decreases as the square-root of time and tails-off at large integrations where the constant CMB component begins to dominate. The thermal SZ effect is strongest on radial scales similar to r_{core}, which correspond to angular scales of approximately 2 and 1 arcminutes at z = 0.15 and 0.3 respectively. Since CBI2 is sensitive to scales in the range $\sim$ 4 -

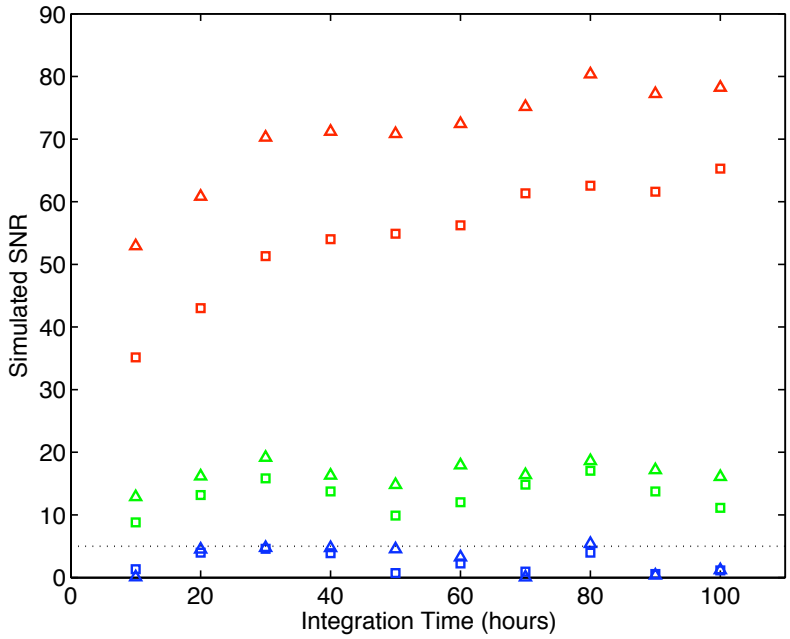

Figure 3.2: The simulated signal-to-noise ratio for the real visibility as a function of integration time, averaged across all CBI2 baselines and weighted by the expected signal. The uncertainty in the data includes both the estimated thermal noise and intrinsic CMB components. The data were generated from the spherically-symmetric isothermal-β model, with enclosed masses of 5 (*blue*), 10 (*green*) and 20 (*red*) $\times 10^{14} M_{\odot}$ at 2 Mpc. The observations were simulated at $z = 0.15$ (*triangles*) and $z = 0.3$ (*squares*) with a gas mass fraction $f_{\rm gas} = 0.120$. A detection is defined by a signal-to-noise ratio of 5 (*Dotted line*). Note that the scatter in the SNR is a result of the fact that each data set is independent.

20 arcminutes, the thermal SZ signal for clusters of a given mass is highest when observing at lower redshifts.

3.2 Observations

3.2.1 Reference Field selection

As explained in Chapter 2, a significant contaminating signal is expected from spill-over of ground emission in the primary beam. This unwanted signal can be removed from the data by observing reference fields which are separated in right ascension from the cluster main field. Since the ground signal is stable on hour time-scales, these reference fields are selected within 8-12 minutes of the cluster field. The primary selection criterion is that a field does not contain any bright radio source within 1-2 primary beam radii of the field centre. Each reference field was constructed by identifying, and avoiding, bright sources ($\gtrsim 100$ mJy) within

the NVSS (Condon et al., 1998) and SUMSS (Mauch et al., 2003) catalogues. Since these surveys were carried out at 1.4 GHz and 0.843 GHz respectively, this method could lead to inclusion of faint sources, with steeply rising spectra, and hence contaminate the SZ data at 31 GHz. However survey work by Mason et al. (2009) indicates that these rising-spectrum mJy sources are unlikely occurrences, with as few as 1 % of the NVSS sample having a spectral index steeper than zero between 1.4 and 31 GHz. Further treatment of point source contamination can be implemented by observing the positions of known low-frequency sources in the CBI2 SZ fields at 31 GHz using, for example, the Green Bank Telescope or Australia Telescope Compact Array. The sources detected with these observations can be correlated with the position of significant flux in the spatially-filtered long-baseline CBI2 maps. This strategy has been carried out for much of the cluster sample and will be described in more detail later in this thesis.

3.2.2 Phase Calibrators

The phases of sources observed with a radio interferometer can change as a function of telescope position, due either to a pointing error, bad weather or an unknown instrument problem. Therefore, in addition to the astronomical source of interest, bright, unresolved sources are observed near to the main field for later phase correction, if required. For each of the target clusters in the CBI2 sample a few phase calibrators were chosen based on whether they were unresolved on the CBI2 baselines and also close to the main field (ideally within a few degrees). The search was performed using a web-based form provided by ATNF[1], which includes the ATCA and VLA calibrator manuals. Sources were selected if they had stable fluxes greater than 1 Jy at wavelengths of 12 mm and 7 mm, closest to the CBI2 observing frequency. During SZ observations a phase calibrator is selected by the control computer and observed for a minute after every rotation of the deck offset angle.

3.2.3 Observing with CBI2

Observations were conducted on a nightly basis, usually starting a few hours before sunset, and ending just after sunrise. The observations were scheduled on the control computer and the predicted positions of the Moon and Sun with respect to the sources noted. Each source is represented by a schedule file containing

[1] http://www.narrabri.atnf.csiro.au/calibrators/

information including its position in the sky, the program of deck rotations, and when to observe the noise source and phase calibrators. Regular rotations of the antenna deck with respect to the source are important to ensure adequate coverage of the (u,v) plane and hence provide spatial information on the source. Each observation contains a common sequence of steps, necessary for quality checking and calibration of the data. A typical observing schedule is shown below, containing all of the necessary calibration observations and a broad range of the types of source observed with CBI2. The hashed statements are comments useful to the telescope operator and for those reducing the data later.

```
#sched_10oct.txt
#Schedule for 10th Oct 2007
#Start ~ 13:40 LST
schedule standard/tp
schedule standard/quad
schedule standard/cal(jupiter, 5m) #Calibrator (Sun 59/Moon 73)
schedule cbi2/G312.5-3.0_wtrail.sch(2, 16:30) #Galactic source (Sun 60/Moon 66)
schedule standard/cal(jupiter, 5m) #Calibrator (Sun 59/Moon 73)
schedule cbi2/G354.1+0.1_wtrail.sch(2, 19:00) #Galactic source (Sun 68/Moon 81)
schedule standard/cal(jupiter, 5m) #Calibrator (Sun 59/Moon 73)
#Sun sets ~ 19:25 LST
schedule cbi2/a3888_mt.sch(1, 21:30) #SZ source (Sun 124/Moon 134)
schedule standard/quad
schedule standard/deckcal(J1924-292, 10m, 0) #Calibrator (Sun 92/Moon 106)
schedule standard/deckcal(J1924-292, 10m, 45) #Calibrator (Sun 92/Moon 106)
schedule cbi2/a2813_mt.sch(1, 00:00) #SZ source (Sun 153/Moon 155)
schedule standard/cal(J2253+161, 10m) #Calibrator (Sun 148/Moon 158)
schedule cbi2/sxds1234-0443.sch(05:00) #CMB field (Sun 158/Moon 147)
schedule standard/cal(taua, 10m) #Calibrator (Sun 112/Moon 98)
schedule standard/quad
#Sun rise ~ 6:40 LST
```

```
schedule cbi2/rxj0528_mt.sch(1, 08:30) #SZ source (Sun 112/Moon 98)
schedule standard/quad
schedule stow.sch
#End ~ 08:40 LST
```

3.3 Data Reduction

Flagging of bad data and subsequent calibration is carried out using CBICAL[2], a specialist data reduction package designed for use on CBI data. Each night of data is reduced separately and a CBICAL script constructed for that observation. The intermediate data set then undergoes a series of iterative checks and flags to produce a final output file of visibilities and associated noise weights.

3.3.1 Flagging Data

Before calibration a number of automated flags are applied in order to remove obviously problematic data. The observer-log records the known problems with the receivers, such as an increase in temperature due to a reduction in cryostat vacuum or if the receiver is in the site laboratory for maintenance work. Data from these receivers can then be flagged and take no further part in the reduction. The total power input into the correlator from each receiver and channel is monitored and flagged if above or below an acceptable range. In addition the power being injected into the receiver signal by the noise calibrator source (see below) is also monitored and flagged for values outside the threshold levels. Both these ranges can be manually set so that they are either stringent, which might result in deleting acceptable data, or lax in which case one must be careful to check the remaining data. A good signal-to-noise level is required for SZ effect data and so the power thresholds are fairly lax in order to allow as much of the data as is reasonable. Therefore the data has to be carefully checked in order to remove any poor baseline channels.

Occasionally the noise calibration measurements for some of the samples can be unusually low due to glitches in the electronics of the noise calibration source. This data can then be flagged by setting an acceptable minimum threshold level. Before and after each calibration step the data are also flagged for individual samples that have anomalously low or high amplitudes in a particular scan and usually include

[2] http://www.astro.caltech.edu/∼tjp/CBI/

those greater than 5 σ from the mean.

3.3.2 Antenna Pointing

Each of the thirteen CBI2 antennas are separately bolted onto the rotatable deck, and so there will be pointing errors associated with each of them. During the initial observing period (until the 22$^{\rm nd}$ April 2007) observations of Jupiter were routinely carried out in order to correct for pointing errors associated with the antennas. The instrument was pointed at Jupiter, and then off-centre at 4 pointings where the amplitude should be half of the total signal from Jupiter. If the amplitudes of the 4 off-centre pointings were significantly unequal for baselines containing a particular antenna, then that antenna needed to be re-pointed. Since the re-pointing process required applying shims between the deck and the base of the primary mirror the data for that antenna would be flagged until corrected. Figure 3.3 shows visibility data from a 5-point observation of Jupiter before and after antenna 9 was correctly pointed.

3.3.3 Quadrature calibration

For the case of a perfect complex correlator, the real and imaginary components of the correlated output are derived from the input signals $y(t)$ and $x(t)$ by the following operations over the sampling time $\tau_{\rm acc}$,

$$\mathscr{R} \approx \frac{1}{\tau_{\rm acc}} \int_0^{\tau_{\rm acc}} x(t)y(t)\mathrm{d}t \tag{3.9}$$

$$\mathscr{I} \approx \frac{1}{\tau_{\rm acc}} \int_0^{\tau_{\rm acc}} x(t)\tilde{y}(t)\mathrm{d}t, \tag{3.10}$$

where $\tilde{y}(t)$ is equal to the Hilbert transform of $y(t)$. For the case of a sinusoidal input signal the Hilbert transform is generated using a linear filter that introduces a $\pi/2$ phase shift in $y(t)$ (see the CBI2 system diagram in Chapter 2 by Padin et al., 2002). However in practice it is impossible to produce an exact $\pi/2$ phase shift in the signal across a finite bandwidth, and so a relative complex gain is introduced between $\mathscr{R}$ and $\mathscr{I}$. The correlator output for CBI typically contains quadrature errors between between $\sim$1 - 3 dBm in amplitude and $\sim$ 5 - 15 degrees in phase (Padin et al., 2002).

These errors are measured, and hence corrected for, by injection of a correlated signal into the front-end of each receiver using the noise source generator. During this process the telescope is moved off-source

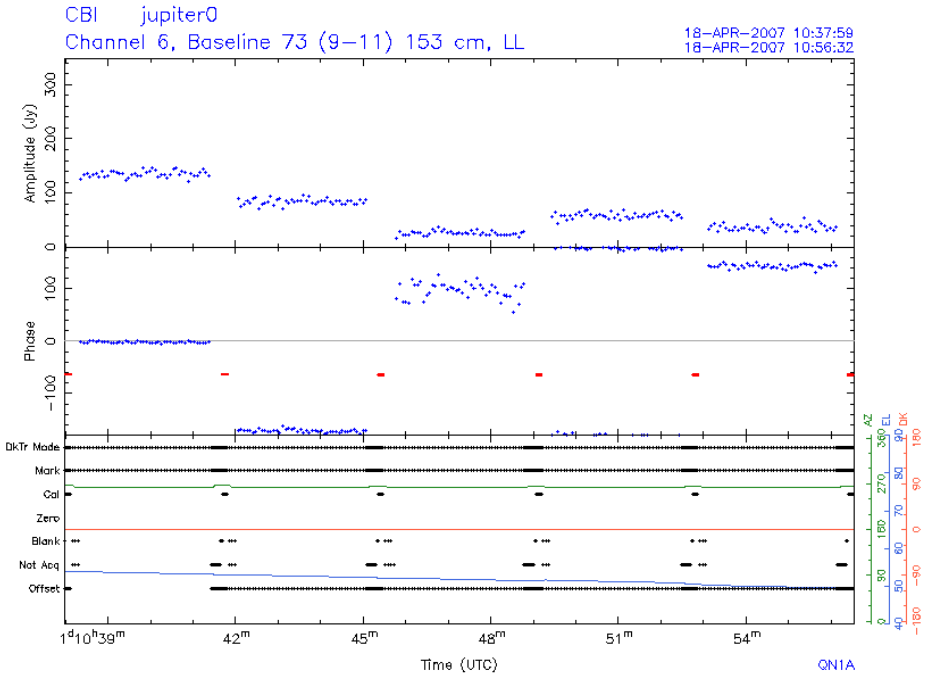

Before

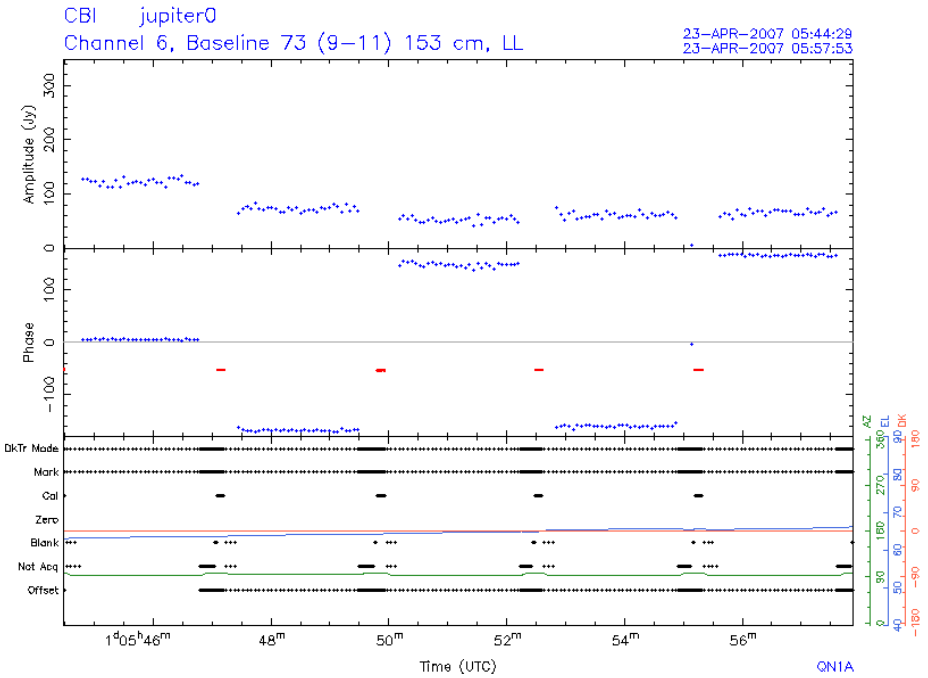

After

Figure 3.3: Visibility data, from a single baseline, showing a Jupiter 5-point observation before and after the pointing correction was applied to antenna 9.

into the stowed position and the noise source switched on to provide the correlated signal. The uncalibrated correlator outputs from the noise signal, $\mathscr{R}_1'$ and $\mathscr{I}_1'$, are related to the true complex visibilities by the following expressions

$$\mathscr{R}_1' = \mathscr{R} \tag{3.11}$$

$$\mathscr{I}_1' = (g_{\rm quad}\cos(\phi_{\rm quad}))\mathscr{I} - (g_{\rm quad}\sin(\phi_{\rm quad}))\mathscr{R}, \tag{3.12}$$

where $g_{\rm quad}$ and $\phi_{\rm quad}$ are the unknown relative gain and phase introduced by the quadrature error. In order to measure these two quantities a $\pi/2$ phase shift is introduced into each receiver signal sequentially (see Figure 3.4). Consider the case where the input signal $x(t)$ is phase shifted by $\pi/2$, in this case the correlator output has the following dependency on the true complex visibilities

$$\mathscr{R}_2' = -\mathscr{I} \tag{3.13}$$

$$\mathscr{I}_2' = (g_{\rm quad}\cos(\phi_{\rm quad}))\mathscr{R} + (g_{\rm quad}\sin(\phi_{\rm quad}))\mathscr{I}. \tag{3.14}$$

By solving for these equations simultaneously, the values of $g_{\rm quad}$ and $\phi_{\rm quad}$ can be estimated from the measured correlated outputs as follows

$$g_{\rm quad} = \frac{\sqrt{(\mathscr{I}_2'\mathscr{R}_1' - \mathscr{I}_1'\mathscr{R}_2')^2 - (\mathscr{I}_1'\mathscr{R}_1' + \mathscr{I}_2'\mathscr{R}_2')^2}}{(\mathscr{R}_1'^2 + \mathscr{R}_2'^2)} \tag{3.15}$$

$$\phi_{\rm quad} = \tan^{-1}\left(\frac{\mathscr{I}_1'\mathscr{R}_1' + \mathscr{I}_2'\mathscr{R}_2'}{\mathscr{I}_1'\mathscr{R}_2' - \mathscr{I}_2'\mathscr{R}_1'}\right). \tag{3.16}$$

Note also that the $\pi/2$ phase shift could have been applied to $y(t)$ instead. This would lead to a similar set of equations for $g_{\rm quad}$ and $\phi_{\rm quad}$, except that now the real and imaginary outputs of the correlator are equal to $-\mathscr{R}_2'$ and $-\mathscr{I}_2'$.

Each quadrature calibration process during the observation takes approximately 4 minutes to run and is repeated 2 or 3 times during the night. The quadrature calibration command will flag the data for a particular baseline-channel if it fails to find an acceptable solution, and this maybe for one of the following reasons. Firstly there may be insufficient data for a solution to be found, in which case it was likely that the procedure was aborted part-way through. Secondly the amplitude of the calibration signal may be below the acceptable

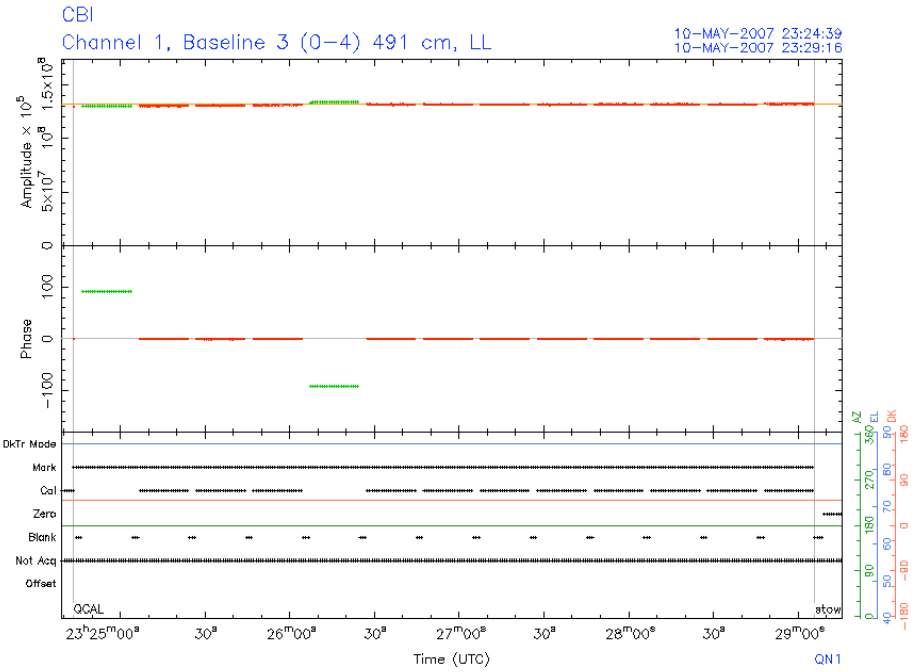

Figure 3.4: An example of the quadrature calibration sequence from a single baseline-channel, plotted as amplitude and phase against time, using CBICAL. The $\pi/2$ phase shift in the input signal from antennas 0 and 4 can be seen on this baseline-channel. Noise source calibration has also been applied to this data, so the phases are at their correct absolute values. The lower plot displays the azimuth, elevation and deck offset angles as a function of time.

threshold level, and if this is the case for all the samples in the baseline channel, then the data are flagged. Thirdly the calculated amplitude and phase errors may be outside what is considered the acceptable range, between 0.45 to 2.0 for the amplitude and -20 to 20 degrees for the phase. In which case the calibration fails for that particular baseline-channel. Finally the correction factors are calculated and applied to each of the correlator outputs, so that the measured real and imaginary values should have the same relative gain.

3.3.4 Noise Source calibration

In order to correct for possible variations in the gain throughout the night, and also any baseline-based calibration error, a series of internal noise source observations are interleaved with those of the target object. During these periods, which last for a few seconds each, the noise generator is switched on and a strong signal injected into each receiver (typically $\sim 10^4$ Jy) while the telescope continues to track the source. The calibration routine calculates the correction required for each noise calibration measurement in order to

make the phase zero and the amplitude at a consistent relative level, set against the desired power level for a meter reading of -27 dBm. This correction can then be applied to the rest of the data in two possible modes. In the first mode the corrections for samples between noise calibration measurements are interpolated in time and then applied. This is suitable if one finds that the noise source signal is more stable than any variation in the receiver gains. In the second mode the corrections are averaged over the whole observation and then applied to all of the samples in each baseline-channel. It was found that the variation in receiver gain for CBI is actually less than that of the noise source signal ($\sim 3\,\%$, Udomprasert et al., 2004), and therefore the second noise calibration method is applied.

3.3.5 Astronomical flux calibration

A bright astronomical source is used to calibrate the amplitude to an absolute scale in Jansky, effectively correcting for the gain in signal from each antenna. For CBI data the absolute flux density scale was based upon single-dish measurements of Jupiter at 32 GHz by Mason et al. (1999) using the 1.5 m telescope at OVRO, where the brightness temperature was measured to be $T_{\rm jup} = 152 \pm 5$ K. The spectrum of Jupiter is non-thermal across the 26-36 GHz band so the 32 GHz Jupiter flux was transferred to Tau A (the Crab Nebula). The flux scale was then calculated for the nine other channels using the known spectral index of Tau A, which is α = 0.299 where $S_\nu = \nu^{-\alpha}$ (Baars et al., 1977). More recent measurements of Jupiter's brightness temperature, using WMAP, find that $T_{\rm jup} = 146.6 \pm 0.75$ K at 33 GHz (Hill et al., 2009), and so a correction factor of 0.965 is applied to the visibility data after primary flux calibration. The error in the primary flux calibration is estimated to be $\sim 0.5\%$.

Every night a bright primary calibrator source (e.g. Jupiter or Tau A) was observed at least once, along with multiple secondary calibrator sources (e.g. 3C 279, 3C 274, 3C 273, J1924-292, J2253+126). A primary source was used for calibration if possible, but occasionally these would be unavailable (either they were not present in the night sky or too close to the moon) and so a bright secondary source would be used instead. The primary calibration command in CBICAL solves for the individual complex antenna gains based on the flux model for the calibrator source. This is an over-constrained problem where the gain for each antenna is calculated based on the signal from all baselines involving that antenna. The correction factors for each baseline-channel are then calculated based on the product of the calculated antenna gains

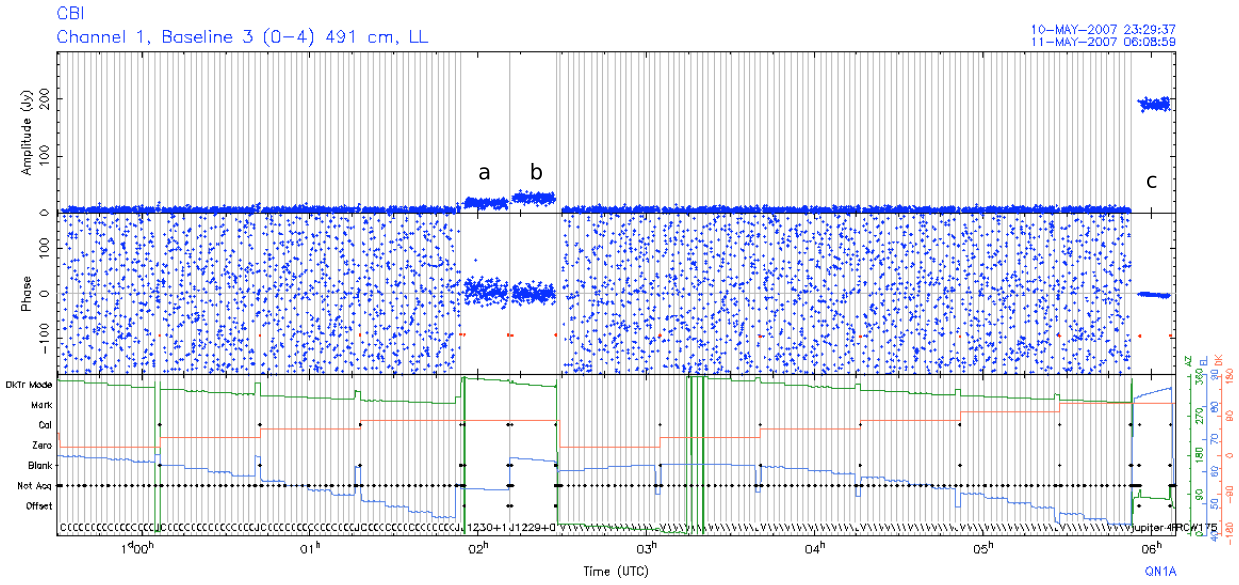

Figure 3.5: An example of flagged and calibrated CBI2 data from a single baseline-channel, plotted as amplitude and phase against time, in CBICAL . The time-range includes observations of (a) J1924-202, (b) 3C 274 and (c) Jupiter. The azimuth, elevation and deck offset angles are also displayed in the lower plot.

and applied to the whole set of visibilities by interpolating between the calibrator scans. After the correction has been applied the data will be in Jansky units and the phases of on-axis point sources should be zero.

3.3.6 Pointing Error

The secondary calibrators are important for characterising the error in phase angle after primary calibration, since their expected phases are zero. Figure 3.6 shows the mean amplitude and RMS phase angle, as a function of the baseline distance, for each of the secondary calibrators. These data were taken from observations of the REFLEX-DXL cluster sample, spanning the complete CBI2 observing run, and are averaged over all frequency channels. There is a clear trend for the RMS phase angle to increase as a function of baseline distance, consistent with a residual pointing error in the CBI2 tracking platform. A pointing error of $\Delta\theta$ produces an RMS phase angle of $\Delta\phi$ given by the following

$$\Delta\phi = 2\pi\Delta\theta\frac{b}{\lambda} \tag{3.17}$$

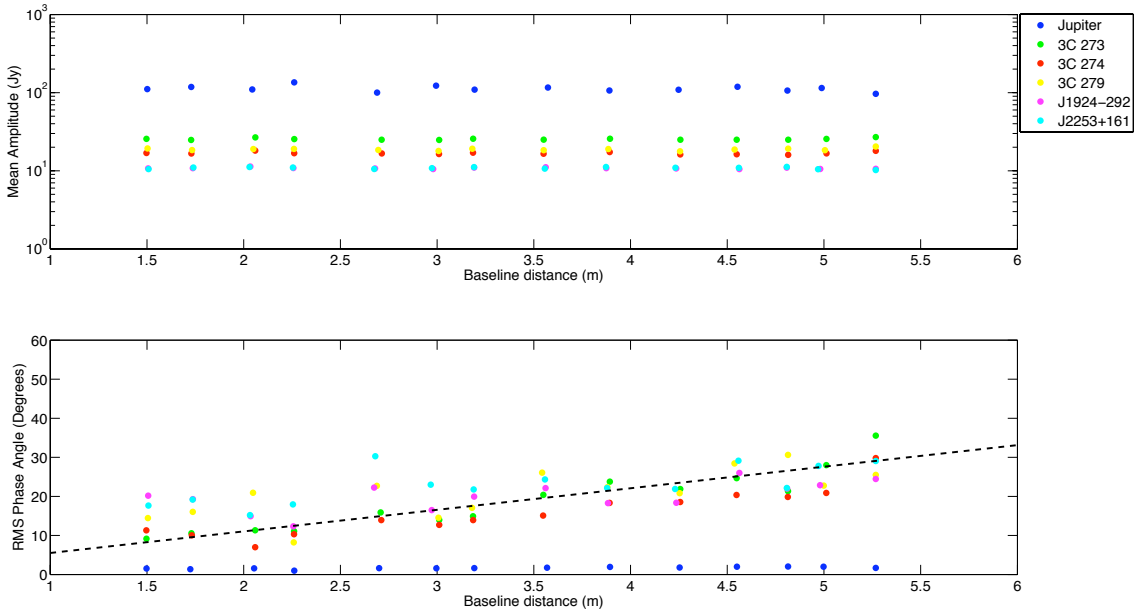

Figure 3.6: The mean amplitude and RMS phase angle as a function of baseline distance for a selection of CBI2 calibrators. The data were taken from observations of the REFLEX-DXL cluster sample and are averaged over all 10 frequency channels. The *dashed line* represents the RMS phase error produced by a pointing error of 0.5 arcminutes at a frequency of 31 GHz. Note that the brightness of Jupiter varies significantly with date, however the amplitude presented here is an average over all observations and channels.

where b is the baseline distance in units of metres. The behaviour of the secondary calibrator data is consistent with a pointing error of approximately 0.5 arcminutes in the tracking platform at a frequency of 31 GHz. This is consistent with the intrinsic pointing error in CBI data reported by Casassus et al. (2006). The primary beam of the instrument has a full-width at half-maximum of 28.2 arcminutes at a frequency of 31 GHz, and so the effect of the pointing error on the measured flux of a small source at the centre of the field-of-view is at the level of 0.1 %. For the case of modelling the SZ effect as a symmetric cluster about the field centre, the phase angle will rotate the non-zero real visibilities into the imaginary visibilities. The resolved SZ signal is typically strongest on the shortest baselines, where the phase error is small, and so introduces a change in the real visibilities of $\sim 3\,\%$. Therefore a 5 % systematic error is included as a nuisance parameter in the analysis described in this thesis, to account for any residual systematic error generated by both the calibration and the pointing. Future work can be done to calibrate out the phase error by use of the interleaved phase calibrators between the target fields.

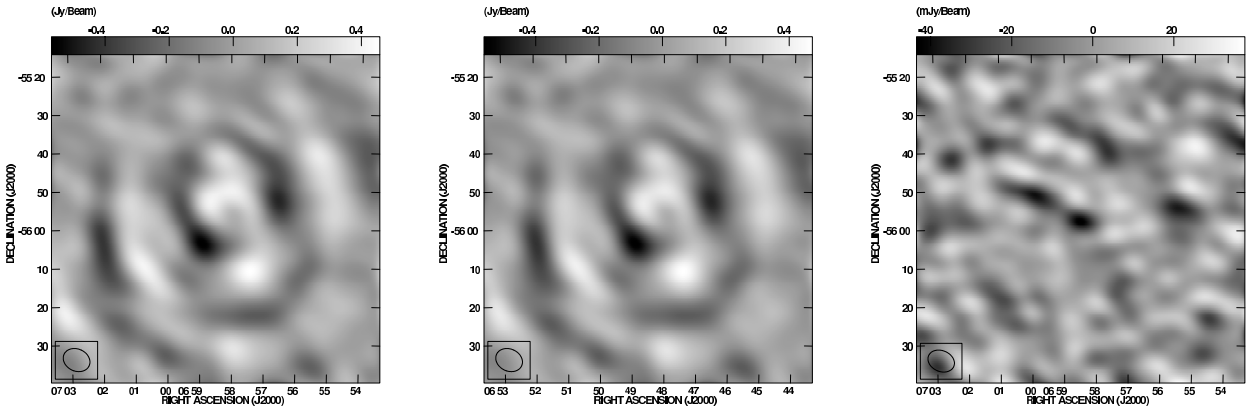

Figure 3.7: Full-resolution maps of a single CBI2 observation demonstrating subtraction of the ground spill-over. *Left*: Cluster field before ground subtraction. *Middle*: Reference field that is offset 10 minutes in right ascension from the main cluster field. *Right*: Cluster field after ground signal subtraction. Note that the grey-scale for the first two images is in units of Jy beam^{-1}, while the ground subtracted image is in units of mJy beam^{-1}.

3.3.7 Final data checks

Once the data have been through both the automated flagging and calibration process, a final check of each baseline channel was performed in order to spot any possible poor data that might have been missed. CBI2 data can contain strong, stable spurious signals from ground spill-over and antenna cross-talk. This can make it difficult to distinguish between the unwanted poor-quality data and that contaminated by a known correlated signal, which can be subtracted later. In order to remove this ambiguity, a ground subtraction command is called in CBICAL that selects all of the cluster fields (both main and reference) and removes the average signal from each. This is a different routine to that described below in Section 3.3.8 and is only used as a visual aid for checking the data. It is not applied to the final data set since one would then be subtracting the SZ signal. Any remaining strongly correlated signal in the cluster data, as a result of problems in the receiver or the correlator electronics, will now appear in the phases, since the phase of the low signal-to-noise cluster and CMB data is expected to be noise-like. These baseline-channels can also be cross-checked with plots of the total power at each input of the correlator.

3.3.8 Ground spill-over subtraction

Emission from the ground and any other repeatable spurious signal in the correlator output can be significant and must be removed from the data (see Chapter 2). The observed ground signal is stable over hour time scales and can be removed by subtracting reference fields that are separated by ~ 10 minutes in right ascension and at the same declination. The subtraction is performed by matching hour angles and then subtracting the corresponding reference field data from the main field data. For CBI2 SZ observations three modes of subtraction strategy were implemented: L-M-T whereby the mean of the lead and trail fields were subtracted from the main field, L-M where a single lead field was subtracted from the main field and M-T where a single trail field was subtracted from the main field. The technique increases the total RMS in the data by a factor of $\sqrt{3/2}$ (for the L-M-T mode) and a factor of $\sqrt{2}$ (for L-M and M-T modes), however the improvement in signal-to-noise by using multiple reference fields is balanced by a reduction in observing efficiency. Figure 3.7 demonstrates the effective removal of the strong ground signal contaminant by L-M subtraction. The map after ground spill-over subtraction is consistent with the expected thermal noise and there is no remnant of the ground signal. Interestingly on this occasion the cluster decrement is strong enough to be visible above the map noise during a single observation.

3.3.9 Stacking and Gridding

In order to achieve a significant detection, each cluster is observed over multiple nights and the thermal noise level decreases as the square-root of the total integration time (see Figure 3.8). Data for each observation were reduced using the above prescription and then concatenated to generate a single file containing the complex visibility and associated weight information. The total noise properties of each ground spill-over subtraction mode are different and so the reduced data are combined based on the separate modes that were implemented.

In preparation for the analysis, the combined data sets are gridded onto a regular grid of estimated visibilities using the MPIGRIDR program[3], which implements the technique developed by Myers et al. (2003). The complex estimators of the visibility for each grid cell are equal to the weighted average of the measured visibilities at that grid position, with the weightings based on the variances in the CBI2 data set. Note that

[3] http://www.cita.utoronto.ca/∼myers/

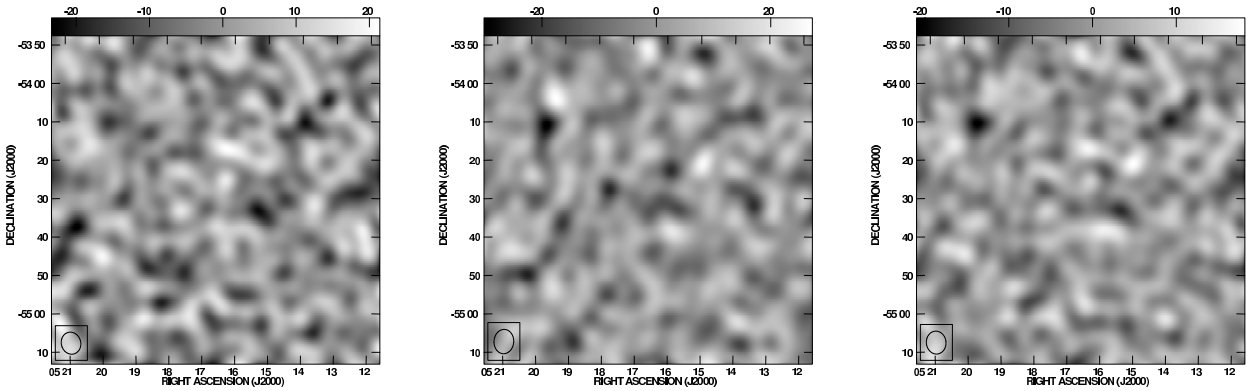

Figure 3.8: Full-resolution maps and associated noise levels from example observations of RXCJ0516.7-5430, demonstrating the correct increase in signal-to-noise by stacking CBI2 observations. *Left*: Reduced and ground subtracted data from the 3$^{\rm rd}$ October 2007. *Middle*: Reduced and ground subtracted data from the 4$^{\rm th}$ October 2007. *Right*: The resulting map and noise from stacking these two observations.

visibilities from each frequency channel, and also from multiple pointings, will contribute to the estimators. The purpose of gridding is to reduce the amount of data that is used in the analysis pipeline, and hence generate a realistic computation speed during model fitting. This is particularly true of the covariance matrices that are used in calculating the likelihood statistic, which have dimensions $n \times n$, and can therefore be very large for n ungridded visibilities.

The effective resolution of the Fourier-plane is set by the field-of-view of the sky, i.e. the primary beam response of the antennas. On these scales any oscillations in the visibilities will be smeared out by the transform of the primary beam, and so this defines the size of the coarse grid cells to be constructed. The CBI2 primary beam has a full-width at half-maximum of $\sim$ 30 arcminutes and so will smear the data on a scale of $\sim$ 100 wavelengths. Therefore in practice the estimator widths are set to sample the Fourier-plane on a scale less than half of this (i.e. $\sim$ 40 wavelengths). The raw sampling function for a typical stacked data set and the gridded estimators are shown in Figure 3.9, highlighting the significant data compression obtained by this method. Note that the estimators are not orthogonal combinations of the true visibilities, and therefore some information loss is expected in the gridding process. However tests show that there is no noticeable biasing or loss in sensitivity as a result of this process, and the model parameters can be correctly reproduced from the estimated visibilities (see for example Myers et al., 2003, and Chapter 4 of this thesis).

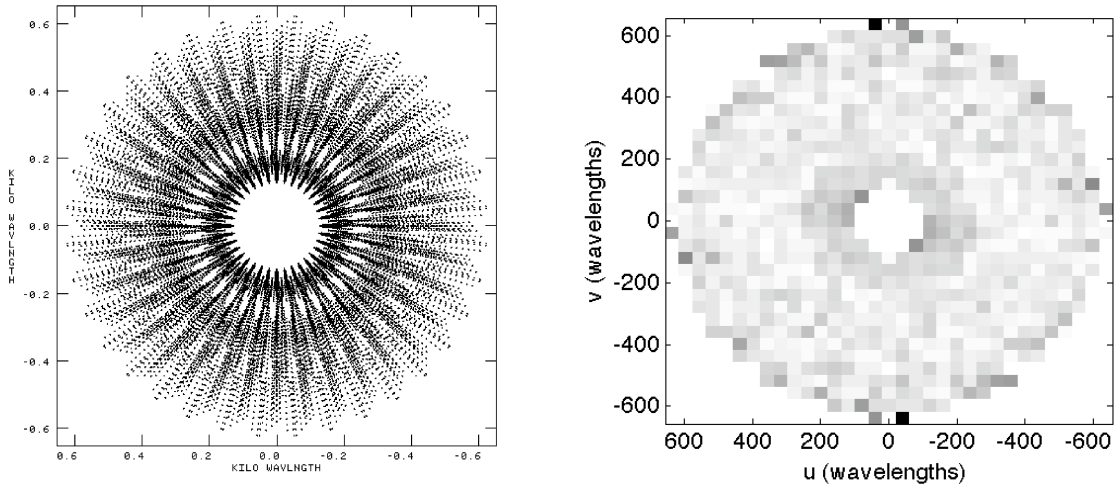

Figure 3.9: A typical CBI2 sampling function from stacked observations (*left*) and the estimated visibilities after gridding has been applied (*right*). In this case the gridding process has reduced the size of the complex data set from $n = 46,800$ to $n = 348$.

In addition to compressing the visibility data into estimators, MPIGRIDR also computes the covariance matrices required for model fitting. The noise covariance matrix is calculated from the accumulated weights of the visibilities that contribute to each estimator. The CMB covariance matrix is derived from calculating the contribution of an input CMB power spectrum to each estimator. Consider a fine grid of points at positions given by $\mathbf{v}$, constructed in the Fourier-plane so as to sample greater than the Nyquist rate. If this fine grid defines the positions of the Fourier transform of the sky brightness in units of thermodynamic temperature $\tilde{I}(\mathbf{v})$, then the k'th visibility datum at position $\mathbf{u}_\mathrm{k}$ is given by

$$V_\mathrm{k} = \sum P_\mathrm{k}(\mathbf{v}) f_\mathrm{k} \tilde{I}(\mathbf{v}), \tag{3.18}$$

where f_k is the Planck factor that converts the units from thermodynamic temperature to Jansky. $P_\mathrm{k}(\mathbf{v})$ is known as the projection kernel and is related to the transform of the antenna primary beam ($\tilde{A}_\mathrm{k}$) by

$$P_\mathrm{k}(\mathbf{v}) = \tilde{A}_\mathrm{k}(\mathbf{u}_\mathrm{k} - \mathbf{v}) \mathrm{e}^{2\pi i \mathbf{v}\cdot\mathbf{x}_\mathrm{k}}. \tag{3.19}$$

If the linear mapping from the visibility data to the i'th estimator is defined by the operator Q_ik, then the

estimators are related to the sky brightness transform by the following expression,

$$S_{\rm i} = \sum_{\rm k} Q_{\rm ik} P_{\rm k}(\mathbf{v}) f_{\rm k} \tilde{I}(\mathbf{v}). \tag{3.20}$$

The projection operator $\mathbf{R}_{\rm i}$ is now defined by the operation $\sum Q_{\rm ik} P_{\rm k}(\mathbf{v}) f_{\rm k}$. Therefore the elements of the CMB covariance matrix ($C^{\rm CMB}_{\rm i,j}$) are derived by performing this operation on the CMB power spectrum at each fine grid position $\mathbf{v}$, as follows

$$C^{\rm CMB}_{\rm i,j} = \mathbf{R}^{*}_{\rm i}(\mathbf{v}) C(\ell) \mathbf{R}_{\rm j}(\mathbf{v}), \tag{3.21}$$

where $\ell = 2\pi v$. In addition to the estimators and covariance matrices, the $\mathbf{R}_{\rm i}(\mathbf{v})$ projection matrices are also contained in the MPIGRIDR data output, and are used later in this work for constructing the model estimators from analytical SZ sky models.

3.4 Summary

In this chapter I have discussed both the selection and observation of SZ clusters with CBI2, and the steps required to reduce the data into a form suitable for analysis. The final data set for each SZ galaxy cluster, in reduced and gridded form, consists of approximately 350 complex estimators with the associated noise and CMB covariance matrices. In the following chapter I discuss how this data, in combination with other observations, can be used to estimate physical properties of galaxy clusters including the total mass and gas mass fraction.

Chapter 4

Modelling the Sunyaev-Zel'dovich effect

4.1 Current Models of the intra-cluster medium

Much of the work to date on combining SZ and X-ray analysis of galaxy clusters has used the isothermal β model prescription for modelling the ICM (Cavaliere & Fusco-Femiano, 1976, 1978). This simple model is typically used to fit regions of the cluster within r_{2500}, the radius at which the mean enclosed density is a factor of 2500 times the universal critical density at the redshift of the cluster. At these small radii the isothermal β model is found to be accurate in reproducing the observable and physical properties of clusters (e.g. Grego et al. (2000); Reese et al. (2002); LaRoque et al. (2006)). However recent deep X-ray spectral observations of nearby cluster samples using the Chandra (Vikhlinin et al., 2006) and XMM-Newton (Pratt et al., 2007) satellites show that at larger radii the ICM temperature declines with radius (see Figure 4.1). Hence for low resolution pointed SZ observations, that are sensitive to the outskirts of the cluster gas, there is a clear requirement for a more physically motivated non-isothermal model that is simple enough to be constrained by the data. There have been a number of approaches amongst SZ and X-ray observers to relax the assumption of isothermality in clusters and model the ICM in a physical way and I will briefly outline some of these approaches here.

When one has X-ray spectral data that are of high sensitivity and spatially resolved, the temperature profile can be re-constructed from just the X-ray data alone. The electron density and temperature are separately parameterised and fitted to the observed surface brightness and spectra. For Chandra observations of nearby relaxed clusters, Vikhlinin et al. (2006) developed a modified β model of the electron density to

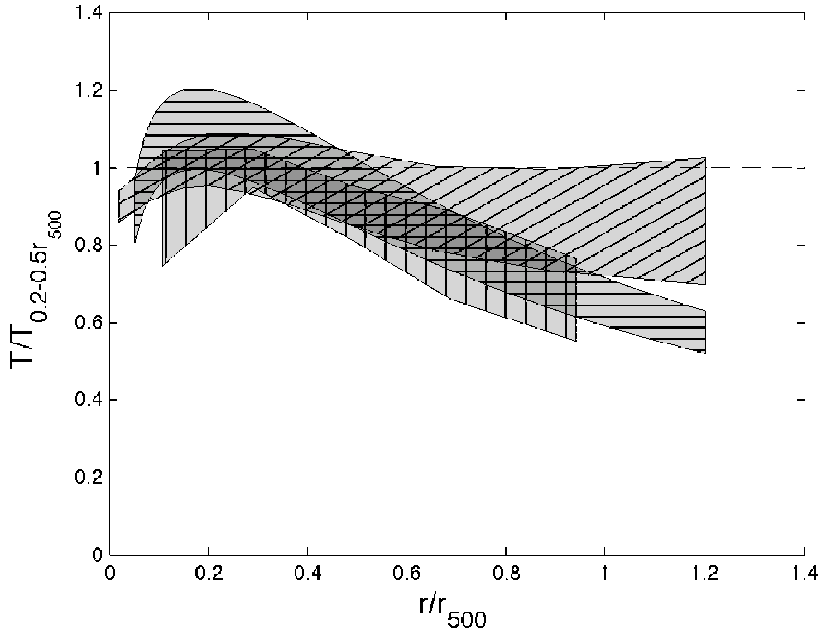

Figure 4.1: Scaled profiles for the ICM temperature derived from spectral X-ray observations. The temperatures are scaled to the volume average over 0.2 to 0.5 r_{500}. The grey regions enclose the average profiles for Chandra observations by Vikhlinin et al. (2006) (*horizontal lines*) and XMM-Newton observations by Pratt et al. (2007) (*vertical lines*) and Zhang et al. (2008) (*diagonal lines*).

fit the observed cores and steeper outer profiles of relaxed clusters, given by

$$n_{\rm e}^2(r) = n_{\rm e0}^2 \frac{(r/r_{\rm c})^{-\alpha}}{[1+(r/r_{\rm c})^2]^{3\beta-\alpha/2}} \frac{1}{[1+(r/r_{\rm s})^\gamma]^{\varepsilon/\gamma}} + \frac{n_{\rm e02}^2}{[1+(r/r_{\rm c2})^2]^{3\beta_2}}. \tag{4.1}$$

In that work the temperature is parameterised by a broken power law at large radii and declines in the central cooling region as given by Allen et al. (2001). The model 3D temperature profile is then projected along the line of sight and fitted to the observed projected temperature. The final form of the fitted 3D temperature profile is given by the product of the behaviour at small and large radii by the following expression

$$T_{\rm 3D}(r) = T_0 t_{\rm cool}(r) t(r), \tag{4.2}$$

where

$$t_{\rm cool}(r) = \frac{(x+T_{\rm min}/T_0)}{(x+1)},\ x = \left(\frac{r}{r_{\rm cool}}\right)^{a_{\rm cool}} \tag{4.3}$$

and

$$t(r) = \frac{(r/r_t)^{-a}}{[1+(r/r_t)^b]^{c/b}}. \tag{4.4}$$

Other X-ray observations by Zhang et al. (2008) take a similar approach to fit to data from XMM-Newton observations of the LoCuSS clusters, where they use a 7 parameter model to produce de-projected spectral temperature profiles, and a modified double β model in order to obtain a reasonable fit to the cluster surface brightnesses. However the sensitivity of X-ray spectral data is typically low at large radii, and many X-ray observations cannot constrain the total mass and temperature estimates beyond r_{500}.

When one wishes to extract the total mass and baryon fraction information from joint SZ and X-ray observations, a relationship must be assumed between the properties of the intra-cluster medium and the dark matter content, usually in the form of hydrostatic equilibrium. In the joint analysis of cluster observations (JACO) software, developed by Mahdavi et al. (2007), they fit to high significance X-ray spectra from Chandra and XMM-Newton, weak lensing shear from Canada-France-Hawaii telescope, optical data on the brightest cluster galaxy from the Hubble space telescope and the SZ effect from the Cosmic Background Imager. The total enclosed cluster mass is assumed to be in hydrostatic equilibrium with the ICM and comprises three explicit components, namely the dark matter, the gas and stellar components. Each of these mass components is then described by separate parameterised models as a function of radius, and are jointly fit for in data space. An important concept is that the model for the total mass is explicitly positive and hence one avoids any possibility of a non-physical mass profile.

When high sensitivity SZ and X-ray surface brightness maps are available, cluster properties can be inferred independently of the use of X-ray spectra. It is typical that the SZ and X-ray surface brightness maps are more sensitive at the largest radii than the X-ray spectral data, allowing one to obtain temperature and mass profiles in the cluster out-skirts. For sufficiently resolved SZ maps, the temperature and mass profiles can be reconstructed by de-projection techniques, for example see Ameglio et al. (2007, 2009) for a comparison of the method to simulations and Nord et al. (2009) for direct application to SZ and X-ray data. However with many SZ experiments the data are generally not very well resolved, and so combined analysis with X-ray surface brightness data requires the application of a simple analytical model that reproduces the observed temperatures and masses from X-ray observations and simulations. Mroczkowski et al. (2009) used a parameterised pressure profile (Nagai et al., 2007) to fit to data from the Sunyaev-Zel'dovich array

(SZA) and then combine with X-ray surface brightness to reproduce temperature profiles out to large radii. The gas pressure is assumed to be determined primarily by the dark matter potential and so follows a two-parameter model of a form similar to that of the NFW profile (Navarro et al., 1995), given by

$$P_{\rm e}(r) = \frac{P_{\rm e,i}}{(r/r_{\rm p})^c \left[1+(r/r_{\rm p})^a\right]^{(b-c)/a}}. \tag{4.5}$$

The X-ray surface brightness is modelled in a simplified form of that developed by Vikhlinin et al. (2006) given by

$$n_{\rm e}(r) = n_{\rm e0}\left[1+(r/r_{\rm c})^2\right]^{-3\beta/2}\left[1+(r/r_{\rm s})^\gamma\right]^{-0.5\varepsilon/\gamma}, \tag{4.6}$$

where it is assumed that the cluster core does not contribute significantly to the SZ signal.

The CBI2 array has relatively low spatial resolution, and a large field-of-view, and hence a simple parameterised model is required to describe the behaviour of the cluster gas and total mass. I therefore parameterise the cluster ICM based on the entropy, which is known to have well-behaved observable characteristics, and combine this with an NFW parametrisation of the dark matter halo component. By modelling the gas in this simple way, the underlying physics of cluster gas in hydrostatic equilibrium is encoded into the model from the outset, and is simple enough to be constrained by X-ray surface brightness and low-resolution SZ data. This also avoids ad hoc parametrisation of the electron density and temperature and therefore removes the possibility of introducing unphysical solutions for the total mass. The following section describes in detail the physical basis and parametrisation of this model.

4.2 An Entropy based model

The Dark Mass Halo

It is intended that a parametric model be constructed that is both physically consistent and is therefore a reasonable description of the ICM on the angular scales to which CBI2 is sensitive. A suitable parametrisation of the dark matter content is the hierarchical clustering NFW profile (Navarro et al., 1995), where the dark

matter (DM) density as a function of radius is given by the following expression

$$\rho_{\rm DM}(r) = \frac{\delta_{\rm c}\rho_{\rm crit}}{(r/r_{\rm s})(1+r/r_{\rm s})^2}, \tag{4.7}$$

where $\rho_{\rm crit}$ is the universal critical density for closure (at the redshift of the cluster), $r_{\rm s}$ is the scale radius and $\delta_{\rm c}$ is the characteristic density contrast. The DM virial radius $r_{\rm DM}$ is defined in this model as the radius of a sphere at which the mean interior DM density is equal to $200\rho_{\rm crit}$. Note that the true virial radius of the cluster is slightly larger ($\sim 10\,\%$) since one must also take into account the contribution from the gas when calculating the total mass. It is related to the scale radius by the following simple expression

$$r_{\rm s} = \frac{r_{\rm DM}}{c_{\rm DM}}, \tag{4.8}$$

where $c_{\rm DM}$ is known as the DM concentration parameter. This is related to the DM density contrast (see Navarro et al., 1996) by

$$\delta_{\rm c} = \frac{200}{3}\frac{c_{\rm DM}^3}{[\ln(1+c_{\rm DM}) - c_{\rm DM}/(1+c_{\rm DM})]}. \tag{4.9}$$

The DM density becomes increasingly large at small radii, and is unbounded at the centre of the cluster. However since the enclosed DM mass is calculated by integrating this density over the volume it, can be solved for all radii. The DM mass is thus given by the following expression

$$M_{\rm DM}(<r) = 4\pi\delta_{\rm c}\rho_{\rm crit}r_{\rm s}^3\left[\ln\left(\frac{r_{\rm s}+r}{r_{\rm s}}\right) - \left(\frac{r}{r_{\rm s}+r}\right)\right]. \tag{4.10}$$

Therefore the DM mass distribution in the cluster is defined for any set of values of the parameters $c_{\rm DM}$ and $r_{\rm DM}$.

The Entropy

In order to derive the electron pressure, and hence the thermal SZ decrement, a physical quantity is required that describes the gaseous properties in an easily understandable and similar way for all clusters. The cluster entropy is expected to behave in a self-similar way for reasonably massive clusters, differing primarily in the cluster cores due to the presence of non-gravitational processes. Assuming that the cluster gas is ideal,

and can be described by the adiabatic relation, then the electron pressure and entropy observable are given by

$$P_{\rm e} = S_{\rm e} n_{\rm e}^{\gamma} \tag{4.11}$$

$$S_{\rm e} = \frac{T_{\rm e}}{n_{\rm e}^{\gamma-1}}, \tag{4.12}$$

where $P_{\rm e}$, $S_{\rm e}$, $n_{\rm e}$ and $T_{\rm e}$ are the electron pressure, entropy, density and temperature (in keV units) respectively. The parameter γ is the adiabatic ratio of heat capacities and for an ideal monatomic gas is equal to 5/3. The true thermodynamic entropy of the ICM is related to the observable quantity $S_{\rm e}$ by a logarithm and an additive constant, and is proportional to the density of states in statistical theory. Therefore the entropy observable is defined by the following expression (Ponman et al., 1999; Lloyd-Davies et al., 2000)

$$S_{\rm e} = \frac{T_{\rm e}}{n_{\rm e}^{2/3}}. \tag{4.13}$$

At small radii ($r < 0.1 r_{200}$, Voit et al. (2005)) the entropy profiles of clusters are expected to have a low-entropy core region as a result of radiative cooling of the gas. However excess entropy may also exist in this region due to additional heating processes from central AGN and star formation. At the opposite end of the radial scale, towards the virial edge of the cluster, simulations of non-radiative clusters predict that the entropy profile should tend to a power law, where $S_{\rm e}(r) \propto r^{1.1}$ (e.g. Tozzi & Norman, 2001; Kay, 2004; Voit et al., 2005; Mitchell et al., 2009). X-ray observations to date are consistent with this predicted behaviour (see e.g. Ponman et al., 2003; Piffaretti et al., 2005; Donahue et al., 2006; Pratt et al., 2006; Morandi & Ettori, 2007; Zhang et al., 2008; Pratt et al., 2010), and a recent study of the high-resolution Chandra Data Archive by Cavagnolo et al. (2009) has provided definitive evidence of this expected behaviour in a collection of 239 clusters. Therefore, for the purposes of providing a physically motivated gas model, the following parametrisation is chosen for the entropy profile

$$S_{\rm e}(r) = S_{\rm e0} \left(1 + \left(\frac{r}{r_{\rm core}} \right)^2 \right)^{\alpha}, \tag{4.14}$$

where S_{e0} is the central entropy value, r_{core} is a scale radius, and α is a parameter describing the behaviour at radii much larger than r_{core}. In terms of the central electron density and temperature, $S_{e0} = T_{e0}/n_{e0}^{2/3}$. Given the findings of the simulation and observational work outlined above, one would expect the entropy profile to be affected by non-graviational physical processes at radii smaller than $r_{core} \sim 0.1 r_{200}$, and at larger radii follow a power-law $S_e \propto r^{2\alpha}$, where $\alpha \sim 0.55$.

The Pressure

The condition of hydrostatic equilibrium relates the total enclosed mass (M) to the electron density and pressure by the following equation

$$\frac{dP_e}{dr} = -\frac{GM\mu m_p n_e}{r^2}, \tag{4.15}$$

where μ is the mean molecular mass per hydrogen atom, which has a value of 0.6. From the expression given in Equation 4.13, and assuming the ideal gas law holds for the electron pressure (where $P_e = n_e T_e$), one can derive the following relation for the electron density as a function of pressure and entropy

$$n_e = (P_e/S_e)^{3/5}. \tag{4.16}$$

The pressure as a function of radius can then be derived by substituting the above expression for n_e into Equation 4.15 and rearranging to give

$$P_e(r) = \left[P_{e0}^{2/5} - \frac{2}{5} G\mu m_p \int_0^r \frac{M dr'}{S_e^{3/5} r'^2} \right]^{5/2}, \tag{4.17}$$

where the central pressure, P_{e0}, is equal to the product of the central density and temperature. The integral in the above expression can be solved numerically so that the electron pressure is calculated as a function of radius. The total mass is calculated by summing the enclosed DM and baryonic masses (note that the fraction of mass contained in stellar material is considered insignificant) at each radius out from the centre of the cluster. A value of 1.16 is assumed for the ratio of baryons to electrons, in order to calculate the baryonic mass. The pressure is then integrated in shells from the cluster centre to the required radius.

4.3 SZ and X-ray Observables

The SZ is a measure of the integrated line-of-sight electron pressure, and when integrated over the whole cluster is a measure of the total thermal energy. The observed change in CMB temperature as a result of the SZ is given by

$$\frac{\Delta T_{\rm SZ}}{T_{\rm CMB}} = f(x)y, \tag{4.18}$$

where x is a dimensionless frequency equal to $h\nu/k_{\rm B}T_{\rm CMB}$ and y is the comptonization parameter, which is equal to the integrated optical depth multiplied by the fractional gain in energy per scattering. Hence y is proportional to the integral of $n_{\rm e}T_{\rm e}$ along the line of sight

$$y = \int n_{\rm e}\frac{k_{\rm B}T_{\rm e}}{m_{\rm e}c^2}\sigma_{\rm T}{\rm d}l. \tag{4.19}$$

The frequency dependency $f(x)$ also has a dependence on the electron temperature $T_{\rm e}$, given by

$$f(x,T_{\rm e}) = \left(x\frac{{\rm e}^x+1}{{\rm e}^x-1} - 4\right)(1+\Delta(x,T_{\rm e})), \tag{4.20}$$

where the relativistic correction $\Delta(x,T_{\rm e})$ is derived from higher-order corrections to the Kompaneets equation (Challinor & Lasenby, 1998; Itoh et al., 1998).

In the general case of modelling a non-isothermal cluster the product of pressure and $f(x,T_{\rm e})$ is integrated along the line-of-sight. Replacing $n_{\rm e}$ and $T_{\rm e}$ by the radial dependence of the electron pressure, the expression for the change in the CMB temperature is given by

$$\Delta T_{\rm SZ} = T_{\rm CMB}\int f(x,T_{\rm e})\frac{P_{\rm e}\sigma_{\rm T}}{m_{\rm e}c^2}{\rm d}l, \tag{4.21}$$

which is then solved numerically.

The integral of pressure over the volume of the cluster is a measure of the total thermal energy and is therefore a useful quantity in characterising the overall thermal SZ effect. The integral of y over the solid angle of the cluster is an observable quantity that is often used for this purpose,

$$Y = \int y(\Omega){\rm d}\Omega, \tag{4.22}$$

where Y is calculated within a given projected radius. However, for the purposes of the work here, I choose to use an intrinsic measure of Y that is independent of the distance to the cluster, and hence will allow comparison of clusters at different redshifts. I therefore assume spherical symmetry and use the following definition

$$Y D_{\rm A}^2 = 4\pi \int \frac{P_{\rm e}\sigma_{\rm T}}{m_{\rm e}c^2} r^2 {\rm d}r, \tag{4.23}$$

where $Y D_{\rm A}^2$ is calculated over the cluster volume, enclosed by a given physical radius.

The observed continuum X-ray surface brightness from galaxy clusters is caused primarily by bremsstrahlung radiation from scattered electrons in the hot ICM, with some emission also from high energy transition lines. The continuum X-ray emission is proportional to the projected electron density squared, multiplied by the emissivity along the line-of-sight. If all of the emission were completely dominated by bremsstrahlung radiation then the emissivity would go as the square root of the temperature. In practice this is not completely the case but in general the emissivity is a weak function of the temperature. The observed X-ray surface brightness per unit energy dE is given by the following expression

$$\frac{{\rm d}S_{\rm X}}{{\rm d}E} = \frac{1}{4\pi(1+z)^3} \int n_{\rm e}^2 \tilde{\Lambda}(E', T_{\rm e}) {\rm d}l, \tag{4.24}$$

where z is the cluster redshift and $\tilde{\Lambda}(E', T_{\rm e})$ is the X-ray spectral emissivity as a function of temperature and emitted energy, $E' = E(1+z)$. The surface brightness for a particular observer-frame energy band is then given by the equation

$$S_{\rm X} = \frac{1}{4\pi(1+z)^4} \int n_{\rm e}^2 \Lambda(T_{\rm e}) {\rm d}l, \tag{4.25}$$

where $\Lambda(T_{\rm e})$ is the emissivity integrated over the equivalent emitted-energy band, and is hence a function of redshift. In this work the emissivity values for every position in the cluster volume are interpolated from a lookup table of values, as a function of temperature and redshift, based upon the Raymond-Smith plasma model (Raymond & Smith, 1977) for the observer-frame energy range 0.5-2 keV.

Combined observations of the SZ and X-ray surface brightness constrain the pressure and electron density and hence provide constraints on all of the model parameters. The physical properties of the cluster, including the total mass and electron temperature, as a function of radius are constrained by the 6 parameters defined by this model: $c_{\rm DM}$, $r_{\rm DM}$, $n_{\rm e0}$, T_{e0}, $r_{\rm core}$ and α.

4.4 Model Fitting

4.4.1 Bayesian Inference of the parameter values

Bayes' theorem is implemented in order to fit parametrised models to the SZ and X-ray data and obtain probability distributions for the derived physical quantities. The joint probability distribution of a set of model parameters (θ), given the data ($\mathbf{d}$) and the model ($\mathscr{M}_{\rm j}$), can be calculated from the following equation

$$\Pr(\theta|\mathbf{d},\mathscr{M}_{\rm j}) = \frac{\Pr(\mathbf{d}|\theta,\mathscr{M}_{\rm j})\Pr(\theta|\mathscr{M}_{\rm j})}{\Pr(\mathbf{d}|\mathscr{M}_{\rm j})}. \tag{4.26}$$

The probability of the data given the set of model parameters $\Pr(\mathbf{d}|\theta,\mathscr{M}_{\rm j})$ is commonly called the likelihood (L) and can be calculated based on assumptions of the distribution of the error in the data. When the data set is large and therefore quasi-continuous (such as the noise generated in radio instrumentation), one can approximate the likelihood by the form given for Gaussian multivariate data

$$L_{\rm gaussian} = \frac{1}{\sqrt{(2\pi)^N|\mathbf{C}|}}\exp\left(-\frac{(\mathbf{d}-\mathbf{m})^{\rm t}\mathbf{C}^{-1}(\mathbf{d}-\mathbf{m})}{2}\right), \tag{4.27}$$

where N is equal to the size of $\mathbf{d}$, $\mathbf{C}$ is the covariance matrix of the uncertainty in the data and $\mathbf{m}$ is the vector of model data. If the data are in the form of photons arriving at a detector, such as the scenario of perfectly background subtracted X-ray surface brightness data, then the likelihood is instead given by the Poisson form

$$L_{\rm poisson} = \sum_{\rm i}[d_{\rm i}\ln(m_{\rm i}) - m_{\rm i} - \ln(d_{\rm i}!)], \tag{4.28}$$

where $d_{\rm i}$ and $m_{\rm i}$ are the elements of $\mathbf{d}$ and $\mathbf{m}$ respectively. When we wish to fit to multiple independent data sets, such that $\mathbf{d} = \sum \mathbf{d}_{\rm k}$, then the total likelihood is just given by the product of the individual likelihoods.

The probability of the parameter values given the model, $\Pr(\theta|\mathscr{M}_{\rm j})$, is known as the prior distribution, and encodes the prior information on the parameter values before fitting to the data. For example, the uncertainty in the position of the cluster centroid might be known from previous observations and from the pointing accuracy of the instrument. One might then wish to apply a Gaussian prior to the model cluster position based on the level of uncertainty. In this thesis the prior distributions for the model parameters are not too stringent, are typically uniform distributions unless indicated otherwise, and comfortably encompass

reasonable values based on previous work.

The normalisation of the posterior probability distribution is given by the evidence, which is equal to the probability of the data given the model. The evidence is a measure of the suitability of the model for fitting to the data and provides a quantitative measure of selecting between competing models. The evidence for the data, assuming a particular model, is calculated by marginalising the product of the likelihood and prior distributions over the model parameters. This is given by

$$\Pr(\mathbf{d}|\mathscr{M}_{\rm j}) = \int \Pr(\mathbf{d}|\theta,\mathscr{M}_{\rm j})\Pr(\theta|\mathscr{M}_{\rm j})\mathrm{d}\theta, \tag{4.29}$$

which follows from Equation 4.26 and the fact that the integrated posterior distribution is normalised to unity. When a model provides a good fit to the data, the likelihood peak will have a high value, and hence the model will have a high evidence value associated with it. However if the model is over-complex then there will be large regions of low likelihood within the prior volume, thus reducing the evidence value for this model, in agreement with Occam's razor. See e.g. Marshall et al. (2003) for a further description of Bayesian inference and its application to cosmological data.

4.4.2 The SZ Likelihood

The focus of this thesis is on interferometric SZ data, which are assumed to have Gaussian distributed errors, and so have a likelihood that is expressed in the form given by Equation 4.27. The SZ data consist of complex visibilities from the output of the correlator, which encode the Fourier transform of the product of the sky brightness and the primary beam of the instrument. The visibilities only sample the Fourier transform at discrete coordinates in the Fourier plane, defined by the configuration of the instrument antennas during the observation. As explained in Chapter 3, the reduced CBI2 data are first gridded into estimators of the visibility, and the covariance matrices are calculated at the grid positions. Hence the data used in the calculation of the likelihood are in the form of these gridded estimators.

Errors in the SZ data originate from three main sources; the thermal noise, the intrinsic CMB anisotropy and finally radio point sources. The total covariance matrix is thus given by the sum of these individual components

$$\mathbf{C}_{\rm SZ} = \mathbf{C}_{\rm noise} + \mathbf{C}_{\rm CMB} + \mathbf{C}_{\rm sources}. \tag{4.30}$$

The thermal noise component originates from the instrument electronics, the atmosphere and the ground and since the noises are not correlated the covariance matrix for this component is diagonal. Error in the SZ signal also arises from the presence of intrinsic fluctuations in the CMB that obscure the cluster. Since these fluctuations are inherent in the sky brightness, they are correlated in the visibilities, and so result in a non-diagonal covariance matrix. The uncertainty due to the CMB is largest on the shortest CBI2 baselines and dominates the error in the SZ signal at $l \lesssim 1000$ (see e.g. Udomprasert et al., 2004).

The remaining significant source of error is the presence of bright radio point sources, especially near to the centre of the field, where there will be less attenuation from the primary beam and more confusion with components of the SZ signal. This error can be treated either by identifying the point sources in the long-baseline CBI2 data, or by simultaneously observing known sources from low-frequency surveys with other 31 GHz telescopes of higher resolution. If one is confident that source variability is not an issue, then the source fluxes can be subtracted directly from the data and any residual flux errors incorporated into the covariance matrix. Alternatively the data at the position of the source can be rejected during the model fitting stage by the inclusion of an appropriate covariance matrix. This is known as source projection, which provides an alternative method to subtracting the point source flux directly from the visibility data, and is approximately equivalent to masking out the data at the position of the source. In this method a covariance matrix is constructed from the contribution to the signal from each known source, and multiplied by a large co-factor as follows

$$\mathbf{C}_{\text{sources}} = \gamma s_{\text{i}} s_{\text{i}}^{\dagger}, \tag{4.31}$$

where s_{i} is the signal from the i^{th} source, and γ is the large co-factor, known as the projection factor. In the limit that γ becomes very large, then the value of s_{i} becomes insignificant, and so the solution is no longer sensitive to the amplitude of each source. Sievers et al. (2009) found whilst working on the CMB angular power spectrum that using large projection factors could cause numerical instability in the calculation and hence lead to an ill-conditioned covariance matrix. Therefore an analytical approach is used, taking the limit as $\gamma \rightarrow \infty$ and using the Woodbury Formula (Press et al., 1992). The inverse of the total covariance matrix

(assuming symmetry in all matrices) can now be calculated analytically by

$$\begin{aligned} \mathbf{C}^{-1} &= (\mathbf{N} + \gamma \mathbf{S}\mathbf{S}^{\dagger})^{-1} \\ &= \mathbf{N}^{-1} - \mathbf{N}^{-1}\mathbf{S}(\mathbf{S}^{\dagger}\mathbf{N}^{-1}\mathbf{S})^{-1}\mathbf{S}^{\dagger}\mathbf{N}^{-1}, \end{aligned} \tag{4.32}$$

where $\mathbf{C}$ is the total covariance matrix, $\mathbf{N}$ is the covariance matrix from the noise and intrinsic CMB contributions, and $\mathbf{S}$ is the matrix of source signals. Note that this calculation will fail if $\mathbf{S}$ is degenerate and hence one must make sure that the same source is not repeated twice in constructing the source signal matrix. For further discussion of this method please refer to Bond et al. (2000); Mason et al. (2003); Sievers et al. (2009).

To calculate the SZ likelihood, the modelling code is used to generate model estimators at the (u,v) positions of the data estimators. The pressure is calculated from an analytical model by numerical integration, as shown in Equation 4.17. Further numerical integration along the line-of-sight produces the change in CMB temperature due to the SZ as a function of projected radius. The model visibility is then calculated by interpolating the SZ temperature onto a fine grid of radial coordinates and performing a fast Fourier transform. In general the size of the (u,v) fine grid, as given by the data, determines the resolution required for the model SZ temperature distribution. The image plane is over-sampled by a factor of three to improve numerical accuracy, which is important when the size of the model cluster might be small. The model estimators m_{i} are then constructed from the fine grid model visibilities by applying the R_{i} projection operators as defined in Chapter 3.

4.4.3 The X-ray Likelihood

The X-ray surface brightness data are typically in the form of photon counts distributed over a CCD detector on an X-ray satellite telescope, and so will have a likelihood that is expressed in the Poisson form given by Equation 4.28. If a parametrised model is to be fit to this data directly, then the model of the photon counts must be constructed based on the known properties of the instrument. The model surface brightness is converted to the photon count rate per solid angle by an instrument dependent factor that is a function of the energy band and the absorbing neutral hydrogen column density along the line-of-sight. The number of photon counts per pixel is then calculated by multiplying the count rate by the integration time on the source

and the solid angle per pixel. If the point spread function (PSF) of the instrument is significant on the angular scales begin considered, then the model must also be convolved with the PSF before being compared with the data. Given that for this thesis it is the large scale behaviour of the cluster properties that are important, the small scale effects of the PSF are ignored here.

4.4.4 Hyper-parameters and combining the data sets

Radio interferometric SZ and X-ray surface brightness data typically have sensitivity to very different angular scales and depend differently on the physical properties that are being constrained. Therefore constructing an analytical physically-based model that provides a satisfactory simultaneous fit to both data sets is difficult, especially if we are unsure about the accuracy of the error estimates. It is therefore good practice to weight the likelihoods for these data sets using two hyper-parameters, which can then be treated as nuisance parameters and marginalised over. The normalised modified Gaussian likelihood for the data now has the following expression

$$\Pr(\mathbf{d}|\theta,\varepsilon,\mathscr{M}_{\rm j}) = \sqrt{\frac{\varepsilon^N}{(2\pi)^N|\mathbf{C}|}}\exp\left(-\varepsilon\frac{(\mathbf{d}-\mathbf{m})^{\rm t}\mathbf{C}^{-1}(\mathbf{d}-\mathbf{m})}{2}\right), \tag{4.33}$$

where ε is the hyper-parameter. Its assumed that very little is known about the true value of ε, except that it has an expectation value of unity, and a suitable prior is given by Hobson et al. (2002), where

$$\Pr(\varepsilon) = \exp(-\varepsilon), \tag{4.34}$$

and ε has a value between 0 and ∞. Note that if the Jeffreys prior were used instead, where $\Pr(\varepsilon) = 1/\varepsilon$, then it would not be possible to normalise the posterior distribution or calculate the evidence. By calculating the ratio of the evidences for the case where hyper-parameters are used, to that where they are not, it can be inferred whether they should indeed be included. If this ratio is much larger than unity then there is a significant relative inconsistency between the two data sets and their inclusion is warranted.

4.4.5 Implementation

Implementation of the model fitting is performed using BAYESYS (Skilling, 2004), a powerful Bayesian optimiser that uses the Markov Chain Monte Carlo method. Estimates of the posterior probability distribution are obtained for the model parameters by using all of the proposal distribution engines available to the program. BAYESYS provides the modelling code with parameter samples in the form of a unit hyper-cube from which the SZ and X-ray surface brightness likelihoods are calculated. The program initialises with a burn-in phase that evolves the MCMC chains from sampling just the prior distribution to locating regions of significant posterior probability. This is performed in a series of steps known as selective annealing (due to the analogous relationship with annealing in thermodynamics), during which samples of parameters are drawn from a modified posterior given by

$$\Pr(\theta|\mathbf{d},\mathscr{M}_{\rm j}) \propto \Pr(\mathbf{d}|\theta,\mathscr{M}_{\rm j})^{\lambda}\Pr(\theta|\mathscr{M}_{\rm j}), \tag{4.35}$$

where the cooling factor (λ) is slowly increased from 0 to 1. The rate of cooling (equal to the change in λ over one step) should be much lower than unity in order to ensure that BAYESYS is robust to finding regions of high posterior value in large prior volumes. Therefore the cooling rate is chosen to be much lower than unity and multiple runs are performed with different seed values to check for good convergence. The robustness of the process is improved by using an ensemble of 10 simultaneous MCMC chains that communicate after each step and so ensure that they do not become trapped in local maxima of likelihood.

After burn-in, the program draws samples from the posterior distribution at $\lambda = 1$, where the total number of samples drawn is equal to the product of the number of MCMC chains and steps. The number density of the model samples should then be a good estimate of the true posterior probability distribution. The resulting output is a list of the samples that can be marginalised over to obtain posterior distributions for the cluster properties.

4.5 Self-consistency check

A self-consistency check is performed on the fitting procedure to ensure that the expected physical cluster properties can be correctly reproduced from mock data. This is a particularly important check given that

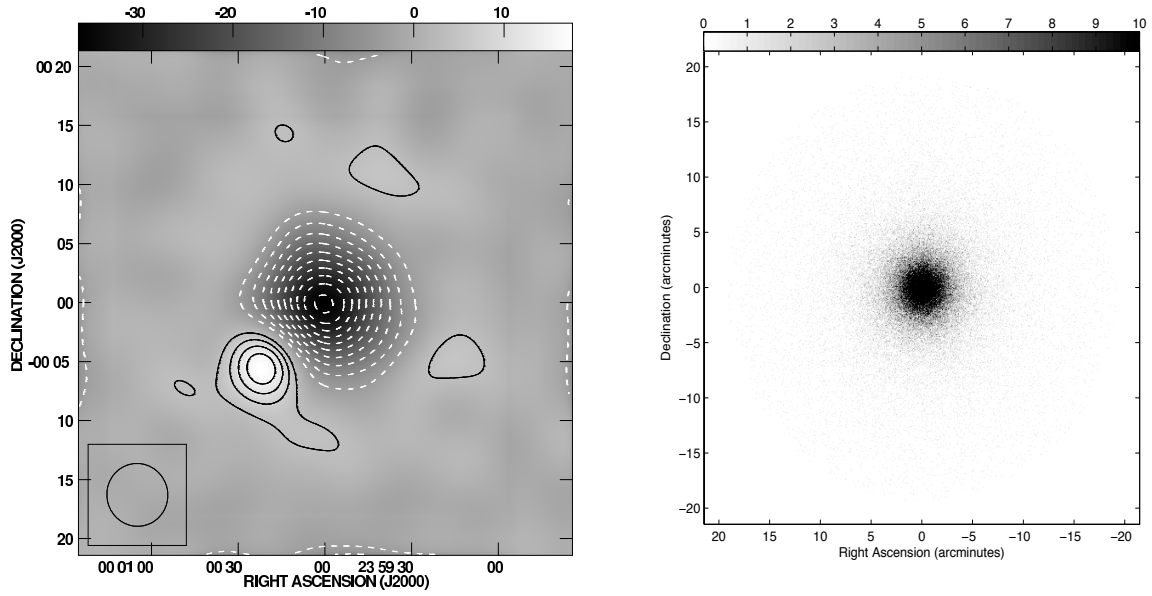

Figure 4.2: *Left*: A full-resolution map of a simulated 10 hour observation of a massive isothermal β cluster with the CBI2 array, in units of mJy beam^{-1}. The contours are in units of the 1 σ noise level on the map and the synthesised beam is shown in the bottom left-hand corner. *Right*: The corresponding simulated X-ray surface brightness map, in units of counts per pixel, for a 10 ks observation with a typical X-ray telescope.

some information loss is expected when converting the visibility data to gridded estimators. A mock cluster was constructed from a simple isothermal β model, with a total mass of $20 \times 10^{14} M_{\odot}$ and a gas mass fraction of 0.12, enclosed within a physical radius of 2 Mpc, and the $r_{\rm core}$ and β parameters were set to 0.3 Mpc and 2/3 respectively. The SZ temperature decrement and X-ray surface brightness, as a function of the projected radius, are calculated from the model parameters and interpolated onto 512×512 maps. Both maps are then converted to angular coordinates assuming that the cluster is located at $z = 0.15$.

4.5.1 Mock CBI2 SZ data

To simulate a real CBI2 observation, the CMB temperature map is constructed from an angular power spectrum generated using CMBFAST [1] (Seljak & Zaldarriaga, 1996), assuming a flat ΛCDM cosmology with $\Omega_{\rm M} = 0.3$, $\Omega_{\Lambda} = 0.7$ and $h = 0.7$. The SZ and CMB thermodynamic temperature maps are converted to sky brightness units for each of the 10 frequency channels (26-36 GHz) using the differential form of the Planck equation. In addition a mock point source, with a brightness of 25 mJy beam^{-1}, is constructed on a map at

[1] http://lambda.gsfc.nasa.gov/toolbox/tb_cmbfast_ov.cfm

a position 5 arcminutes in right ascension and declination from the cluster centre, and it is assumed that the source's spectral index is flat across the CBI2 frequency band. All three brightness maps are then summed together to form a combined sky simulation.

The sky brightness map is multiplied by the CBI2 primary beam and fast Fourier transformed to the (u,v) plane, where the visibility is then interpolated onto the positions given by a template observation. The noise weightings associated with each visibility are then scaled based on the length of the simulated integration. The effect of the ground spill-over subtraction technique used in real CBI2 observations is simulated by taking the average of the visibilities from two mock CMB maps and subtracting this from the mock data set. Once this has been applied, the data are then in the same form as a real CBI2 data set, and can therefore be gridded using the same procedure as outlined in Chapter 3. Figure 4.2 shows the full-resolution map from a mock observation of the model cluster with the full CBI2 array, for an integration of 10 hours including the time spent observing the two reference fields. The point source can also be seen in the bottom left-hand corner of the map.

4.5.2 Mock X-ray surface brightness data

To simulate real X-ray surface brightness data, the physical surface brightness map is multiplied by the count rate conversion factor of a typical instrument (such as the EPIC camera on XMM-Newton), which is assumed to be constant across the 0.5-2 keV energy band. I use a typical neutral hydrogen column density of $10^{20}\,\mathrm{cm}^{-2}$, and an integration time equal to 10 ks. The map is then multiplied by the solid angle per pixel ($\Delta\Omega$) to convert the data to the expected counts per pixel. The number of counts on each pixel is therefore related to the surface brightness and the pixel solid angle by the following expression

$$N_{\mathrm{counts}} = 5\left(\frac{S_{\mathrm{X}}}{\mathrm{erg\,s^{-1}\,cm^{-2}\,sr^{-1}}}\right)\left(\frac{\Delta\Omega}{\mathrm{sr}}\right)\times 10^{15}\,\mathrm{counts}. \tag{4.36}$$

Instrumental noise is introduced into the map by applying the Poisson distribution to each pixel, with the mean equal to the photon count. For the purposes of the mock observation I do not take into account the point spread function, the effect of which is assumed to be insignificant on the cluster scales that are being modelled. I also do not the take into account the residual background X-ray emission which might need to be considered for a real observation. Figure 4.2 shows the counts map from the mock observation, with

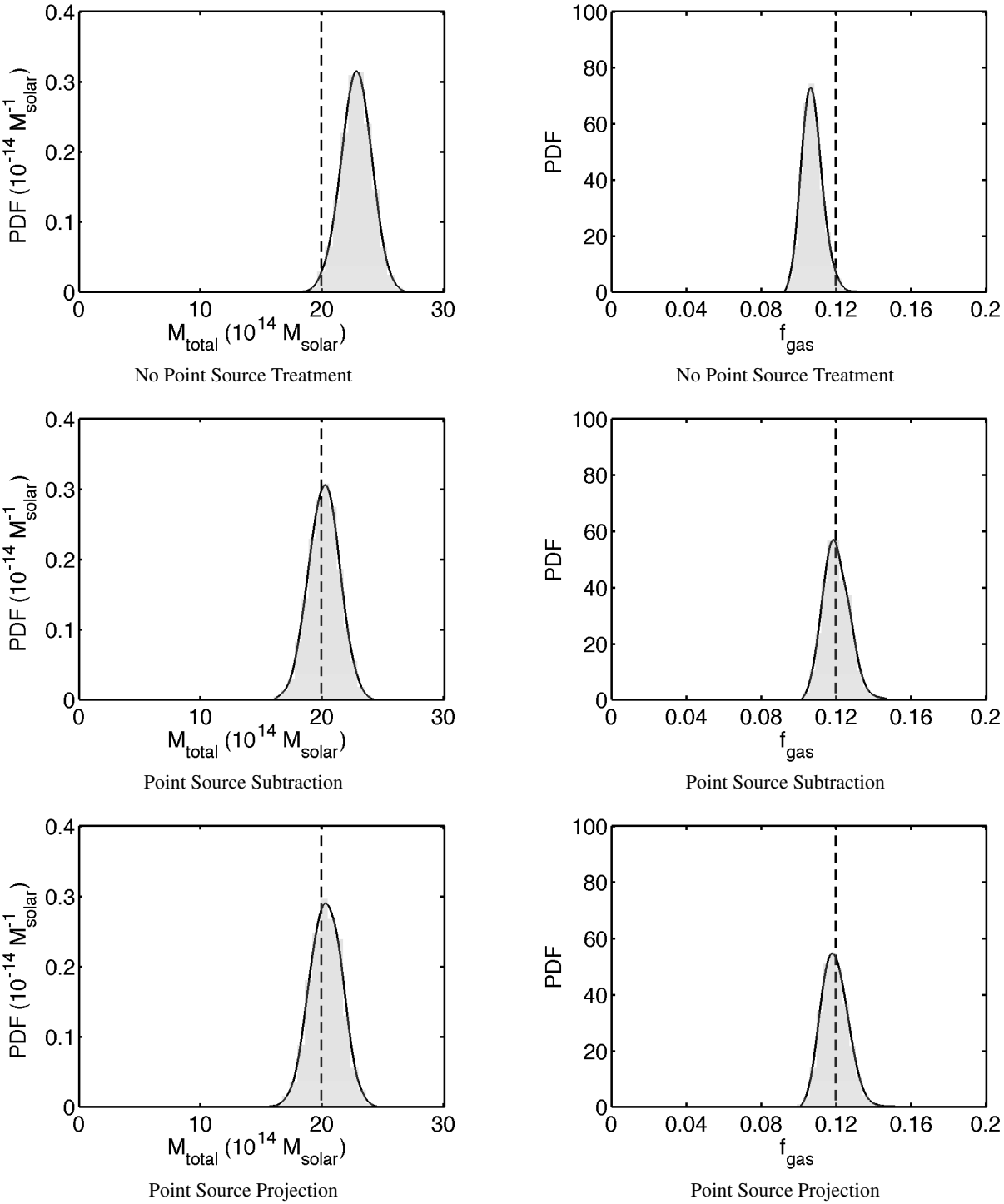

Figure 4.3: Results of the self-consistency checks for the model fitting pipeline. The mock CBI2 data have realistic signal-to-noise (equivalent of 10 hrs integration) and include the intrinsic CMB error component. *Left*: The posterior probability density for the estimated total mass enclosed within a physical radius of 2 Mpc. *Right*: The posterior probability density for the estimated gas mass fraction enclosed within a physical radius of 2 Mpc. The *dashed line* represents the true value for the estimated quantity.

Poisson error applied to the pixel values.

4.5.3 Results of the self-consistency check

The isothermal β model is used to fit to the mock CBI2 and X-ray surface brightness data, with three different methods used to treat radio point source contamination of the SZ data. In the first case no source treatment is applied, secondly the source's flux was subtracted from the visibility data, and finally the source's position was projected out. Note that hyper-parameters are not used in these fits, since it is known that the analytical model perfectly follows the mock data. I also assume that the mock data are perfectly calibrated, while in later work I account for the error introduced by calibration. The results of the fit, showing the posterior probability density for the derived total mass and gas mass fraction, are shown in Figure 4.3. In the case where no treatment was applied to the data to take into account the point source, a systematic overestimate of the total mass is obtained. Subtraction of the source flux from the data produces an estimate of the total mass and gas mass fraction that is consistent with the true values for these quantities. Likewise if one applies source projection at the fitting stage, a consistent estimate of the total mass and gas mass fraction is obtained. The source projection method is used in this thesis since it does not rely on knowing the absolute flux of the source, and is hence robust to variability.

4.6 Testing the model

In the previous section a known parametrised model was fit to a mock data set constructed from that same model. This self-consistency check showed that the analysis pipeline could correctly reproduce the enclosed total mass and baryon fractions from jointing fitting to the CBI2 SZ and X-ray surface brightness data. However it is also instructive to see how well the entropy-based model described in Section 4.2 can be used to reproduce the known properties of a realistic cluster. In this section I therefore test this model by fitting to the mock data generated from realistic hydrodynamic/N-body simulations.

4.6.1 Hydrodynamic/N-body Simulations

Hydrodynamic/N-Body simulations, previously studied by Kay et al. (2004) and Kay et al. (2008), are used to test the entropy-based model. In these simulations the gas initially cools to 10^4 K through radiative

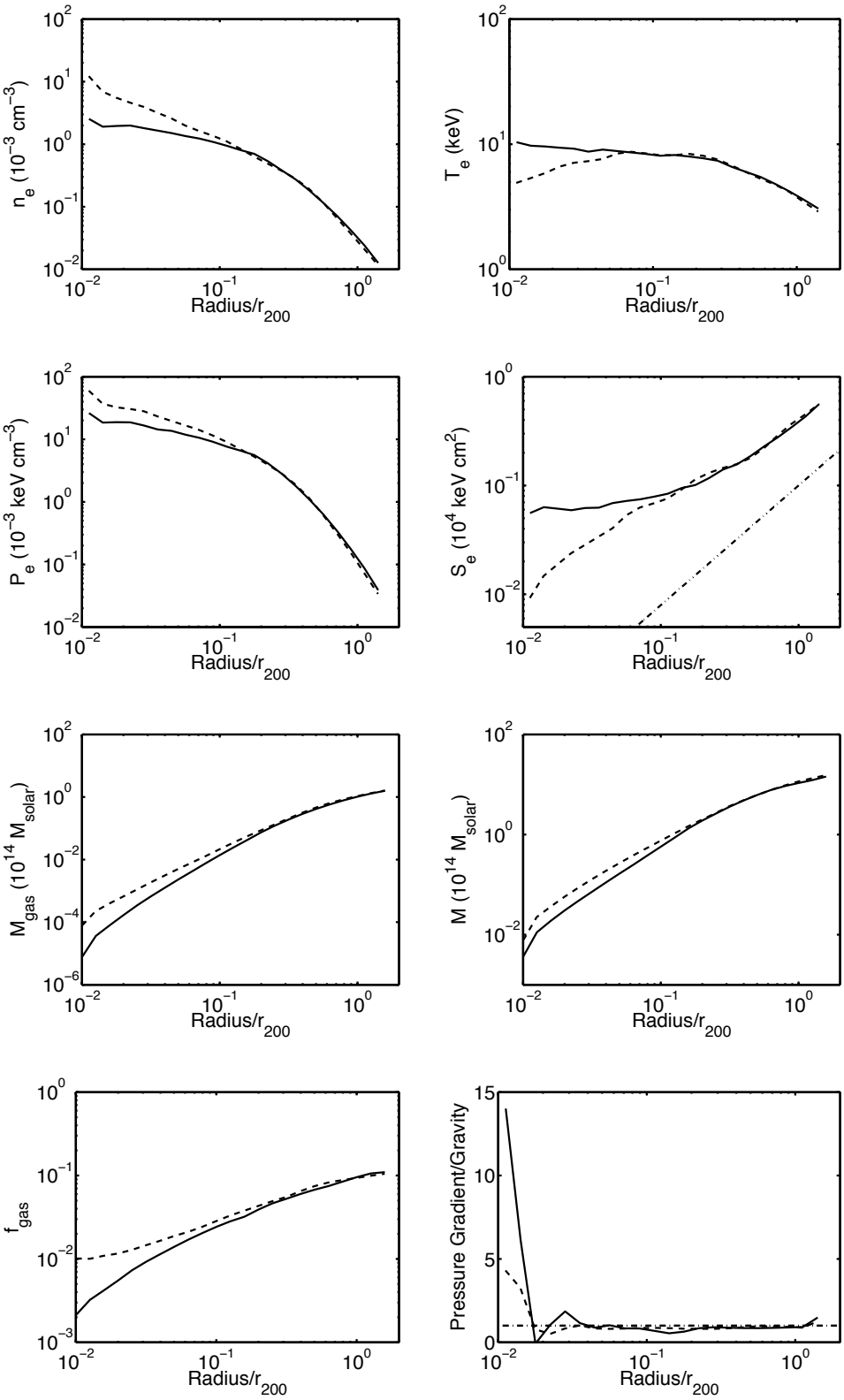

Figure 4.4: The physical properties of the simulated clusters FB1 (*dashed line*) and FB3 (*solid line*) as a function of radius. The slope of the dash-dotted line in the radial Entropy plot represents the power law predicted by the spherical accretion shock model. The dash-dotted line in the frame showing the ratio of the pressure gradient to gravity represents hydrostatic equilibrium.

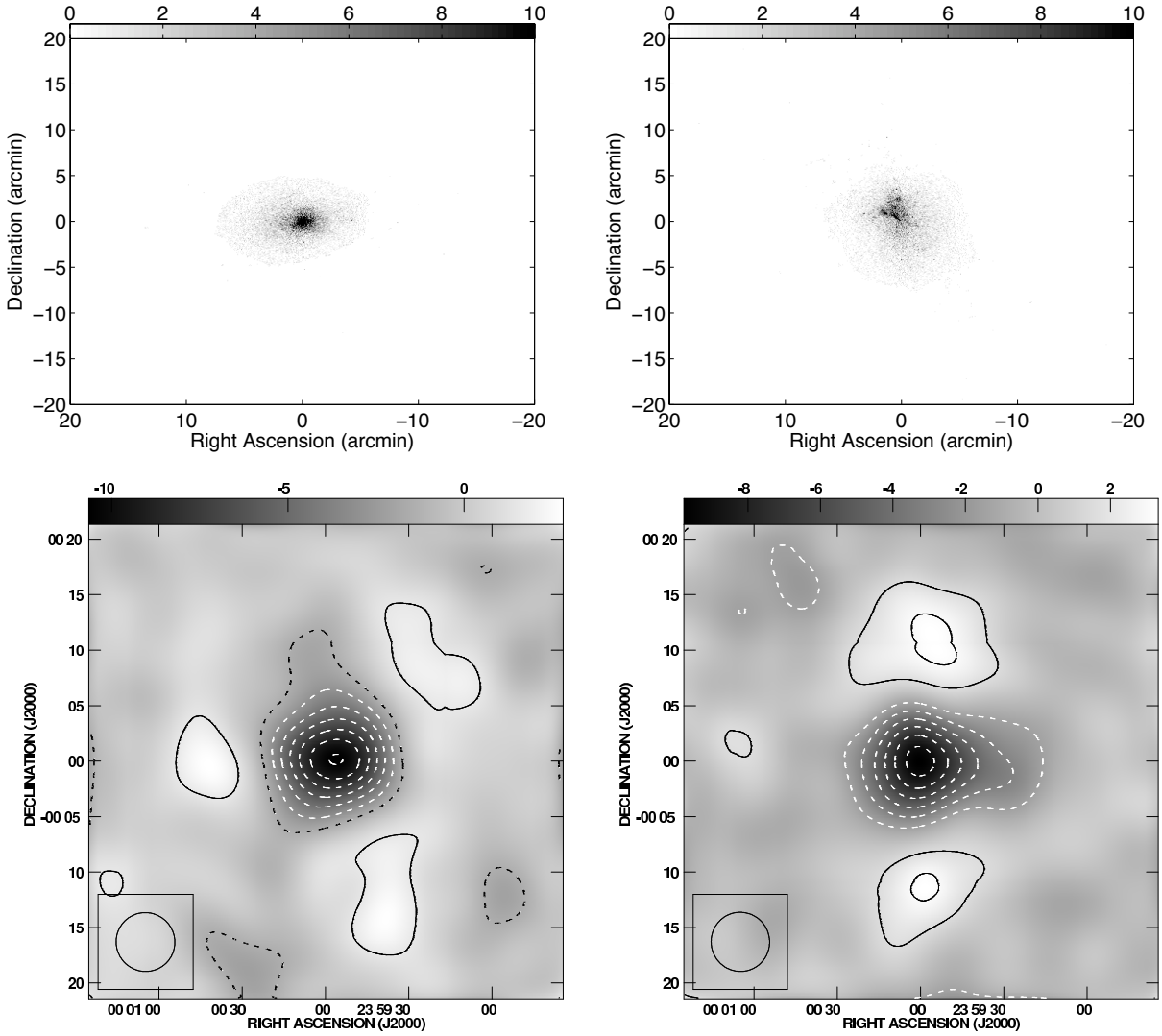

Figure 4.5: *Top*: Maps of the simulated X-ray surface brightness, for clusters FB1 (*left*) and FB3 (*right*), with the grey-scale in units of photon counts. *Bottom*: The corresponding full-resolution, CLEANed maps of mock CBI2 SZ observations. The contours represent multiples of the $2\,\sigma$ level, where the noise on each map is $1\,\mathrm{mJy\,beam^{-1}}$.

processes and is allowed to lose entropy. The cooling rate is then cut-off and a fixed fraction of the cluster gas goes on to form stellar material, while the rest is re-heated by the stars. This phenomenological approach to re-heating and galaxy formation in the cluster was found by Kay et al. (2004) to re-produce the observed $L_X - T_X$ relation, and so provides a good test for the entropy model. The sub-sample used in this thesis consists of two clusters with similar total masses ($\sim 10^{15}\,M_\odot$) and temperatures ($\sim 5\,\mathrm{keV}$), but with quite different merger histories. FB1 has a cool core and is in a relaxed state, while FB3 is a non-cool core cluster and recently underwent a strong merger at $z \sim 0.4$. Therefore our model should not only be able to reproduce the global properties of each cluster, but also correctly constrain the different profiles at large radii.

Maps of ΔT_{SZ} (at 31 GHz) and S_X (in the 0.5 - 2.0 keV band) were generously provided by S.T. Kay, and were generated for each cluster by calculating the electron density and temperature properties for every hot particle within a cylinder of length $6\,r_{200}$ and projected radius $3\,r_{200}$. Each particle contribution is smoothed and projected along the length of the cylinder onto a 1024×1024 2D pixel array, using the projected version of the GADGET2 SPH kernel. The SZ decrement and X-ray surface brightnesses were calculated using Equations 4.21 and 4.25. The maps are centred about the most gravitationally-bound dark matter particle and thus the most globally symmetric point. For the relaxed cluster FB1, this coincides with the brightest SZ and X-ray surface brightness points. In the case of FB3, this cluster underwent a recent merger event that has produced an asymmetric core region, and therefore the brightest pixels in the maps are offset from the centre. However the symmetry of the global structure of this cluster is centred about the central pixel of the map and not the fine substructure of the brightest peaks. This therefore acts to flatten the central part of the electron density profile, and hence also the X-ray surface brightness. The profiles for the physical properties of the simulated clusters are shown in Figure 4.4. Clusters of galaxies typically depart from hydrostatic equilibrium within their core region due to physical processes other than gravitational collapse, such as disturbance from recent merger activity, pre-heating from active galactic nuclei and radiative cooling. Both simulated clusters exhibit this behaviour within a radius of $\lesssim 100\,\mathrm{kpc}$, and their gas properties diverge considerably in this region. I therefore choose to ignore the central cluster core in fitting to the data since the gas density, and hence X-ray surface brightness, will strongly influence the model fit. The mock SZ and X-ray data sets were constructed from the ΔT_{SZ} and S_X maps using the same method as outlined in the self-consistency check above. The simulated SZ and X-ray maps are shown in Figure 4.5 with realistic instrumental noise.

Parameter	Type	Lower Bound	Upper Bound
$c_{\rm DM}$	Uniform	0.1	10
$r_{\rm DM}({\rm Mpc})$	Uniform	0.1	5
$n_{\rm e0}(10^{-3}{\rm cm}^{-3})$	Uniform	0	20×10^3
$r_{\rm core}({\rm Mpc})$	Uniform	0.01	2
α	Uniform	0.1	2
$T_{\rm e0}({\rm keV})$	Uniform	0	20

Table 4.1: Prior values for each of the model parameters. Column 1 gives the parameter; column 2 the type of prior; column 3 the lower prior value; column 4 the upper prior value.

4.6.2 The Prior

It is important to first understand the intrinsic constraints introduced by the prior before performing a joint fit to the data. The prior includes both the volume of the parameter space being considered and the assumptions upon which the model is based. Figure 4.6 shows the estimated prior distribution for each of the parameters in the entropy model. This plot was constructed by running the analysis pipeline with all of the model constraints in place, but with no SZ or X-ray surface brightness data. The MCMC chains are allowed to search parameter space within the constraints of the model until a large number of samples are generated ($\sim 100,000$) and thus produce a reasonable estimation of the prior distribution.

Constraints on the parameters arise from the assumption that the intra-cluster medium is in hydrostatic equilibrium and that the pressure profile must be physical at all radii. The model also prefers higher central electron temperature values due to the constraint on the pressure. In order for the condition of hydrostatic equilibrium to be satisfied, large mass values can only correlate to relatively high temperatures, and this will provide a constraint on the value of $r_{\rm DM}$ which is seen in the figure. The nature of interferometric data is such that they are not able to constrain a signal that is non-varying over the angular scales to which the instrument is sensitive. Therefore in the case of low signal-to-noise data it would be possible to obtain solutions within the acceptable prior range of the model, where the temperature gradient increases rapidly at large radii and while the density profile decreases, leading to an SZ signal with a large constant additive component. Note that this situation is not typical of many parametric models used for fitting to the SZ, since many are inherently constructed such that the signal changes with all radii. To avoid this clearly unphysical situation I impose the constraint that the electron temperature must either be constant or decreasing at radii larger than the virial radius. The principal effect of this constraint is to significantly reduce the probability

Figure 4.6: The estimated prior distribution for the parameters from the entropy model. The constraints arise from the underlying assumptions about the cluster physics. The prior ranges encompass typical values of these parameters observed to date. The grey scale represents estimates of the 68 and 95 % intervals.

of having an unphysical high value for the entropy power law parameter α at large radii.

4.6.3 Results from high signal-to-noise CBI2 data with X-ray data

Parametric fits are performed to ideal, high signal-to-noise SZ and X-ray data, in order to find the systematics that are introduced into the derived cluster properties when using the entropy model. The SZ data consist of a mock observation of the simulated cluster signal, with no intrinsic CMB error, and a very small noise component. The X-ray data consist of the simulated X-ray surface brightness, in the form of a radial profile, with 5 arcsecond bins and error bars derived from the Poisson noise on the simulated map. No calibration error has been introduced into either data set in these fits.

Figure 4.7 shows the constraints introduced from separately fitting to high signal-to-noise SZ and X-ray data. The SZ data constrain the integrated line-of-sight pressure and therefore generate an anti-correlation

FB1: High signal-to-noise CBI2 data only

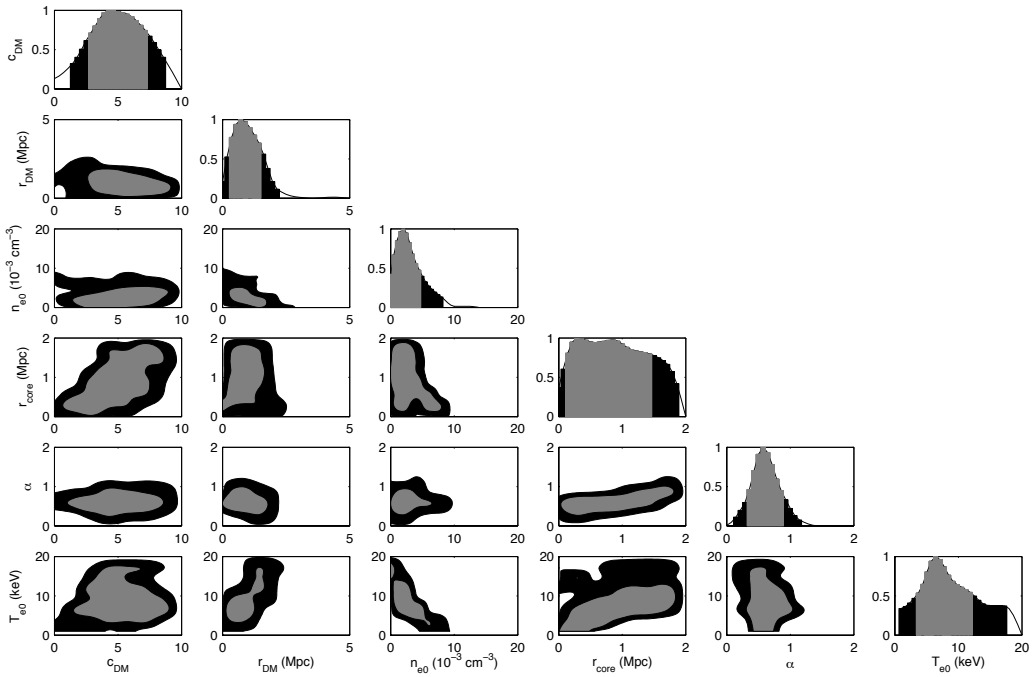

FB1: X-ray Surface brightness data only

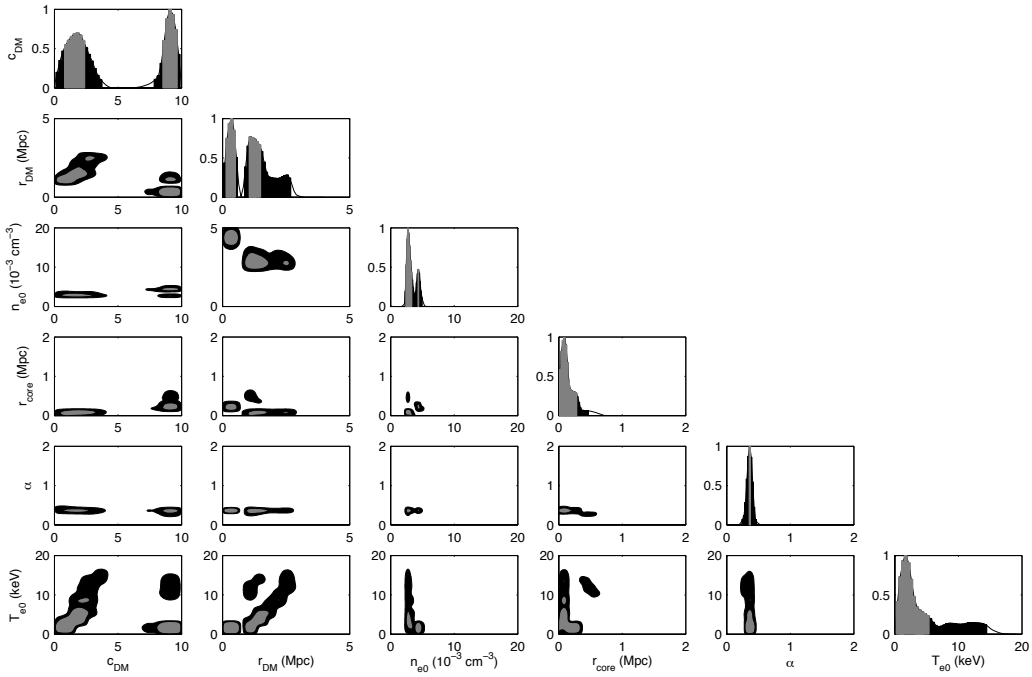

Figure 4.7: The estimated posterior probability density for entropy model parameters from separately fitting to simulated high signal-to-noise CBI2 SZ data and X-ray surface brightness data. The grey-scale represents the 68 and 95 % intervals.

FB3: High signal-to-noise CBI2 data only

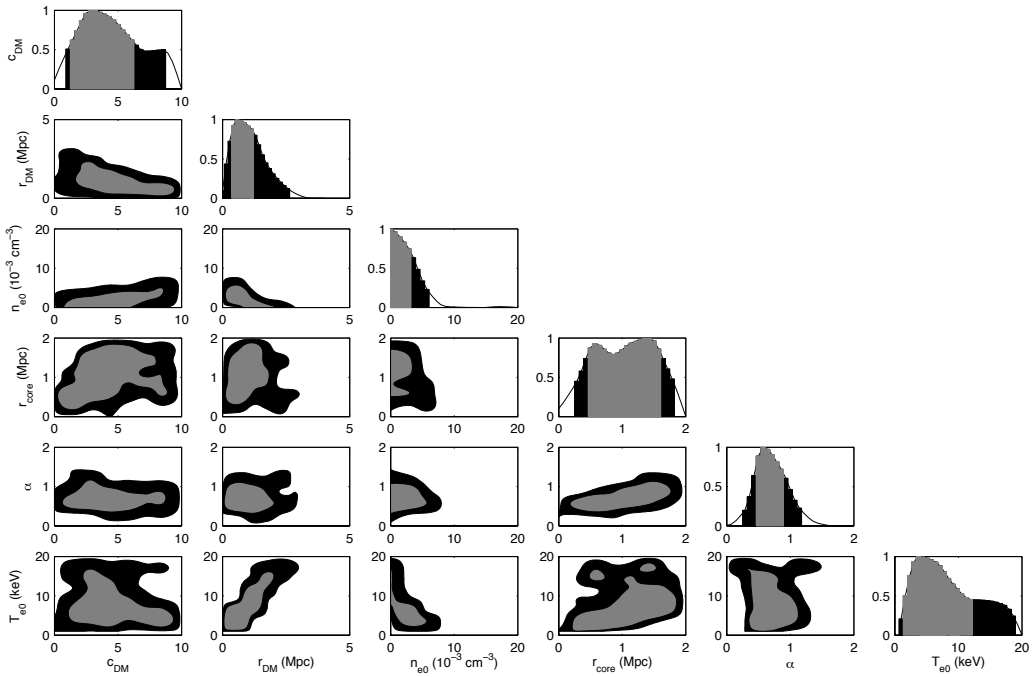

FB3: X-ray Surface brightness data only

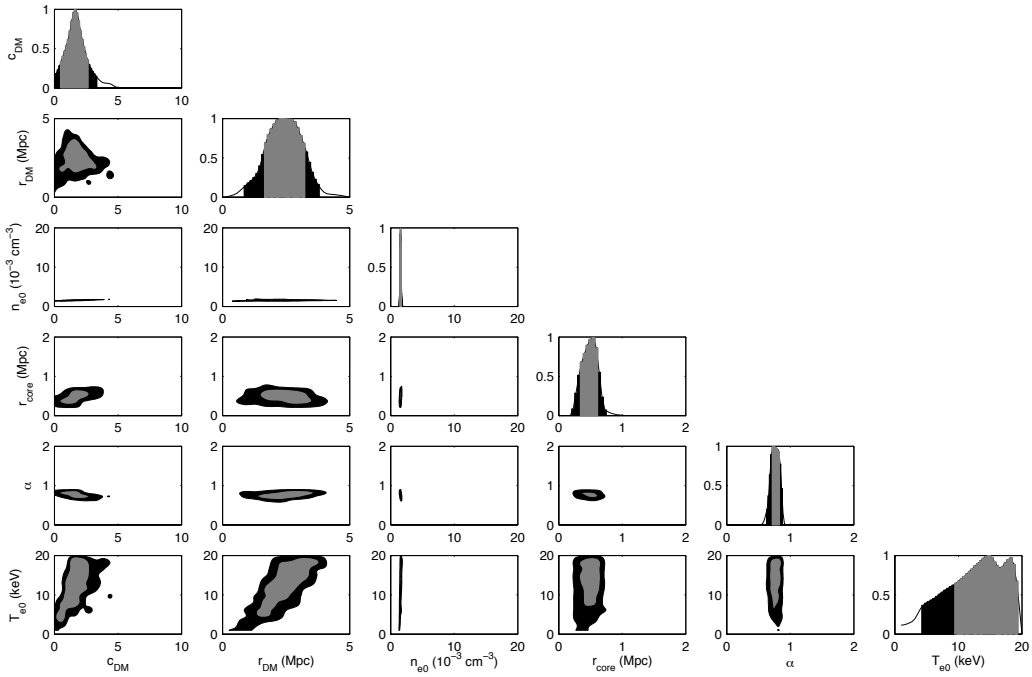

Figure 4.7: Continued

between the central electron density and temperature parameters. In addition the SZ data reduce the likelihood of having large central electron density and temperature values since these would generate large SZ signals that are inconsistent with the data. The X-ray surface brightness data are proportional to the integrated line-of-sight electron density and therefore strongly constrain the central electron density parameter. The X-ray data is of relatively higher resolution than the SZ data and is therefore much more dependent upon the shape of the entropy profile providing strong constraints on $r_{\rm core}$ and α. The high signal-to-noise surface brightness data do not provide a strong constraint on the temperature and mass of the cluster. In the case of FB1 the X-ray surface brightness data appear to generate a series of high likelihood peaks within parameter space. However the data are unable to distinguish between these in the absence of an additional constraint from the SZ data.

Results from fitting jointly to both data sets are shown in Table 4.2 and Figure 4.8, where estimates of the posterior distribution for the model parameters, profiles of the cluster properties and selected enclosed quantities are plotted. The model parameters are strongly constrained by the combination of both data sets. For the purposes of comparison with the known simulated cluster properties the radial profiles are scaled by the known true r_{200} value, and all global quantities are calculated by integrating within this radius. The radial profiles and global parameters of the true physical properties are reproduced well by the parametric fit, with systematic error $\lesssim 10\,\%$ at r_{200}. This result is fairly consistent with Kay et al. (2004), who find that the hydrostatic mass estimated from a combination of β model fits to the X-ray surface brightness data and spatial temperature information agrees to within $10\,\%$ ($r \lesssim r_{500}$) for the simulated clusters which contain feedback. They find that the presence of feedback from radiative cooling and pre-heating produces a higher degree of thermalisation than if the cluster were simply described by a non-radiative model and so the estimated mass is close to the true value.

Table 4.3 gives the natural logarithm of the evidence for different models given the data. The evidence values support the inclusion of hyper-parameters in fitting to the high signal-to-noise data. The ratios of best fit values for the SZ and X-ray hyper-parameters are 15:1 and 3.5:1 for FB1 and FB3 respectively, indicating that the hyper-parameters weight the likelihood in favour of the SZ data in both cases. While the CBI2 SZ data are insensitive to variation on scales smaller than 500 kpc, the X-ray data are much more sensitive to variations over this range. The nature of the parametric model is such that it is inherently smooth on these

Cluster Name	Data	$Y_{200} D_A^2$	M_{200}	$f_{gas,200}$
FB1	Simulation	0.931	11.6	0.094
	High S/N	$0.986^{+0.011}_{-0.016}$	$11.4^{+0.2}_{-0.3}$	$0.098^{+0.003}_{-0.002}$
	Low S/N	$1.25^{+0.41}_{-0.133}$	$15.8^{+3.8}_{-5.1}$	$0.064^{+0.016}_{-0.009}$
FB3	Simulation	0.863	10.7	0.096
	High S/N	$0.89^{+0.03}_{-0.02}$	$11.3^{+0.4}_{-0.4}$	$0.091^{+0.002}_{-0.003}$
	Low S/N	$1.05^{+0.40}_{-0.23}$	$15.8^{+5.0}_{-5.4}$	$0.064^{+0.02}_{-0.02}$

Table 4.2: Results from joint entropy model fits to the simulated clusters. Column 1 gives the cluster name; column 2 the data description; column 3 the integrated comptonisation within the virial radius, in units of $10^{-4}\,\mathrm{Mpc}^2$; column 4 the total mass within the virial radius, in units of $10^{14} M_\odot$, column 5 the gas mass fraction within the virial radius. Errors represent the 68 % interval.

smaller scales; hence clumping of the gas will deviate the model from the X-ray data, while still producing a relatively good fit to the SZ data. Therefore the weights will typically favour the SZ data relative to the X-ray surface brightness. In the case of the FB3 data, the relative weightings are quite similar since the X-ray data are a closer match to the model over the considered radius range.

4.6.4 Results from low signal-to-noise CBI2 data with X-ray data

The entropy model is jointly fitted to low signal-to-noise data, where the SZ data contain a realistic simulation of the intrinsic CMB uncertainty and a higher noise component from mock CBI2 observations. The instrumental noise in the X-ray surface brightness profile is again derived from the simulated Poisson noise on the map. Calibration errors are introduced as nuisance parameters to be marginalised over and are distributed by a Gaussian prior with σ_{cal} given by the quoted error value. A calibration error of 5 % is used for the SZ data, typical of the calibration of CBI2 visibility data, and the X-ray surface brightness data typically contain a calibration error of 10 % (Andersson & Madejski, 2004).

The results of these joint fits are shown Table 4.2 and Figure 4.8, and demonstrate the effect of introducing noise into the data. The increase in noise leads to much larger widths in the probability distributions of the cluster quantities and, while shifting the peaks of the distributions, are still consistent with the known simulation values within the errors. As with the high signal-to-noise case in the previous section, the differences in logarithmic evidence values support the inclusion of hyper-parameters in fitting to the low signal-to-noise data. The ratios of best fit hyper-parameter values for the SZ and X-ray data, estimated from the posterior distribution, are 2.5:1 and 1.1:1 for FB1 and FB3 respectively. The likelihood calculation is

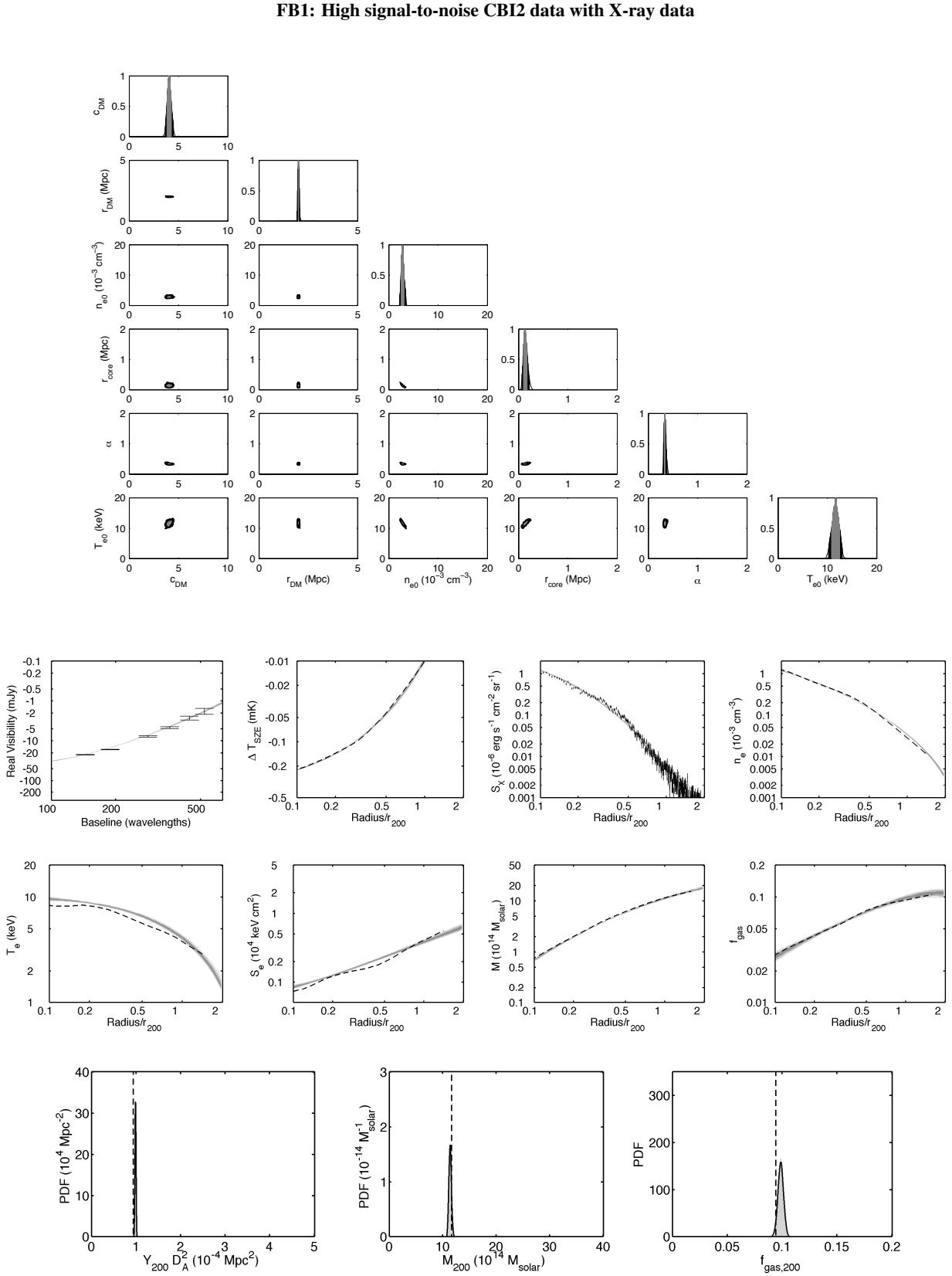

Figure 4.8: Results of fitting to simulated SZ and X-ray surface brightness data with the entropy model. *Top:* The estimated posterior probability density for the model parameters. The grey-scale represents the 68 and 95 % intervals. *Middle:* The estimated posterior probability density for the properties of the cluster, as a function of the radius scaled to the true r_{200} value. The grey scale represents the 68, 95 and 99 % intervals. The dashed lines represent the true simulation values and the error-bars the mock data. *Bottom:* The estimated posterior probability density for the integrated SZ effect, total mass and gas mass fraction within the true r_{200} value. The dashed vertical lines represent the true simulation values.

FB3: High signal-to-noise CBI2 data with X-ray data

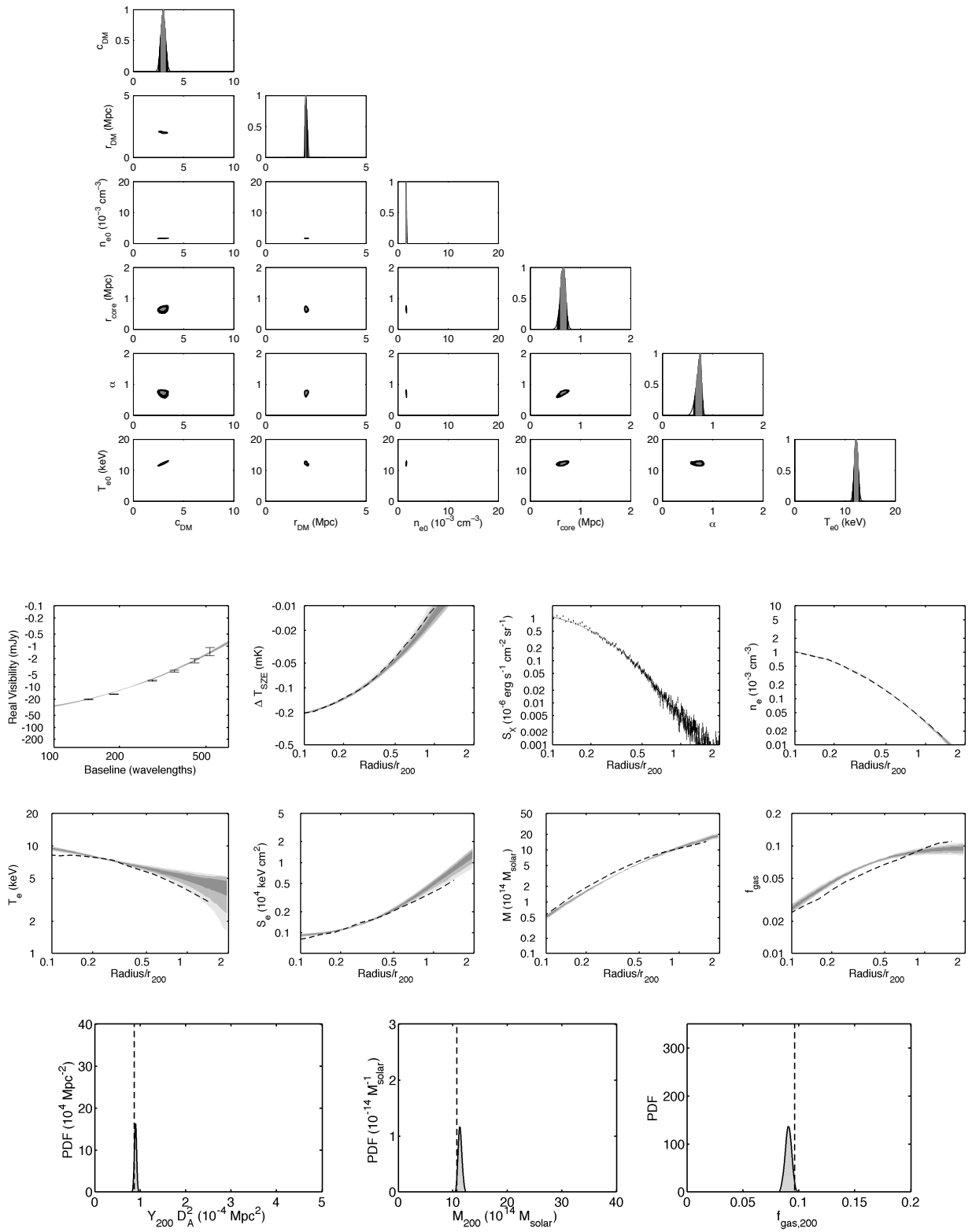

Figure 4.8: Continued

FB1: Low signal-to-noise CBI2 data with X-ray data

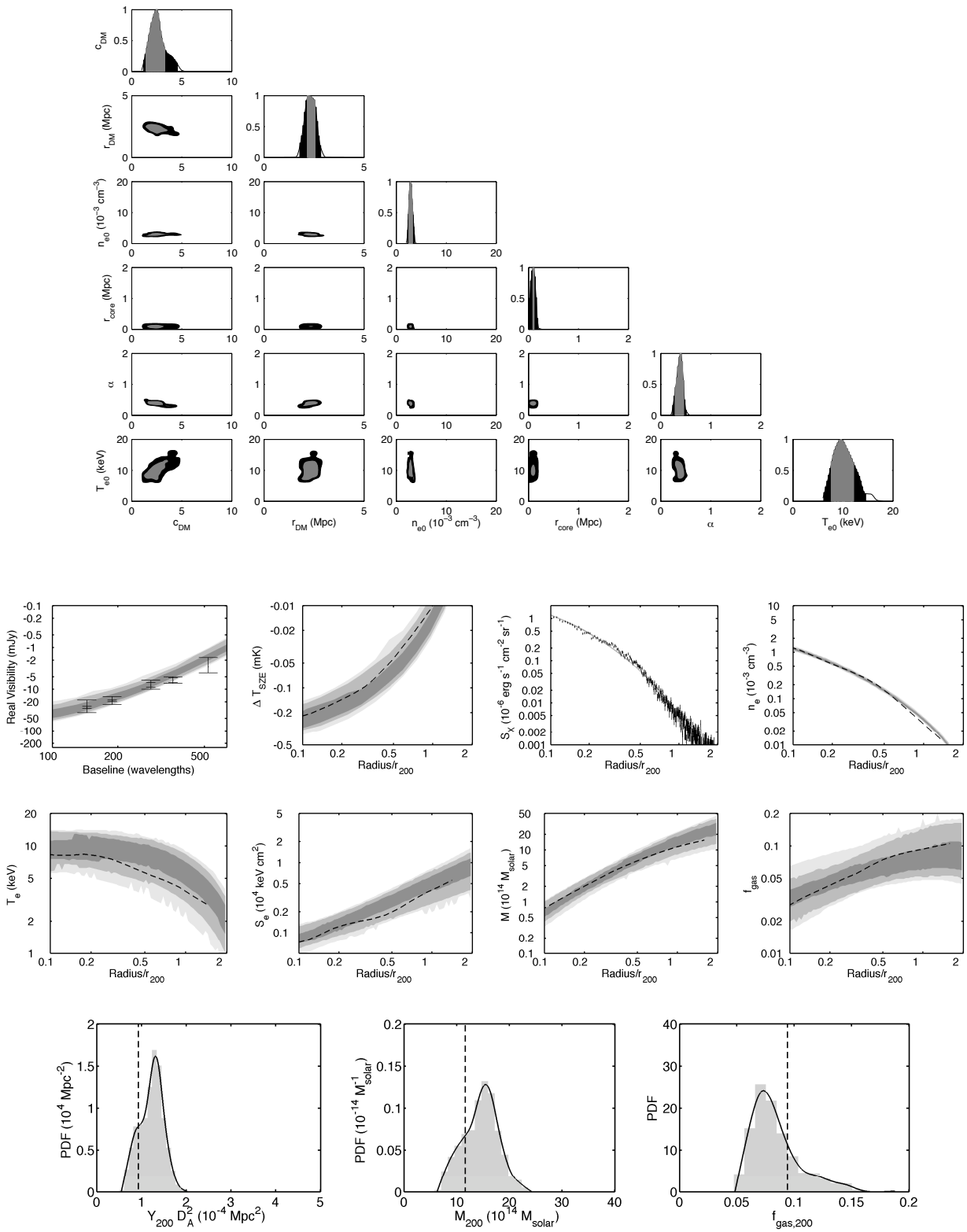

Figure 4.8: Continued

FB3: Low signal-to-noise CBI2 data with X-ray data

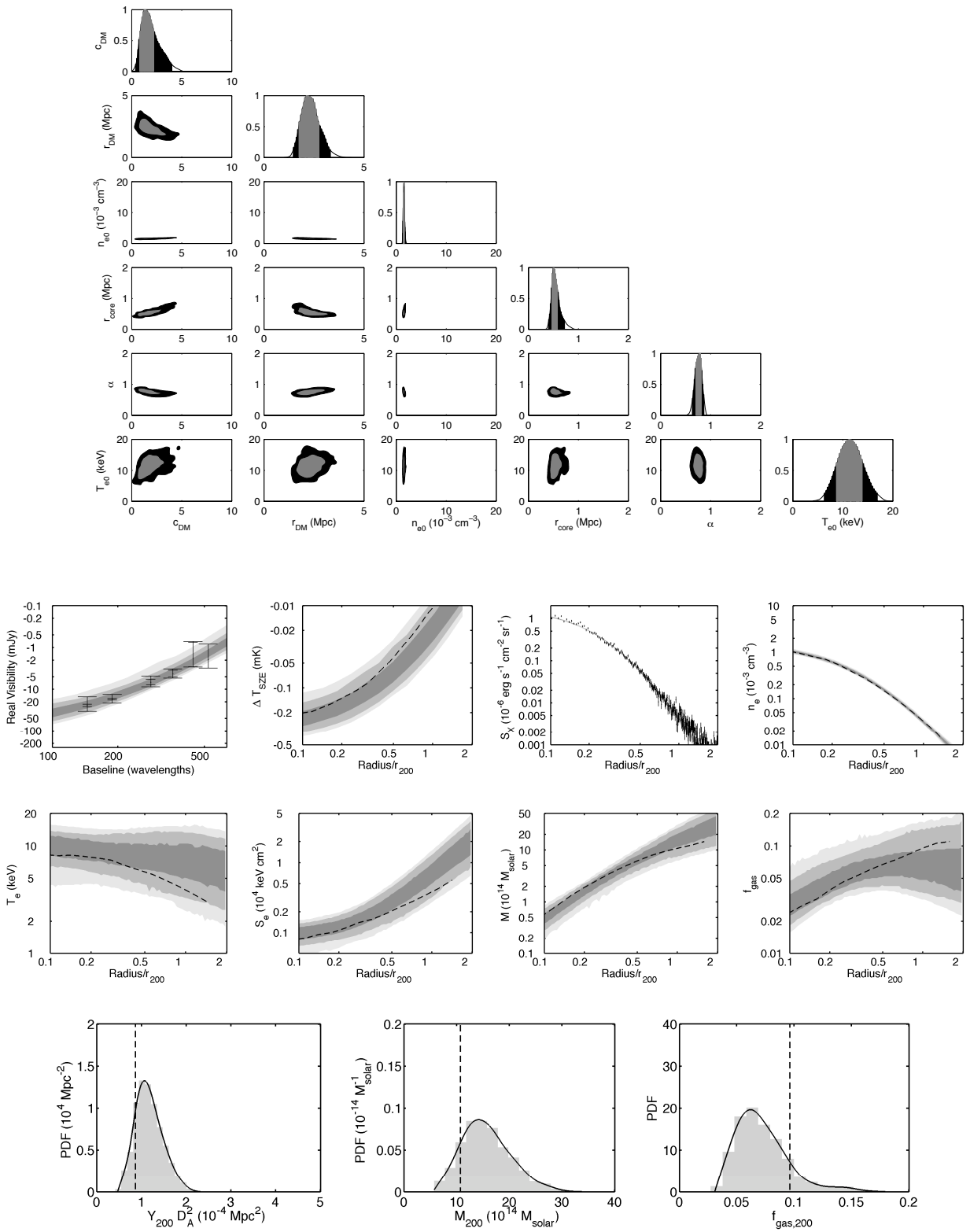

Figure 4.8: Continued

therefore weighted in favour of the SZ data as in the high signal-to-noise scenario. The reduction in signal-to-noise leads to a decrease in the ratios of hyper-parameters for each cluster, suggesting that both the SZ and X-ray data sets provide a more equal match to the model.

4.6.5 Comparison with the Isothermal β model

Even though the simulated clusters are clearly not isothermal, for the purposes of comparison joint fits are performed using the single isothermal β model to both the high and low signal-to-noise data. Figure 4.9 shows the resulting posterior distributions for the model parameters, the profiles, and global values within r_{200}. There is a strong systematic difference between the estimated and true simulation values when using this model, resulting from over-estimates of the electron temperature and SZ decrement, a situation that is highlighted by the logarithmic plots in the figure. The result is a systematic over-estimate of the total mass of $\sim 20\,\%$ at r_{200} and an under-estimate of the total mass at $r \lesssim r_{500}$. These results are consistent with the findings by Kay et al. (2004) who measure similar errors in estimating the total mass based upon the isothermal model. The systematic error in derived cluster properties is seen in both the high and low signal-to-noise scenarios, and therefore the introduction of both thermal noise and intrinsic CMB anisotropy is not enough to dominate over the effects of the intrinsic isothermal β model discrepancy with the simulations.

It is informative to compare the relative quality of the fit that the entropy and single isothermal β models give, based upon their respective logarithmic evidence values. In almost all the cases the evidence for the isothermal β model is significantly lower than that of the entropy model, with the exception of the low signal-to-noise scenario for the FB3 simulated cluster. This is due to the flat core of the X-ray surface brightness profile for this cluster, as a result of the displacement of the gas peak in the central region. As such when significantly lower signal-to-noise data is used the isothermal β model, with its flat core behaviour at small radii, provides an equally good fit (if not slightly better) than the entropy model. However in the case of the FB1 simulated cluster, the X-ray profile is strongly peaked in the central region and therefore the isothermal β model provides a significantly poorer fit to both high and low signal-to-noise data. This can be seen upon visual inspection of the electron density profiles for FB1 in Figure 4.9, where the isothermal β model fails to provide a suitable fit at both small and large radii.

The evidence values in Table 4.3 support the inclusion of hyper-parameters in both the high and low

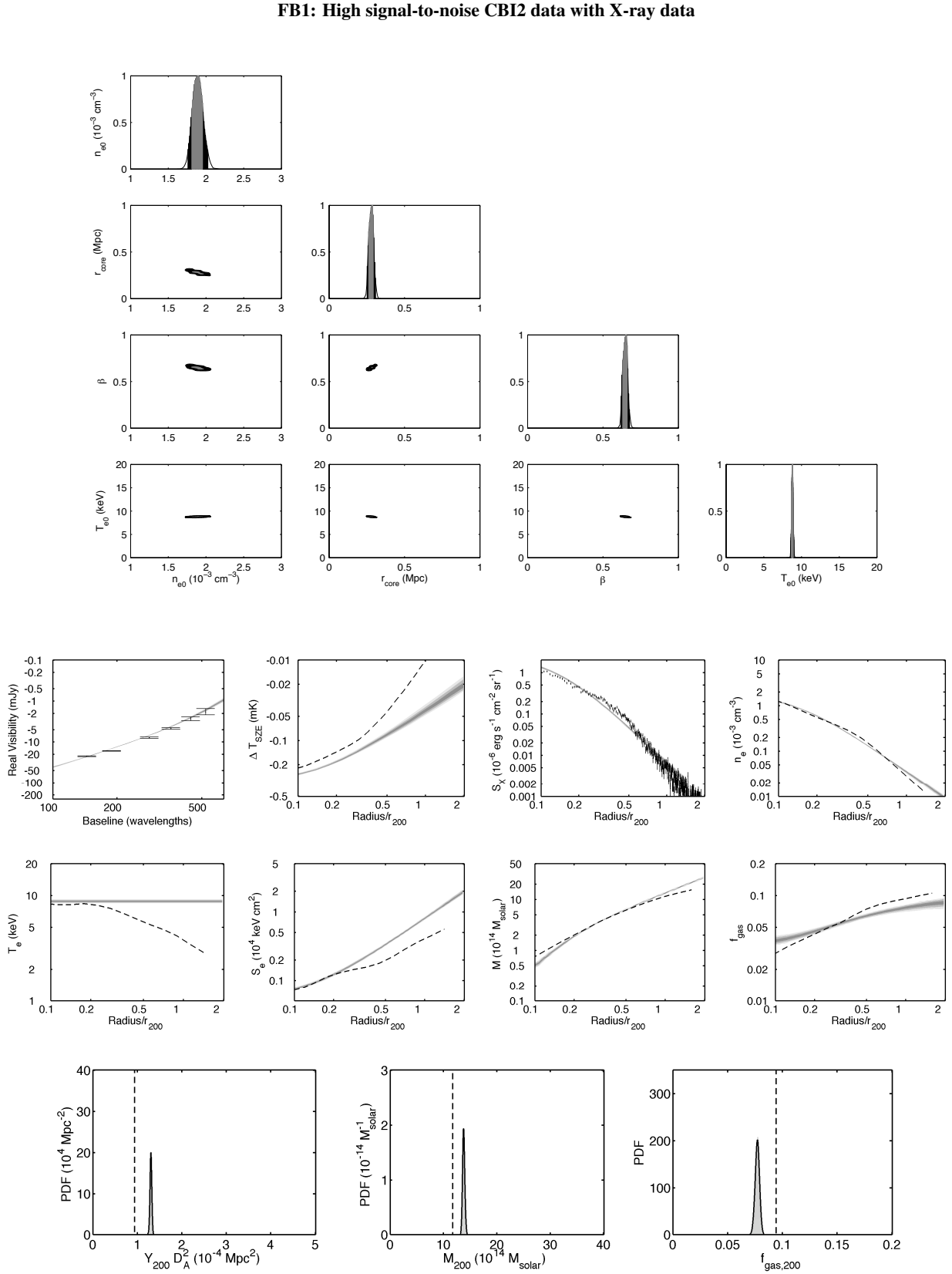

Figure 4.9: Results of fitting to simulated SZ and X-ray surface brightness data with the Isothermal β model. *Top:* The estimated posterior probability density for the model parameters. The grey-scale represents the 68 and 95 % intervals. *Middle:* The estimated posterior distribution for each cluster property, as a function of radius scaled to the true r_{200} value. The grey scale represents the 68, 95 and 99 % intervals. The dashed lines represent the true simulation values and the error-bars the mock data. *Bottom:* The estimated posterior distribution for the integrated SZ effect, total mass and gas mass fraction within the true r_{200} value. The dashed vertical lines represent the true simulation values.

FB3: High signal-to-noise CBI2 data with X-ray data

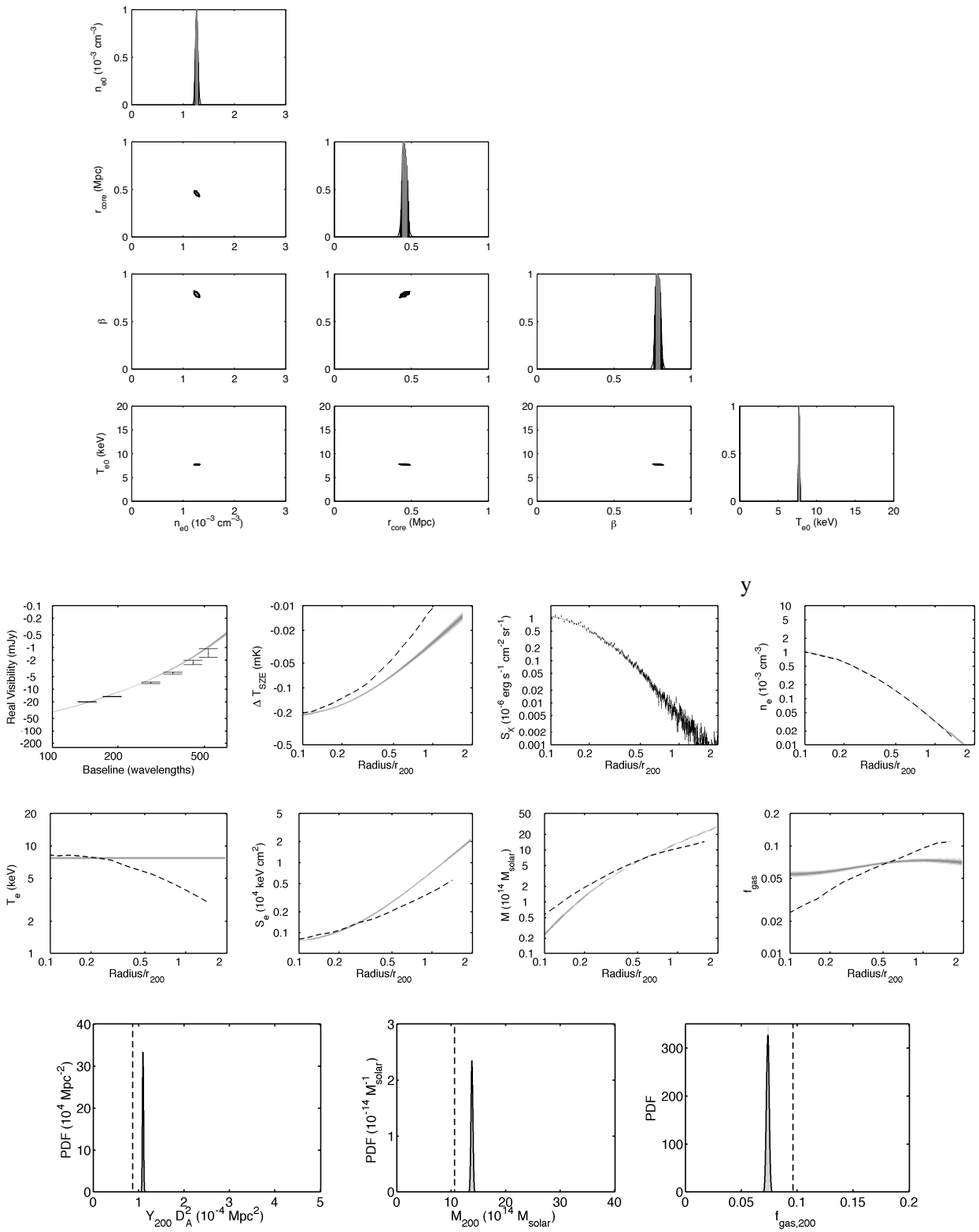

Figure 4.9: Continued

FB1: Low signal-to-noise CBI2 data with X-ray data

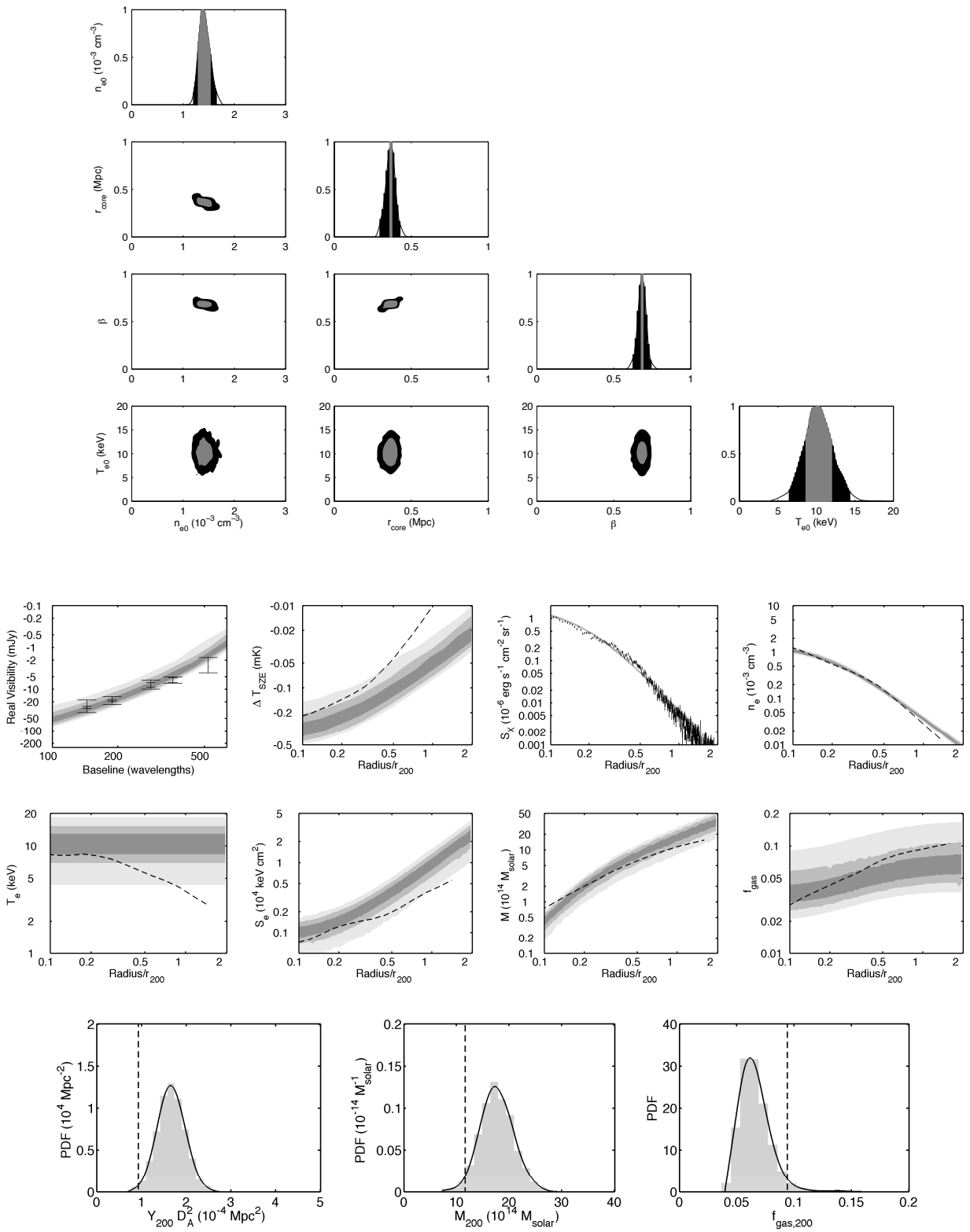

Figure 4.9: Continued

FB3: Low signal-to-noise CBI2 data with X-ray data

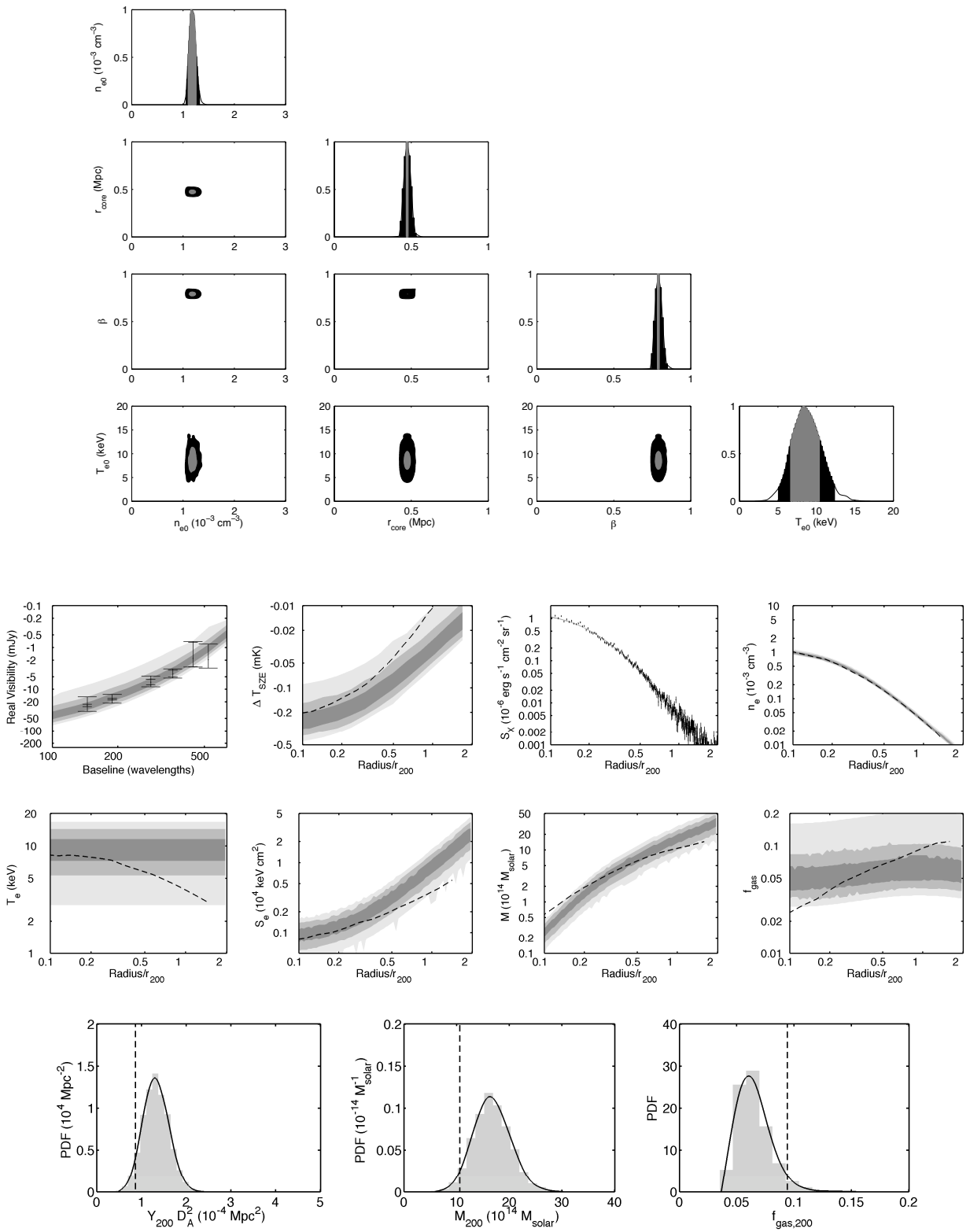

Figure 4.9: Continued

		High Signal-to-noise		Low Signal-to-Noise	
Cluster Name	Model	$\mathscr{M}_0$	$\mathscr{M}_1$	$\mathscr{M}_0$	$\mathscr{M}_1$
FB1	Entropy	6113	6476	4757	4764
	Isothermal β	5946	6405	4559	4724
FB3	Entropy	6147	6273	4807	4816
	Isothermal β	6131	6231	4810	4817

Table 4.3: The natural logarithm of the evidence (the probability of the data given a particular parametric model, see Equation 4.29) for high and low signal-to-noise CBI2 and X-ray surface brightness data. Note that the absolute value of the evidence is dependent upon the data, and so the quantity of interest is the difference between these values. Models that include SZ and X-ray hyper-parameters are represented by $\mathscr{M}_1$ and those that do not are represented by $\mathscr{M}_0$.

signal-to-noise scenarios for the isothermal β model. The relative weightings of each of the SZ and X-ray data sets are 30:1 (FB1) and 3:1 (FB3) for the high signal-to-noise data, and 4:1 and 1.1:1 for the corresponding low signal-to-noise data. The likelihood calculation is therefore weighted in favour of the SZ data, except in the case of the low signal-to-noise FB3 data where both are almost equally favoured.

4.7 Summary

In this chapter I have presented an analysis pipeline for performing joint fits to the CBI2 thermal SZ effect data and X-ray surface brightness data. The pipeline is checked for self-consistency and is found to reproduce the expected results from an input set of model parameters. I have also developed a parametric model, designed to be jointly fitted to low resolution SZ data and the X-ray surface brightness, that is based upon the NFW prescription for the dark mass halo and a simple parametrisation of the gas entropy. The model is tested against hydrodynamic/N-body simulations of two clusters, with different merger histories, and high signal-to-noise data show that it has relatively low intrinsic systematic error for the derived properties, when compared with similar results from the isothermal β model.

Chapter 5

1E 0657-558 "The Bullet Cluster"

1E 0657-558 is a massive cluster at $z = 0.2965$ with a significant merger event, orientated perpendicularly to the line-of-sight (Barrena et al., 2002). The mass and temperature of this object make it one of the brightest X-ray and SZ galaxy clusters in the southern sky, and therefore a perfect case-study for CBI2 observations of the thermal SZ effect. In this chapter I present the observation and analysis of one of the most interesting galaxy clusters in the Universe. The merger event consists of two sub-clusters, where the smaller object (known as the "bullet") has recently passed through the main cluster. A bow-shock can clearly be seen in Chandra X-ray observations by Markevitch et al. (2002), with an inferred shock velocity of $4500\,\mathrm{km\,s^{-1}}$. Hayashi & White (2006) suggest that this high sub-cluster velocity makes the existence of the Bullet Cluster system very unlikely within the current ΛCDM cosmology. However further N-body/SPH simulations by Springel & Farrar (2007) show that the actual speed of the bullet sub-cluster in the rest frame of the system might well be significantly lower than the inferred shock velocity, therefore implying that the Bullet Cluster is not so implausible. Weak and strong lensing observations by Clowe et al. (2006) and Bradač et al. (2006) show that the peaks of the surface mass distribution are significantly displaced from the X-ray surface brightness, providing one of the best direct indications of the existence of dark matter. Observations by Liang et al. (2000), using the ATCA and MOPRA telescopes, detected a strong diffuse radio halo in the centre of this cluster, suggesting a strong correlation between the ultra-relativistic electrons and thermal ICM gas that generate the radio and X-ray emission. The Bullet Cluster has also been detected using the SZ effect by Andreani et al. (1999) and Gomez et al. (2004), and was recently observed by Halverson et al.

(2009) with the APEX-SZ instrument. CBI2 observations do not resolve the merging substructure, but a combined analysis with recent X-ray observations using XMM-Newton (Zhang et al., 2006) will provide a strong constraint on the total mass and gas mass fraction of the system out to large radii.

5.1 CBI2 Observations

CBI2 observations of the Bullet Cluster were carried out over a period of 23 nights from the 2nd April 2007 to the 29th September 2007 and are summarised in Table 5.1. The pointing centre was chosen so as to be co-incident with the X-ray centroid given by Zhang et al. (2006). Jupiter was used as the primary flux calibrator when it was available for observation, and sufficiently separated from the Moon (greater than $\sim$40 degrees), otherwise Tau A was selected instead. In the case of the 12th April and 4th May, neither source was available for observation, and so 3C 274 and Saturn were used respectively. Three differencing modes were employed to remove spurious signals from the data and the resulting dirty maps are shown in Figure 5.1. For some of these observations, when the integration achieved relatively high individual signal-to-noise, the SZ decrement can actually be seen in the full-resolution map. These individual maps were used to find possible spurious artifacts that might have been over-looked during the first iteration of data reduction. After all spurious data have been accounted for, any residual artifacts seen in the individual maps are most likely due to the convolution of the sky with a non-circularly symmetric synthesised beam. This is caused by low sampling of Fourier space where the cluster was only observed for a brief integration time on that night (see for example 03-May-2007 in Figure 5.1).

Maps of the total data set are shown in Figure 5.2 and were deconvolved from the synthesised beam using the CLEAN algorithm implemented by the APCLN task in AIPS[1]. The full-resolution map indicates a strong detection of the thermal SZ effect at a level of $10\,\sigma$ above the noise. The presence of a decrement in the long baseline map, which includes baselines greater than 300 wavelengths, suggests that the cluster has a strong compact SZ component on scales smaller than 5 arcminutes. It is possible that the strong compact component could be due to the presence of a bright radio source or spurious signal in the centre of one of the reference fields. However the subtraction of the lead reference field from one of the trail reference fields produces a noise-like map and so a spurious signal or bright source in one of these fields is not the cause

[1] http://www.aips.nrao.edu/

Date	Flagged Receivers	Noise level	Moon distance	Differencing Mode	Calibrator
02-Apr-2007	0 3 6 7 9	9.1	83	L-M-T	Jupiter
03-Apr-2007	0 3 7	9.8	85	L-M	Jupiter
04-Apr-2007	0 3 7	12.7	86	M-T	Jupiter
05-Apr-2007	0 3 7 8	14.1	89	L-M	Tau A
06-Apr-2007	0 3 7 8	16.6	91	M-T	Tau A
08-Apr-2007	0 3 7 9	20.4	95	M-T	Tau A
09-Apr-2007	0 3 7 9	12.4	97	L-M	Tau A
10-Apr-2007	0 3 7 9	15.5	99	L-M	Tau A
11-Apr-2007	0 3 7 8 9	13.6	100	L-M-T	Tau A
12-Apr-2007	0 3 6 7	9.1	101	L-M-T	3C 274
13-Apr-2007	0 3 6 7	9.6	101	L-M-T	Jupiter
17-Apr-2007	0 3 6 7 8 9	15.5	96	M-T	Jupiter
03-May-2007	3 6 7 8 10 12	35.8	90	L-M-T	Jupiter
04-May-2007	3 7 12	10.1	92	L-M-T	Saturn
09-May-2007	1 2 3 7 6	12.3	101	L-M	Jupiter
10-May-2007	1 2 3 7	10.4	101	M-T	Jupiter
11-May-2007	1 2 3 7	14.6	101	L-M	Jupiter
12-May-2007	1 2 3 7	17.0	101	M-T	Jupiter
15-May-2007	1 2 3 7	8.4	95	L-M-T	Jupiter
16-May-2007	1 2 3 7	18.8	92	M-T	Jupiter
18-May-2007	1 2 3 7 9	29.3	86	M-T	Jupiter
28-Sep-2007	4	9.2	95	L-M-T	Jupiter
29-Sep-2007	1 4 8 9 10	8.9	92	L-M-T	Jupiter

Table 5.1: A complete summary of CBI2 observations of the Bullet Cluster. Column 1 gives the date of observation; column 2 the numbers of those receivers that were flagged during data reduction; column 3 an estimate of the map noise level in mJy beam^{-1}; column 4 the distance of the Moon from the main cluster field in degrees; column 5 the differencing mode used to subtract spurious signals; column 6 the primary calibrator.

of this strong compact decrement. Targeted and survey observations of point sources in the centres of the reference fields were also conducted to ensure that no strong radio sources exist in those regions. In addition to the CMB maps, the real visibility as a function of baseline distance (see Figure 5.3) also shows a strong SZ decrement above the level of the noise and intrinsic CMB anisotropy. In fitting for the SZ decrement I include a 5 % calibration error to account for uncertainty introduced in the overall calibration of the CBI2 data. This is included as a nuisance parameter in the fits with a Gaussian prior that is then marginalised over when deriving estimates of the model parameters.

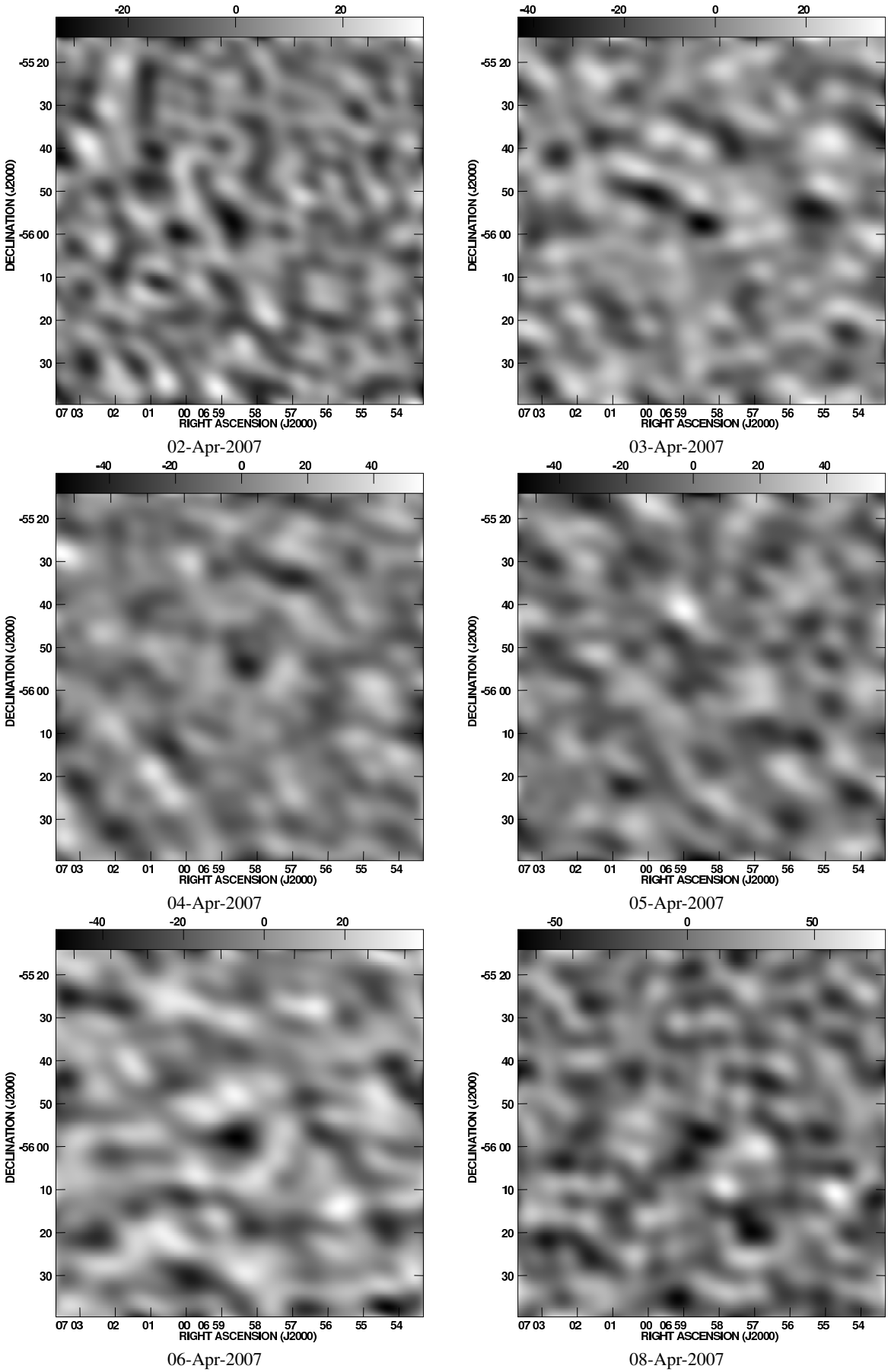

Figure 5.1: Full-resolution maps of individual CBI2 observations of the Bullet Cluster. The grey scale units are in mJy beam^{-1}.

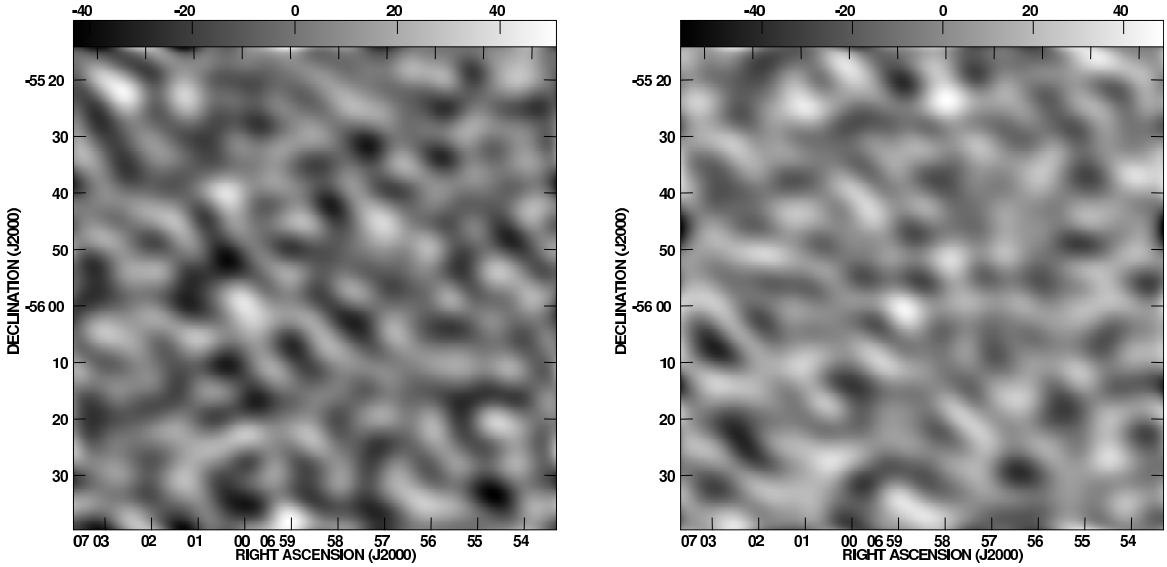

09-Apr-2007

10-Apr-2007

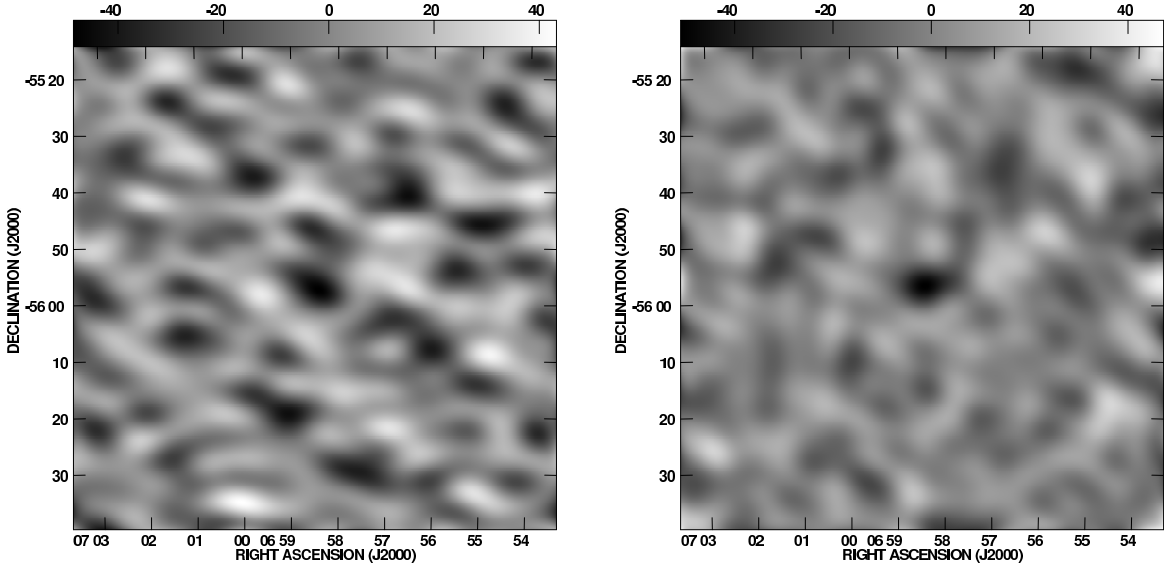

11-Apr-2007

12-Apr-2007

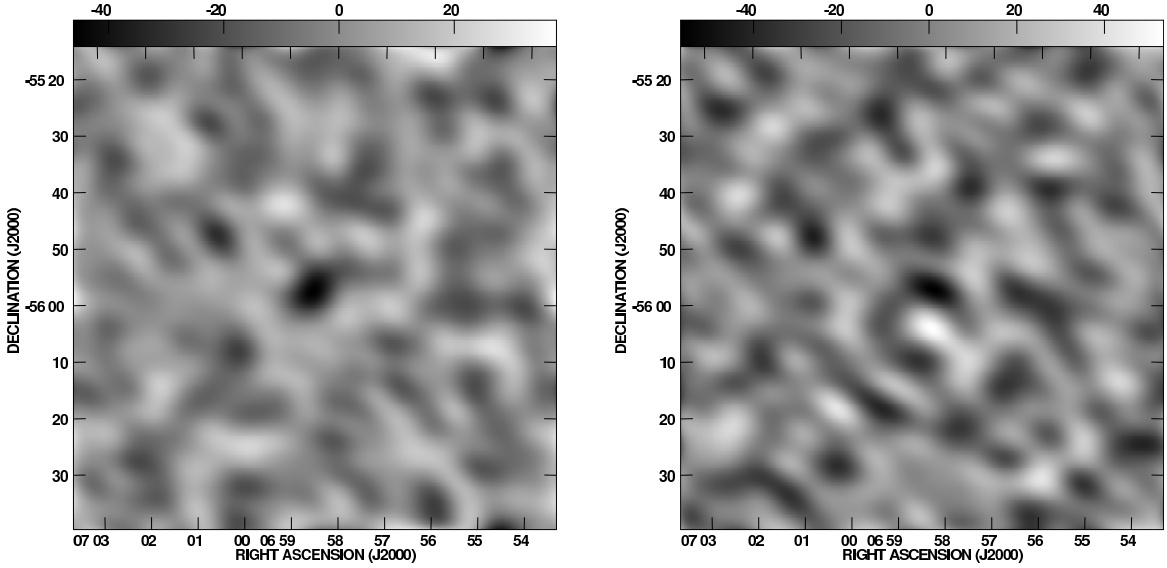

13-Apr-2007

17-Apr-2007

Figure 5.1: Continued

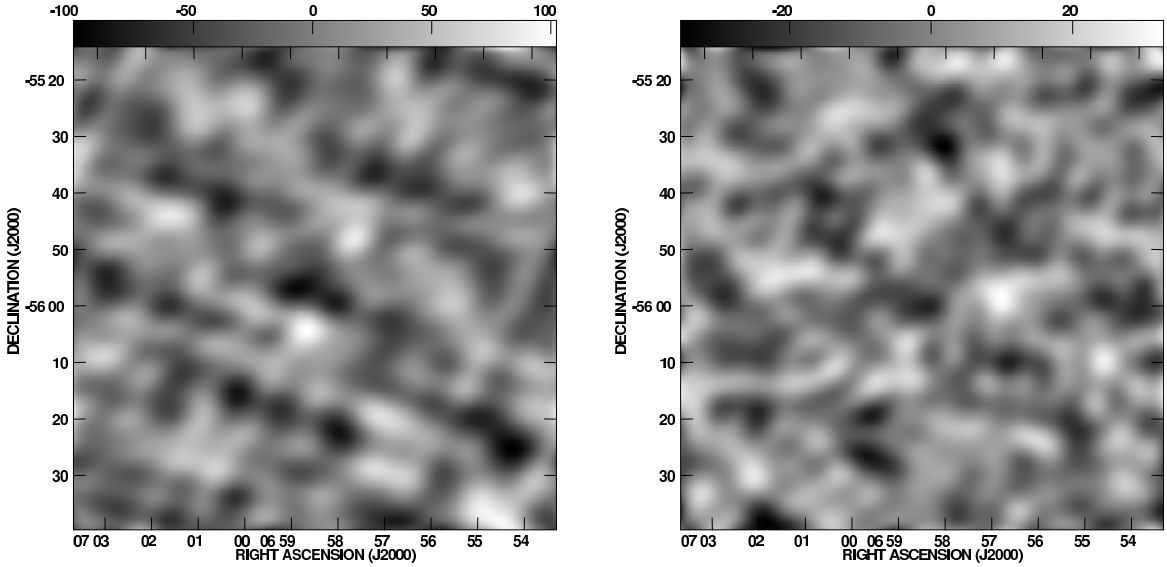

03-May-2007

04-May-2007

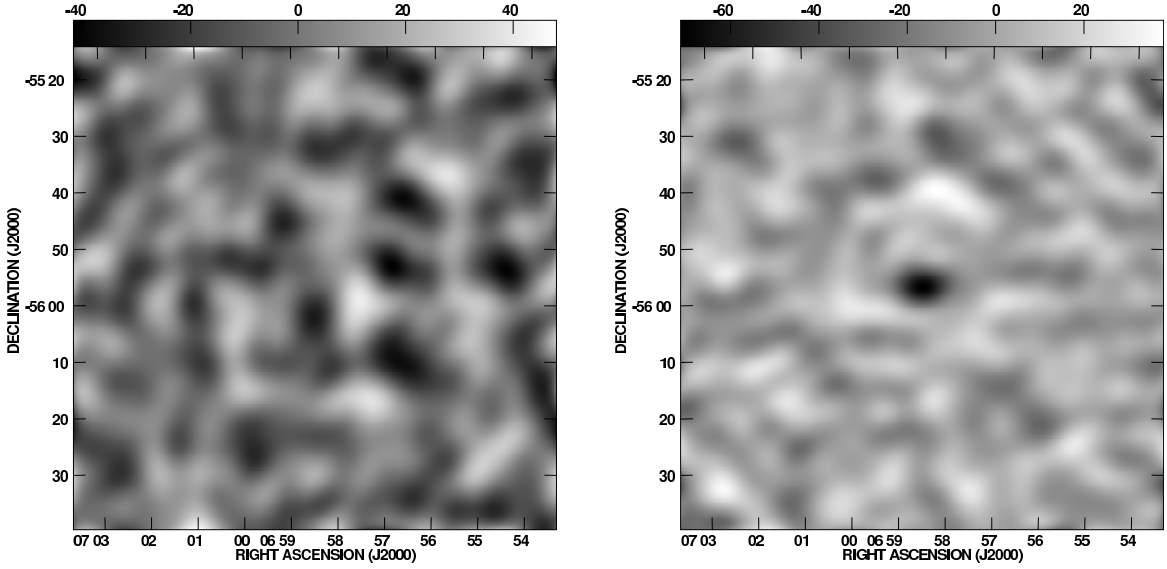

09-May-2007

10-May-2007

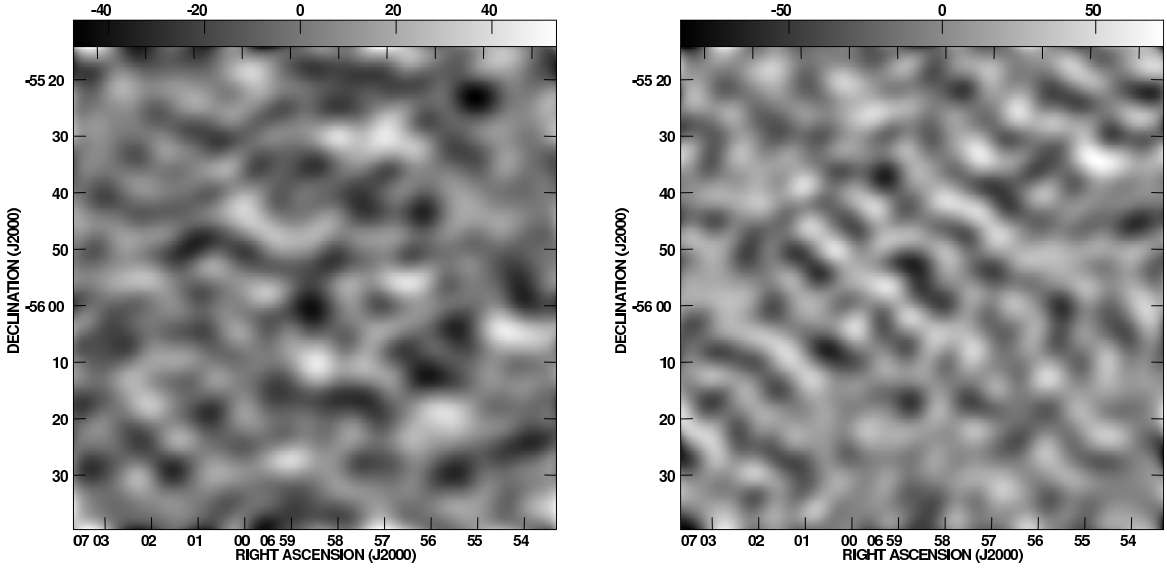

11-May-2007

12-May-2007

Figure 5.1: Continued

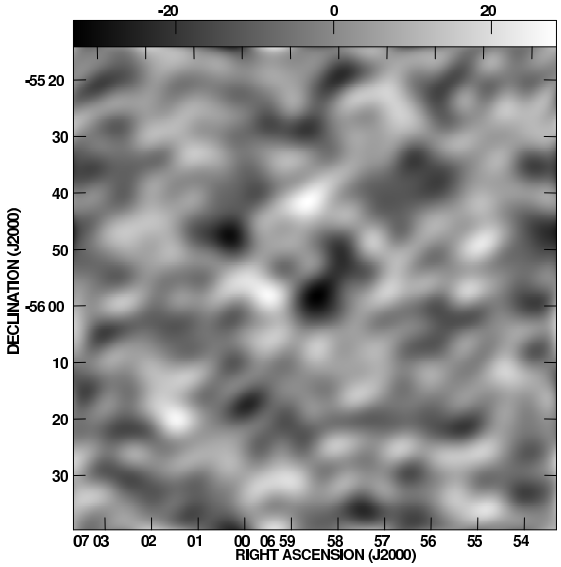

15-May-2007

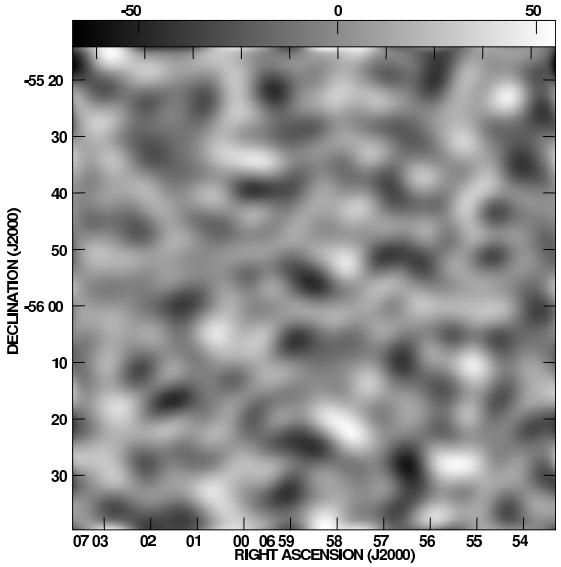

16-May-2007

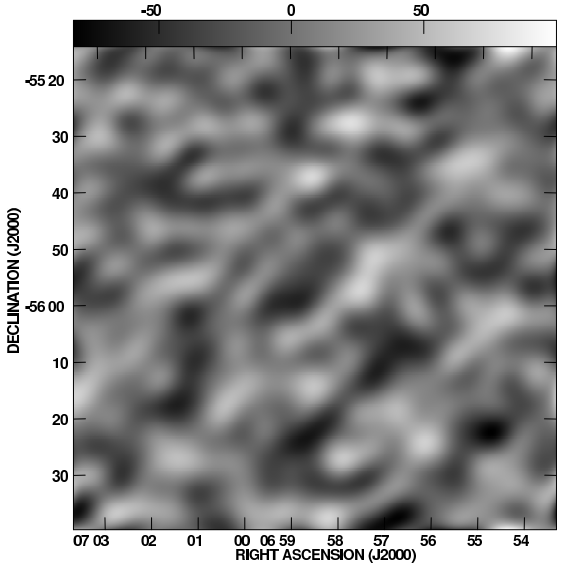

18-May-2007

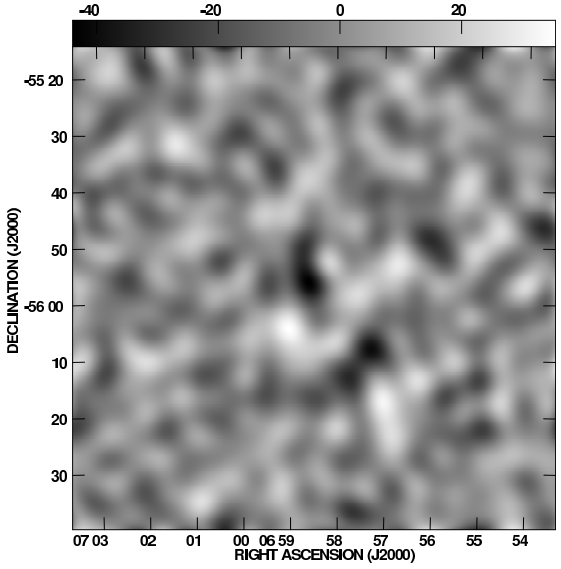

28-Sep-2007

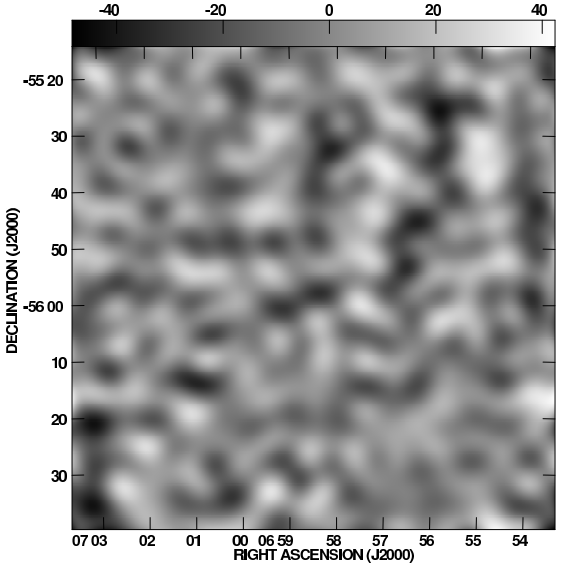

29-Sep-2007

Figure 5.1: Continued

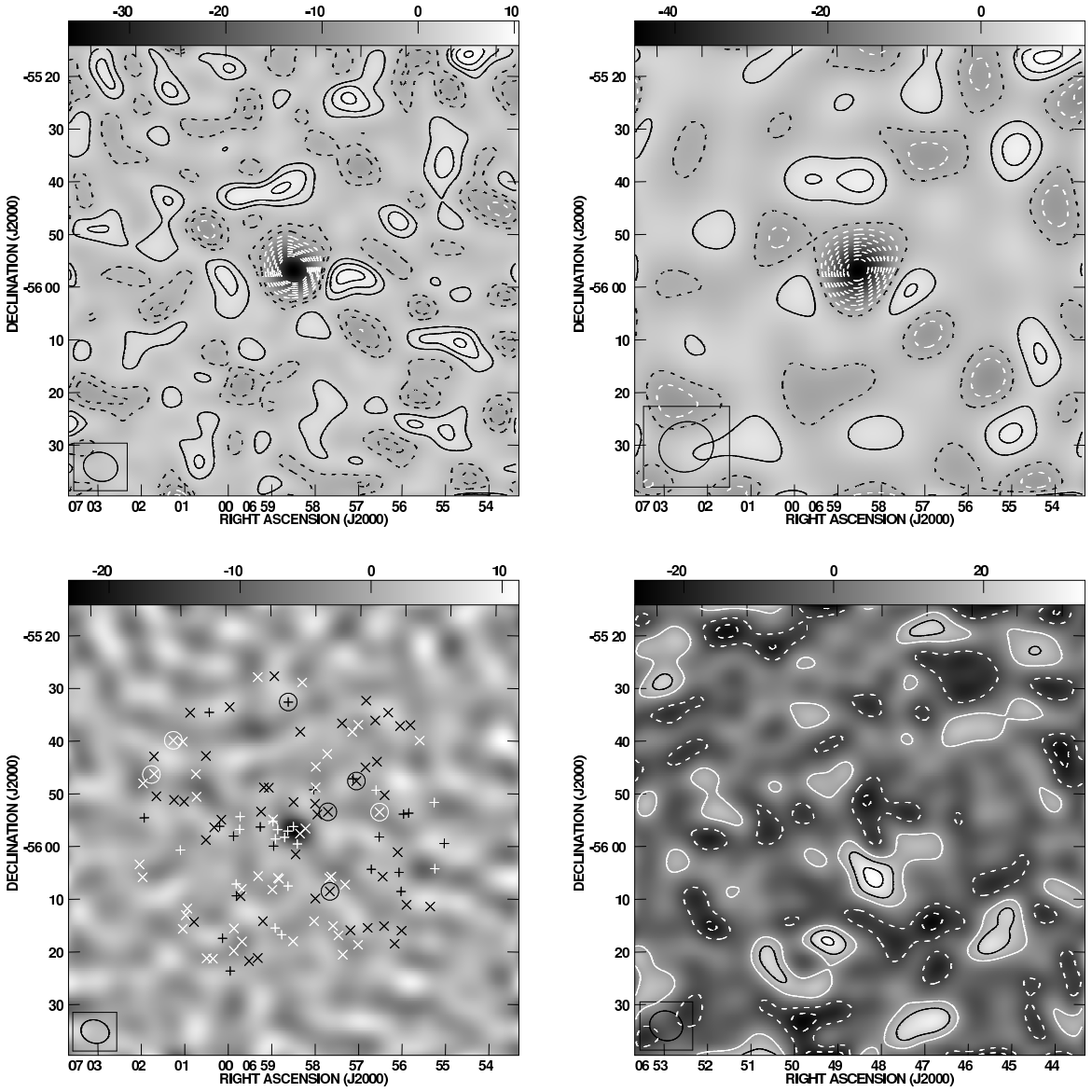

Figure 5.2: CLEANed maps of the total data set from CBI2 Observations of the Bullet Cluster. The grey scale units are mJy beam^{-1}. *Top Left*: Full-resolution map with contours representing the $1\,\sigma$ noise level, equal to 3 mJy beam^{-1}. *Top Right*: Short-baseline map (less than 300 wavelengths) with contours representing the $1\,\sigma$ noise level, equal to 4 mJy beam^{-1}. *Bottom Left*: Long-baseline map (greater than 300 wavelengths) with the positions of known point sources. The positive crosses represent known SUMSS sources (Mauch et al., 2003) within a radius of 30 arcminutes of the centre of the main cluster field. The diagonal crosses represent known SUMSS sources within a radius of 30 arcminutes of the centres of the reference fields. The circles are those sources detected at the $5\,\sigma$ level with targeted ATCA observations at 32 GHz. *Bottom Right*: Full-resolution map of trail field 1, subtracted from the lead field, using data from L-M-T observations. The contours represent the $1\,\sigma$ noise level equal to 10 mJy beam^{-1}.

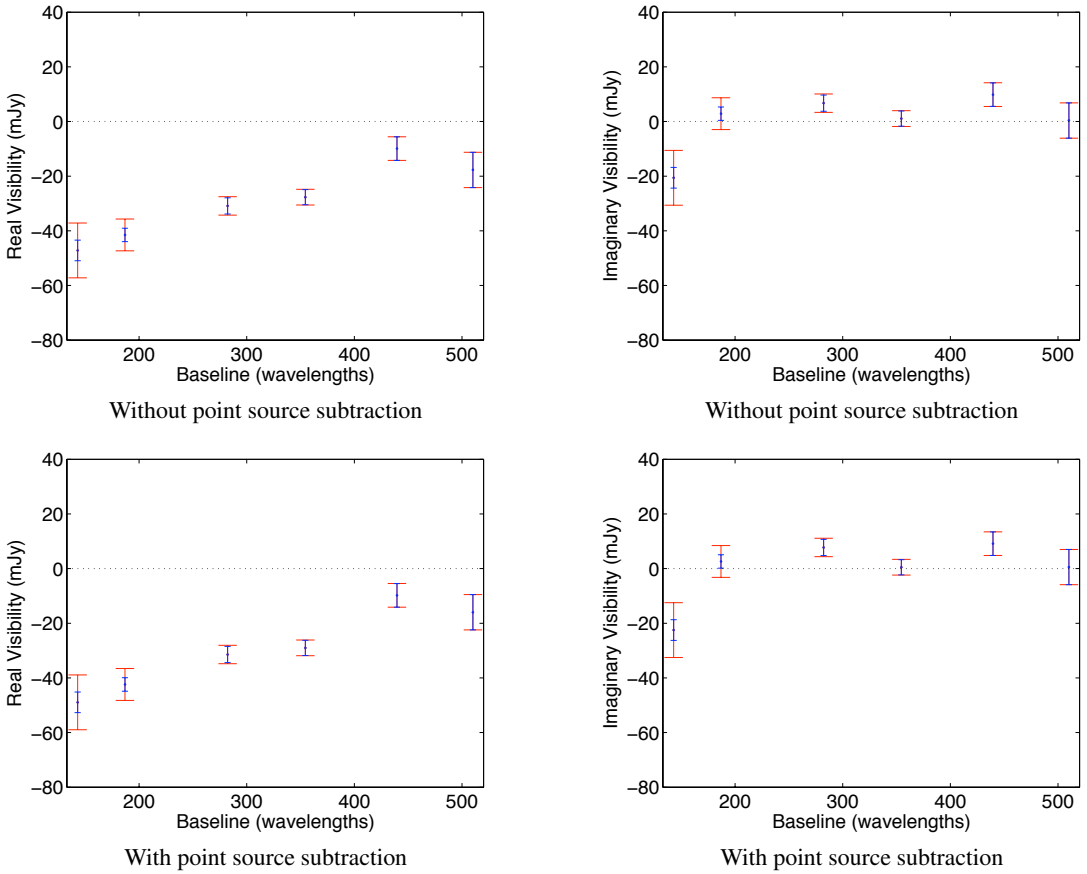

Figure 5.3: The complex visibility as a function of baseline distance, with and without subtraction of radio point sources. While the source positions are in fact projected out in the analysis, this comparison highlights the very small contribution made to the signal from known contaminating point sources. The blue and red error-bars represent the thermal noise and total uncertainty (including the intrinsic CMB anisotropy) at the $1\,\sigma$ level respectively. The visibility profile is flatter than expected from a single frequency channel, due to the fact that the shorter baselines contain visibilities from only lower frequency channels, where the SZ signal is weaker.

5.2 Radio Point Sources

5.2.1 Sources in CBI2 data

Contamination of the SZ signal in CBI2 data may arise from the presence of bright radio point sources in the main and reference fields. Sources close to the centre of the map are less attenuated by the primary beam and are more likely to be confused with the cluster decrement. At present there are few source surveys at this frequency and so one has to rely on sparse information in the literature and new observational data. Results from 31 GHz observations by Mason et al. (2009) of the 1.4 GHz NVSS sources (Condon et al., 1998)

suggest that we would expect ~ 3 sources at $3\,\sigma$ above the noise ($S_{31} \geq 9$ mJy beam^{-1}, un-attenuated by the CBI2 primary beam) within 1 degree^2 of the pointing centre of each field. The CBI2 primary beam has a full-width at half-maximum (FWHM) of 28.2 arcminutes and based on these results one would expect to see approximately 1-2 of these sources in each field. However this survey was taken from blank CMB fields, and since the positions radio point sources and galaxy clusters are expected to be correlated, there are likely to be more detected sources. Figure 5.2 shows a long-baseline CBI2 map, with the positions of 843 MHz sources from the SUMSS catalogue (Mauch et al., 2003) within a radius of 30 arcminutes. Maps containing just the long baselines have less contribution from the extended SZ signal and therefore bright point sources will be more apparent. From visual inspection of the map there appears to be no significant contribution from bright sources in the CBI2 data. However to provide a more rigorous analysis of the source contribution, targeted 32 GHz observations were conducted at the positions of known SUMSS sources within 30 arcminutes, as well as 4.80 GHz and 8.64 GHz surveys of the centres of the CBI2 fields. All observations were carried out with the Australia Telescope Compact Array (ATCA), a 6 element interferometer with 22 m diameter antennas, in the compact H75 configuration.

5.2.2 ATCA observations

The SUMSS source survey provided the basis for targeted 32 GHz observations of potential source contamination within the Bullet Cluster fields. The SUMSS catalogue contains measurements of source fluxes at a frequency of 843 MHz, down to a flux limit of 6 mJy. For our 32 GHz observations all sources were selected that had CBI2 primary beam attenuated fluxes above 8 mJy at 843 MHz, within a radius of 30 arcminutes. In this thesis I define the spectral behaviour of the source flux by the following expression

$$S_\nu \propto \nu^\alpha, \tag{5.1}$$

where α is the spectral index. Mason et al. (2009) found that 90 % of NVSS sources have a spectral index $\alpha \sim -1.0$, between 1.4 and 31 GHz , while only 1 % have $\alpha > 0$. Assuming that the NVSS and SUMSS sources belong to the same population, it is expected that a flux limit of 8 mJy is more than sufficient for observing potential SUMSS sources in the CBI2 fields. However to ensure that extreme outlier sources were not missed, 4.80 GHz and 8.64 GHz pointed observations were conducted of the centres of the main

and reference fields.

ATCA observations of the Bullet Cluster fields were undertaken in October 2007 over a period 3 nights, and were spaced evenly in three cuts throughout the observing period in order to ensure uniform (u,v) coverage. Raw data flagging and calibration were applied by A. C. Taylor, using the MIRIAD[2] reduction package. Flags were applied to poor data, including channel edges and antennas that were significantly shadowed due to low elevation observing. The data from baselines containing antenna 6 were flagged, since these baselines are significantly longer and the sources are resolved. Band-pass and polarization calibrations were applied to the data using a bright secondary calibrator. This was then transferred to all of the phase calibrators that were interleaved between the source observations. The phase calibrators were chosen to be close to the source fields and therefore could accurately correct for the changes in phase during the observation. Once the data were correctly calibrated for the band-pass, polarization and phases, a final flux calibration was applied to the antenna gains using observations of Uranus.

5.2.3 Identified sources

The long-baseline map in Figure 5.2 shows the positions of SUMSS point sources detected with ATCA at 5 σ above the noise, at a frequency of 32 GHz, within 30 arcminutes of the field centres. Table 5.2 presents the measured fluxes of these sources, as well as those seen in 4.80 GHz and 8.64 GHz observations of the field centres (see Appendix A). All sources detected in these lower frequency observations are identified in the SUMMS catalogue and were observed at 32 GHz, and therefore no unexpected outlier sources are observed in the field centres. Two sources that were detected by Liang et al. (2000), at 4.846 and 8.832 GHz, were also detected by the 4.80 GHz ATCA observation of the main field. While these sources were confused by the ATCA synthesised beam, the upper limit on the measured peak brightness is consistent with the results from their work.

Of the 104 discrete sources observed with ATCA at 32 GHz, six were detected with 5 σ significance. These sources are accounted for in the data by projecting at the source position during the analysis stage (see Chapter 4). The source is projected, rather than subtracted directly from the data, in order to avoid the risk of incurring systematic error from source variability. Projecting out source positions appears to have negligible effect on the final results. Therefore those sources that are bright at 31 GHz in the Bullet Cluster

[2] http://www.atnf.csiro.au/computing/software/miriad/.

Field	R.A. (J2000)	Decl. (J2000)	[1]$S_{0.843}$	$S_{4.80}$	[2]$S_{4.85}$	$S_{8.64}$	S_{32}	Proj.
Lead	6:47:04.9	-55:47:54	335.1±10.1	-	75±8	-	11.3±0.8	Yes
Lead	6:47:40.2	-56:08:52	11±1.4	-	-	-	6.7±0.7	Yes
Lead	6:51:11.7	-55:40:06	197.7±6	-	75±9	-	11.1±0.8	Yes
Main	6:58:24.7	-55:59:53	32.2±2.2	10.7±0.7	-	7.3±1.0	< 2.4	No
Main	6:58:29.9	-55:56:34	79.4±4.4	< 19.0[4]	-	< 3.0	< 2.4	No
Main	6:58:36.9	-55:32:56	37.3±1.3	-	-	-	12.0±0.8	Yes
Main	6:58:37.6	-55:57:25	79.4±4.4	< 19.0[3,4]	-	< 3.0[3]	< 2.4	No
Main	6:58:42.0	-55:58:37	60.4±2.0	< 19.0[3,4]	-	< 3.0[3]	< 2.4	No
Main	6:58:51.4	-55:57:09	129.3±5.3	< 19.0[4]	-	9.0±1.0	< 2.4	No
Trail 1/2	7:07:43.3	-55:53:46	107.3±3.3	49.1±3.5	-	-	18.7±0.8	Yes
Trail 1	7:11:51.7	-55:46:32	21.7±1.2	-	21.7±1.2	-	14.3±0.8	Yes

Table 5.2: Radio point sources detected in the Bullet Cluster main and reference fields. Column 1 gives the CBI2 field; column 2 the right ascension; column 3 the declination; column 4 the SUMSS integrated flux in units of mJy; columns 4 measured peak brightness from ATCA observations at 4.80 GHz in units of mJy beam^{-1}; column 5 the PMN integrated flux in units of mJy; columns 6 measured peak brightness from ATCA observations at 8.64 GHz in units of mJy beam^{-1}; column 7 the integrated flux from ATCA observations at 32 GHz in units of mJy; column 8 whether the source is projected out. The errors in the measured fluxes correspond to 1 σ. Four sources are confused by the synthesised beam at 4.80 GHz, and so an upper limit is estimated for their flux. All other upper limits indicate that the source flux is below the 3 σ level for the observation.

[1] SUMSS catalogue (Mauch et al., 2003).

[2] PMN catalogue (Griffith & Wright, 1993).

[3] Source also observed by Liang et al. (2000) at 4.846 and 8.832 GHz.

[4] Source confused by synthesised beam at 4.80 GHz.

main and reference fields have negligible effect on the thermal SZ signal at the resolution and sensitivity of the CBI2 experiment.

5.3 X-ray data

In order to obtain constraints on the physical properties of the cluster the inherent degeneracy must be removed between the electron density and temperature. I therefore use published X-ray surface brightness data (in the 0.5-2.0 keV energy band) provided by Zhang et al. (2006) that introduces a strong constraint on the electron density. The data have been background subtracted and the vignetting correction applied (Zhang et al., 2006). I include a 10 % systematic error in the analysis to account for possible constant residual background, and error associated with calibration (see Andersson & Madejski (2004) and Mateos et al. (2009) for further discussion of the calibration error associated with observations using the XMM-

Newton satellite). The published count rate profile is equal to the sum of the individual count rates for each of the MOS1, MOS2 and PN CCD arrays on the XMM-Newton satellite, radially binned to 2 arcseconds. The ratio of the expected count rate from the MOS detectors, to that of the PN detector, is determined empirically and is equal to 1:3.3 (Y.-Y. Zhang, private communication). If the point spread function (PSF) associated with each detector is included, then the relationship between the X-ray surface brightness ($S_{\rm X}$) in energy units and the observed count rate ($S_{\rm obs}$) is given by the following expression

$$S_{\rm obs} = (S_{\rm X} K_{\rm PN}) * \left({\rm PSF}_{\rm PN} + \frac{{\rm PSF}_{\rm MOS1}}{3.3} + \frac{{\rm PSF}_{\rm MOS2}}{3.3} \right) \tag{5.2}$$

where $K_{\rm PN}$ is the conversion factor for the PN detector in units of counts erg^{-1} cm^2. The FWHM of the PSF for each of the three telescopes is equal to 6 arcseconds, which at $z \sim 0.3$ equates to a physical radius of 27 kpc. For the work in the thesis I am interested in how the cluster properties behave on scales larger than 100 kpc and so the effect of the PSF is ignored here. The X-ray surface brightness can then be derived in the required units by using the following simplified expression

$$S_{\rm X} = \frac{S_{\rm obs}}{1.6 K_{\rm PN}}. \tag{5.3}$$

The PIMMS[3] package is used to calculate the conversion factor ($K_{\rm PN}$) over the 0.5-2.0 keV energy band. This factor depends upon both the effective area of the PN detector (with the thin filter), the assumed X-ray emission model and the neutral hydrogen column density. The X-ray emission is assumed to be well described by the Raymond-Smith plasma model (Raymond & Smith, 1977) with a plasma temperature equal to the average spectral temperature (10.6 keV) and neutral hydrogen column density (6.53×10^{20} cm^{-2}) measured by Zhang et al. (2006). The 0.5-2.0 keV band was chosen because the X-ray emission co-efficient is almost temperature independent across these energies.

For the purposes of fitting a parametric model to the X-ray surface brightness data, I ignore the core of the cluster out to a radius of 100 kpc. The intra-cluster medium within the core is most likely to be affected by non-gravitational processes, such as recent merger activity or radiative cooling, in which case it cannot be assumed that the equation of hydrostatic equilibrium holds. At the largest radii the X-ray surface brightness

[3] http://heasarc.nasa.gov/docs/software/tools/pimms.html.

Model	r_{200}(Mpc)	$Y_{200}D_{\rm A}^2(10^{-4}{\rm Mpc}^2)$	$M_{200}(10^{14}M_\odot)$	$f_{\rm gas,200}$
Entropy	$2.28^{+0.13}_{-0.29}$	$4.90^{+0.69}_{-1.53}$	$18.1^{+2.8}_{-6.4}$	$0.188^{+0.055}_{-0.025}$
Isothermal β	$2.51^{+0.20}_{-0.14}$	$6.87^{+1.61}_{-1.47}$	$25.3^{+6.13}_{-4.80}$	$0.154^{+0.021}_{-0.027}$

Table 5.3: Estimates of derived quantities from joint parametric model fits to CBI2 and XMM-Newton data from observations of the Bullet cluster. Column 1 gives the parametric model; column 2 the virial radius; column 3 the integrated comptonization; column 4 the total mass; column 5 the gas mass fraction. All quantities are derived from integration over a spherical volume within r_{200} for each sample of the posterior distribution. The errors represent the 68 % interval.

profile is truncated when the signal-to-noise reaches a level of 3 σ, in accordance with the approach adopted by Zhang et al. (2006). While the treatment here is suitable for the requirements of the work in this thesis, in future work I wish to incorporate a more sophisticated treatment of the X-ray data into the joint analysis pipeline using the reduction package XSPEC[4].

5.4 Results and Discussion

Joint parametric fits were performed to the CBI2 SZ and XMM-Newton surface brightness data, using both the entropy model described in Chapter 4 and the single isothermal β model for comparison. The results from using both models are summarised in Figure 5.4 and Table 5.3. The global quantities are calculated by integrating over a spherical volume within r_{200} for each sample of the posterior distribution and the radial profiles are scaled to the best estimate of the virial radius given in Table 5.3. Results from both models show that the total mass and gas mass fractions are constrained by combining the CBI2 SZ and X-ray surface brightness data out to r_{200}. The entropy model fit shows a globally declining electron temperature profile over all radii, but converging to a value ≈ 7 keV at the virial radius. The gas entropy has a core radius of $\sim$400 kpc and a large-radius dependency tending towards a power-law of 1.3.

5.4.1 Comparison with results from other SZ and X-ray experiments

Table 5.4 summarises the comparison of the results of this work with those from other recent SZ and X-ray observations of the Bullet Cluster. The central comptonization values are independent of the observing frequency and therefore provide an effective quantity for comparing the results from different SZ experi-

[4] http://heasarc.gsfc.nasa.gov/docs/xanadu/xspec/

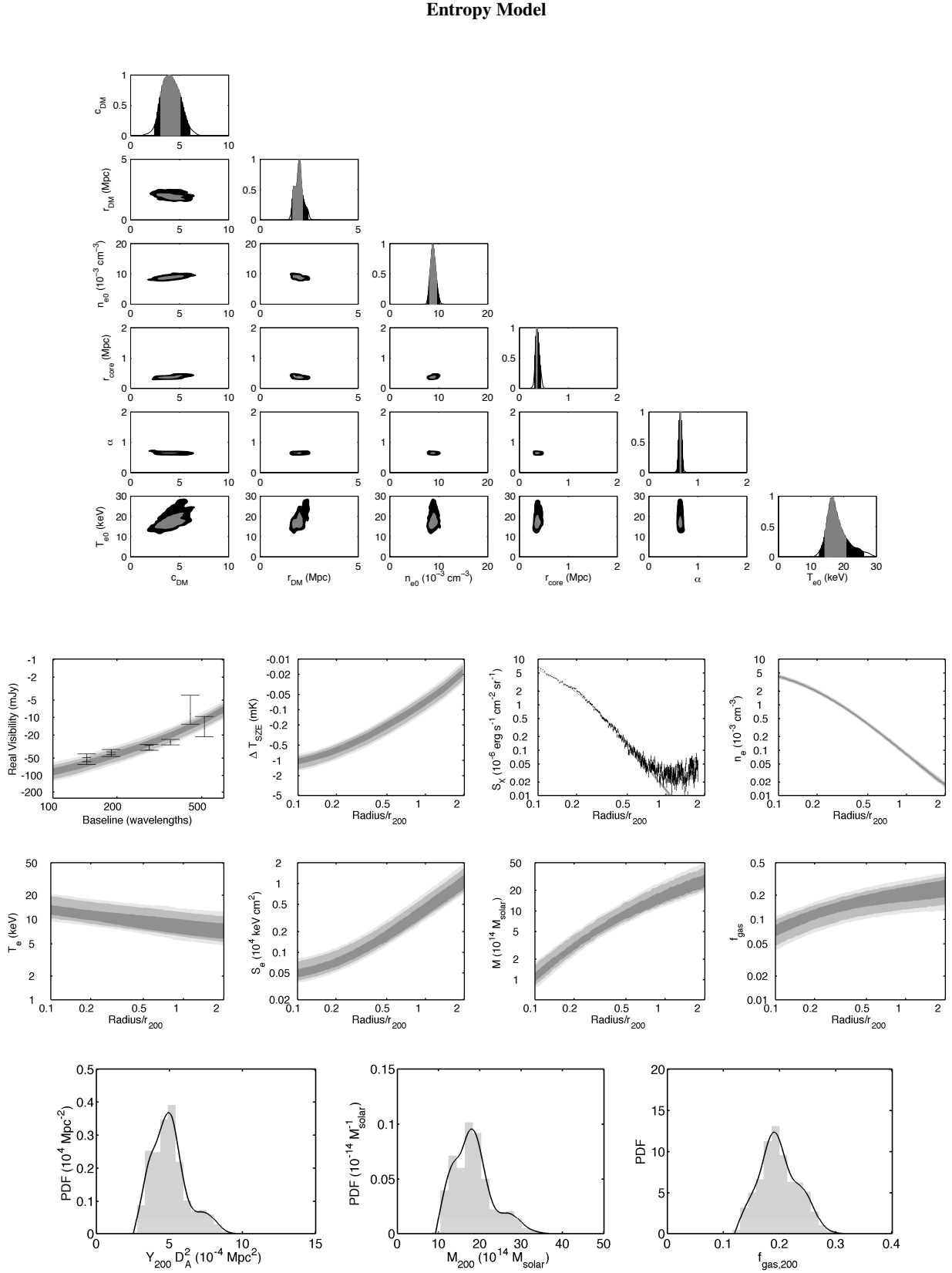

Figure 5.4: Results of parametric model fitting to CBI2 and XMM-Newton data. *Top:* The estimated posterior distribution for the model parameters. The grey scale represents the 68 and 95 % intervals. *Middle:* The estimated posterior distribution for each cluster property, as a function of the physical radius scaled to the best estimate of r_{200} as given in Table 5.3. The grey scale represents the 68, 95 and 99 % intervals. *Bottom:* The estimated posterior distributions for the integrated SZ effect, total mass and gas mass fraction within r_{200}.

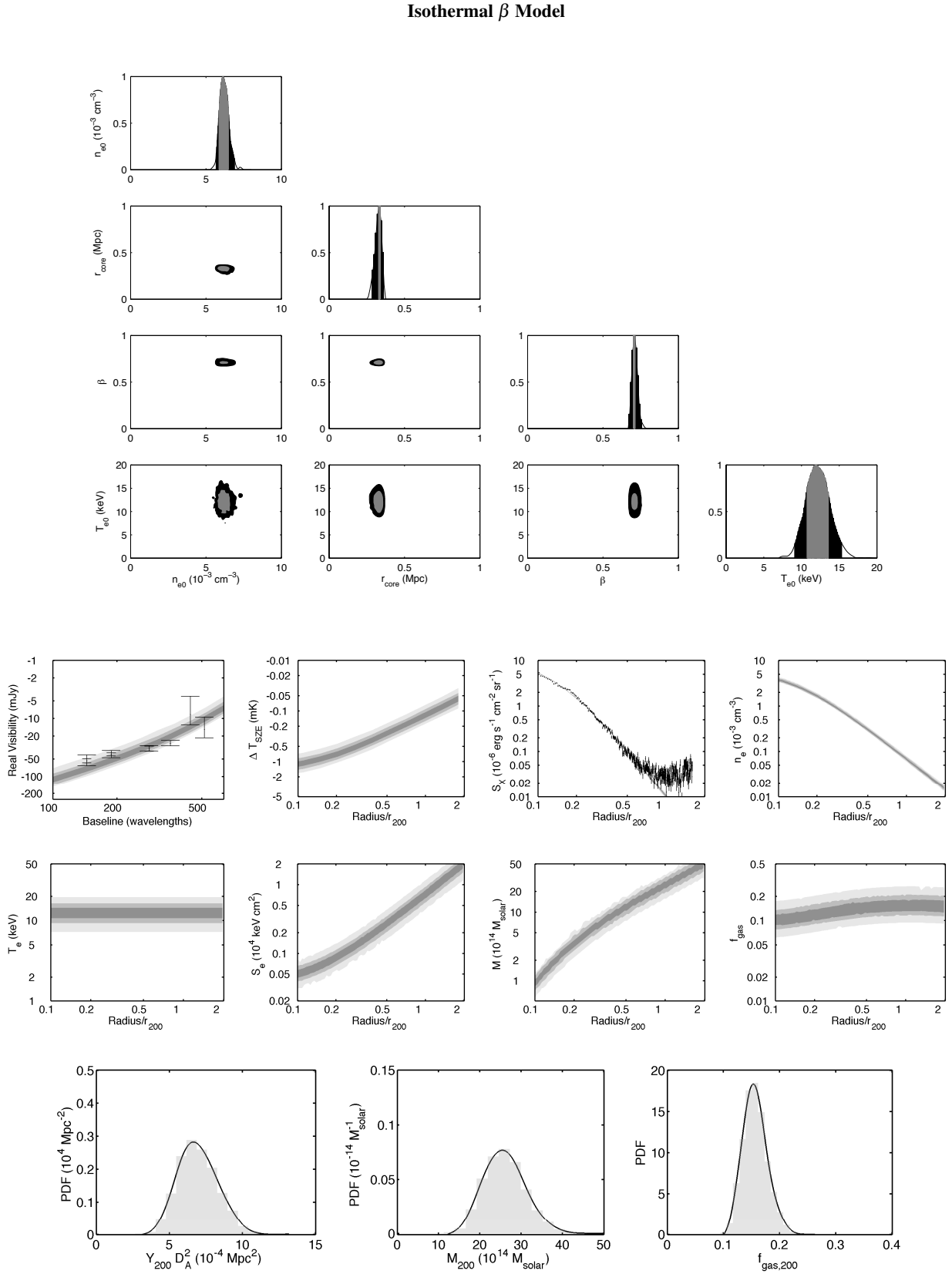

Figure 5.4: Continued

ments. Our results are consistent with both the measured values of y_0 from Andreani et al. (1999) and from Halverson et al. (2009) within the quoted errors.

The average electron temperature from each of the observations given in Table 5.4 are weighted differently and so some caution is required in comparing them. For direct comparison with the result from Zhang et al. (2008), I calculate the volume average over the radius range 0.2 to 0.5 $r_{500,\mathrm{X}}$, where $r_{500,X}$ is equal to 1.42 Mpc for the Bullet cluster. The volume average temperature estimated from the entropy model fit agrees well with the equivalent value estimated by Zhang et al. (2008). The β model fit produces a slightly higher estimate of the average temperature with respect to the X-ray result, however the two values still agree within the 68 % error. Halverson et al. (2009) use a χ^2 fit to compare their APEX-SZ map to the Chandra X-ray surface brightness (Clowe et al., 2006), and so by assuming isothermality estimate the average mass weighted temperature. Their result is in good agreement with both Zhang et al. (2008) and the CBI2/XMM-Newton results presented here. Govoni et al. (2004) estimate the electron temperature using the X-ray spectrum extracted from within a radius of 3 arcminutes of the Chandra observations. They calculate an emission weighted value that is significantly higher than temperature estimates that go out to higher radii. By using the temperature profile from the entropy model fit to calculate the equivalent average emission weighted temperature within 3 arcminutes of the centre, I estimate that $T_{\mathrm{ew}} = 12.6 \pm 2.0$, which is consistent with the Govoni et al. (2004) result within the 68 % error interval.

The total mass and gas mass fraction quoted in Table 5.4 are derived by assuming a spherically symmetric volume and integrating the total and gas masses out to a fixed radius of 1.42 Mpc, chosen for direct comparison with the results by Zhang et al. (2008) and Halverson et al. (2009). The CBI2/XMM-Newton results from fits using both parametric models agree with the estimates by Zhang et al. (2008) within the 68 % error. The isothermal β model produces a slightly higher mass estimate, and hence a lower value for f_{gas}. This is not surprising given the results of Chapter 4, which show that this model systematically over estimates the mass at large radii. The mass estimate given by Halverson et al. (2009) is significantly higher than both the CBI2/XMM-Newton and Zhang et al. (2008) results. This discrepancy is ~ 60 % and so cannot be accounted for purely by the smaller difference in the SZ measurements which, based on the estimates of y_0, is approximately 25 %. The difference might well be due to a combination of both the underlying modelling assumptions and the average temperature that is used to make the mass estimate. Halverson et al.

Ref.	Conf.	$y_0(10^{-4})$	T_e (keV)	$M_{1.42\,\mathrm{Mpc}}(10^{14}M_\odot)$	$f_{\mathrm{gas},1.42\,\mathrm{Mpc}}$
This work (Entropy model)	68	$3.10^{+0.33}_{-0.64}$	$11.7^{+1.70}_{-1.78}$	$11.8^{+1.38}_{-2.84}$	$0.167^{+0.051}_{-0.020}$
This work (Isothermal β model)	68	$2.90^{+0.46}_{-0.34}$	$12.0^{+1.81}_{-1.31}$	$13.3^{+1.91}_{-1.45}$	$0.146^{+0.023}_{-0.024}$
Halverson et al. (2009)	68	3.77 ± 0.34	11.0 ± 0.9	20.7 ± 2.5	0.121 ± 0.038
Zhang et al. (2008)	68	-	11.1 ± 0.4	10.99 ± 5.31	0.160 ± 0.018
Govoni et al. (2004)	90	-	13.9 ± 0.7	-	-
Andreani et al. (1999)	70/90	2.60 ± 0.79	17.0 ± 4.0	-	-

Table 5.4: Comparison with results from other SZ and X-ray observations of the Bullet Cluster. Column 1 gives the reference; column 2 the percentage confidence interval for quoted errors; column 3 the central comptonization parameter; column 4 the best estimate of the average electron temperature (note that the values will be weighted differently, see text for details); columns 5 and 6 the total mass and gas mass fraction enclosed within a physical radius of 1.42 Mpc, for direct comparison with estimates by Zhang et al. (2008) and Halverson et al. (2009).

(2009) use an isothermal β model fit, combined with an average electron temperature of 13.9 keV, based on Chandra data by Govoni et al. (2004). This average temperature was calculated from fitting to a spectrum extracted within a radius of 3 arcminutes (equal to 0.8 Mpc at $z = 0.2965$). Since the average temperature out to larger radii is found to be lower than this value by both Zhang et al. (2008) and the work presented here, this would lead to an over estimate of the total mass at larger radii. In addition the assumption of isothermality is known to systematically bias the hydrostatic mass estimate to higher values at larger radii (see e.g. Kay et al., 2004). A combination of both these factors would lead to the observed discrepancy in hydrostatic mass estimates.

5.4.2 The virial mass and velocity of the Bullet Cluster

X-ray observations by Markevitch et al. (2004) show that the sub-cluster in the Bullet system is moving away from the centre of the main cluster with high velocity. The bow shock that has formed in front of the sub-cluster indicates a Mach number $\mathscr{M} = 3.2^{+0.8}_{-0.6}$ and an inferred shock velocity $v_{\mathrm{shock}} = 4500^{+1100}_{-800}\,\mathrm{kms}^{-1}$. Hayashi & White (2006) use the results of weak lensing observations by Clowe et al. (2004) to extrapolate the mass estimate out to r_{200}, and from this infer a virial velocity $v_{200} = 2380\,\mathrm{kms}^{-1}$. By studying the fraction of halos with substructure velocities greater than v_{sub} in the Millennium run (Springel et al., 2005), they could obtain an expression for the likelihood of the Bullet Cluster system in the current ΛCDM cosmology.

The fraction of main cluster halos with this property is given by

$$\log_{10}(f(>v_{\rm sub})) = -\left(\frac{v_{\rm sub}}{1.55v_{200}}\right)^{3.3}. \tag{5.4}$$

Given the results of the weak lensing analysis by Clowe et al. (2004) the likelihood of the Bullet Cluster system in the current accepted cosmological model is $f_{\rm bullet} \approx 0.01$. In fact more recent constraints on the virial mass of the Bullet Cluster from weak lensing observations (Clowe et al., 2006; Farrar & Rosen, 2007) indicate that the mass value is lower by a factor ~ 2, and hence the virial velocity is $v_{200} \approx 1770\,{\rm kms}^{-1}$. Farrar & Rosen (2007) use these results to estimate that the Bullet Cluster system is significantly unlikely within a ΛCDM cosmology, with the fraction of halos $f \lesssim 10^{-7}$. Since this result shows such a system to be highly improbable they suggest the existence of a new long range interaction that could provide the required additional attractive force to accelerate the sub-cluster to the observed velocity. However Springel & Farrar (2007) have recently conducted simulations of a toy merger event that match the observable properties of the Bullet Cluster system and show that the true velocity of the sub-cluster maybe be significantly lower than that inferred from the shock velocity. This is in part due to the inflow of gas in front of the shock, and secondly due to the fact that the bow shock maybe moving away with greater velocity than the sub-cluster. In this case the value of the system likelihood will be substantially higher.

The joint analysis of CBI2 and XMM-Newton surface brightness data can be used to constrain the total mass out to r_{200} (assuming that hydrostatic equilibrium holds on the largest scales) and so provide an estimate of the virial velocity that is independent of lensing observations and galaxy kinematics. The virial velocity is calculated for every sample of the posterior distribution by the following expression

$$v_{200} = \left(\frac{GM_{200}}{r_{200}}\right)^{0.5}. \tag{5.5}$$

For the entropy model, $v_{200} = (1844^{+113}_{-233})\,{\rm kms}^{-1}$, and for the isothermal β model, $v_{200} = (2046^{+167}_{-111})\,{\rm kms}^{-1}$, where the discrepancy between the values arises from the difference in the two mass estimates. Assuming that the entropy model fit gives the best representation of the true virial mass, and that the sub-cluster halo is moving at a velocity similar to that given by Springel & Farrar (2007) i.e. $v_{\rm sub} \approx 2860\,{\rm kms}^{-1}$, then the likelihood is given by $f_{\rm bullet} \approx 10\%$. This supports the conclusion that the observed Bullet Cluster system is

an entirely probable system within the currently accepted cosmological model.

5.4.3 The concentration parameter

The entropy model fit to the SZ and X-ray data produces a best fit dark matter halo concentration for the whole system of $c_{\rm DM} = 4.3 \pm 1.0$, which is both higher than the value obtained from recent analysis of weak lensing observations ($c = 2$), and more consistent with the range of values ($c \approx 3 - 6$) predicted from observational and cosmological constraints for a massive cluster (Buote et al., 2007; Comerford & Natarajan, 2007; Macciò et al., 2007, 2008). N-body/SPH simulations by Springel & Farrar (2007) also suggest that a higher main halo concentration is required in order to reproduce the observed relative positions of the two mass peaks, the edge of the bullet component and the bow shock. They find that the concentration of the main cluster should be $c \approx 3$. Higher concentrations lead to an over-prediction of the separation of the bullet mass peak and the bullet edge, while a lower concentration under-predicts the separation. Furthermore, high resolution simulations by Mastropietro & Burkert (2008) have also been used to investigate the effect of altering the mass ratio of the main and bullet components, as well as the initial velocity of the bullet and the impact parameter for the merger. The virial mass (M_{200}) assigned to the main cluster is a factor ~ 2 less than used in the simulations by Springel & Farrar (2007) and found from fitting to the CBI2/XMM-Newton data in this work. Comparisons of the observed X-ray and Lensing morphologies, and those predicted from these simulations, are used to suggest that the concentration of the main cluster should be much higher ($c \approx 6$) in order to avoid complete disruption of the gas in the main X-ray peak. The outcomes of both these simulations are dependent upon the assumptions made about the virial mass and other properties of the system, and so differences in these assumed properties will lead to discrepancies between the results. Simulations that reflect the true dynamical state of the system require reliable and direct observational constraints on the virial mass and other global properties, and it is hoped that the results of this work will help contribute to this constraint in future.

5.5 Summary

The Bullet Cluster is one of the brightest SZ and X-ray clusters in the sky, and as such provides a perfect case study for pointed SZ effect observations with the CBI2 array. In this chapter I have outlined in detail

the observation and analysis of CBI2 data, and conducted a joint analysis with published X-ray surface brightness data to estimate the total mass and gas mass fraction out to r_{200}. Estimates are made of the profiles for various cluster properties, using the entropy model described in Chapter 4 including the total mass and temperature, out to large radii. In the next chapter I use observations of the REFLEX-DXL sample at $z \sim 0.3$ to estimate the scaling relations between the observable SZ effect and intrinsic physical properties of the clusters.

Chapter 6

Scaling relations from the REFLEX-DXL sample

The REFLEX-DXL sample is a flux-limited sub-sample of distant ($z = 0.27 - 0.31$) and X-ray luminous ($L_X \gtrsim 10^{45}\,\mathrm{ergs}^{-1}$, 0.1-2.4 keV) clusters from the REFLEX survey (Böhringer et al., 2001). These clusters were selected by Zhang et al. (2006) and used in their work to construct scaling relations between the X-ray observables and physical properties out to r_{500}. A sub-sample of these clusters was also observed at 610 MHz by Venturi et al. (2007), as part of a GMRT survey of radio halos in REFLEX clusters. In this chapter I discuss observations using CBI2, and the subsequent analysis performed to obtain scaling relations between the thermal SZ effect and physical properties, under the assumptions of sphericity and hydrostatic equilibrium. Understanding the calibration of these relations and their intrinsic scatter is vitally important for interpreting the results from large-scale SZ surveys, where the goal is to detect galaxy clusters through measurements of the integrated SZ effect. Deviations of the observed scaling relations from those predicted by the simple self-similar model also provide an insight into the underlying non-gravitational processes that govern the physics of clusters. The work presented here is an initial analysis using 11 clusters, however it is intended that eventually twice as many clusters will be added to the CBI2 sample, leading to an improved empirical measurement of the scaling relations out to the largest radii.

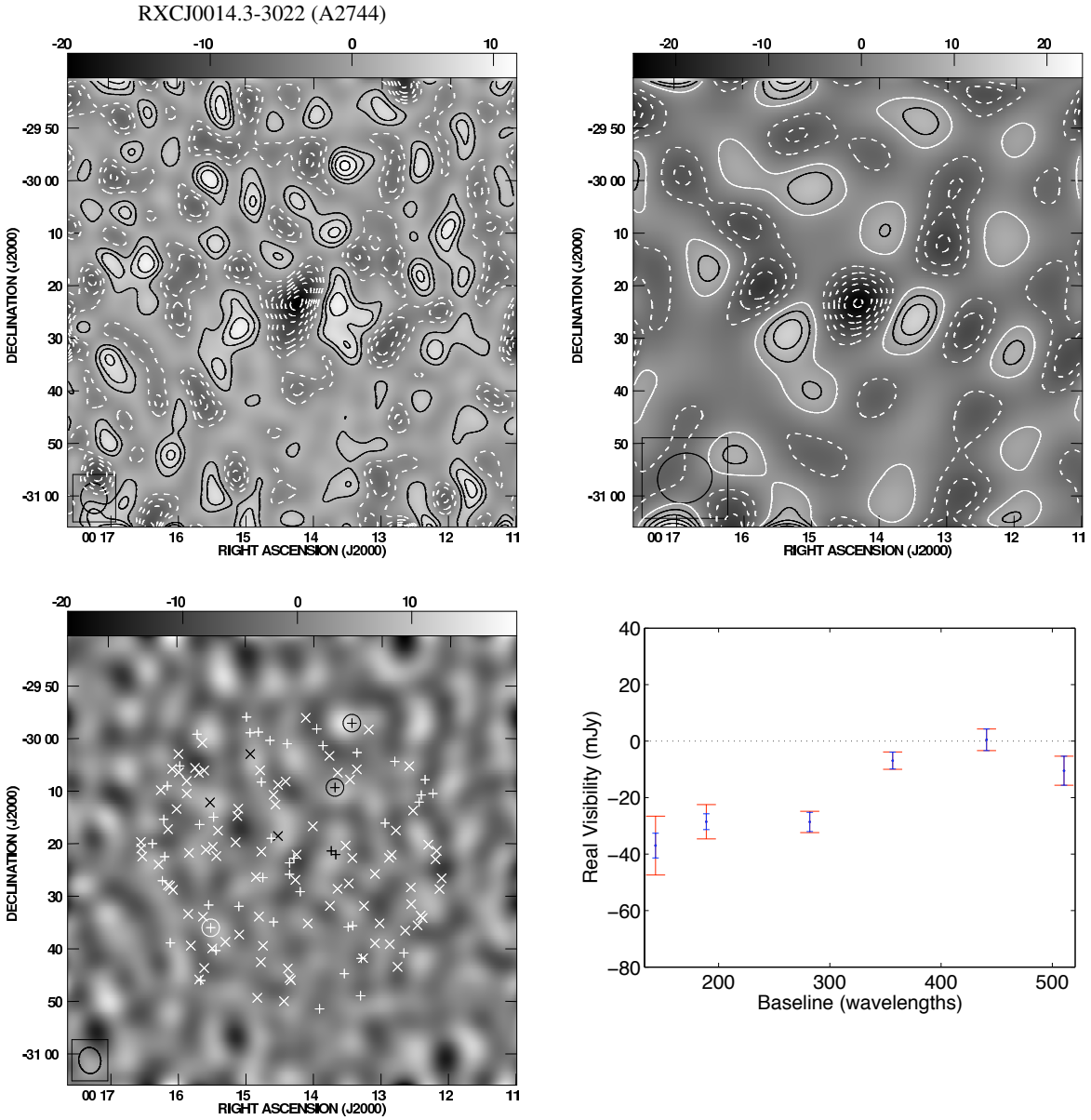

Figure 6.1: CLEANed maps from CBI2 observations of the REFLEX-DXL sample (Zhang et al., 2006). The grey scale units are in mJy beam^{-1}. *Top Left*: Full-resolution map with contours representing the $1\,\sigma$ noise level. *Top Right*: Short-baseline map (less than 300 wavelengths) with contours representing the $1\,\sigma$ noise level. *Bottom Left*: Long-baseline map (greater than 300 wavelengths) with the positions of known point sources. The positive crosses represent known NVSS (Condon et al., 1998) or SUMSS sources (Mauch et al., 2003) within a radius of 30 arcminutes of the centre of the main cluster field. The diagonal crosses represent known NVSS or SUMSS sources within a radius of 30 arcminutes of the centres of the reference fields. The circles are those source positions projected in the SZ analysis. *Bottom Right*: The real visibility as a function of baseline distance. The blue and red error-bars represent thermal noise and total uncertainty (including the intrinsic CMB anisotropy) at the $1\,\sigma$ level respectively.

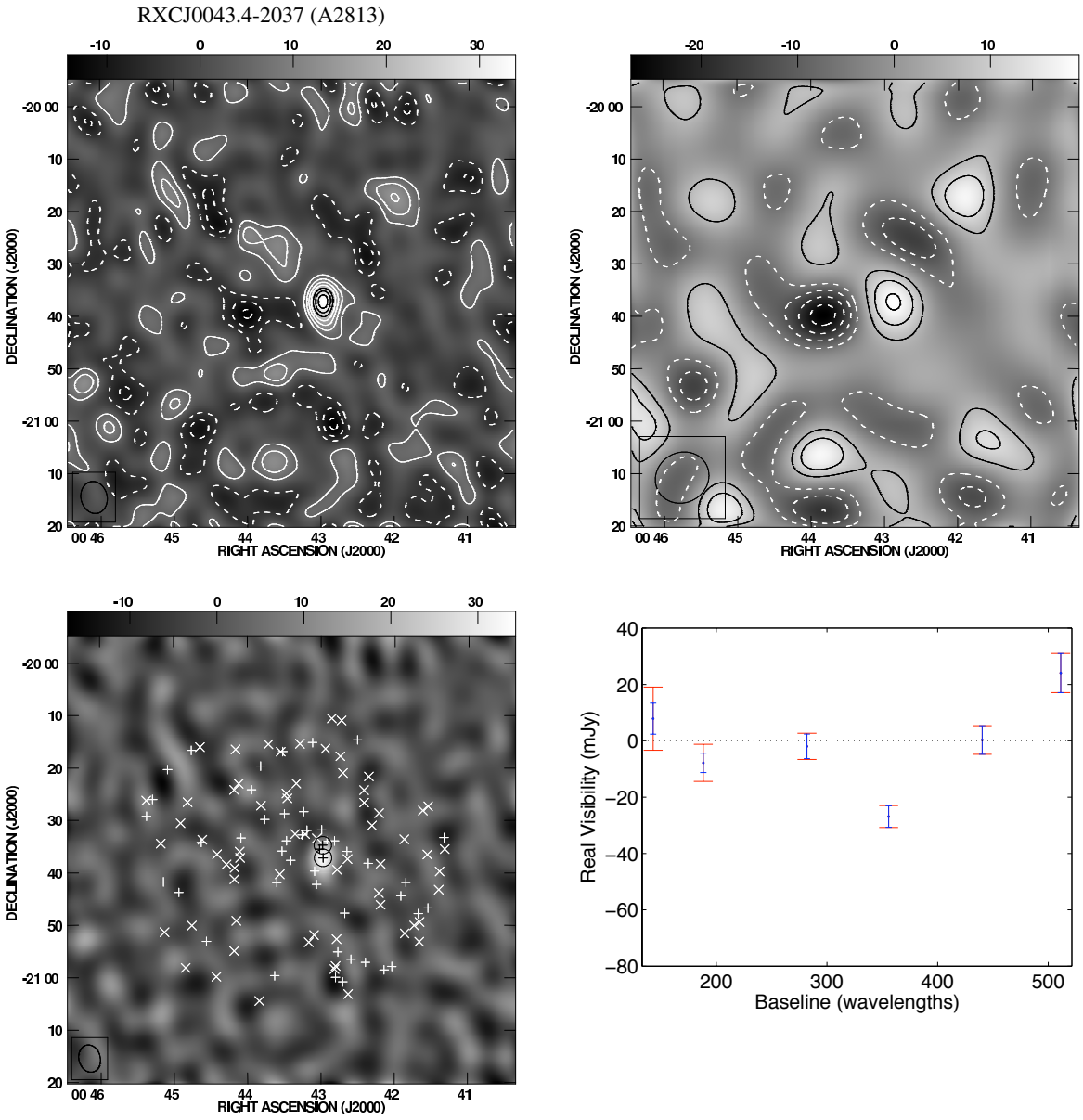

Figure 6.1: Continued

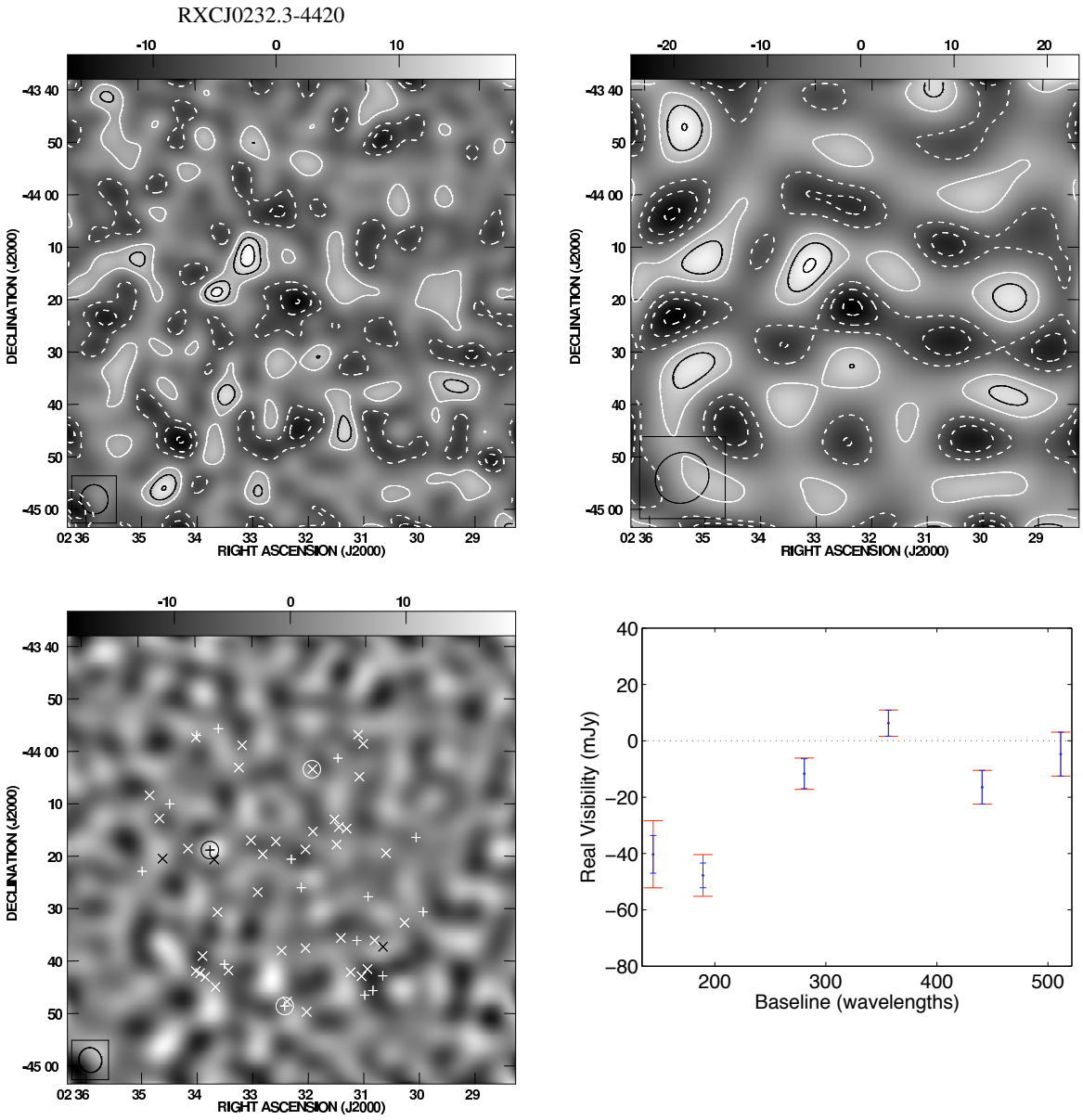

Figure 6.1: Continued

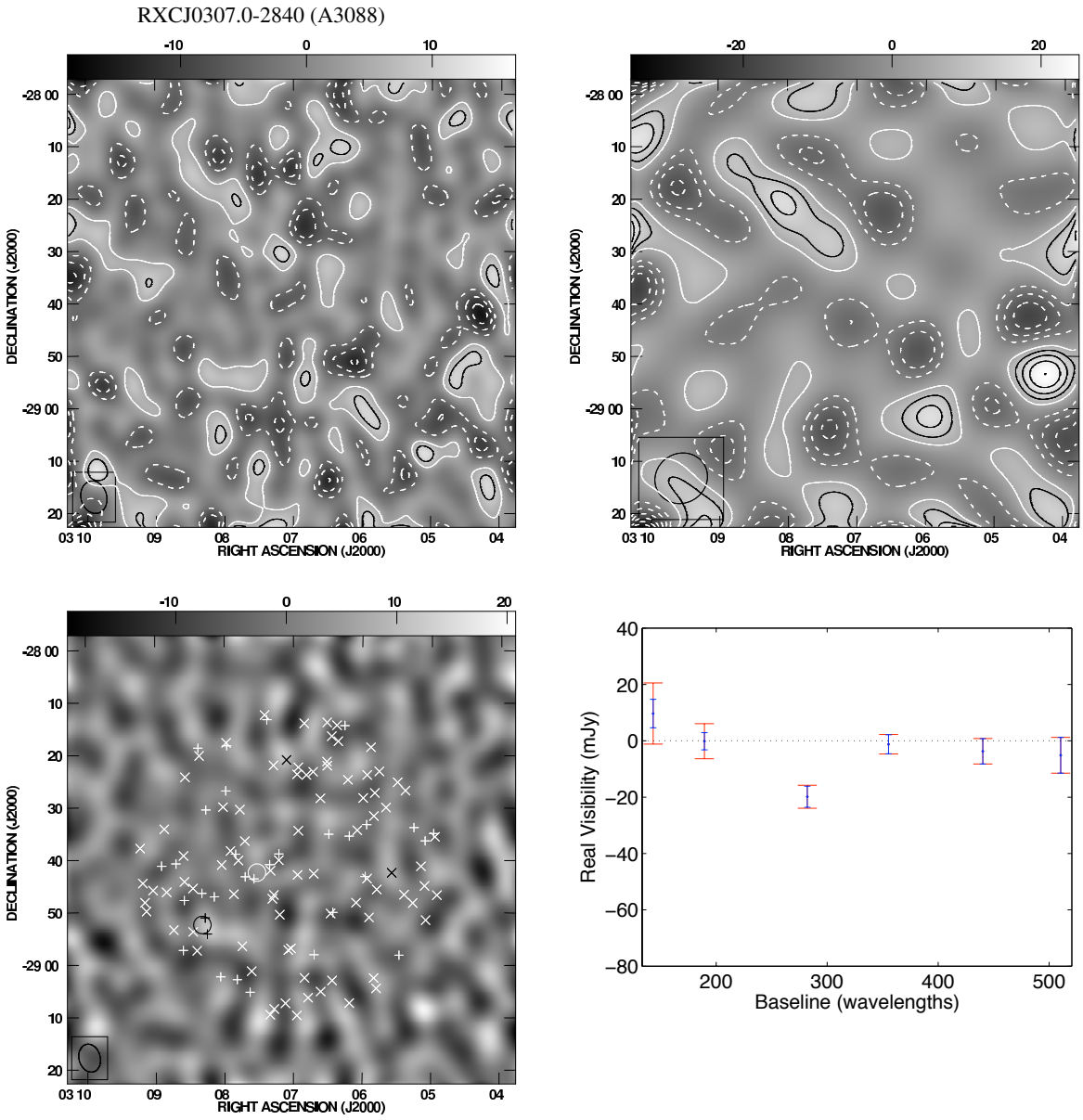

Figure 6.1: Continued

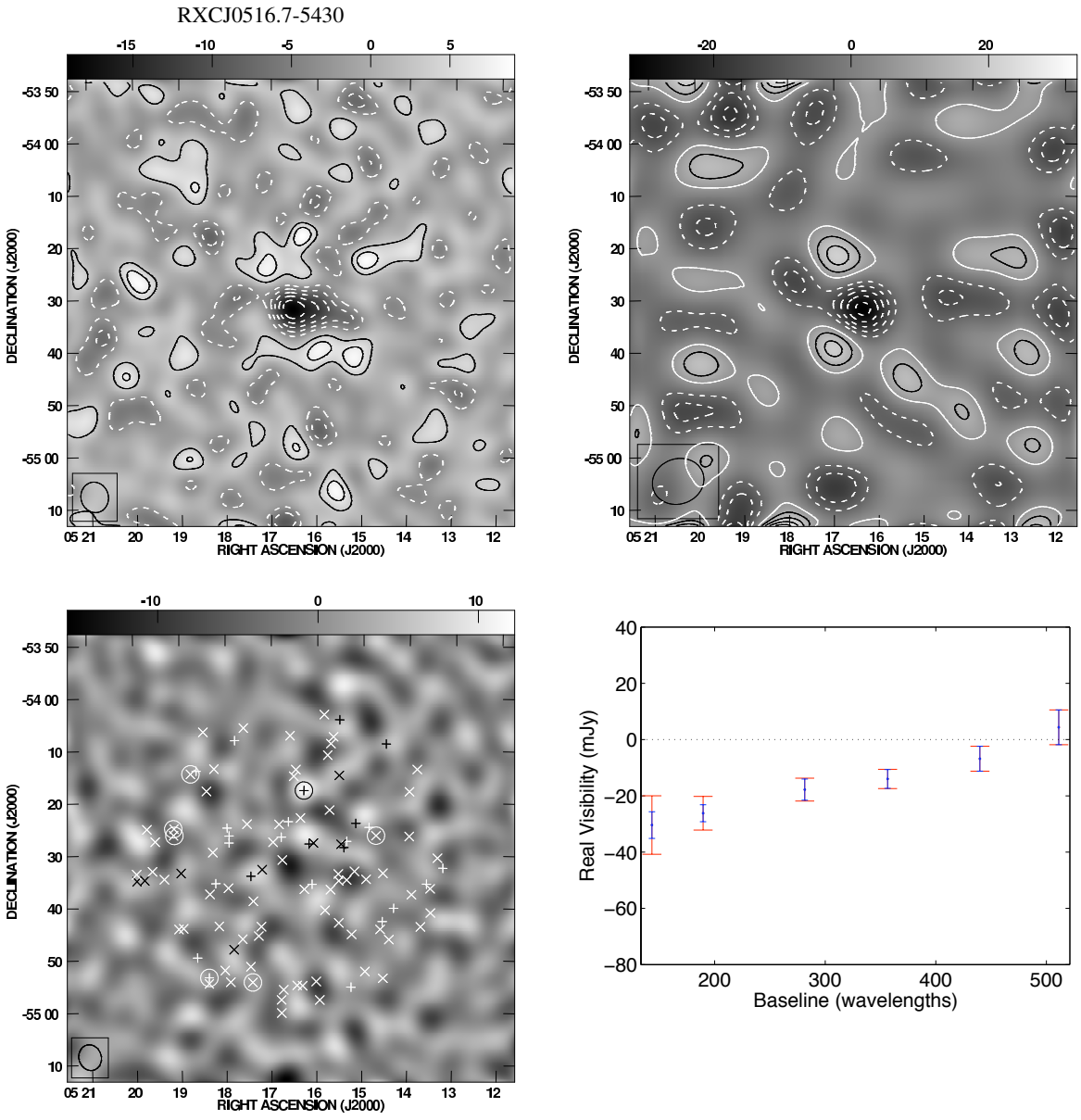

Figure 6.1: Continued

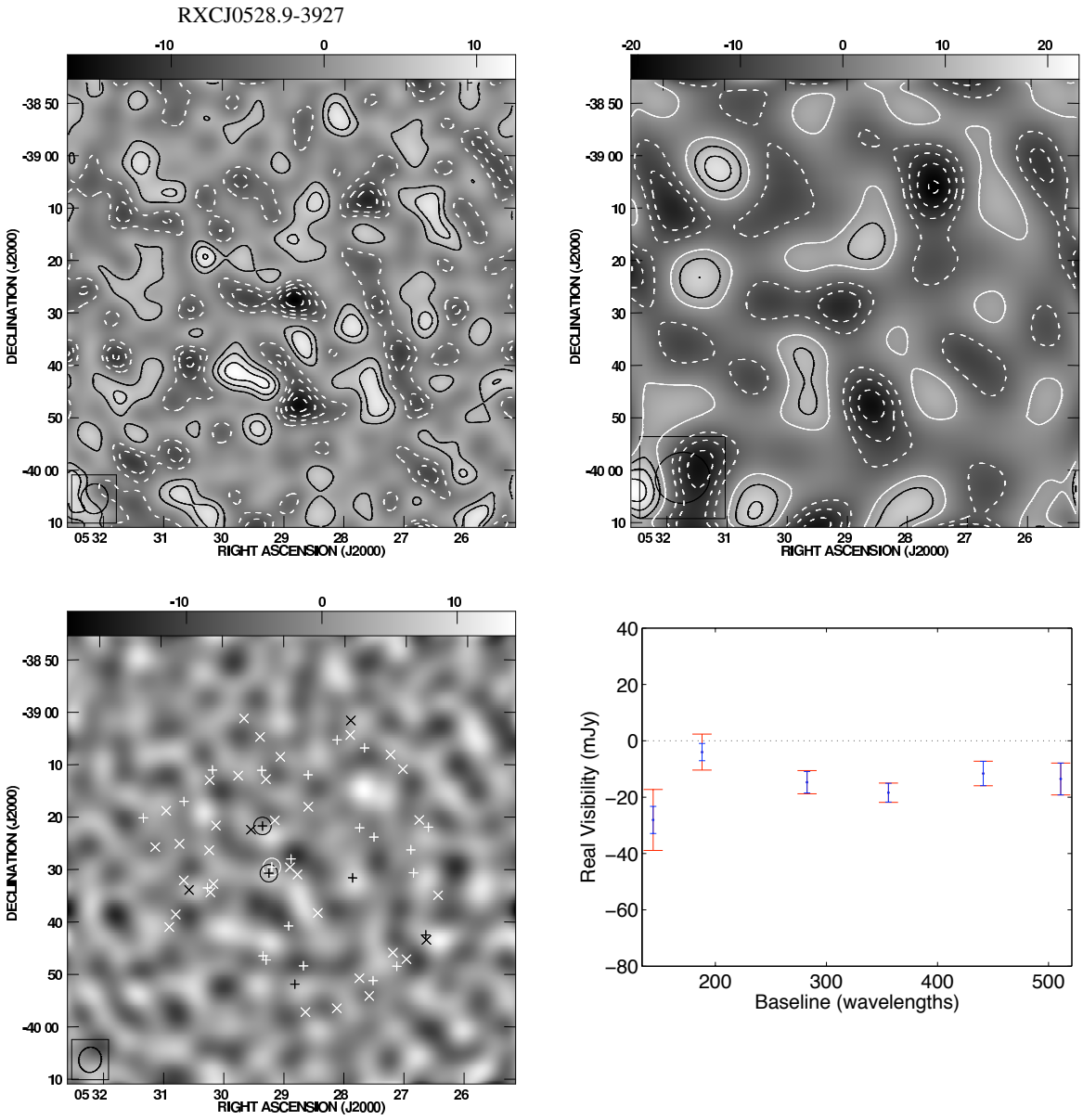

Figure 6.1: Continued

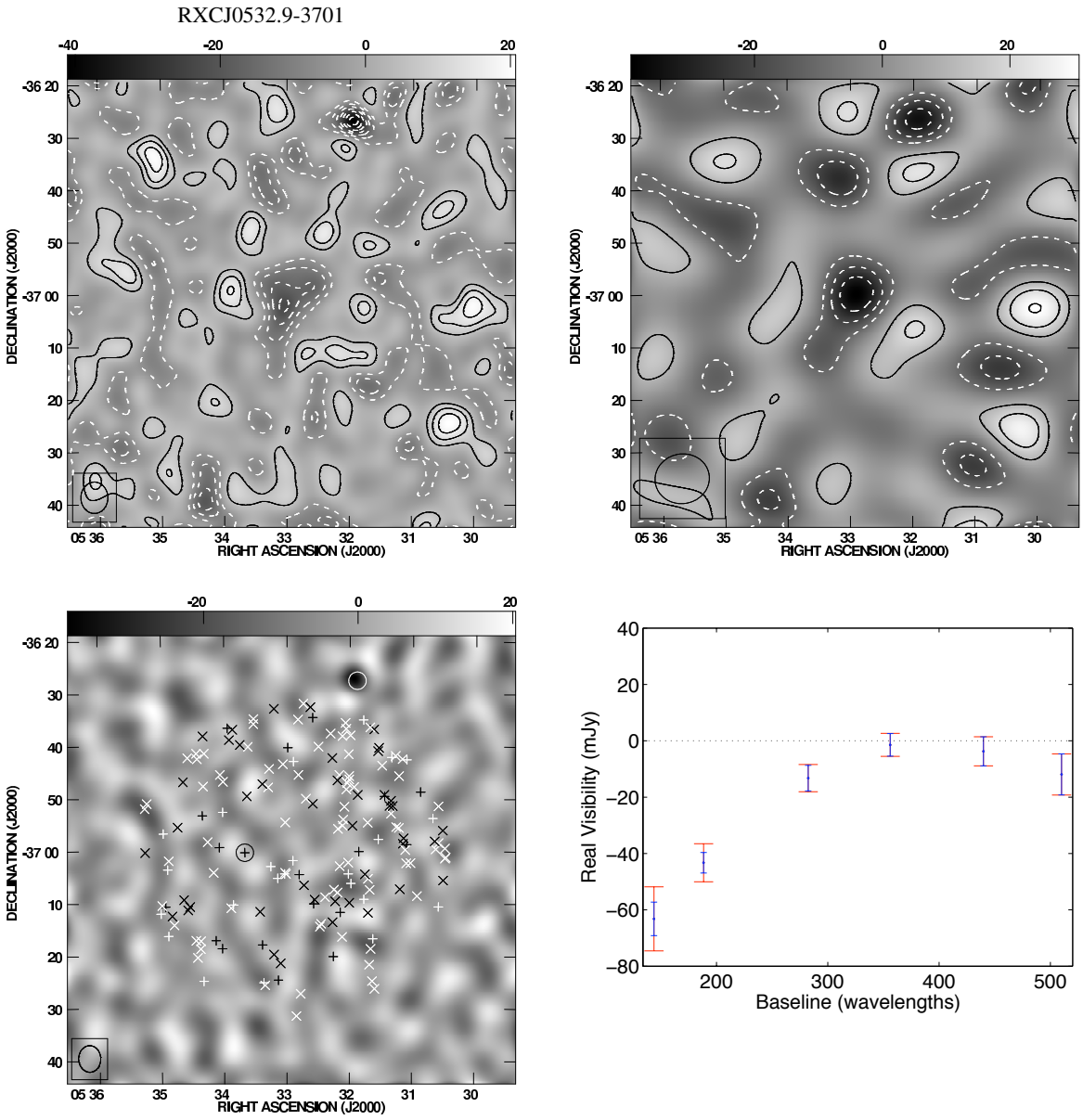

Figure 6.1: Continued

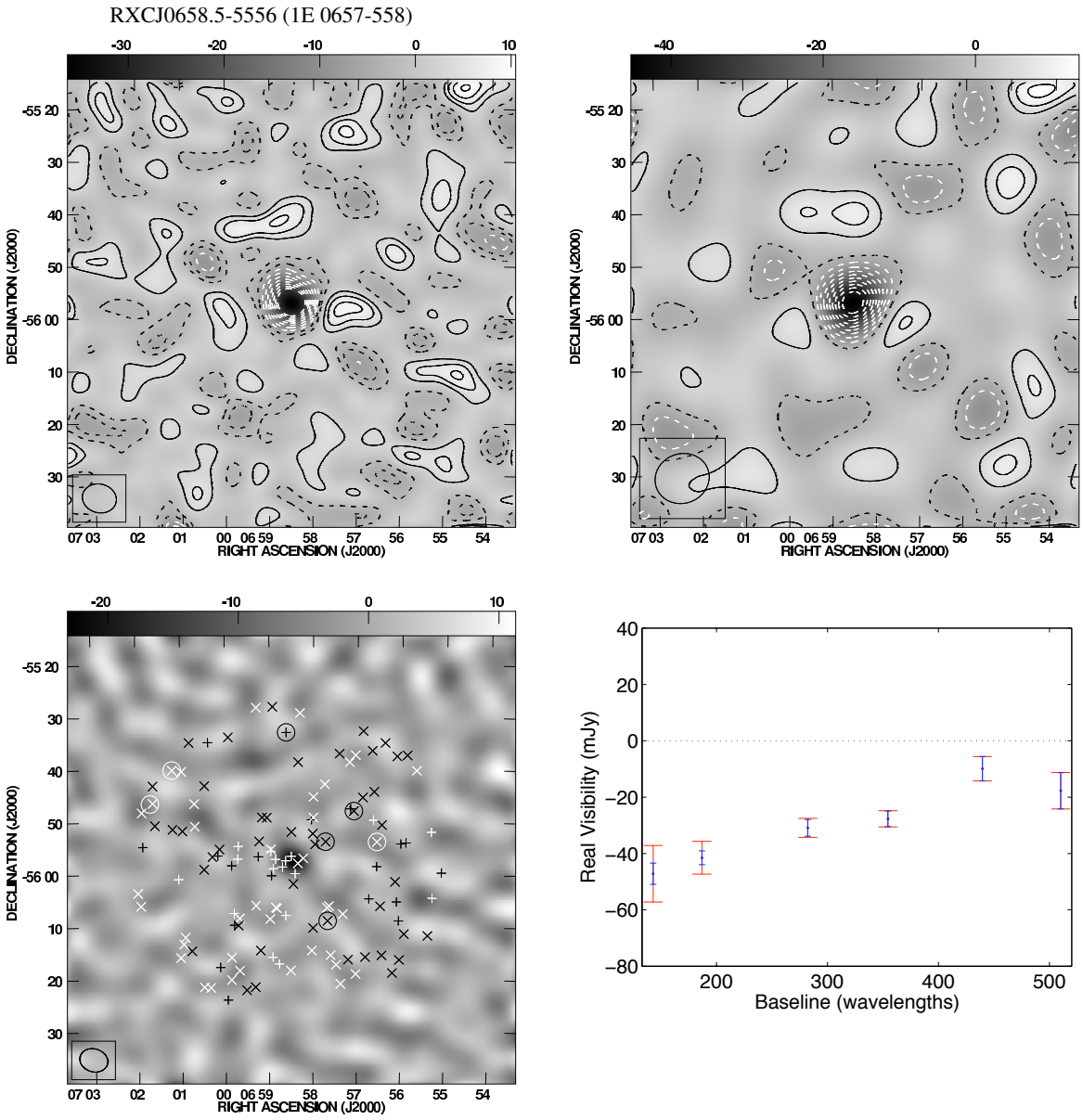

Figure 6.1: Continued

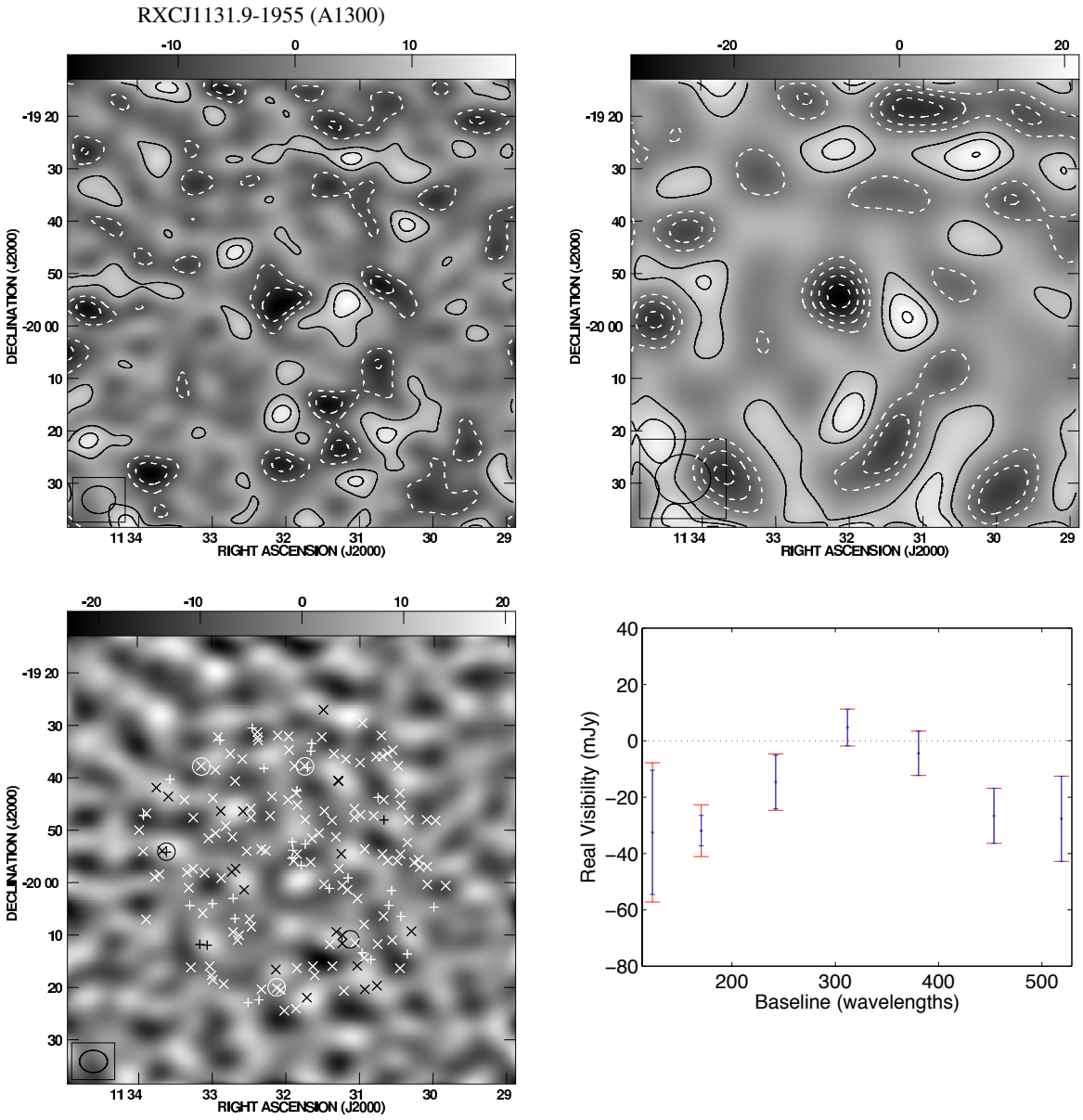

Figure 6.1: Continued

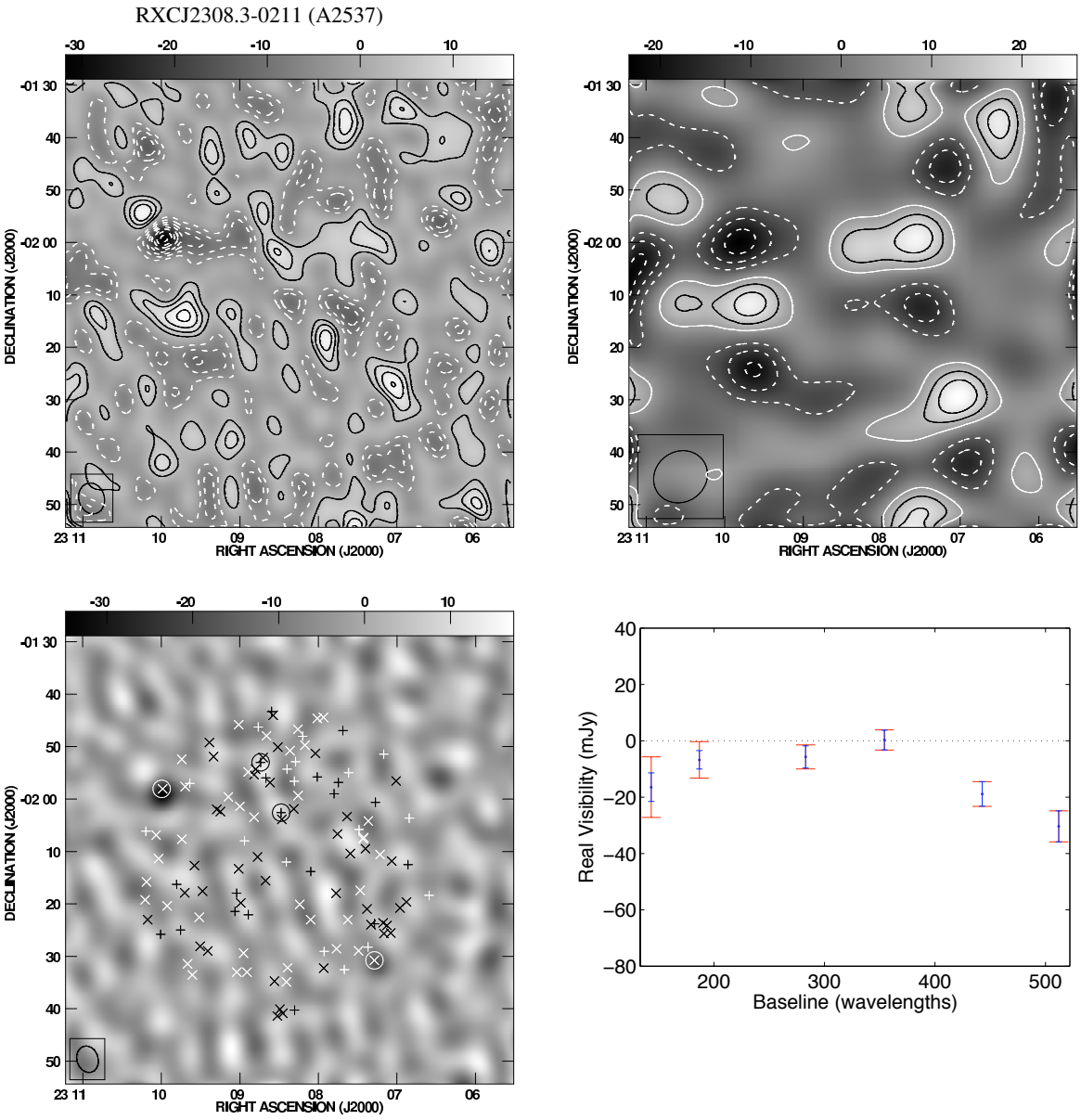

Figure 6.1: Continued

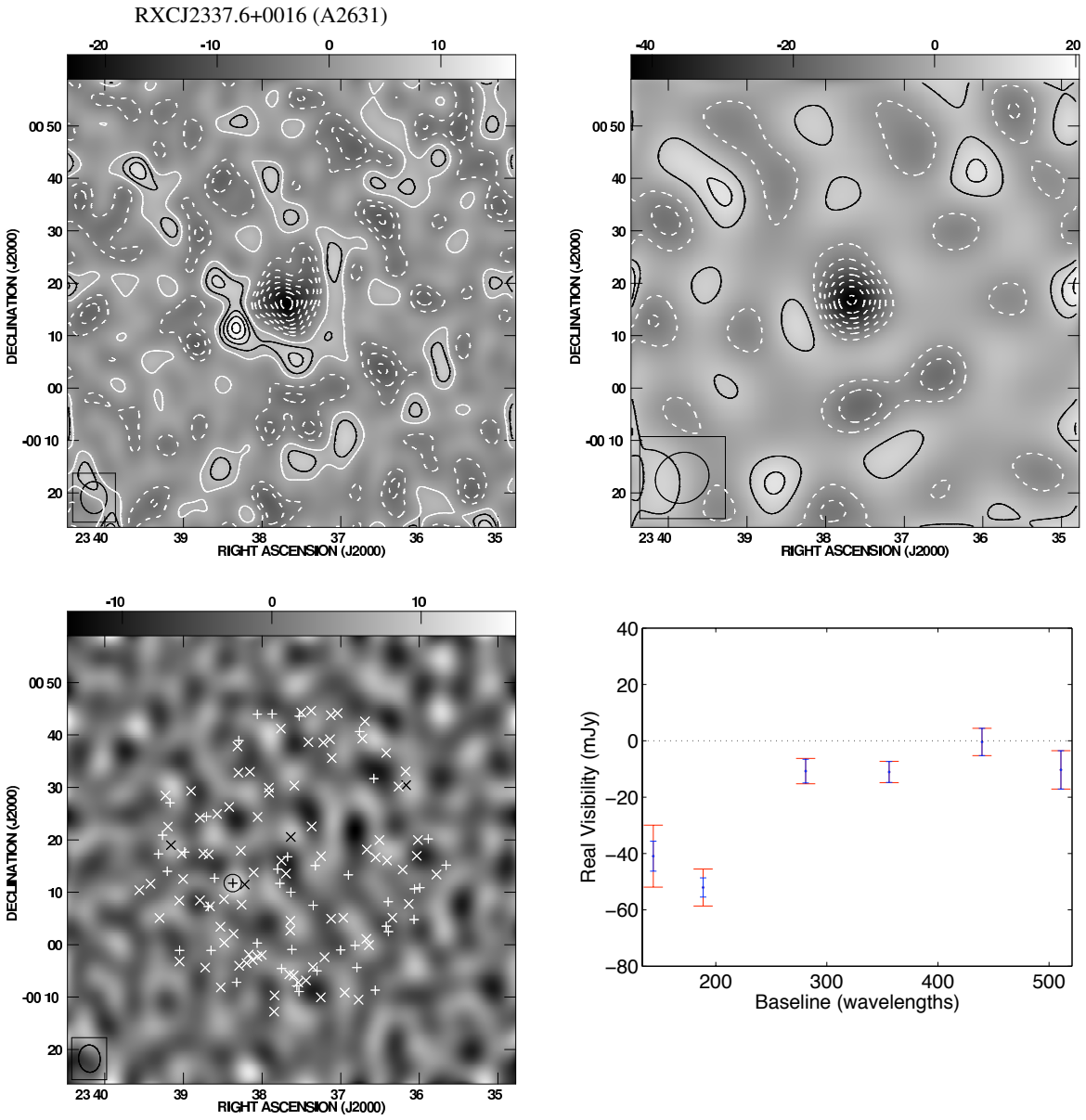

Figure 6.1: Continued

RXCJ	Alt. Name	z_{opt}	R.A. (J2000)	Decl. (J2000)	$L_{bol,X}$	t_{int}	RMS
0014.3-3022	A2744	0.3066	00:14:18.6	-30:23:15.4	1.91±0.16	10.1	2.7
0043.4-2037	A2813	0.2924	00:43:24.5	-20:37:31.2	0.89±0.09	6.9	4.4
0232.3-4420	-	0.2836	02:32:18.8	-44:20:51.9	1.27±0.11	4.8	5.5
0307.0-2840	A3088	0.2578	03:07:02.2	-28:39:55.2	1.00±0.10	13.3	4.5
0516.7-5430	-	0.2943	05:16:35.2	-54:30:36.8	0.84±0.11	6.9	2.5
0528.9-3927	-	0.2839	05:28:52.5	-39:28:16.7	1.25±0.13	8.0	3.7
0532.9-3701	-	0.2747	05:32:55.9	-37:01:34.5	0.95±0.10	6.1	5.5
0658.5-5556	1E 0657-558	0.2965	06:58:30.2	-55:56:33.7	4.21±0.21	18.9	2.5
1131.9-1955	A1300	0.3075	11:31:54.7	-19:55:40.5	1.58±0.14	2.3	6.7
2308.3-0211	A2537	0.2966	23:08:22.3	-02:11:32.1	0.88±0.11	12.5	3.8
2337.6+0016	A2631	0.2753	23:37:37.8	+00:16:15.5	0.79±0.08	7.0	3.1

Table 6.1: Summary of clusters from the REFLEX-DXL sample, selected for CBI2 observations. Column 1 gives the REFLEX catalogue name; column 2 the alternative name; column 3 the optical redshift (Böhringer et al., 2004); column 4 and 5 the right ascension and declination of the X-ray centroid (Zhang et al., 2006); column 6 the X-ray bolometric luminosity in units of $10^{45}\,\mathrm{erg\,s^{-1}}$ (Zhang et al., 2006); column 7 the total CBI2 integration time on the main cluster field in hours; column 8 the RMS noise on the full-resolution CBI2 map in $\mathrm{mJy\,beam^{-1}}$.

6.1 CBI2 Observations

Of the 13 clusters selected in the REFLEX-DXL sample, 11 were observed with CBI2 during the period from the 2nd April 2007 to the 21st May 2008. RXCJ0437.1+0043 was not observed due to technical problems with the instrument, and RXCJ0303.7-7752 has a declination that is too low to be observed from the CBI2 site. The pointing centres were chosen to be co-incident with the positions of the X-ray centroids given by Zhang et al. (2006). Primary flux calibration was performed either to Jupiter or Tau A where possible, otherwise a suitable bright planet or unresolved source was selected. A 5 % calibration error is included in model fitting to account for the error in the overall calibration of CBI2 data. The data were reduced and gridded as outlined in Chapter 3, with differencing employed to remove any spurious signals. Table 6.1 provides a summary of the REFLEX-DXL clusters observed with CBI2, including the total integration time on the main field of each cluster and an estimate of the RMS noise on the full-resolution map. The intention was to integrate on each cluster equally and long enough to obtain a significant detection. However this was not always possible because the requirement for instrument maintenance prevented obtaining a long total integration before some clusters became unavailable. Note that the total integration time does not necessarily correlate with the quality of the detection, since the number of receivers in operation and the inherent mass

and temperature of the cluster also effects the sensitivity. Maps of the complete data set are shown in Figure 6.1, and were deconvolved from the synthesised beam using the CLEAN algorithm implemented by the APCLN task in AIPS[1] .

6.2 Radio Point Sources

The existence of bright radio sources in CBI2 data can cause systematic uncertainty in the measured thermal SZ signal, especially if the source lies near to a field centre so that the brightness is not attenuated by the primary beam. It is therefore important to identify significant sources in the CBI2 data, and apply the source projection procedure described in Chapter 4 at their measured positions. The CBI2 long-baseline maps in Figure 6.1 show the position of all known NVSS (1.4 GHz) and SUMSS (843 MHz) sources, as well as the sources identified as contaminants at 31 GHz. Where possible observations with the Australia Telescope Compact Array (ATCA) are used to identify contaminating sources in the CBI2 fields, with surveys in the field centres at 4.85 GHz and 8.64 GHz and targeted observations at 32 GHz. All raw ATCA data were reduced by A. C. Taylor, using the method outlined in Chapter 5. Due to the limited availability of ATCA for observation it is not possible to provide a standard point source analysis for all clusters in the REFLEX-DXL sample. Hence the following discussion describes the point source treatment for each cluster separately. When source information was not available from observation with ATCA, the Parkes-MIT-NRAO (PMN, Griffith & Wright, 1993) survey was used, which provides source fluxes down to a limit of 30 mJy at 4.85 GHz. The sources detected in the RXCJ0658.5-5556 fields were reported in Chapter 5 and so are not repeated in this section. A summary of all identified point sources from the available data is given in Table 6.2. The reader should refer to Appendix A for maps of the mosaics from 4.80 GHz and 8.64 GHz ATCA observations. While the radio point sources described in this section are considered only for their role as a component of the error in the SZ signal, future work is planned that will focus on the scientific aspect of source counts in galaxy clusters as a function of frequency.

[1] http://www.aips.nrao.edu/

RXCJ	Field	R.A. (J2000)	Decl. (J2000)	[1]$S_{0.843}$	[2]$S_{1.4}$	$S_{4.80}$	[3]$S_{4.85}$	$S_{8.64}$	S_{32}	S_{CBI2}	Proj.
0014.3-3022	Main	00:13:26.5	-29:57:12	-	4.8±0.6	-	-	-	-	250 ± 100[5]	Yes
0014.3-3022	Main	00:13:41.2	-30:09:26	401.3±12.3	222.5±6.7	-	97±12	-	30.1±1.1	< 30	Yes
0014.3-3022	Main	00:15:31.0	-30:36:07	420.2±12.7	264.2±7.9	-	121±13	-	25.4±1.1	< 30	Yes
0043.4-2037	Main	00:42:58.4	-20:37:13	-	406.1±12.2	-	182±14	-	20.8±1.6	< 40[4]	Yes
0043.4-2037	Main	00:42:58.6	-20:34:48	-	155.9±5.3	-	-	-	8.4±1.6	< 40[4]	Yes
0232.3-4420	Lead	02:22:52.8	-44:03:39	511.6±15.4	-	-	129±11	-	17.6±1.8	< 70	Yes
0232.3-4420	Main	02:32:25.4	-44:48:50	180.7±5.5	-	-	-	-	7.8±1.5	< 300[5]	Yes
0232.3-4420	Main	02:32:07.6	-44:26:14	34.8±2.6	-	5.7±0.9	-	< 3.6	< 5	< 18	No
0232.3-4420	Main	02:32:18.4	-44:20:50	50.0±3.1	-	7.9±0.5	-	< 2.4	< 5	< 18	No
0232.3-4420	Main	02:33:45.1	-44:19:02	15.7±1.3	-	-	-	-	-	39±12	Yes
0232.3-4420	Trail	02:41:45.3	-44:18:57	61.5±2.0	-	14.8±1.2	-	< 9.0	< 5	< 40	No
0307.0-2840	Main	03:07:31.8	-28:42:26	-	-	-	65±11	-	-	< 18	Yes
0307.0-2840	Main	03:08:19.4	-28:52:24	-	-	-	57±11	-	-	< 60[5]	Yes
0516.7-5430	Lead 1	05:07:31.0	-54:27:45	398.9±12.0	-	76.0±1.9	100±9	-	< 5	< 20	No
0516.7-5430	Lead 1	05:10:34.3	-54:25:01	23.5±1.1	-	-	-	-	7.2±1.3	< 140[5]	Yes
0516.7-5430	Main	05:16:06.8	-54:35:37	10.8±0.9	-	4.7±1.0	-	< 5.7	< 5	< 10	No
0516.7-5430	Main	05:16:17.7	-54:17:43	12.4±0.9	-	-	-	-	6.8±1.3	< 20	Yes
0516.7-5430	Main	05:16:47.3	-54:26:38	123.3±5.1	-	21.1±0.5	53±8	9.8±0.7	< 5	< 10	No
0516.7-5430	Main	05:16:47.9	-54:37:16	-	-	4.2±0.8	-	< 3.6	-	< 10	No
0516.7-5430	Main	05:17:27.5	-54:34:06	231.9±7.0	-	46.2±2.0	-	-	< 5	< 10	No
0516.7-5430	Main	05:18:23.1	-54:53:28	53.2±2.0	-	-	-	-	8.1±1.3	< 180[5]	Yes
0516.7-5430	Trail 1/2	05:27:42.9	-54:26:17	197.2±6.0	-	-	287±17	-	54.2±1.0	< 80	Yes
0516.7-5430	Trail 1	05:30:12.7	-54:32:50	59.2±2.0	-	29.3±2.5	-	-	< 5	< 40	No
0516.7-5430	Trail 1	05:30:25.2	-54:54:22	1220.2±36.6	-	-	156±11	-	7.2±1.3	< 300[5]	Yes
0516.7-5430	Trail 1	05:31:46.2	-54:14:33	134.3±4.1	-	-	123±10	-	28.5±1.3	< 300[5]	Yes
0528.9-3927	Main	05:29:11.8	-39:29:42	-	19.5±1.0	< 8.3[4]	-	< 5.0	-	< 12	Yes
0528.9-3927	Main	05:29:14.7	-39:30:54	-	10.8±1.0	< 8.3[4]	-	< 5.0	-	< 12	Yes
0528.9-3927	Main	05:29:21.0	-39:21:53	-	9.8±0.6	10.3±2.0	-	< 15.0	-	< 15	Yes
0532.9-3701	Lead	05:22:57.8	-36:27:31	22653.0±679.6	15620.0±468.6	-	8180±572	-	-	8400 ± 1000[5]	Yes
0532.9-3701	Main	05:32:54.2	-37:01:48	17.6±1.8	8.1±0.5	3.1±0.5	-	< 2.3	-	< 20	No
0532.9-3701	Main	05:33:40.2	-37:00:17	41.0±2.0	30.2±1.3	15.7±2.1		-	-	< 30	Yes
0658.5-5556	Lead	06:47:04.9	-55:47:54	335.1±10.1	-	-	75±8	-	11.3±0.8	< 120	Yes
0658.5-5556	Lead	06:47:40.2	-56:08:52	11±1.4	-	-	-	-	6.7±0.7	< 75	Yes
0658.5-5556	Lead	06:51:11.7	-55:40:06	197.7±6	-	-	75±9	-	11.1±0.8	< 600[5]	Yes
0658.5-5556	Main	06:58:24.7	-55:59:53	32.2±2.2	-	10.7±0.7	-	7.3±1.0	< 2.4	< 8	No
0658.5-5556	Main	06:58:29.9	-55:56:34	79.4±4.4	-	< 19.0[4]	-	< 3.0	< 2.4	< 8	No

Continued on next page

RXCJ	Field	R.A. (J2000)	Decl. (J2000)	[1]$S_{0.843}$	[2]$S_{1.4}$	$S_{4.80}$	[3]$S_{4.85}$	$S_{8.64}$	S_{32}	$S_{\rm CBI2}$	Proj.
0658.5-5556	Main	06:58:36.9	-55:32:56	37.3±1.3	-	-	-	-	12.0±0.8	< 100[5]	Yes
0658.5-5556	Main	06:58:37.6	-55:57:25	79.4±4.4	-	< 19.0[4]	-	< 3.0	< 2.4	< 8	No
0658.5-5556	Main	06:58:42.0	-55:58:37	60.4±2.0	-	< 19.0[4]	-	< 3.0	< 2.4	< 8	No
0658.5-5556	Main	06:58:51.4	-55:57:09	129.3±5.3	-	< 19.0[4]	-	9.0±1.0	< 2.4	< 8	No
0658.5-5556	Trail 1/2	07:07:43.3	-55:53:46	107.3±3.3	-	49.1±3.5	-	-	18.7±0.8	< 50	Yes
0658.5-5556	Trail 1	07:11:51.7	-55:46:32	21.7±1.2	-	-	42±8	-	14.3±0.8	< 300[5]	Yes
1131.9-1955	Lead 1/2	11:23:10.7	-19:37:50	-	111.0±3.4	-	97±12	-	-	< 375	Yes
1131.9-1955	Lead 2	11:23:33.5	-20:20:13	-	76.0±2.3	-	159±13	-	-	< 400[5]	Yes
1131.9-1955	Main	11:33:36.9	-19:54:10	-	1223.6±36.7	-	290±18	-	-	< 150	Yes
1131.9-1955	Trail 1	11:39:48.2	-20:11:43	-	26.0±2.0	-	42±11	-	-	< 180	Yes
2308.3-0211	Lead	23:01:07.9	-01:58:03	-	365.2±11.0	-	703±38	-	93.9±1.5	680±70[5]	Yes
2308.3-0211	Main	23:08:28.5	-02:02:36	-	70.5±2.2	-	-	-	9.1±1.5	< 20	Yes
2308.3-0211	Main	23:08:44.1	-01:53:00	-	209±7.4	-	84±11	-	10.6±1.5	< 60	Yes
2308.3-0211	Trail	23:17:17.8	-02:31:27	-	7.5±0.5	-	-	-	-	210±75[5]	Yes
2337.6+0016	Main	23:38:22.3	+00:11:45	-	22.3±0.8	-	-	-	19.2±1.4	22±5	Yes

Table 6.2: A summary of sources in the REFLEX-DXL main and reference fields that are identified as potential contaminants in the SZ signal. Please refer to the text for further discussion of the point sources in individual clusters. Column 1 gives the REFLEX cluster name; column 2 the CBI2 field name; column 3 the right ascension; column 4 the declination; column 5 the SUMSS integrated flux in units of mJy; column 6 the NVSS integrated flux in units of mJy; column 7 the measured peak brightness from ATCA observations at 4.80 GHz in units of mJy beam^{-1}; column 8 the PMN integrated flux in units of mJy; column 9 the measured peak brightness from ATCA observations at 8.64 GHz in units of mJy beam^{-1}; column 10 the measure integrated flux from ATCA observations at 32 GHz in units of mJy; column 11 the best estimated peak brightness from CBI2 long baseline maps in units of mJy beam^{-1}; column 12 whether the source is projected out. All source fluxes are given with 1 σ errors. Upper limits either indicate that the source flux is confused with the synthesised beam or below the 3 σ level of the observation.

[1] SUMSS catalogue (Mauch et al., 2003).

[2] NVSS catalogue (Condon et al., 1998).

[3] PMN catalogue (Griffith & Wright, 1993).

[4] Source confused by synthesised beam.

[5] Source lies on extreme edge of CBI2 field-of-view and so the estimated CBI2 source brightness is strongly dependent on the primary beam model.

RXCJ0014.3-3022

A potentially very bright source is apparent from visual inspection of the CBI2 long-baseline map, located at a distance of 28.5 arcminutes from the centre of the main RXCJ0014.3-3022 field. The primary beam attenuated brightness is greater than 4σ and the source has an estimated peak brightness equal to 250 ± 100 mJy beam^{-1}. This bright peak coincides with the position of a known NVSS source with a 1.4 GHz integrated flux of 4.8 ± 0.6 mJy. If this source is the cause of the bright peak in the CBI2 map, it must have a steeply rising spectral index of $\alpha = 1.28 \pm 0.14$ in the 1.4-31 GHz frequency range.

Targeted observations of NVSS sources were carried out using ATCA at 32 GHz, where the selection criteria included those sources within 15 arcminutes of the field centres with fluxes greater than 5 mJy, and between 15 and 30 arcminutes with CBI2 primary beam attenuated fluxes greater than 20 mJy. Of the 25 sources selected for observation with ATCA, two were detected with $5\,\sigma$ significance. Both these sources are bright and in the main field, but are significantly attenuated by the CBI2 primary beam and their peak fluxes are below the $3\,\sigma$ level in the CBI2 maps. Note that the bright peak observed in the CBI2 long-baseline map was not observed with ATCA since its NVSS integrated flux is much lower than the selection limit. Both the bright peak in the CBI2 map and the two sources are projected out in the SZ analysis.

RXCJ0043.4-2037

This cluster is strongly contaminated at 31 GHz by a bright peak due to the presence of two confused sources close to the centre of the main field. Sources in the NVSS 1.4 GHz catalogue were selected for observation with ATCA at 32 GHz, using the same criteria as were used for the RXCJ0014.3-3022 fields. Of the 26 observed sources, two are detected with $5\,\sigma$ significance, and both are consistent with the position of the bright peak in the CBI2 map. This bright peak has a primary beam corrected brightness equal to 39.2 ± 7.0 mJy beam^{-1}, measured using the CBI2 long-baseline map. Figure 6.2 shows a full-resolution map with the bright peak subtracted. The cluster is not apparent in the map following subtraction, and therefore is not detected with significance in the CBI2 data.

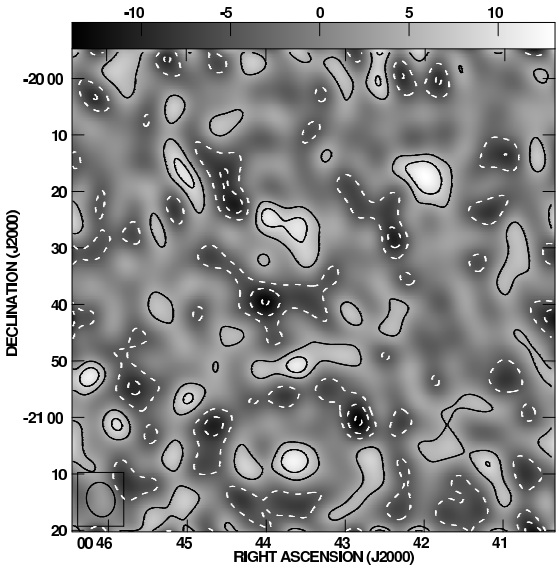

Figure 6.2: A CLEANed full-resolution map of RXCJ0043.4-2037, with the bright peak subtracted. The grey scale units are in mJy beam^{-1} and the contours represent the 1 σ noise level.

RXCJ0232.3-4420

Visual inspection of the CBI2 long-baseline map reveals a possible candidate source in the main field, at the position of a known SUMSS source. This source has a primary beam corrected peak brightness of 39.4$\pm$12.1 mJy beam^{-1}, measured using the CBI2 long-baseline map. Targeted ATCA observations were carried out, at 32 GHz, of sources in the SUMSS catalogue within the main and reference fields. The selection criteria for these observations included all sources within 15 arcminutes of the field centres, and those sources in the region between 15 and 20 arcminutes with a CBI2 primary beam corrected flux greater than 20 mJy. The bright source detected in the CBI2 long-baseline map was not observed with ATCA, since it has a flux of 15.7$\pm$1.3 mJy at 843 MHz in the SUMSS catalogue and is located just over 15 arcminutes away from the field centre. The source has a rising spectrum between 0.846 GHz and 32 GHz with $\alpha = 0.26 \pm 0.09$. Of the 50 sources observed with ATCA at 32 GHz, two were detected with 5 σ significance, one in the main field and one in the lead reference field. Both are attenuated strongly by the CBI2 primary beam and are not apparent above the 3 σ level in the CBI2 maps.

In order to look for other sources that might have rising spectra, or that do not belong to the SUMSS population, the centres of the RXCJ0232.4-4420 main and reference fields were observed with ATCA at 4.80 GHz and 8.64 GHz. Three sources were detected above 5 σ at 4.80 GHz, but were not detected at

8.64 GHz. None of these sources are in the PMN catalogue since they have fluxes much lower than 30 mJy, however they are all in the SUMSS catalogue and therefore do not constitute an unknown population. Since they do not have significant flux at 32 GHz they are not projected out in the SZ analysis.

RXCJ0307.0-2840

It was not possible to obtain ATCA observations of the RXCJ0306.0-2840 fields, and there is no strong evidence of source contamination above the noise level in the CBI2 long-baseline map. Upon visual inspection of the full-resolution map and the real visibility profile, it appears that the cluster has not been detected at the position of the known X-ray centroid. There is also very little information on this cluster from the literature, with recent references from the X-ray observations by Zhang et al. (2006) and 610 MHz GMRT observations by Venturi et al. (2007).

In the absence of further source information I use the 4.85 GHz source survey from the PMN catalogue. There are nine PMN (4.85 GHz) sources within 30 arcminutes of the field centres for RXCJ0307.0-2840. Seven of these sources are located at radii greater than 28 arcminutes and so are likely to be significantly attenuated by the CBI2 primary beam. One source is at a distance of 21 arcminutes from the centre of the main field and coincides with the position of a 2 σ bright peak in the long-baseline map. The remaining source lies closer to the centre of the main field ($\sim$6.7 arcminutes) and is hence treated as a potential contaminant. The latter two sources are therefore projected out in the SZ analysis.

RXCJ0516.7-5430

Targeted observations at the positions of SUMSS sources were carried out using ATCA at 32 GHz, selecting all sources within 15 arcminutes of the field centres and all sources within 15-30 arcminutes with a CBI2 primary beam attenuated flux above 20 mJy. A total of 88 sources were observed in the main and reference fields, of which six were detected with 5 σ significance and projected out of the CBI2 data in the following analysis. One of these sources corresponds with the position of a bright 3 σ peak in the CBI2 long-baseline map. The other sources are further out from the centre of the fields and are therefore strongly attenuated by the CBI2 primary beam below the 3 σ level.

Surveys were also conducted of the field centres, using ATCA at 4.80 GHz and 8.64 GHz, to look for

possible sources with inverted spectra that were not observed at 32 GHz. A total of six sources were detected above the $5\,\sigma$ level in the field centres, of which five are in the SUMSS catalogue and were not detected above $5\,\sigma$ at 32 GHz. One source was detected at 4.80 GHz in the main field and does not exist in the SUMSS catalogue. Since it has a peak brightness less than $3\,\sigma$ at 8.64 GHz (equal to 3.6 mJy beam^{-1}), I assume that the contribution to the systematic uncertainty in the data at 31 GHz can be ignored in the SZ analysis.

RXCJ0528.9-3927

The CBI2 long-baseline map of this cluster shows no apparent evidence for the existence of bright sources in these fields at 31 GHz. However, to make sure that the thermal SZ effect is not significantly dominated by the presence of, for example a bright source in the centre of a reference field, the field centres were observed with ATCA at 4.80 GHz and 8.64 GHz. Three sources were detected in the main field, with peak brightness greater than $5\,\sigma$ at 4.80 GHz, but were not detected at 8.64 GHz. Since these sources potentially have rising spectra from 4.80 GHz to 26-36 GHz their positions are projected out in the CBI2 data.

RXCJ0532.9-3701

A bright source is detected in the CBI2 long-baseline map of this cluster. This source has a primary beam attenuated peak brightness greater than $5\,\sigma$, at a distance greater than the primary beam FWHM from the pointing centre. The source is likely to be significantly bright at 26-36 GHz, since it is located in the lead reference field, and will therefore be diluted when the fields are averaged during ground signal subtraction. The position of this source coincides with two bright sources in the NVSS catalogue ($S_{1.4} = 15620 \pm 468.6$ mJy), and has been observed at many other wavelengths (e.g. $S_{33} = 3400 \pm 200$ mJy, Bennett et al., 2003). Due to the known published brightness, and significance above the CBI2 map noise, the source position is projected out.

Two sources are detected from observations of the field centres at 4.80 GHz. The brighter of these two sources was not observed within the ATCA primary beam at 8.64 GHz, and since its spectral behaviour cannot be inferred, this source is projected out. The fainter source has a peak brightness that is less than 2.3 mJy beam^{-1} ($3\,\sigma$) at 8.64 GHz, and therefore has a falling spectrum over this frequency range. This

source can therefore be safely ignored in the analysis.

RXCJ1131.9-1955

There is no apparent point source contamination above the noise level of the CBI2 long-baseline map of this cluster. While it was not possible to obtain 32 GHz ATCA observations of the NVSS sources in these fields, I use radio observations of the central region of this cluster by Reid et al. (1999) to identify possible sources in the centre of the main field. Point source observations were conducted in that work within a radius of $\sim$5 arcminutes of the X-ray centroid, observed at 843 MHz (Mongolo Observatory Synthesis Telescope), 1.34, 2.4, 4.8 and 8.6 GHz (ATCA) and 1.4 GHz (NVSS). None of these sources have rising spectra over this frequency range, or have significant flux at the higher frequencies and are therefore not projected the following analysis.

Four sources from the PMN catalogue at 4.85 GHz lie within 30 arcminutes of the field centres, and appear to all coincide with the positions of NVSS sources. In the absence of further point source information at higher frequencies these sources are projected out.

RXCJ2308.3-0211

The lead reference field for CBI2 observations of RXCJ2308.3-02111 contains a significant source detection, with a primary beam attenuated brightness greater than 5 σ, at a radius of 27 arcminutes from the field centre. The flux of this point source is diluted in the CBI2 long-baseline map due to averaging of the reference fields. This source is also detected in targeted observations of the NVSS sources at 32 GHz using ATCA, with an integrated flux of 93.9$\pm$1.5 mJy. The selection criteria for ATCA observations were based on all NVSS sources with an integrated flux greater than 5 mJy within 15 arcminutes of the field centres, and with a CBI2 primary beam attenuated flux greater than 20 mJy at radii between 15 and 30 arcminutes. From these observations two further sources were detected with 5 σ significance in the main field with integrated fluxes $\sim$10 mJy. These three sources are projected in our SZ analysis.

In addition there is a possible source detection in the trail reference field, with a primary beam attenuated flux just greater than 3 σ in the CBI2 long-baseline map, that corresponds with the position of a known NVSS source. Since this source has an NVSS integrated flux of 7.5$\pm$0.5 mJy, and is a distance of

26 arcminutes from the field centre, it was not selected for observation with ATCA. However is possibly has significant flux in the CBI2 data and so is projected out in the following analysis.

RXCJ2337.6+0016

The main field for CBI2 observations of RXCJ2337.6+0016 contains a bright point source with a peak brightness greater than $4\,\sigma$, visible in both the long-baseline and full-resolution maps. This was the only source detected with $5\,\sigma$ significance in 32 GHz ATCA observations of the NVSS sources. The selection criteria for ATCA 32 GHz observations were the same as that used for the RXCJ2308.3-0211 fields. Since this source has an integrated flux of 21.8 ± 0.8 mJy at 1.4 GHz and 19.2 ± 1.4 mJy at 32 GHz, it is not bright enough to be in the PMN catalogue at 4.85 GHz.

6.3 X-ray data

In order to provide constraints on the physical cluster properties from joint fitting, I use published X-ray surface brightness data (0.5-2.0 keV energy band) obtained from XMM-Newton observations by Zhang et al. (2006). The data are treated in the same way as described in Chapter 5, using the Raymond-Smith plasma model Raymond & Smith (1977) to convert from the observed photon count rate to the inferred surface brightness. The neutral hydrogen column density and average spectral temperatures measured by Zhang et al. (2006) are used as input parameters in the plasma model. As in the case of the Bullet Cluster analysis in Chapter 5, the profile is truncated at radii smaller than 100 kpc, and when the signal-to-noise falls below $3\,\sigma$ at larger radii. The errors in the data are those published by Zhang et al. (2006), derived from the Poisson noise in the measurement and the background uncertainty, as well as a 10 % calibration error that is introduced as a marginalised nuisance parameter in the fit.

RXCJ	Alt. Name	Over-density	Radius (Mpc)	$YD_A^2(10^{-4}\mathrm{Mpc}^2)$	$T(\mathrm{keV})$	$M(10^{14}M_\odot)$	f_{gas}
0014.3-2022	A2744	2500	$0.57^{+0.04}_{-0.10}$	$0.41^{+0.33}_{-0.33}$	$10.4^{+1.7}_{-2.1}$	$2.8^{+1.5}_{-1.9}$	$0.104^{+0.038}_{-0.007}$
		500	$1.26^{+0.23}_{-0.10}$	$1.47^{+1.22}_{-0.64}$	$8.1^{+2.9}_{-1.7}$	$7.1^{+5.6}_{-3.5}$	$0.179^{+0.014}_{-0.049}$
		200	$1.91^{+0.45}_{-0.23}$	$2.21^{+1.73}_{-0.80}$	$7.5^{+2.9}_{-1.3}$	$10.9^{+6.5}_{-4.0}$	$0.207^{+0.020}_{-0.075}$
0043.4-2037	A2813	2500	$0.44^{+0.09}_{-0.07}$	$0.10^{+0.20}_{-0.03}$	$5.7^{+3.3}_{-1.6}$	$1.4^{+1.5}_{-0.7}$	$0.124^{+0.017}_{-0.040}$
		500	$0.95^{+0.25}_{-0.15}$	$0.32^{+0.43}_{-0.10}$	$5.1^{+2.6}_{-1.6}$	$3.2^{+3.3}_{-1.5}$	$0.149^{+0.088}_{-0.024}$
		200	$1.42^{+0.38}_{-0.24}$	$0.50^{+0.68}_{-0.19}$	$4.2^{+3.3}_{-1.0}$	$3.7^{+4.3}_{-1.4}$	$0.249^{+0.050}_{-0.098}$
0232.3-4420	-	2500	$0.67^{+0.05}_{-0.11}$	$0.54^{+0.39}_{-0.24}$	$10.3^{+4.6}_{-2.0}$	$8.5^{+5.6}_{-2.9}$	$0.079^{+0.026}_{-0.011}$
		500	$1.44^{+0.12}_{-0.24}$	$1.70^{+0.67}_{-0.85}$	$11.0^{+2.0}_{-3.2}$	$8.5^{+5.6}_{-2.9}$	$0.100^{+0.041}_{-0.017}$
		200	$2.10^{+0.44}_{-0.30}$	$2.28^{+1.40}_{-0.79}$	$10.0^{+1.6}_{-3.0}$	$14.0^{+6.8}_{-5.6}$	$0.114^{+0.061}_{-0.018}$
0307.0-2840	A3088	2500	$0.50^{+0.20}_{-0.03}$	$0.22^{+0.33}_{-0.10}$	$6.4^{+6.7}_{-1.4}$	$2.1^{+6.1}_{-2.2}$	$0.070^{+0.046}_{-0.011}$
		500	$1.10^{+0.36}_{-0.16}$	$0.60^{+0.72}_{-0.26}$	$5.8^{+4.8}_{-1.7}$	$4.8^{+6.1}_{-2.2}$	$0.094^{+0.075}_{-0.019}$
		200	$1.67^{+0.54}_{-0.26}$	$0.84^{+1.04}_{-0.35}$	$5.2^{+4.4}_{-1.4}$	$6.7^{+7.7}_{-3.2}$	$0.102^{+0.096}_{-0.014}$
0516.7-5430	-	2500	$0.63^{+0.04}_{-0.12}$	$0.34^{+0.43}_{-0.15}$	$13.5^{+2.2}_{-4.1}$	$4.3^{+1.6}_{-2.5}$	$0.066^{+0.016}_{-0.003}$
		500	$1.31^{+0.16}_{-0.19}$	$1.70^{+0.67}_{-0.85}$	$10.4^{+1.7}_{-2.9}$	$9.1^{+3.1}_{-4.3}$	$0.137^{+0.027}_{-0.023}$
		200	$1.97^{+0.25}_{-0.30}$	$2.28^{+1.40}_{-0.79}$	$8.6^{+1.6}_{-2.3}$	$12.2^{+4.7}_{-5.4}$	$0.168^{+0.060}_{-0.022}$
0528.9-3927	-	2500	$0.57^{+0.08}_{-0.09}$	$0.23^{+0.42}_{-0.05}$	$11.2^{+2.0}_{-3.7}$	$3.1^{+2.3}_{-1.3}$	$0.081^{+0.020}_{-0.012}$
		500	$1.30^{+0.22}_{-0.26}$	$1.44^{+0.43}_{-0.84}$	$8.9^{+2.4}_{-3.0}$	$8.8^{+3.4}_{-5.2}$	$0.128^{+0.032}_{-0.027}$
		200	$2.04^{+0.28}_{-0.48}$	$2.22^{+0.71}_{-1.27}$	$7.7^{+1.8}_{-2.7}$	$12.8^{+2.8}_{-7.5}$	$0.156^{+0.059}_{-0.059}$
0532.9-3701	-	2500	$0.55^{+0.04}_{-0.19}$	$0.09^{+0.28}_{-0.05}$	$4.3^{+5.1}_{-0.8}$	$1.0^{+2.8}_{-0.6}$	$0.089^{+0.057}_{-0.019}$
		500	$1.18^{+0.07}_{-0.42}$	$0.27^{+0.72}_{-0.12}$	$7.8^{+0.5}_{-4.6}$	$2.2^{+4.8}_{-1.1}$	$0.127^{+0.101}_{-0.054}$
		200	$1.76^{+0.27}_{-0.69}$	$0.44^{+1.05}_{-0.19}$	$3.6^{+4.1}_{-0.6}$	$3.2^{+5.9}_{-1.4}$	$0.256^{+0.123}_{-0.028}$
0658.5-5556	1E 0657-558	2500	$0.63^{+0.04}_{-0.05}$	$1.06^{+0.25}_{-0.29}$	$12.0^{+1.2}_{-1.8}$	$4.7^{+1.2}_{-1.7}$	$0.134^{+0.018}_{-0.018}$
		500	$1.49^{+0.08}_{-0.21}$	$3.33^{+0.55}_{-1.22}$	$10.9^{+1.0}_{-2.7}$	$13.4^{+1.4}_{-5.5}$	$0.172^{+0.050}_{-0.040}$
		200	$2.28^{+0.13}_{-0.29}$	$4.90^{+0.69}_{-1.53}$	$10.5^{+2.8}_{-0.7}$	$18.1^{+2.8}_{-6.4}$	$0.188^{+0.055}_{-0.025}$
1131.9-1955	A1300	2500	$0.50^{+0.10}_{-0.05}$	$0.34^{+0.22}_{-0.21}$	$8.7^{+3.3}_{-2.5}$	$2.4^{+1.7}_{-1.4}$	$0.106^{+0.024}_{-0.022}$
		500	$1.13^{+0.16}_{-0.19}$	$1.11^{+0.69}_{-0.69}$	$7.9^{+2.5}_{-2.7}$	$5.5^{+2.7}_{-3.2}$	$0.181^{+0.042}_{-0.039}$
		200	$1.71^{+0.23}_{-0.27}$	$2.03^{+0.79}_{-1.13}$	$7.2^{+2.4}_{-2.2}$	$7.8^{+3.1}_{-4.2}$	$0.237^{+0.053}_{-0.049}$
2038.3-0211	A2537	2500	$0.57^{+0.11}_{-0.07}$	$0.35^{+0.23}_{-0.24}$	$9.2^{+3.0}_{-2.3}$	$2.5^{+3.7}_{-1.1}$	$0.062^{+0.026}_{-0.008}$
		500	$1.17^{+0.37}_{-0.11}$	$0.72^{+0.68}_{-0.40}$	$7.0^{+3.4}_{-2.5}$	$6.3^{+7.4}_{-3.3}$	$0.079^{+0.054}_{-0.013}$
		200	$1.84^{+0.59}_{-0.50}$	$0.98^{+0.87}_{-0.44}$	$8.5^{+1.0}_{-3.6}$	$9.5^{+6.5}_{-5.9}$	$0.111^{+0.044}_{-0.047}$
2337.6+0016	A2631	2500	$0.76^{+0.04}_{-0.15}$	$0.44^{+0.71}_{-0.05}$	$14.8^{+2.2}_{-5.0}$	$7.8^{+2.4}_{-4.3}$	$0.061^{+0.026}_{-0.010}$
		500	$1.76^{+0.22}_{-0.46}$	$2.64^{+0.67}_{-1.54}$	$13.3^{+2.6}_{-5.0}$	$20.3^{+5.7}_{-12.7}$	$0.061^{+0.026}_{-0.010}$
		200	$2.69^{+0.49}_{-0.73}$	$3.81^{+1.30}_{-2.24}$	$13.5^{+1.9}_{-5.8}$	$29.8^{+13.5}_{-18.7}$	$0.057^{+0.042}_{-0.007}$

Table 6.3: Results of parametric model fitting to joint CBI2 SZ and X-ray surface brightness REFLEX-DXL data. Column 1 gives the REFLEX catalogue name; column 2 the alternative name; column 3 the over-density; column 4 the physical radius; column 5 the integrated comptonization; column 6 the mass-weighted average temperature; column 7 the total mass; column 8 the gas mass fraction.

6.4 Results and Discussion

Joint parametric fits are performed to the CBI2 and X-ray surface brightness data using the entropy model and the results are summarised in Table 6.3. The global quantities are derived by integrating over the spherical volume within each scaled radius, and in the case of M, Y and $f_{\rm gas}$ this is simply just the total enclosed value. However when quoting a global temperature estimate one must choose a suitable averaging scheme. In the case of temperatures derived from the thermal SZ effect and X-ray surface brightness, it is appropriate to quote the mass-weighted value, since the SZ signal is dependent upon the product of the line-of-sight electron temperature and density. In which case the global temperature is defined by the following expression

$$T \equiv \frac{\int_0^r T_{\rm e} n_{\rm e} r'^2 {\rm d}r'}{\int_0^r n_{\rm e} r'^2 {\rm d}r'}, \tag{6.1}$$

where r is the outer radius equal to r_{2500}, r_{500} or r_{200}. In the following section I discuss the results of scaling relations between these global quantities constrained by the CBI2 and X-ray surface brightness data and the implications for the cluster physics.

6.4.1 Predictions and Deviations from the Self-similar model

Assuming that a galaxy cluster can be modelled based purely on gravitational collapse, with no heating or cooling from other sources, then it is expected that the physical quantities will behave in a self-similar way (Kaiser, 1986; Navarro et al., 1995). For a galaxy cluster in virial equilibrium, the average kinetic ($E_{\rm K}$) and gravitational potential ($E_{\rm G}$) energies are related as follows

$$E_{\rm K} = -\frac{1}{2} E_{\rm G}, \tag{6.2}$$

and hence the temperature and total mass are related by

$$k_{\rm B} T \propto \frac{GM\rho}{R}, \tag{6.3}$$

where T is the average gas temperature, ρ the density, M the total mass and R the radius. It is typically appropriate, when deriving the scaling relations between cluster properties, to integrate within a radius that

has a mean enclosed density equal to a fixed multiple of the universal critical density, e.g. $\bar{\rho}(< r_{200}) = 200\rho_{\rm crit}$. This is usually done in order to provide direct comparison with theoretical work, where the outer radius of a virialised system is defined by an enclosed density that is a redshift and cosmology dependent factor of the critical density. Bryan & Norman (1998) find that the virial density contrast $\Delta_{\rm v}$ as a function of redshift, in the case of a flat Universe, is given by the following expression

$$\Delta_{\rm v} \equiv \frac{\bar{\rho}_{\rm v}}{\rho_{\rm crit}} = 18\pi^2 + 82(\Omega_{\rm z} - 1) - 39(\Omega_{\rm z} - 1)^2, \tag{6.4}$$

where $\Omega_{\rm z} = \Omega_{\rm M}(1+z)^3/E(z)^2$. The factor $E(z)$ defines the redshift dependency of the Hubble parameter and is given by $E(z)^2 = \Omega_{\rm M}(1+z)^3 + (1-\Omega_{\rm M}-\Omega_\Lambda)(1+z)^2 + \Omega_\Lambda$. For example, in the special case of an Einstein-de Sitter Universe with no curvature or cosmological constant, the mean enclosed density of all virialised clusters is $\bar{\rho}_{\rm v} = 18\pi^2\rho_{\rm crit}$. It is noted by Maughan et al. (2006) that ideally one would wish to calculate all cluster global properties within the virial radius as a function of radius, thus providing the best comparison with redshift independent self-similarity. However, most current experiments are unlikely to reach the sensitivity required to provide model independent estimates to these radii, and so most scaling relations are calculated at smaller radii and at a higher fraction of the critical density (see e.g. Vikhlinin et al., 2006; Zhang et al., 2008; Bonamente et al., 2008; Pratt et al., 2009). When working at smaller scaled radii one should technically include the redshift dependence of the virial density, and work to an over-density density given by

$$\Delta(z) = \Delta(0)\frac{\Delta_{\rm v}(z)}{\Delta_{\rm v}(0)}. \tag{6.5}$$

For simplicity, and direct comparison with other work, the cluster global properties in the work are calculated to fixed over density values at r_{2500}, r_{500} and r_{200}. Therefore the total mass scales with radius as

$$M \propto E(z)^2 R^3, \tag{6.6}$$

where the redshift dependency results from the evolution of the critical density. The relationship between the total mass and temperature is then given by

$$M \propto E(z)^{-1} T^{3/2}. \tag{6.7}$$

As explained in both the introduction to this chapter and this thesis, it is vitally important to understand how the observable SZ effect scales with the intrinsic physical properties of clusters. The integral of the thermal SZ effect, over the volume of the cluster, is representative of the total enclosed thermal energy. The integrated comptonization parameter (Y) is defined by the following equation

$$YD_{\rm A}^2 = \int_V n_{\rm e} \frac{k_{\rm B} T_{\rm e}}{m_{\rm e} c^2} \sigma_{\rm T} {\rm d}V, \tag{6.8}$$

where $D_{\rm A}$ is the angular diameter distance to the cluster. Under the assumption that $\langle T_{\rm e} \rangle \sim T$, and using the expression relating mass and temperature in Equation 6.7, the integrated comptonization scales as

$$\begin{aligned} YD_{\rm A}^2 &\propto E(z)^{-1} f_{\rm gas} T^{5/2} & (6.9)\\ &\propto E(z)^{2/3} f_{\rm gas} M^{5/3} & (6.10)\\ &\propto E(z)^{2/3} f_{\rm gas}^{-2/3} M_{\rm gas}^{5/3}. & (6.11) \end{aligned}$$

Clearly if $f_{\rm gas}$ is a constant for all clusters over the sample range, then we have the following simple scaling relations between the SZ observable and the physical quantities, where $YD_{\rm A}^2 \propto E(z)^{-1} T^{5/2} \propto E(z)^{2/3} M^{5/3} \propto E(z)^{2/3} M_{\rm gas}^{5/3}$. However the introduction of both cooling and non-gravitational pre-heating processes will change the amount of hot gas within a cluster, as a function of mass and temperature, and therefore alter these simple relations. In cooling the cluster gas through radiative processes, the fraction of hot gas is reduced, while the observed temperature increases due to the removal of cooled ICM from the hot gas phase. Hydrodynamical simulations show that the radiative cooling process is more efficient for lower-mass clusters, where the reduction in $f_{\rm gas}$ dominates over the increase in temperature of the remaining gas, and we would therefore expect to see a steeper slope in the $YD_{\rm A}^2 - M$ relation (da Silva et al., 2004). In addition pre-heating at high redshift, caused by the injection of energy from non-gravitational sources such as active galactic nuclei and star formation, results in expelling some of the hot gas from the cluster and reducing $f_{\rm gas}$. da Silva et al. (2004) demonstrate that the effect of heating is most pronounced for low-mass clusters, while having less influence on the the higher-mass clusters ($M \gtrsim 10^{14} M_{\odot}$), again steepening the $YD_{\rm A}^2 - M$ relation. Non-gravitational processes are expected to have an even stronger effect on the observed X-ray luminosity scaling relations, due to the dependency on the square of the gas density. The dependency between the X-ray

y	x	Over-density	a	b	χ^2
$\frac{YD_A^2E(z)}{10^{-4}\,\mathrm{Mpc}^2}$	$\frac{T}{\mathrm{keV}}$	2500	$10^{-(3.22\pm1.23)}$	2.92 ± 1.16	0.40
		500	$10^{-(2.62\pm1.12)}$	2.96 ± 1.13	0.18
		200	$10^{-(1.83\pm0.78)}$	2.43 ± 0.81	0.26
$\frac{YD_A^2E(z)}{10^{-4}\,\mathrm{Mpc}^2}\frac{f_B}{f_{gas}}$	$\frac{T}{\mathrm{keV}}$	2500	$10^{-(2.32\pm1.02)}$	2.28 ± 0.97	0.16
		500	$10^{-(2.61\pm1.12)}$	3.07 ± 1.13	0.10
		200	$10^{-(2.14\pm0.83)}$	2.80 ± 0.85	0.06
$\frac{YD_A^2E(z)^{-3/2}}{10^{-4}\,\mathrm{Mpc}^2}$	$\frac{M}{10^{14}M_\odot}$	2500	$10^{-(1.25\pm0.40)}$	1.58 ± 0.62	0.27
		500	$10^{-(1.13\pm0.41)}$	1.36 ± 0.41	0.12
		200	$10^{-(1.13\pm0.45)}$	1.34 ± 0.40	0.17
$\frac{YD_A^2E(z)^{-3/2}}{10^{-4}\,\mathrm{Mpc}^2}\frac{f_B}{f_{gas}}$	$\frac{M}{10^{14}M_\odot}$	2500	$10^{-(0.85\pm0.35)}$	1.32 ± 0.55	0.08
		500	$10^{-(1.10\pm0.43)}$	1.46 ± 0.43	0.04
		200	$10^{-(1.33\pm0.49)}$	1.55 ± 0.44	0.02
$\frac{ME(z)}{10^{14}M_\odot}$	$\frac{T}{\mathrm{keV}}$	2500	$10^{-(1.22\pm0.73)}$	1.79 ± 0.69	0.06
		500	$10^{-(1.04\pm0.82)}$	2.11 ± 0.82	0.13
		200	$10^{-(0.48\pm0.55)}$	1.76 ± 0.58	0.05

Table 6.4: Scaling relations of the form $y = ax^b$, from combined CBI2 SZ and X-ray surface brightness data. Errors represent the 68 % interval.

scaling relations and the gas mass distribution was recently studied in detail by Pratt et al. (2009, 2010) and Arnaud et al. (2009), using XMM-Newton observations of 33 clusters in the REXCESS sample at $z \sim 0.15$. They find a strong dependency on the complex physical processes in the core, that particularly effect low mass and low temperature systems, and therefore support the theory that baryonic gas is removed from the cores of these clusters.

6.4.2 Scaling Relations from combined CBI2 and XMM-Newton data

Empirical scaling relations between the derived global quantities are obtained by fitting a simple parametric power law of the form $y = ax^b$ using linear regression within logarithmic space (see e.g. Benson et al., 2004; Bonamente et al., 2008; Marrone et al., 2009). It is assumed that the scatter in the data is dominated by statistical error, rather than intrinsic scatter from inherent differences within the cluster sample. In which

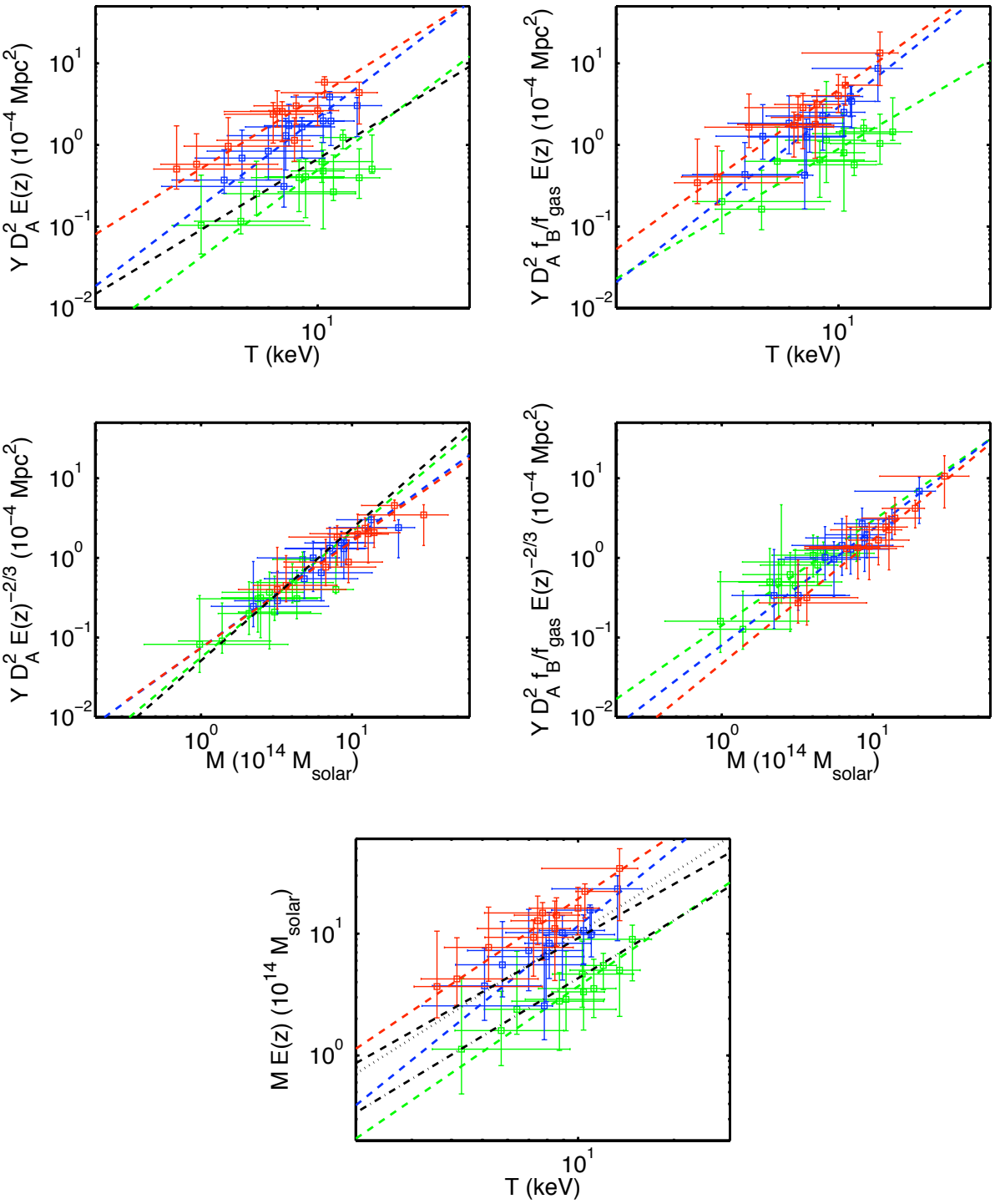

Figure 6.3: Scaling relations of the form $y = ax^b$, from combined CBI2 SZ and X-ray surface brightness data. Errors represent the 68 % interval. The colours represent data at r_{2500} (*green*), r_{500} (*blue*) and r_{200} (*red*) and the corresponding coloured dashed lines represent the best-fit power-law to the data. The black lines in the $YD_A^2 - T$ and $YD_A^2 - M$ relations represent the equivalent results from Bonamente et al. (2008) at r_{2500} (*dashed*). The black lines in the $M - T$ relation represent results from Vikhlinin et al. (2006) at r_{2500} (*dashed-dotted*) and r_{500} (*dashed*) and from Zhang et al. (2008) at r_{500} (*dotted*).

case the χ^2 statistic to be minimised is given by

$$\chi^2 = \frac{1}{N-2}\sum_{i=1}^{N}\frac{(\log(y_i) - b\log(x_i) - a)^2}{\sigma^2_{\log(y_i)} + b^2\sigma^2_{\log(x_i)}}, \tag{6.12}$$

where $\sigma_{\log(x)}$ and $\sigma_{\log(y)}$ are the errors in the logarithms of the variables x and y respectively. They are related to the linear error by

$$\sigma_{\log(x)} = \frac{(\sigma_x^+ + \sigma_x^-)}{2x}\log(e), \tag{6.13}$$

where σ_x^+ and σ_x^- are the positive and negative errors respectively in the variable x . The results of power law fits to the scaled quantities are summarised in Table 6.4 and Figure 6.3. The low χ^2 values indicate that the scatter in the data is dominated by the experimental noise, rather than intrinsic scatter that results from the underlying non-gravitational processes in the cluster gas.

Scaling relations are derived for the integrated comptonization YD_A^2, versus both the mass-weighted temperature T and the total mass M, within scaled radii corresponding to each of the three over-densities. In both cases the power-law values are consistent with the expected values from the self-similar model within the quoted 68 % error interval. However it is apparent that the scatter in the data is dominated by the measurement error, and therefore these relations can be significantly improved upon by the inclusion of more clusters from the total CBI2 sample. The $YD_A^2 - T$ and $YD_A^2 - M$ relations at r_{2500} are compared with those constructed from BIMA/OVRO and Chandra data by Bonamente et al. (2008). In that work, YD_A^2 is derived by integrating the comptonization parameter over the infinite cylinder, bounded by r_{2500} and the plane of the sky. Bonamente et al. (2008) find that the spherical and cylindrical volumes bounded by r_{2500} differ on average by a correction factor of ~ 2. Hence I divide their scaling relations by this correction factor in order to perform a direct comparison between the normalisation parameters, and calculate an equivalent normalisation and power-law of $\log(a) = -2.54 \pm 0.22$ and $b = 2.37 \pm 0.23$ for the $YD_A^2 - T$ relation, and $\log(a) = 1.26 \pm 0.20$ and $b = 1.66 \pm 0.20$ for $YD_A^2 - M$ relation. The scaling relations derived in this work are therefore consistent with those of Bonamente et al. (2008) within the quoted 68 % errors. In order to study whether there is a strong effect on the scaling relations from non-constant values of the gas mass fraction at each over-density, the YD_A^2 relations are re-scaled by the appropriate factor of $f_{\rm gas}/f_{\rm B}$, where $f_{\rm B}$ is the universal baryon fraction measured by Dunkley et al. (2009). There is no significant evidence from the

data that this correction improves the comparison between the derived power-law values and those predicted from self-similarity.

The $M-T$ relation is also constructed at each scale radius, and is found to have a power-law behaviour that is consistent, within the 68 % error, with that predicted from self-similarity. Vikhlinin et al. (2006) derive an equivalent relation between the total mass and the average mass-weighted temperature using Chandra data for 13 low-redshift and relaxed clusters. They obtain equivalent normalisation and power-law values of $\log(a) = -0.95 \pm 0.05$ and $b = 1.58 \pm 0.07$ at r_{2500}, and $\log(a) = -0.51 \pm 0.03$ and $b = 1.47 \pm 0.10$ at r_{200}, both of which are consistent with the results in this work. Note that in that work the average temperature was calculated within a fixed radial window of $70\,\mathrm{kpc} - r_{500}$ for deriving the $M-T$ relation at both r_{2500} and r_{500}. The relation derived here is also compared with that constructed from the LoCuSS sample by Zhang et al. (2008), where the global temperatures are defined by the volume average over the radial range 0.2 - 0.5 r_{500}, and are found to be similar to the spectroscopic temperature calculated over this radius. Vikhlinin et al. (2006) find that the mass-weighted and spectroscopic temperatures differ by a factor of approximately 1.1 over a similar radial range, and so this correction is used for the comparison with Zhang et al. (2008). The equivalent normalisation and power-law values from Zhang et al. (2008) are therefore found to be $\log(a) = -0.51 \pm 0.22$ and $b = 1.654 \pm 0.256$, and are again consistent with the results presented in this work.

6.4.3 The gas mass fraction

Figure 6.4 shows the gas mass fraction as a function of both the total mass and gas mass for each of the three over-density values. Results from simulations (e.g. Kravtsov et al., 2005) and observations (e.g. Vikhlinin et al., 2006) suggest that the gas mass fraction should increase with cluster mass. However it is clear from the available sensitivity of the data presented here that one cannot claim whether the gas mass fraction is significantly dependent upon the cluster mass. This is consistent with the results in the previous section, which show that the power-law values of the $YD_{\mathrm{A}}^2 - M$ and $YD_{\mathrm{A}}^2 - T$ scaling relations are not significantly altered, within the error, by correcting for the gas mass fraction.

At radii equal to an over-density of 2500, the weighted-average of the gas mass fraction is $f_{\mathrm{gas},2500} = 0.080 \pm 0.005$. This result is relatively low compared to the values of 0.117 ± 0.002 and 0.116 ± 0.005

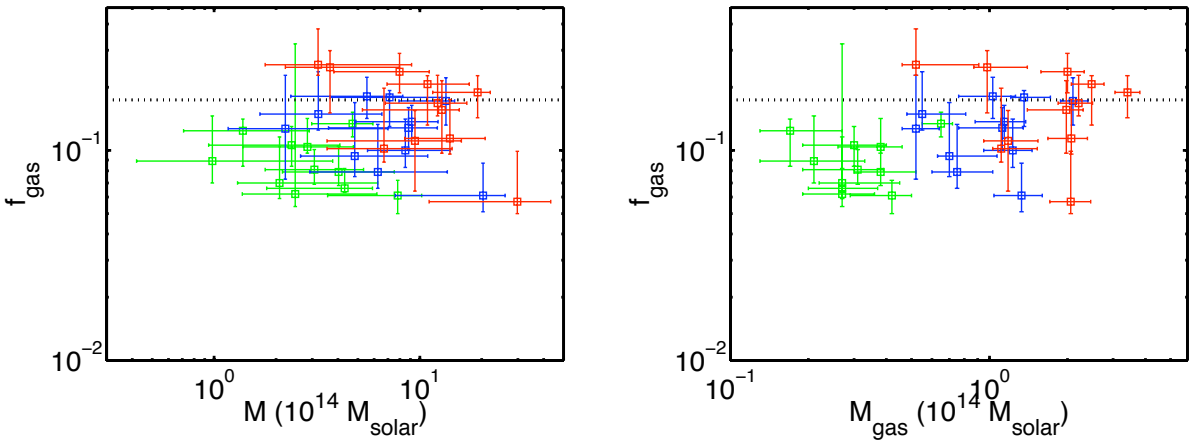

Figure 6.4: The gas mass fraction as a function of the total mass (*left*) and gas mass (*right*). Errors represent the 68 % interval. The colors represent data at r_{2500} (*green*), r_{500} (*blue*) and r_{200} (*red*) and the black dotted lines represent the universal baryon fraction value from WMAP 5-year data (Dunkley et al., 2009).

obtained using Chandra X-ray data by Allen et al. (2004) and SZ data by LaRoque et al. (2006) respectively, but is more consistent with the lower value of 0.091 ± 0.002 obtained by Vikhlinin et al. (2006) from Chandra data. This inconsistency suggests that further investigation of the gas mass fraction at smaller radii is required, since non-gravitational processes are expected to cause a large scatter in measured gas fraction values. At larger radii, defined by an over-density of 500, the estimated average gas mass fraction from the sample presented here is equal to $f_{\rm gas,500} = 0.112 \pm 0.010$. This result is consistent with values given in the literature, including a value of 0.121 ± 0.004 obtained from XMM-Newton observations of the LoCuSS sample by Zhang et al. (2008), 0.105 ± 0.002 from Chandra observations by Vikhlinin et al. (2006), and $0.116^{+0.013}_{-0.016}$ from SZ and X-ray data by Grego et al. (2001), who extrapolate to r_{500} using relations calibrated from numerical simulations.

At the largest enclosed radii, where the properties of the cluster gas are expected to be dominated by gravitational processes, the baryon fraction is predicted to converge to the universal value as measured by CMB power-spectrum experiments. However some of the baryonic content of the cluster is contained within cooler stellar material, and so the measured gas mass fraction at a given scale radius is likely to be less than the total baryonic fraction. The weighted-average of the gas mass fraction at r_{200} from the work presented here is $f_{\rm gas,200} = 0.136 \pm 0.013$, and the current best measured universal baryon fraction value, from WMAP 5-year data, is equal to $f_{\rm B} = 0.171 \pm 0.023$ (Dunkley et al., 2009). Therefore the inferred average stellar mass

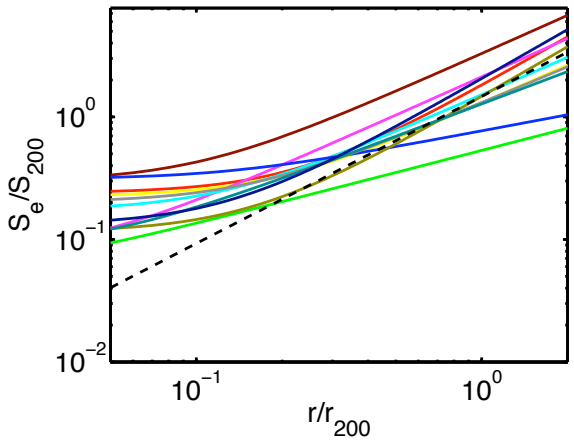

Figure 6.5: Best-fit scaled entropy profiles from parametric fits to the CBI2 SZ and X-ray surface brightness data. The black dashed line represents the average profile from non-radiative simulations by Voit et al. (2005).

fraction, for the sample presented in this work, is estimated to be $f_{\rm gal} = 0.035 \pm 0.026$ or $(0.26 \pm 0.19) f_{\rm gas}$. This value is consistent with studies of the Coma cluster by White et al. (1993) ($f_{\rm gal} = 0.02 \pm 0.01 h_{50}^{-1}$) and from simulations by Kravtsov et al. (2005) ($f_{\rm gal} \approx 0.15 f_{\rm gas}$).

6.4.4 Scaled Entropy profiles

The gas entropy is strongly dependent upon the thermal history of the cluster gas and is therefore a good indicator of the underlying processes that have led to the observed physical state of the cluster. In particular one would expect that observed entropy profiles have divergent behaviour at small radii, where non-gravitational processes (such as heating and cooling) are expected to dominate, and at larger radii follow a self-similar power-law behaviour (see e.g. Ponman et al., 2003; Kay, 2004; Voit et al., 2005; Mitchell et al., 2009). Figure 6.5 shows the best-fit scaled entropy profiles at $r \gtrsim 100\,$Mpc from parametric fits to the CBI2 SZ and XMM-Newton surface brightness data. The radius is scaled to the best estimate of r_{200}, and the entropy is scaled to a characteristic global value S_{200} (Voit et al., 2005), given by the following expression

$$S_{200} = 362\,{\rm keVcm}^2 \left(\frac{T_{200}}{1\,{\rm keV}}\right) \left[\frac{H(z)}{H_0}\right]^{-4/3} \left(\frac{\Omega_{\rm M}}{0.3}\right)^{-4/3}, \qquad (6.14)$$

where

$$T_{200} \equiv \frac{GM_{200}\mu m_{\rm p}}{2r_{200}}, \tag{6.15}$$

and M_{200} and r_{200} are the best estimates of these quantities respectively. The scaled profiles are compared to the non-radiative power-law used in simulations by Mitchell et al. (2009), and predicted from both AMR and SPH simulations by Voit et al. (2005), given by the following form

$$\frac{S_{\rm e}(r)}{S_{200}} = 1.47\left(\frac{r}{r_{200}}\right)^{1.22}. \tag{6.16}$$

The scaled entropy profiles are found to be on average larger than the predicted non-radiative profile over all radii until $r \sim r_{200}$, converging to the non-radiative case at the largest radii. The weighted mean of the power-law parameter for the sample is $\alpha = 0.56 \pm 0.01$, corresponding to a power-law behaviour of $S_{\rm e}(r) \propto r^{1.12\pm0.02}$ at the largest radii. This is consistent with the most recent studies of cluster entropy profiles that include measured power-laws of 0.98 (with a wide spread in values) from XMM-Newton data by Pratt et al. (2010), and 1.21 ± 0.39 from Chandra data by Cavagnolo et al. (2009). The range of values for the power-law behaviour of the large-scale entropy is much greater than the measurement uncertainty, varying from $\approx 0.6 - 1.4$, suggesting an intrinsic scatter due to underlying physical differences. This spread in values warrants further investigation in future work, including a more in-depth investigation of the two outlier clusters RXCJ0516.7-5430 and RXCJ0528-3927, with lower than average scaled entropy at large radii.

6.4.5 Direct comparison with results from X-ray observations

The results of scaled quantities from this work are compared with those derived by Zhang et al. (2006) for the same clusters, from X-ray surface brightness and spectral data. For the purposes of direct comparison, the scaled quantities are calculated using the same method as Zhang et al. (2006), by integrating within a fixed physical radius equal to the value of r_{500} given in that work. The average temperature is calculated by taking a volume average over the radius range from 0.1 - 0.5 r_{500}. In order to perform a quantitative analysis, a simple linear relationship of the form $y = cx$ is fit to the scaled quantities by minimising the χ^2 statistic

y	x	a	χ^2
$\frac{T}{\mathrm{keV}}$	$\frac{T_{Z06}}{\mathrm{keV}}$	1.12 ± 0.08	0.56
$\frac{M}{10^{14} M_\odot}$	$\frac{M_{Z06}}{10^{14} M_\odot}$	1.11 ± 0.13	0.24
f_{gas}	$f_{\mathrm{gas,Z06}}$	0.98 ± 0.08	0.11

Table 6.5: Comparison between derived quantities in this work (column 1) and those from X-ray observations (column 2) by Zhang et al. (2006), by fitting a straight line of the form $y = ax$. Errors represent the 68 % interval.

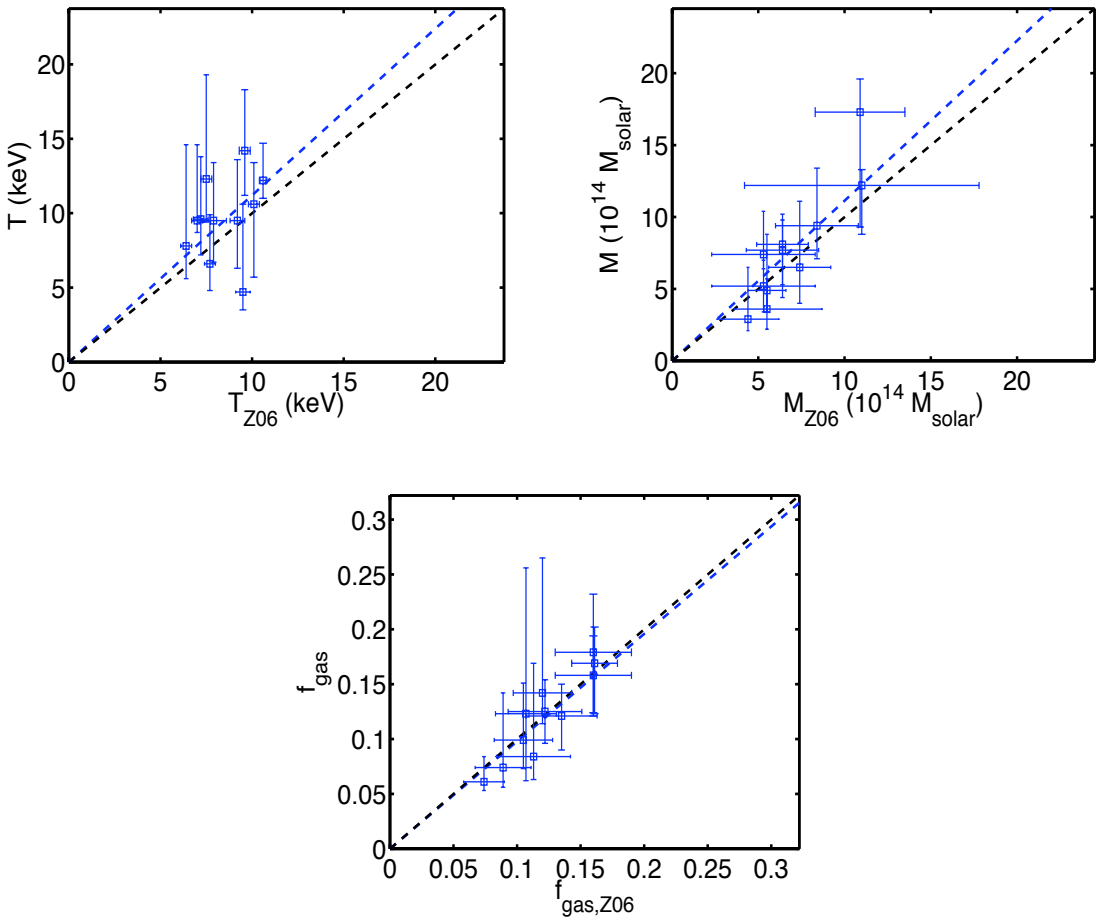

Figure 6.6: Comparison between scaled quantities in this work and those derived from X-ray observations by Zhang et al. (2006). The *blue dashed line* represents the best fitting straight line to the data. The *black dotted line* represents the case where $y = x$.

given by

$$\chi^2 = \frac{1}{N-1}\sum_{i=1}^{N}\frac{(y_i - cx_i)^2}{\sigma_{y_i}^2 + c^2\sigma_{x_i}^2}, \tag{6.17}$$

where σ_y and σ_x are the errors in the variables y and x respectively (these are derived from the mean of the positive and negative errors). The results of these fits are summarised in Table 6.5 and Figure 6.6. In the case that the results of this work and Zhang et al. (2006) agree, one would expect that the estimated values for the slope parameter a would be consistent with unity. Deviation from unity would most likely be caused by systematics resulting from, for example, the differences in the models used or the assumptions required in interpreting the SZ and X-ray spectral data. The results here show that the estimated global quantities are in general agreement with those derived by Zhang et al. (2006). The most discrepant result arises between the estimated global temperatures. This difference is only slightly greater than $1\,\sigma$ and is not unexpected, given that the SZ and spectral X-ray measurements are sensitive to different angular scales of the cluster and are dependent upon different powers of n_e.

6.4.6 Y_{SZ} Scaling Relations

It is instructive to study how the observable SZ effect can be used to measure the scaled global properties of clusters, since this is the ultimate goal of large-scale SZ surveys. Therefore scaling relations are constructed between $Y_{SZ}D_A^2$, constrained purely by the CBI2 SZ data, and the scaled quantities from joint CBI2 SZ and XMM-Newton surface brightness data. Since the CBI2 SZ data on their own provide negligible constraint on the total density profile of the cluster, the value of $Y_{SZ}D_A^2$ is calculated within a spherical volume bounded by fixed angular radii. For a sample of clusters at $z \sim 0.3$, r_{500} and r_{200} correspond approximately to 4.5 and 7.5 arcminutes respectively, and so $Y_{SZ}D_A^2$ is calculated by integrating within these radii.

$Y_{SZ}D_A^2$ is first compared with the YD_A^2 values derived from the joint data set. In order to perform a quantitative analysis, a linear fit is made to the data, of the form $y = ax$, and the results are shown in Table 6.6 and in Figure 6.7. These results show that the integrated comptonization at 4.5 and 7.5 arcminutes, constrained by CBI2 data only, are consistent with that at r_{500} and r_{2500} from joint analysis of the CBI2 and XMM-Newton data sets. However one cluster (RXJ0532.9-3701) is a significant outlier in this relation and suggests an inconsistency between the measured SZ signal and X-ray surface brightness measurements, which will be investigated in further detail in future work.

y	x	Over-density	a	χ^2
$\frac{Y_{SZ,4.5}D_A^2}{10^{-4}\,\mathrm{Mpc}^2}$	$\frac{YD_A^2}{10^{-4}\,\mathrm{Mpc}^2}$	2500	3.37 ± 0.54	0.64
		500	0.91 ± 0.12	0.83
		200	0.62 ± 0.08	0.83
$\frac{Y_{SZ,7.5}D_A^2}{10^{-4}\,\mathrm{Mpc}^2}$	$\frac{YD_A^2}{10^{-4}\,\mathrm{Mpc}^2}$	2500	5.29 ± 1.03	1.13
		500	1.33 ± 0.19	1.22
		200	0.90 ± 0.13	1.25

Table 6.6: Comparison between the integrated SZ effect within 4.5 and 7.5 arcminutes from CBI2 data only (column 1) and from combined CBI2 and X-ray surface brightness data (column 2), by fitting a straight line of the form $y = ax$. Errors represent the 68 % interval.

y	x	Over-density	a	b	χ^2
$\frac{Y_{SZ,4.5}D_A^2}{10^{-4}\,\mathrm{Mpc}^2}$	$\frac{T}{\mathrm{keV}}$	2500	$10^{-(5.35\pm3.66)}$	5.27 ± 3.48	0.58
		500	$10^{-(3.17\pm2.04)}$	3.39 ± 2.06	0.34
		200	$10^{-(3.77\pm2.36)}$	4.11 ± 2.46	0.65
$\frac{Y_{SZ,4.5}D_A^2}{10^{-4}\,\mathrm{Mpc}^2}$	$\frac{M}{10^{14}\,M_\odot}$	2500	$10^{-(1.17\pm0.97)}$	2.21 ± 1.56	0.45
		500	$10^{-(1.42\pm0.75)}$	1.60 ± 0.74	0.55
		200	$10^{-(1.73\pm0.84)}$	1.67 ± 0.74	0.55
$\frac{Y_{SZ,7.5}D_A^2}{10^{-4}\,\mathrm{Mpc}^2}$	$\frac{T}{\mathrm{keV}}$	2500	$10^{-(7.21\pm8.05)}$	7.20 ± 7.65	0.60
		500	$10^{-(4.33\pm3.10)}$	4.78 ± 3.13	0.38
		200	$10^{-(4.58\pm3.25)}$	5.15 ± 3.39	0.64
$\frac{Y_{SZ,7.5}D_A^2}{10^{-4}\,\mathrm{Mpc}^2}$	$\frac{M}{10^{14}\,M_\odot}$	2500	$10^{-(0.87\pm0.72)}$	2.03 ± 1.15	0.38
		500	$10^{-(1.66\pm0.95)}$	2.02 ± 0.94	0.58
		200	$10^{-(2.27\pm1.27)}$	2.31 ± 1.11	0.62

Table 6.7: Scaling relations of the form $y = ax^b$, between the integrated SZ effect within 4.5 and 7.5 arcminutes from CBI2 data only (column 1) and scaled quantities from combined CBI2 and X-ray surface brightness data (column 2). Errors represent the 68 % interval.

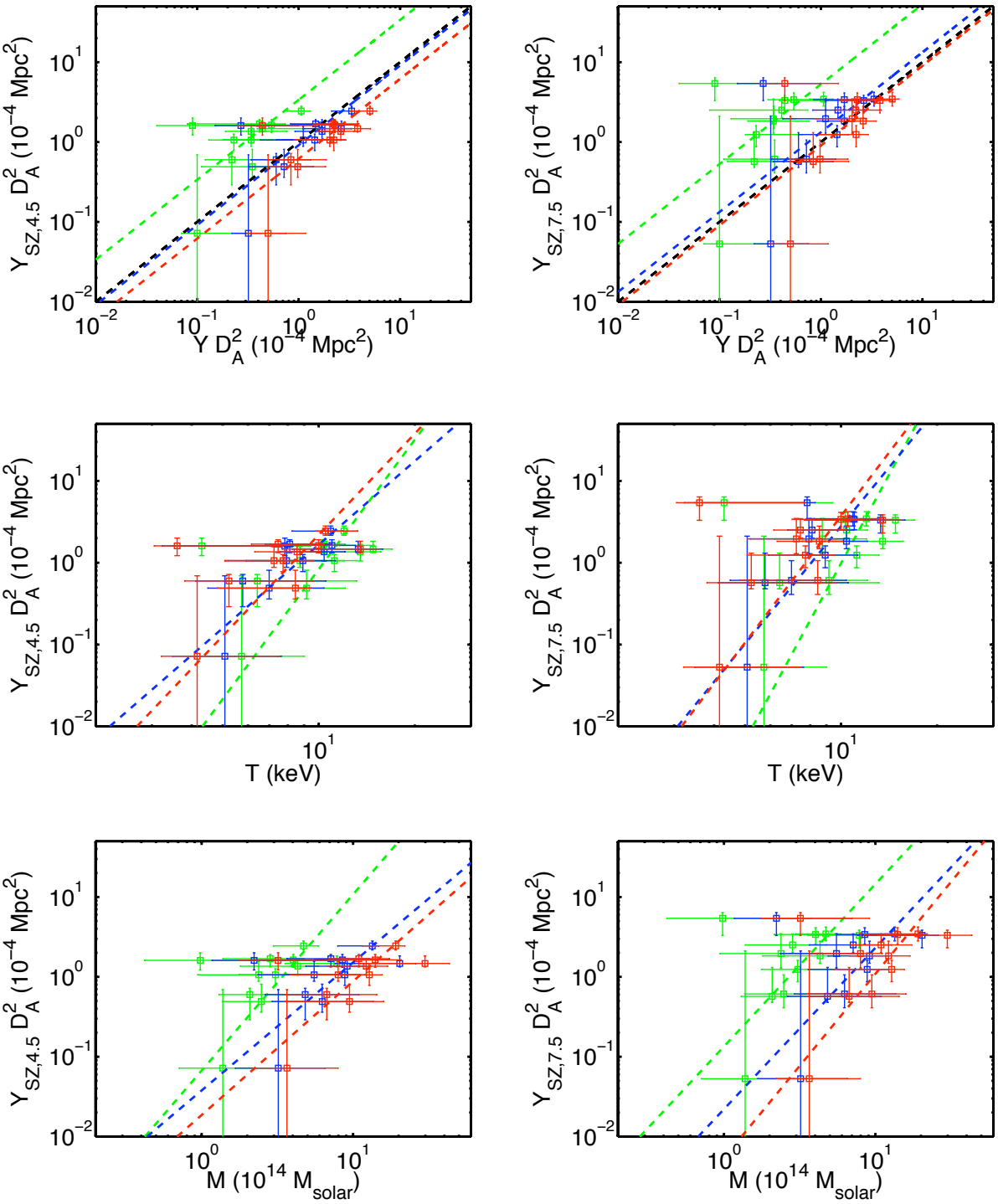

Figure 6.7: Scaling relations between the integrated SZ effect within 4.5 and 7.5 arcminutes from CBI2 data only and scaled quantities from combined CBI2 and X-ray surface brightness data. Errors represent the 68 % interval. The colours represent data at r_{2500} (*green*), r_{500} (*blue*) and r_{200} (*red*) and the corresponding coloured dashed lines represent the best-fit power-law to the data. Please refer to the text for details.

The scaling relations $Y_{SZ}D_A^2 - M$ and $Y_{SZ}D_A^2 - T$, are derived using the same linear regression method as described in Section 6.4.2. The results of these fits are shown in Table 6.7 and Figure 6.7. The low χ^2 values indicate that the scatter in the data is predominantly caused by the statistical error from the measurement. The $Y_{SZ}D_A^2 - T$ and $Y_{SZ}D_A^2 - M$ relations both have normalisations and power-law values that are significantly non-zero above the 68 % error, and are therefore constructive towards obtaining calibrated relations between the observable SZ effect and the intrinsic global properties of the cluster. However, it is intended that statistical error in these scaling relations will be improved, by including data from CBI2 observations of clusters from both the REXCESS sample (Böhringer et al., 2007) and individual known bright clusters with existing X-ray data.

6.5 Summary

In this chapter I have presented preliminary scaling relations between the integrated comptonization (a measure of the total energy of the cluster) and the average temperature and total mass, measured out to a large radius of r_{200}. These were constructed using CBI2 SZ and XMM-Newton surface brightness data from 11 clusters in the REFLEX-DXL sample ($z \sim 0.3$). The derived scaling relations are consistent with the self-similar model within the error. However it is expected that they can be significantly further constrained by including data from other clusters observed with CBI2, such as the REXCESS sample at $z \sim 0.15$.

Chapter 7

Current and Future Work

7.1 The Complete Cluster Sample

Over 40 clusters were observed with the CBI2 experiment, of which 11 are discussed in this thesis. In the near future it is intended that the analysis outlined here will be applied to the whole cluster sample. In this section I will describe the remaining clusters to be studied and the important science that can be obtained by their analysis.

7.1.1 The REXCESS Sample

The REXCESS sample is a relatively low redshift ($z \leq 0.2$) sub-sample of the REFLEX survey, with X-ray luminosities in the range $0.407 - 20 \times 10^{44}\, h_{50}^{-2}\mathrm{ergs}^{-1}$ in the 0.1-2.4 keV rest frame band (Böhringer et al., 2007). Ten of the most X-ray bright clusters from this sample will be added to help constrain further the SZ scaling relations out to r_{200} from CBI2 observations. The combination of CBI2 data from the $z \sim 0.3$ REFLEX-DXL and $z \sim 0.15$ REXCESS samples will also provide a study of possible redshift evolution in the SZ scaling relations. The scaling relations between the X-ray luminosity, the total mass and temperature have already been studied in detail for this sample by Pratt et al. (2009), who find that the observed deviation from the self-similar gravitational collapse model is consistent with an increase in the gas mass fraction as a function of mass. They measure the intrinsic scatter in these relations and find that it is greatly reduced when ignoring the inner core ($\lesssim 0.1\, r_{500}$), indicating that the scatter is consistent with the complex morphology of individual cluster cores.

Further work by Pratt et al. (2010) gave a detailed study of the entropy of these clusters, and their results are shown to be consistent with the expected model that entropy modification due to non-gravitational processes is typically located in the centre, with modification beyond the core being seen in lower mass clusters. Re-normalisation of the entropy profiles of these clusters by their gas mass fraction profiles is shown to decrease the dispersion and bring them into agreement with the non-radiative scenario, implying that it is the distribution of the gas that determines the observed properties of the entropy profile. Since such a detailed study has already been carried out on this sample at X-ray wavelengths, it will be insightful to perform a comparison with the measured SZ decrement from CBI2 observations of these clusters.

7.1.2 The High Redshift Sample and XMMU J2235.3 - 2557

Four high redshift clusters, located at $z \sim 0.5$, have also been observed with CBI2. They are massive clusters, known to be significantly bright in the SZ, and were included in the CBI2 sample in order to study the physics of clusters at redshifts higher than the scaling relations sample. In addition XMMU J2235.3 - 2557, a very high redshift X-ray luminous cluster, has also been observed for long integrations by both the CBI1 and CBI2 arrays. This cluster was serendipitously discovered in 2005 from XMM-Newton archival data by Mullis et al. (2005). It has since been observed in the near-infrared by Lidman et al. (2008) and was detected by the Hubble Space for weak lensing analysis by Jee et al. (2009). The weak lensing result estimates that the projected mass within 1 Mpc is equal to $8.5 \pm 1.7 \times 10^{14} M_{\odot}$, and current Chandra observations give the temperature at a value of $8.6^{+1.3}_{-1.2}$ keV. There has also been a very recent multi-wavelength analysis on this cluster by Rosati et al. (2009), who find similar total mass and temperature values. Given the original X-ray survey volume and the current cosmological model this is expected to be a very rare discovery, with an estimated probability $\leq 1\,\%$, and hence have implications for our understanding of the origin of large-scale structure formation. A combined X-ray surface brightness and CBI SZ analysis might be able to provide an independent mass estimate, assuming hydrostatic equilibrium.

7.1.3 The extended SZ effect in the core region of the Shapley Supercluster

Extensive observations have been made across the A3558 complex in the core region of the Shapley Supercluster with both the CBI1 and CBI2 arrays, as well as pointed observations with CBI2 of the X-ray bright

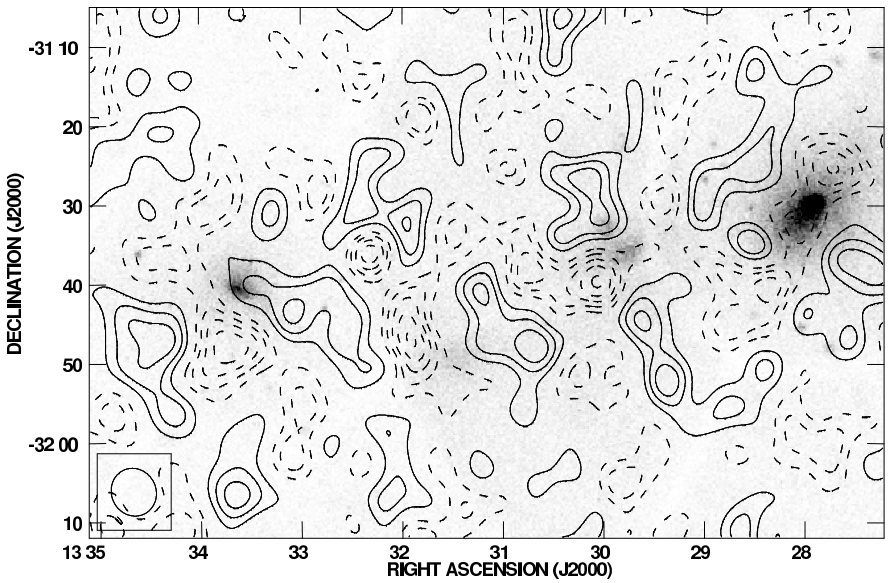

Figure 7.1: A preliminary mosaic from CBI2 observations of the core region of the Shapley Supercluster. The grey scale represents the X-ray surface brightness counts, where I have made use of the ROSAT Data Archive of the Max-Planck-Institut für extraterrestrische Physik (MPE) at Garching, Germany. The contours represent the $1\,\sigma$ intervals of noise on the full-resolution map where the solid and dashed lines represent positive and negative values respectively. This region has also been observed by CBI1, and it is hoped that a combined analysis from both data sets will reveal the large scale structure of the system in the thermal SZ.

cluster A3558 (see Figure 7.1 for a preliminary mosaic of CBI2 observations). This region and its constituent clusters have been studied in detail with X-ray observations (see e.g. Bardelli et al., 1996; Bonamente et al., 2001; Akimoto et al., 2003; Rossetti et al., 2007) and at optical (see e.g. Bardelli et al., 1998) and radio wavelengths (see e.g. Venturi et al., 2000; Miller, 2005). The system is in a complex dynamical state with three massive clusters involved in past mergers (A3556, A3558, A3562), and two poor clusters embedded within the super-structure (SC 1327-312 and SC 1329-313). Thermal SZ effect observations from the CBI1 and CBI2 arrays cover the area from A3562 to A3558, including the two poor clusters in-between. It is hoped that a combined analysis of the CMB signal from these observations will reveal a possible excess of SZ decrement from extended gas within the regions between the main cluster components. There has been limited success so far in the search for an extended gas component between clusters of galaxies, the most recent work by Battistelli et al. (2007) measured a very weak SZ detection towards the centre of the Corona Borealis Supercluster with the Very Small Array (VSA) and the millimeter and infrared testa grigia observatory (MITO). In addition to CBI observations, a series of targeted observations have been made across the mosaic with the Australia Telescope Compact Array at 32 GHz, pointing at known NVSS sources Condon

et al. (1998) in order to constrain the radio points source contaminant.

7.2 Combining CBI2 data with other SZ Experiments

The analysis outlined in this thesis can be applied to any interferometer, over any range of baseline distances or antenna size, and it is therefore entirely feasible to combine the CBI2 data with that from any other SZ interferometric experiment. It is advantageous to combine information from several interferometers of different sizes in order to cover a whole range of angular scales, and therefore provide useful information on cluster physics at differing scales.

7.2.1 CBI1 and CBI2

Many of the galaxy clusters in the CBI2 sample were also observed using the original CBI1 array. Estimates of the thermal SZ effect from these two observations can therefore be improved upon by combining the data sets. Figure 7.2 shows the real visibility as a function of baseline from mock observations of a massive cluster with the CBI1 and CBI2 arrays, and the combined data sets. In this mock example the simulated observing times for each of the two arrays have been artificially constructed to be equal, which of course will not be typically true of real observations. Figure 7.2 also displays estimates of the posterior distribution for the enclosed total mass at 2 Mpc, using a joint fit with generic mock X-ray surface brightness data. It is clear that CBI2 provides a stronger constraint on the total mass estimate, since it has almost twice the effective collecting area, and less contamination from the intrinsic CMB anisotropy component on the shorter baselines. However including the CBI1 data in a combined analysis does provide a useful improvement on the estimate and may be significant if, for example, there were more receivers in commission during the CBI1 observation. In the example shown in Figure 7.2 the percentage errors in the mass are 10 %, 8.8 % and 8 % for CBI1, CBI2 and combined respectively. Combining the data sets from both arrays also provides a broader range of angular scales, with data from the compact CBI1 array providing extra information on the larger scales.

7.2.2 SZA and CBI2

The Sunyaev-Zel'dovich array (SZA) is a 30 GHz interferometer with 8 antennas, located at the Cedar Flats CARMA high-site in California, USA. The dishes are 3.5 m in diameter, with a maximum baseline distance (for SZ observations) of 13 m, providing an instantaneous field-of-view equal to 100 arcseconds and a resolution of 7 arcminutes. The SZA is therefore a perfect instrument with which to combine thermal SZ effect data with CBI2, since both operate at the same frequency and have complimentary baseline ranges. Unfortunately these two experiments are located in different hemispheres, and therefore only a few clusters are common to both sets of observations, however it is hoped that very good SZ images can be obtained for these few and will provide excellent angular scale coverage for model fitting.

7.3 The spectral SZ effect

Recent experimental work has begun to move the focus away from the thermal SZ effect to measuring the spectral properties of the SZ signal (see e.g. Benson et al., 2003; Nord et al., 2009). In particular the position of the null frequency, where the SZ signal changes from being a decrement to an increment, is a function of both the temperature of the intra-cluster medium and the bulk peculiar velocity of the cluster. It is difficult to separate the contributions of these two components by SZ observations alone, however it may be possible to do so with either independent X-ray spectral constraints of the temperature or very good spectral SZ coverage.

7.3.1 SuZIE and CBI2 Data

The SuZIE II experiment is a bolometric infrared experiment, measuring the change in CMB temperature due to the SZ effect at 145, 221 and 273/355 GHz. This instrument provided peculiar velocity constraints for six of the brightest galaxy clusters, and constrained the universal bulk flow in the direction of the CMB dipole, with a 95 % limit on the peculiar velocity being less than $1420\,\mathrm{km}^{-2}$ (Benson et al., 2003). The CBI2 experiment has obtained data on all the clusters observed in the work by Benson et al. (2003), and 50 % of the additional clusters observed by Benson et al. (2004). Measurement of the SZ decrement at 31 GHz, using CBI2 data, will provide a lower frequency handle on the spectrum of these clusters. This will

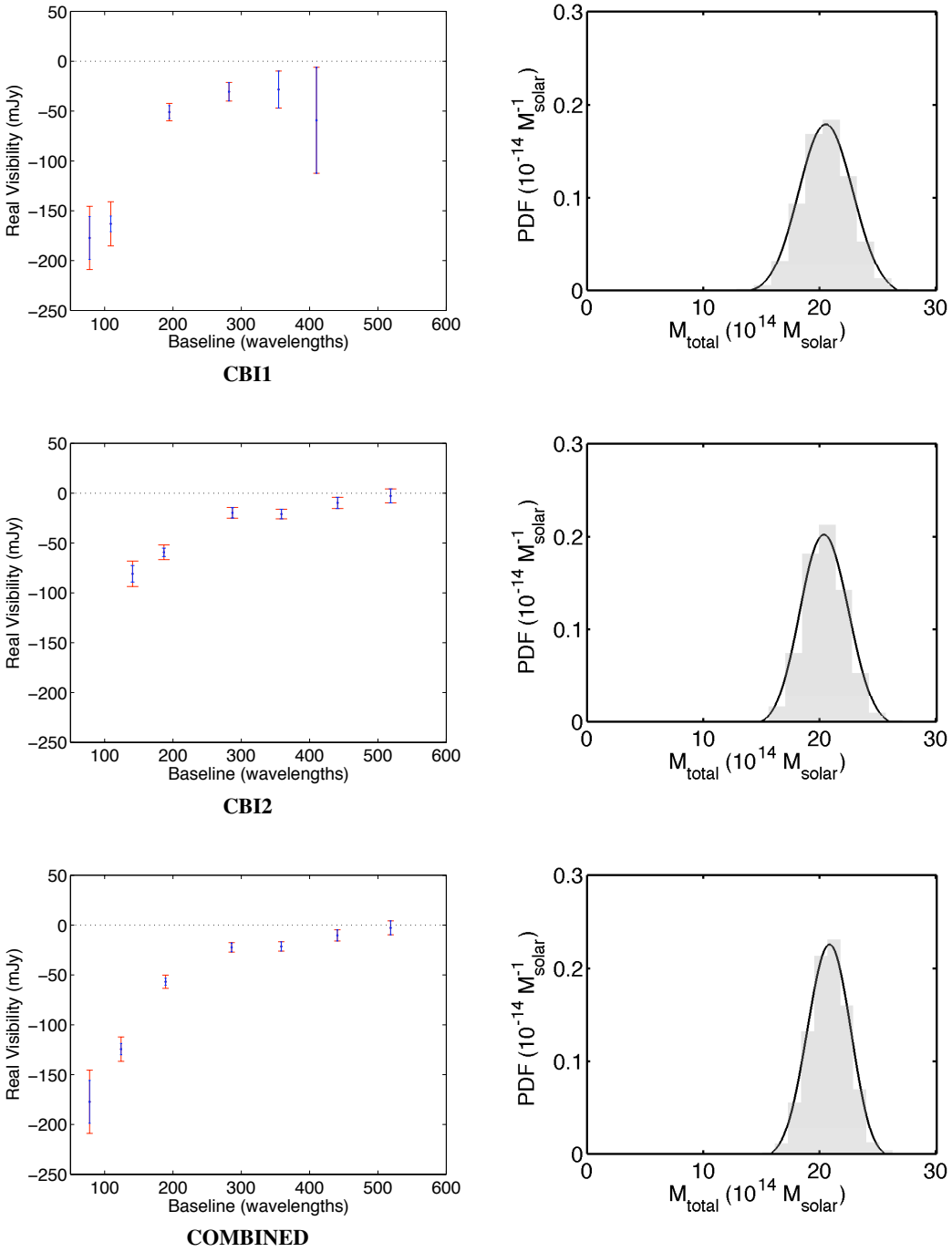

Figure 7.2: *Left*: Mock real visibility data from thermal SZ effect observations of a massive cluster at $z = 0.15$ with the CBI1 and CBI2 arrays, and the combined data sets. *Right*: The estimated posterior probability density for the total enclosed mass at 2 Mpc, for each of the three cases, from a joint fit to the SZ and X-ray data.

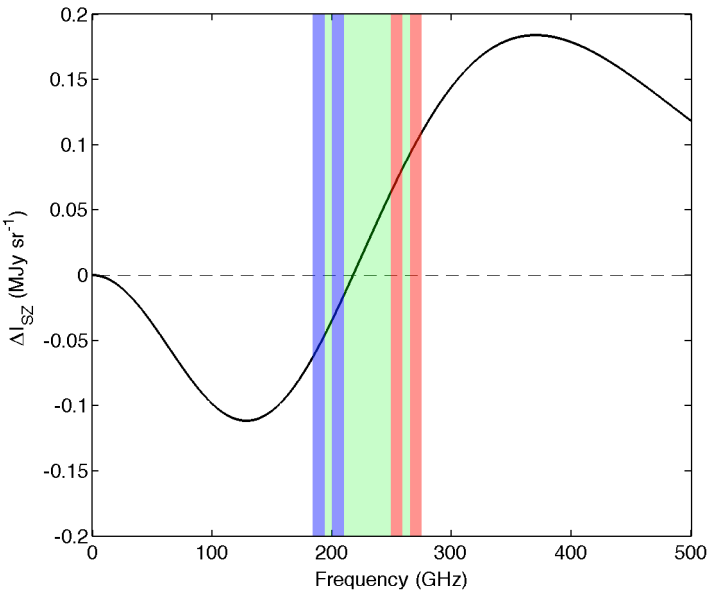

Figure 7.3: The tunable frequency coverage available to the GUBBINS Phase-1 instrument (*Green*), with the instantaneous coverage at the low (*Blue*) and high (*Red*) extremes. See Grimes et al. (2009) for a technical description of the experiment.

allow further separation of the thermal and kinematic signature and hence provide a stronger constraint on the peculiar velocity limits.

7.3.2 GUBBINS - A prototype spectral SZ experiment

The 220-GHz Ultra-BroadBand INterferometer for the SZ (GUBBINS) is a prototype single-baseline experiment designed to observe the thermal and kinematic SZ signal, with a tunable frequency range from 185 - 275 GHz and an instantaneous bandwidth of 2×10 GHz. The aim of the experiment is to provide an independent estimate of the cluster gas temperature by accurately constraining the position of the SZ null frequency to within 1 GHz. The position of the null frequency due to the thermal SZ effect alone is approximated by $[217 + 0.45(T_e/\mathrm{keV})]$ GHz. Hence, if one can accurately distinguish the thermal from the kinematic SZ signal, observations by GUBBINS should be able to constrain the temperature of the ICM to within a few keV. Figure 7.3 shows both the instantaneous and tunable frequency coverage available to GUBBINS, superimposed on a plot of the differential change in CMB intensity due to the thermal SZ effect from a typical cluster. As with the discussion of the SuZIE experiment in the above section, the CBI2

31 GHz data will be used to separate the thermal and kinematic signature, and hence distinguish between effects of the peculiar motion of the cluster and the electron temperature.

7.4 The Future of targeted SZ observations

7.4.1 Motivation for pointed observations

With the arrival of large bolometric detector arrays the SZ effect has come of age as a technique able to detect previously unknown clusters and probe the distribution of large-scale structure in its own right. However, despite these advances in SZ surveying, there is still an important role to be played by experiments that provide targeted observations of known galaxy clusters. The results of surveys from the South Pole Telescope (SPT) and the Atacama Cosmology Telescope (ACT) will rely upon the ability to convert the measured integrated SZ effect into a viable mass estimate, and therefore constrain the numbers of clusters detected as a function of mass. We require good understanding of the scaling relations and their intrinsic scatter between the observables and the total mass, which in turn require good multi-wavelength targeted observations from the SZ effect, X-rays and Weak lensing. The physics of the intra-cluster medium has been shown to deviate from the simple model provided by purely gravitational processes. The observed complexity of cluster gas physics is thought to be a result of both radiative cooling and pre-heating due to injection of energy from the formation of stars and active galactic nuclei. Combined pointed SZ and X-ray surface brightness observations constrain the gas entropy and therefore allow inference of the thermal history of the cluster. By quantifying how the scaling relations are effected by the observed properties of the gas entropy, we will be able to understand how the intrinsic scatter is introduced by the underlying thermal processes.

7.4.2 CBI3 - A small antenna array for SZ observations

The work in this thesis has shown that there is a clear motivation to continue the study of cluster physics via pointed SZ observations. Interferometric experiments have the advantage that they can obtain a high signal-to-noise detection by integrating on a single pointing for many hours, and so by selecting baselines of differing lengths, one can spatially filter the angular scales which are required. At present there are rela-

tively few new radio interferometers for use in CMB observing, with SZA and AMIBA being the principle examples in operation, both of which are in the northern hemisphere. It is proposed that an array of ~ 13 small antennas, independently mounted in the style of a traditional radio interferometer, would provide a complimentary set of data in follow up observations to the SZ surveys, specifically the SPT and ACT experiments.

7.5 Summary

There is still a great deal to be understood about the underlying physical processes that have led to the evolution of galaxy clusters we observe today. Targeted observations of the SZ effect provide a powerful tool to constrain the global properties of clusters. In this thesis I have presented CBI2 observations of a sample of galaxy clusters from the distant and X-ray luminous REFLEX-DXL sample. The antenna size and baseline range available to the CBI2 array allows measurements to be made of the SZ effect out to the viral radius, thus providing constraints on the global integrated comptonization parameter and, when combined with X-ray data, the total mass and gas mass fraction. Using an appropriate parametric model, based upon the known observable behaviour of the gas entropy and the dark matter content, radial profiles have been constructed of the electron temperature, total mass and gas mass fraction. Preliminary scaling relations are constructed between the observable SZ effect and intrinsic physical properties for radii at r_{2500}, r_{500} and r_{200}. By constraining the power-law behaviour and intrinsic scatter of these scaling relations, we can begin to understand the non-gravitational processes that dictate the observable properties of galaxy clusters, and therefore interpret the results of SZ and X-ray surveys.

Appendix A

ATCA Mosaics of the Field centres

The following figures show 4.80 GHz and 8.64 GHz CLEANed maps from ATCA observations of the centres of some REFLEX-DXL fields. The grey-scale maps are in signal-to-noise units, and the contours are in units of $5\,\sigma$. The typical RMS noise level on the maps is approximately $1\,\mathrm{mJy\,beam^{-1}}$ with sensitivity decreasing towards the edge of the mosaic. These lower-frequency observations were conducted in order to look for sources at the centre of the fields that weren't selected for targeted observation at 32 GHz. Some sources might have inverted spectral indices that would make them bright at 31 GHz, but have a low flux in the SUMSS and NVSS catalogues. A source with this characteristic could contribute a significant systematic error to the observed thermal SZ effect decrement at the centre of the field. These observations are significantly deeper than the PMN survey (Griffith & Wright, 1993) at 4.85 GHz, which reached a flux limit of approximately 30 mJy.

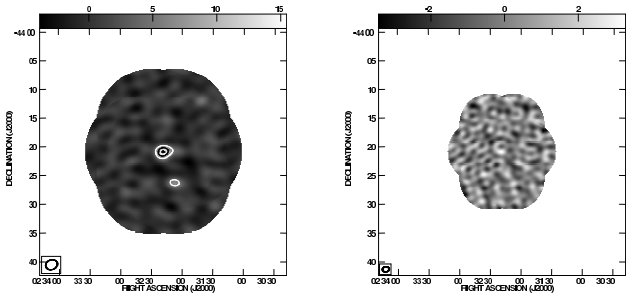

Main Field (4.80 GHz) Main Field (8.64 GHz)

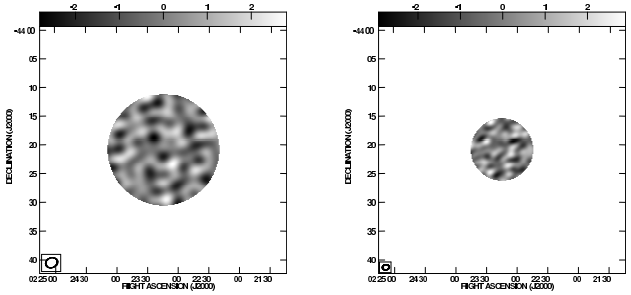

Lead Field (4.80 GHz) Lead Field (8.64 GHz)

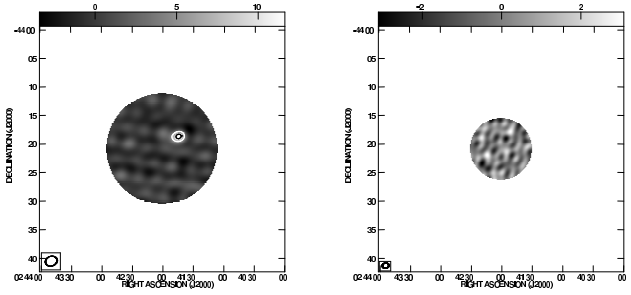

Trail Field (4.80 GHz) Trail Field (8.64 GHz)

Figure A.1: **RXCJ0232.3-4420**

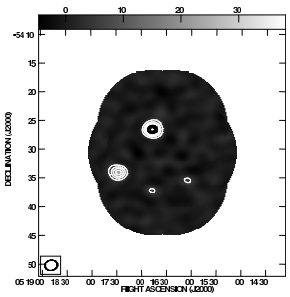

Main Field (4.80 GHz)

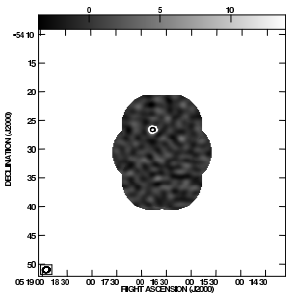

Main Field (8.64 GHz)

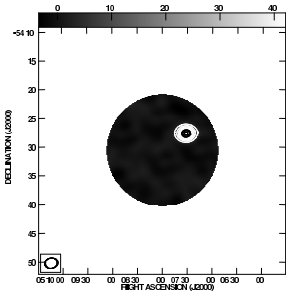

Lead Field 1 (4.80 GHz)

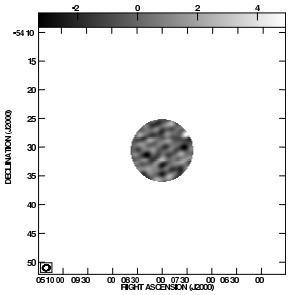

Lead Field 1 (8.64 GHz)

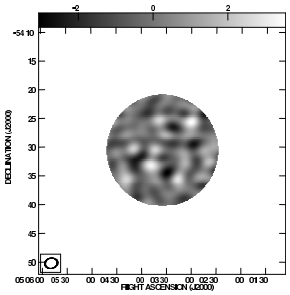

Lead Field 2 (4.80 GHz)

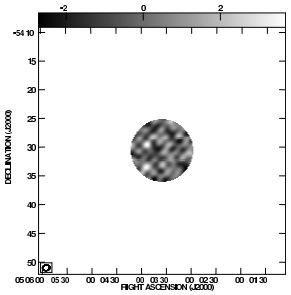

Lead Field 2 (8.64 GHz)

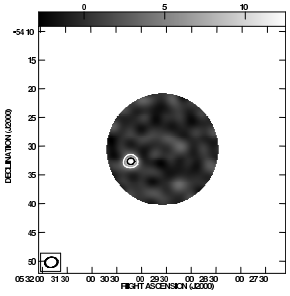

Trail Field 1 (4.80 GHz)

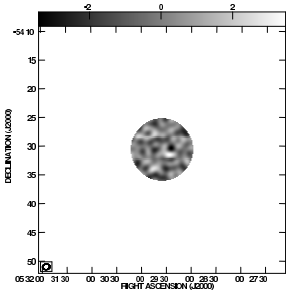

Trail Field 1 (8.64 GHz)

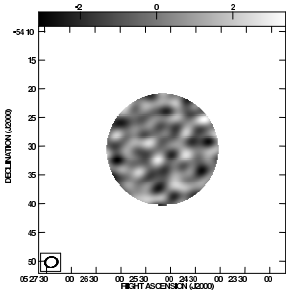

Trail Field 2 (4.80 GHz)

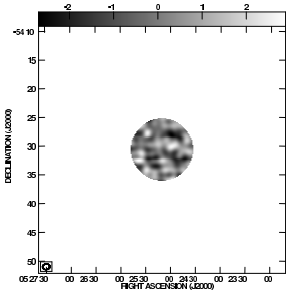

Trail Field 2 (8.64 GHz)

Figure A.2: **RXCJ0516.7-5430**

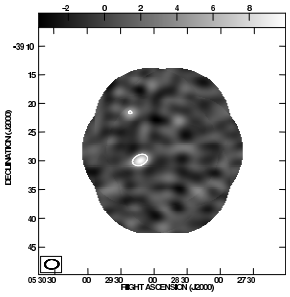

Main Field (4.80 GHz)

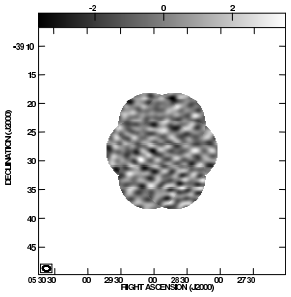

Main Field (8.64 GHz)

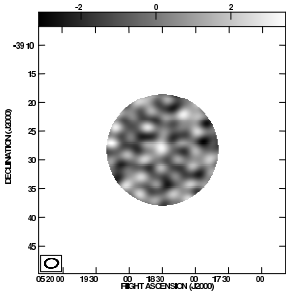

Lead Field (4.80 GHz)

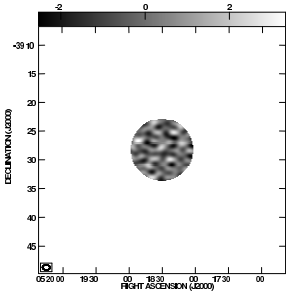

Lead Field (8.64 GHz)

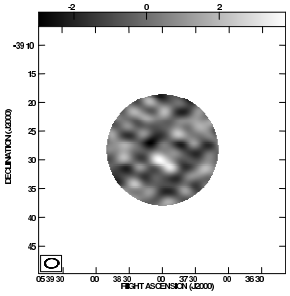

Trail Field (4.80 GHz)

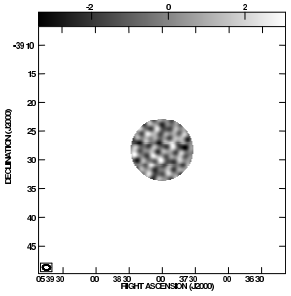

Trail Field (8.64 GHz)

Figure A.3: **RXCJ0528.9-3927**

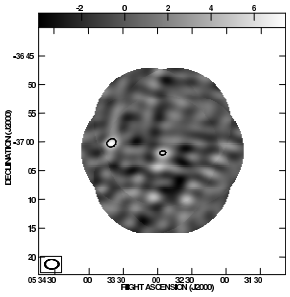

Main Field (4.80 GHz)

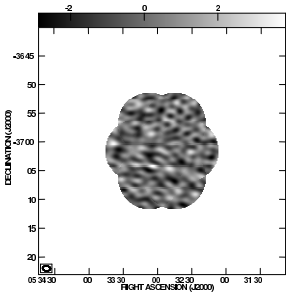

Main Field (8.64 GHz)

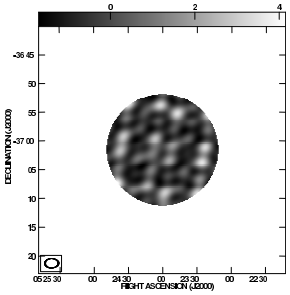

Lead Field (4.80 GHz)

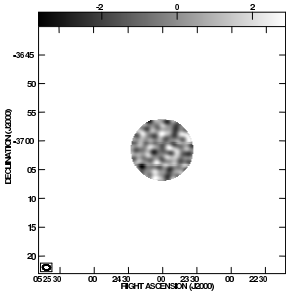

Lead Field (8.64 GHz)

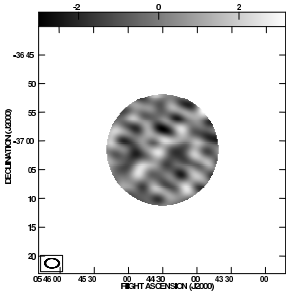

Trail Field (4.80 GHz)

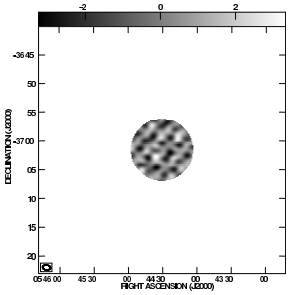

Trail Field (8.64 GHz)

Figure A.4: **RXCJ0532.9-3701**

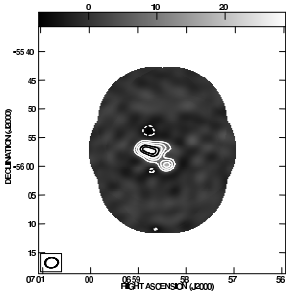

Main Field (4.80 GHz)

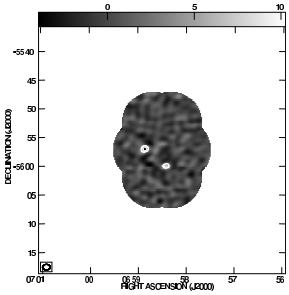

Main Field (8.64 GHz)

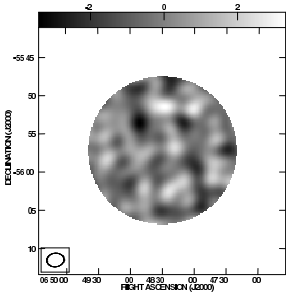

Lead Field (4.80 GHz)

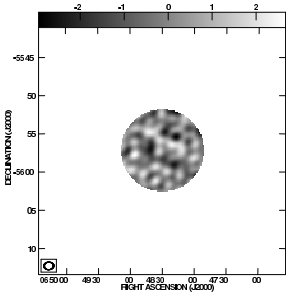

Lead Field (8.64 GHz)

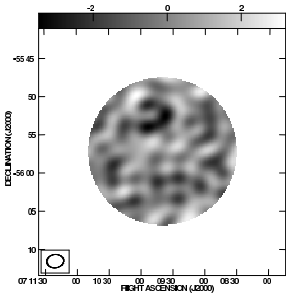

Trail Field 1 (4.80 GHz)

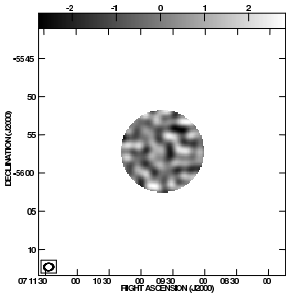

Trail Field 1 (8.64 GHz)

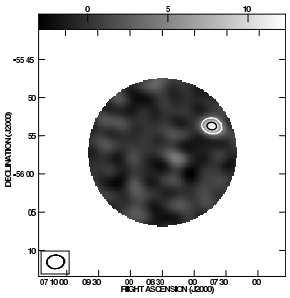

Trail Field 2 (4.80 GHz)

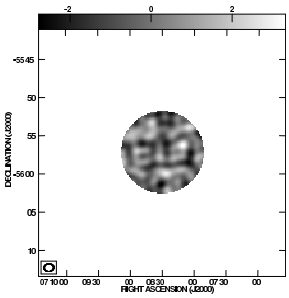

Trail Field 2 (8.64 GHz)

Figure A.5: **RXCJ0658.5-5556 (IE0657-558)**

Bibliography

ABELL, G. O., 1958. The Distribution of Rich Clusters of Galaxies. *ApJS*, **3**, 211–+.

AKIMOTO, F., KONDOU, K., FURUZAWA, A., TAWARA, Y. & YAMASHITA, K., 2003. Spatial Distributions of A3558 in the Core Region of the Shapley Supercluster. *ApJ*, **596**, 170–180.

ALLEN, S. W., SCHMIDT, R. W., EBELING, H., FABIAN, A. C. & VAN SPEYBROECK, L., 2004. Constraints on dark energy from Chandra observations of the largest relaxed galaxy clusters. *MNRAS*, **353**, 457–467.

ALLEN, S. W., SCHMIDT, R. W. & FABIAN, A. C., 2001. The X-ray virial relations for relaxed lensing clusters observed with Chandra. *MNRAS*, **328**, L37–L41.

ALPHER, R. A. & HERMAN, R., 1948. Evolution of the Universe. *Nature*, **162**, 774–775.

AMEGLIO, S., BORGANI, S., PIERPAOLI, E. & DOLAG, K., 2007. Joint deprojection of Sunyaev-Zeldovich and X-ray images of galaxy clusters. *MNRAS*, **382**, 397–411.

AMEGLIO, S., BORGANI, S., PIERPAOLI, E., DOLAG, K., ETTORI, S. & MORANDI, A., 2009. Reconstructing mass profiles of simulated galaxy clusters by combining Sunyaev-Zeldovich and X-ray images. *MNRAS*, **394**, 479–490.

ANDERSSON, K. E. & MADEJSKI, G. M., 2004. Complex Structure of Galaxy Cluster A1689: Evidence for a Merger from X-Ray Data? *ApJ*, **607**, 190–201.

ANDREANI, P., BÖHRINGER, H., DALL'OGLIO, G., MARTINIS, L., SHAVER, P., LEMKE, R., NYMAN, L.-Å., BOOTH, R., PIZZO, L., WHYBORN, N., TANAKA, Y. & LIANG, H., 1999. The Enhancement and Decrement of the Sunyaev-Zeldovich Effect toward the ROSAT Cluster RX J0658-5557. *ApJ*, **513**, 23–33.

ARNAUD, M., PRATT, G. W., PIFFARETTI, R., BOEHRINGER, H., CROSTON, J. H. & POINTECOUTEAU, E., 2009. The universal galaxy cluster pressure profile from a representative sample of nearby systems (REXCESS) and the Y_SZ-M_500 relation. *ArXiv e-prints*.

BAARS, J. W. M., GENZEL, R., PAULINY-TOTH, I. I. K. & WITZEL, A., 1977. The absolute spectrum of CAS A - an accurate flux density scale and a set of secondary calibrators. *AAP*, **61**, 99–106.

BACCHI, M., FERETTI, L., GIOVANNINI, G. & GOVONI, F., 2003. Deep images of cluster radio halos. *AAP*, **400**, 465–476.

BARDELLI, S., ZUCCA, E., MALIZIA, A., ZAMORANI, G., SCARAMELLA, R. & VETTOLANI, G., 1996. A study of the core of the Shapley concentration. II. ROSAT observation of A 3558. *AAP*, **305**, 435–+.

BARDELLI, S., ZUCCA, E., ZAMORANI, G., VETTOLANI, G. & SCARAMELLA, R., 1998. A study of the core of the Shapley Concentration - III. Properties of the clusters in the A3558 complex. *MNRAS*, **296**, 599–613.

BARRENA, R., BIVIANO, A., RAMELLA, M., FALCO, E. E. & SEITZ, S., 2002. The dynamical status of the cluster of galaxies 1E0657-56. *AAP*, **386**, 816–828.

BATTISTELLI, E. S., DE PETRIS, M., LAMAGNA, L., WATSON, R. A., REBOLO, R., GÉNOVA-SANTOS, R., LUZZI, G., DE GREGORI, S. & RUBIÑO-MARTIN, J. A., 2007. SZ effect from Corona Borealis supercluster. *New Astronomy Review*, **51**, 374–380.

BENNETT, C. L., BANDAY, A. J., GORSKI, K. M., HINSHAW, G., JACKSON, P., KEEGSTRA, P., KOGUT, A., SMOOT, G. F., WILKINSON, D. T. & WRIGHT, E. L., 1996. Four-Year COBE DMR Cosmic Microwave Background Observations: Maps and Basic Results. *ApJL*, **464**, L1+.

BENNETT, C. L., HILL, R. S., HINSHAW, G., NOLTA, M. R., ODEGARD, N., PAGE, L., SPERGEL, D. N., WEILAND, J. L., WRIGHT, E. L., HALPERN, M., JAROSIK, N., KOGUT, A., LIMON, M., MEYER, S. S., TUCKER, G. S. & WOLLACK, E., 2003. First-Year Wilkinson Microwave Anisotropy Probe (WMAP) Observations: Foreground Emission. *ApJS*, **148**, 97–117.

BENSON, B. A., CHURCH, S. E., ADE, P. A. R., BOCK, J. J., GANGA, K. M., HENSON, C. N. & THOMPSON, K. L., 2004. Measurements of Sunyaev-Zel'dovich Effect Scaling Relations for Clusters of Galaxies. *ApJ*, **617**, 829–846.

BENSON, B. A., CHURCH, S. E., ADE, P. A. R., BOCK, J. J., GANGA, K. M., HINDERKS, J. R., MAUSKOPF, P. D., PHILHOUR, B., RUNYAN, M. C. & THOMPSON, K. L., 2003. Peculiar Velocity Limits from Measurements of the Spectrum of the Sunyaev-Zeldovich Effect in Six Clusters of Galaxies. *ApJ*, **592**, 674–691.

BIRKINSHAW, M., 1999. The Sunyaev-Zel'dovich effect. *PhysRep*, **310**, 97–195.

BIRKINSHAW, M., GULL, S. F. & HARDEBECK, H., 1984. The Sunyaev-Zeldovich effect towards three clusters of galaxies. *Nature*, **309**, 34–+.

BIVIANO, A., 2008. Galaxy systems in the optical and infrared. *ArXiv e-prints*.

BOGGESS, N. W., MATHER, J. C., WEISS, R., BENNETT, C. L., CHENG, E. S. ET AL., 1992. The COBE mission - Its design and performance two years after launch. *ApJ*, **397**, 420–429.

BÖHRINGER, H., SCHUECKER, P., GUZZO, L., COLLINS, C. A., VOGES, W., CRUDDACE, R. G., ORTIZ-GIL, A., CHINCARINI, G., DE GRANDI, S., EDGE, A. C., MACGILLIVRAY, H. T., NEUMANN, D. M., SCHINDLER, S. & SHAVER, P., 2004. The ROSAT-ESO Flux Limited X-ray (REFLEX) Galaxy cluster survey. V. The cluster catalogue. *AAP*, **425**, 367–383.

BÖHRINGER, H., SCHUECKER, P., GUZZO, L., COLLINS, C. A., VOGES, W., SCHINDLER, S., NEUMANN, D. M., CRUDDACE, R. G., DE GRANDI, S., CHINCARINI, G., EDGE, A. C., MACGILLIVRAY, H. T. & SHAVER, P., 2001. The ROSAT-ESO flux limited X-ray (REFLEX) galaxy cluster survey. I. The construction of the cluster sample. *AAP*, **369**, 826–850.

BÖHRINGER, H., SCHUECKER, P., PRATT, G. W., ARNAUD, M., PONMAN, T. J. ET AL., 2007. The representative XMM-Newton cluster structure survey (REXCESS) of an X-ray luminosity selected galaxy cluster sample. *AAP*, **469**, 363–377.

BONAMENTE, M., JOY, M., LAROQUE, S. J., CARLSTROM, J. E., NAGAI, D. & MARRONE, D. P., 2008. Scaling Relations from Sunyaev-Zel'dovich Effect and Chandra X-Ray Measurements of High-Redshift Galaxy Clusters. *ApJ*, **675**, 106–114.

BONAMENTE, M., LIEU, R., NEVALAINEN, J. & KAASTRA, J. S., 2001. ROSAT and BeppoSAX Evidence of Soft X-Ray Excess Emission in the Shapley Supercluster: A3571, A3558, A3560, and A3562. *ApJL*, **552**, L7–L11.

BOND, J. R., JAFFE, A. H. & KNOX, L., 2000. Radical Compression of Cosmic Microwave Background Data. *ApJ*, **533**, 19–37.

BRADAČ, M., CLOWE, D., GONZALEZ, A. H., MARSHALL, P., FORMAN, W., JONES, C., MARKEVITCH, M., RANDALL, S., SCHRABBACK, T. & ZARITSKY, D., 2006. Strong and Weak Lensing United. III. Measuring the Mass Distribution of the Merging Galaxy Cluster 1ES 0657-558. *ApJ*, **652**, 937–947.

BRADAČ, M., SCHNEIDER, P., LOMBARDI, M. & ERBEN, T., 2005. Strong and weak lensing united. *AAP*, **437**, 39–48.

BROADHURST, T., BENÍTEZ, N., COE, D., SHARON, K., ZEKSER, K. ET AL., 2005. Strong-Lensing Analysis of A1689 from Deep Advanced Camera Images. *ApJ*, **621**, 53–88.

BROADHURST, T., HUANG, X., FRYE, B. & ELLIS, R., 2000. A Spectroscopic Redshift for the Cl 0024+16 Multiple Arc System: Implications for the Central Mass Distribution. *ApJL*, **534**, L15–L18.

BRYAN, G. L. & NORMAN, M. L., 1998. Statistical Properties of X-Ray Clusters: Analytic and Numerical Comparisons. *ApJ*, **495**, 80–+.

BUOTE, D. A., GASTALDELLO, F., HUMPHREY, P. J., ZAPPACOSTA, L., BULLOCK, J. S., BRIGHENTI, F. & MATHEWS, W. G., 2007. The X-Ray Concentration-Virial Mass Relation. *ApJ*, **664**, 123–134.

CARLSTROM, J. E., HOLDER, G. P. & REESE, E. D., 2002. Cosmology with the Sunyaev-Zel'dovich Effect. *ARA&A*, **40**, 643–680.

CASASSUS, S., CABRERA, G. F., FÖRSTER, F., PEARSON, T. J., READHEAD, A. C. S. & DICKINSON, C., 2006. Morphological Analysis of the Centimeter-Wave Continuum in the Dark Cloud LDN 1622. *ApJ*, **639**, 951–964.

CAVAGNOLO, K. W., DONAHUE, M., VOIT, G. M. & SUN, M., 2009. Intracluster Medium Entropy Profiles for a Chandra Archival Sample of Galaxy Clusters. *ApJS*, **182**, 12–32.

CAVALIERE, A. & FUSCO-FEMIANO, R., 1976. X-rays from hot plasma in clusters of galaxies. *AAP*, **49**, 137–144.

CAVALIERE, A. & FUSCO-FEMIANO, R., 1978. The Distribution of Hot Gas in Clusters of Galaxies. *AAP*, **70**, 677.

CHALLINOR, A. & LASENBY, A., 1998. Relativistic Corrections to the Sunyaev-Zeldovich Effect. *ApJ*, **499**, 1.

CHENG, E. S., SAULSON, P. R., WILKINSON, D. T. & COREY, B. E., 1979. Large-scale anisotropy in the 2.7 K radiation. *ApJL*, **232**, L139–L143.

CLOWE, D., BRADAČ, M., GONZALEZ, A. H., MARKEVITCH, M., RANDALL, S. W., JONES, C. & ZARITSKY, D., 2006. A Direct Empirical Proof of the Existence of Dark Matter. *ApJL*, **648**, L109–L113.

CLOWE, D., GONZALEZ, A. & MARKEVITCH, M., 2004. Weak-Lensing Mass Reconstruction of the Interacting Cluster 1E 0657-558: Direct Evidence for the Existence of Dark Matter. *ApJ*, **604**, 596–603.

COMERFORD, J. M. & NATARAJAN, P., 2007. The observed concentration-mass relation for galaxy clusters. *MNRAS*, **379**, 190–200.

CONDON, J. J., COTTON, W. D., GREISEN, E. W., YIN, Q. F., PERLEY, R. A., TAYLOR, G. B. & BRODERICK, J. J., 1998. The NRAO VLA Sky Survey. *AJ*, **115**, 1693–1716.

COORAY, A. R., 1999. An SZ temperature decrement-X-ray luminosity relation for galaxy clusters. *MNRAS*, **307**, 841–848.

DA SILVA, A. C., KAY, S. T., LIDDLE, A. R. & THOMAS, P. A., 2004. Hydrodynamical simulations of the Sunyaev-Zel'dovich effect: cluster scaling relations and X-ray properties. *MNRAS*, **348**, 1401–1408.

DICKINSON, C., DAVIES, R. D., ALLISON, J. R., BOND, J. R., CASASSUS, S., CLEARY, K., DAVIS, R. J., JONES, M. E., MASON, B. S., MYERS, S. T., PEARSON, T. J., READHEAD, A. C. S., SIEVERS, J. L., TAYLOR, A. C., TODOROVIĆ, M., WHITE, G. J. & WILKINSON, P. N., 2009. Anomalous Microwave Emission from the H II Region RCW175. *ApJ*, **690**, 1585–1589.

DONAHUE, M., HORNER, D. J., CAVAGNOLO, K. W. & VOIT, G. M., 2006. Entropy Profiles in the Cores of Cooling Flow Clusters of Galaxies. *ApJ*, **643**, 730–750.

DRAINE, B. T. & LAZARIAN, A., 1998a. Diffuse Galactic Emission from Spinning Dust Grains. *ApJL*, **494**, L19+.

DRAINE, B. T. & LAZARIAN, A., 1998b. Electric Dipole Radiation from Spinning Dust Grains. *ApJ*, **508**, 157–179.

DREICER, H., 1964. Kinetic Theory of an Electron-Photon Gas. *Physics of Fluids*, **7**, 735–753.

DUNKLEY, J., KOMATSU, E., NOLTA, M. R., SPERGEL, D. N., LARSON, D. ET AL., 2009. Five-Year Wilkinson Microwave Anisotropy Probe Observations: Likelihoods and Parameters from the WMAP Data. *ApJS*, **180**, 306–329.

ETTORI, S., FABIAN, A. C. & WHITE, D. A., 1997. On the mass distribution in the Shapley Supercluster inferred from X-ray observations. *MNRAS*, **289**, 787–800.

FARRAR, G. R. & ROSEN, R. A., 2007. A New Force in the Dark Sector? *Physical Review Letters*, **98**(17), 171302–+.

FERRARI, C., GOVONI, F., SCHINDLER, S., BYKOV, A. M. & REPHAELI, Y., 2008. Observations of Extended Radio Emission in Clusters. *Space Science Reviews*, **134**, 93–118.

FIXSEN, D. J., CHENG, E. S., GALES, J. M., MATHER, J. C., SHAFER, R. A. & WRIGHT, E. L., 1996. The Cosmic Microwave Background Spectrum from the Full COBE FIRAS Data Set. *ApJ*, **473**, 576.

FREEDMAN, W. L., MADORE, B. F., GIBSON, B. K., FERRARESE, L., KELSON, D. D., SAKAI, S., MOULD, J. R., KENNICUTT, JR., R. C., FORD, H. C., GRAHAM, J. A., HUCHRA, J. P., HUGHES, S. M. G., ILLINGWORTH, G. D., MACRI, L. M. & STETSON, P. B., 2001. Final Results from the Hubble Space Telescope Key Project to Measure the Hubble Constant. *ApJ*, **553**, 47–72.

GAMOW, G., 1942. Concerning the origin of chemical elements. *J. Wash. Acad. Sci.*, **32**, 353–355.

GAMOW, G., 1946. Expanding Universe and the Origin of Elements. *Physical Review*, **70**, 572–573.

GOMEZ, P., ROMER, A. K., PETERSON, J. B., CHASE, W., RUNYAN, M., HOLZAPFEL, W., KUO, C. L., NEWCOMB, M., RUHL, J., GOLDSTEIN, J. & LANGE, A., 2004. Sunyaev-Zeldovich Observations of Massive Clusters of Galaxies. In G. Bertin, D. Farina & R. Pozzoli, eds., *Plasmas in the Laboratory and in the Universe: New Insights and New Challenges*, vol. 703 of *American Institute of Physics Conference Series*, 361–366.

GOVONI, F., MARKEVITCH, M., VIKHLININ, A., VANSPEYBROECK, L., FERETTI, L. & GIOVANNINI, G., 2004. Chandra Temperature Maps for Galaxy Clusters with Radio Halos. *ApJ*, **605**, 695–708.

GREGO, L., CARLSTROM, J. E., JOY, M. K., REESE, E. D., HOLDER, G. P., PATEL, S., COORAY, A. R. & HOLZAPFEL, W. L., 2000. The Sunyaev-Zeldovich Effect in Abell 370. *ApJ*, **539**, 39–51.

GREGO, L., CARLSTROM, J. E., REESE, E. D., HOLDER, G. P., HOLZAPFEL, W. L., JOY, M. K., MOHR, J. J. & PATEL, S., 2001. Galaxy Cluster Gas Mass Fractions from Sunyaev-Zeldovich Effect Measurements: Constraints on $\Omega_{\rm M}$. *ApJ*, **552**, 2–14.

GRIFFITH, M. R. & WRIGHT, A. E., 1993. The Parkes-MIT-NRAO (PMN) surveys. I - The 4850 MHz surveys and data reduction. *AJ*, **105**, 1666–1679.

GRIMES, P. K., BROCK, M. J. R., HOLLER, C. M., JOHN, J., JONES, M. E., KING, O. G., LEECH, J., TAYLOR, A. C., YASSIN, G., JACOBS, K. & GROPPI, C., 2009. GUBBINS: A Novel Millimeter-Wave Heterodyne Interferometer. In E. Bryerton, A. Kerr, & A. Lichtenberger, ed., *Twentieth International Symposium on Space Terahertz Technology*, 82–+.

HALLIDAY, C., MILVANG-JENSEN, B., POIRIER, S., POGGIANTI, B. M., JABLONKA, P., ARAGÓN-SALAMANCA, A., SAGLIA, R. P., DE LUCIA, G., PELLÓ, R., SIMARD, L., CLOWE, D. I., RUDNICK, G., DALCANTON, J. J., WHITE, S. D. M. & ZARITSKY, D., 2004. Spectroscopy of clusters in the ESO Distant Cluster Survey (EDisCS). Redshifts, velocity dispersions and substructure for 5 clusters. *AAP*, **427**, 397–413.

HALVERSON, N. W., LANTING, T., ADE, P. A. R., BASU, K., BENDER, A. N. ET AL., 2009. Sunyaev-Zel'Dovich Effect Observations of the Bullet Cluster (1E 0657-56) with APEX-SZ. *ApJ*, **701**, 42–51.

HALVERSON, N. W., LEITCH, E. M., PRYKE, C., KOVAC, J., CARLSTROM, J. E., HOLZAPFEL, W. L., DRAGOVAN, M., CARTWRIGHT, J. K., MASON, B. S., PADIN, S., PEARSON, T. J., READHEAD, A. C. S. & SHEPHERD, M. C., 2002. Degree Angular Scale Interferometer First Results: A Measurement of the Cosmic Microwave Background Angular Power Spectrum. *ApJ*, **568**, 38–45.

HAYASHI, E. & WHITE, S. D. M., 2006. How rare is the bullet cluster? *MNRAS*, **370**, L38–L41.

HILL, R. S., WEILAND, J. L., ODEGARD, N., WOLLACK, E., HINSHAW, G. ET AL., 2009. Five-Year Wilkinson Microwave Anisotropy Probe Observations: Beam Maps and Window Functions. *ApJS*, **180**, 246–264.

HINSHAW, G., WEILAND, J. L., HILL, R. S., ODEGARD, N., LARSON, D. ET AL., 2009. Five-Year Wilkinson Microwave Anisotropy Probe Observations: Data Processing, Sky Maps, and Basic Results. *ApJS*, **180**, 225–245.

HO, P. T. P., ALTAMIRANO, P., CHANG, C., CHANG, S., CHANG, S. ET AL., 2009. The Yuan-Tseh Lee Array for Microwave Background Anisotropy. *ApJ*, **694**, 1610–1618.

HOBSON, M. P., BRIDLE, S. L. & LAHAV, O., 2002. Combining cosmological data sets: hyperparameters and Bayesian evidence. *MNRAS*, **335**, 377–388.

HÖGBOM, J. A., 1974. Aperture Synthesis with a Non-Regular Distribution of Interferometer Baselines. *AAPS*, **15**, 417–+.

HUMMEL, E., DAHLEM, M., VAN DER HULST, J. M. & SUKUMAR, S., 1991. The large-scale radio continuum structure of the edge-on spiral galaxy NGC 891. *AAP*, **246**, 10–20.

ITOH, N., KOHYAMA, Y. & NOZAWA, S., 1998. Relativistic Corrections to the Sunyaev-Zeldovich Effect for Clusters of Galaxies. *ApJ*, **502**, 7.

JEE, M. J., ROSATI, P., FORD, H. C., DAWSON, K. S., LIDMAN, C., PERLMUTTER, S., DEMARCO, R., STRAZZULLO, V., MULLIS, C., BÖHRINGER, H. & FASSBENDER, R., 2009. Hubble Space Telescope Weak-lensing Study of the Galaxy Cluster XMMU J2235.3-2557 at z $\sim$ 1.4: A Surprisingly Massive Galaxy Cluster When the Universe is One-third of its Current Age. *ApJ*, **704**, 672–686.

JOHNSON, J. B., 1928. Thermal Agitation of Electricity in Conductors. *Physical Review*, **32**, 97–109.

JONES, M., SAUNDERS, R., ALEXANDER, P., BIRKINSHAW, M., DILON, N., GRAINGE, K., HANCOCK, S., LASENBY, A., LEFEBVRE, D. & POOLEY, G., 1993. An image of the Sunyaev-Zel'dovich effect. *Nature*, **365**, 320–323.

JONES, M. E., EDGE, A. C., GRAINGE, K., GRAINGER, W. F., KNEISSL, R., POOLEY, G. G., SAUNDERS, R., MIYOSHI, S. J., TSURUTA, T., YAMASHITA, K., TAWARA, Y., FURUZAWA, A., HARADA, A. & HATSUKADE, I., 2005. H_0 from an orientation-unbiased sample of Sunyaev-Zel'dovich and X-ray clusters. *MNRAS*, **357**, 518–526.

KAISER, N., 1986. Evolution and clustering of rich clusters. *MNRAS*, **222**, 323–345.

KAY, S. T., 2004. The entropy distribution in clusters: evidence of feedback? *MNRAS*, **347**, L13–L17.

KAY, S. T., POWELL, L. C., LIDDLE, A. R. & THOMAS, P. A., 2008. The Sunyaev-Zel'dovich temperature of the intracluster medium. *MNRAS*, **386**, 2110–2114.

KAY, S. T., THOMAS, P. A., JENKINS, A. & PEARCE, F. R., 2004. Cosmological simulations of the intracluster medium. *MNRAS*, **355**, 1091–1104.

KNEISSL, R., JONES, M. E., SAUNDERS, R., EKE, V. R., LASENBY, A. N., GRAINGE, K. & COTTER, G., 2001. Surveying the sky with the Arcminute MicroKelvin Imager: expected constraints on galaxy cluster evolution and cosmology. *MNRAS*, **328**, 783–794.

KOMPANEETS, A. S., 1956. The establishment of thermal equilibrium between photons and electrons. *Sov. Phys. JETP*, **4**, 730.

KOSOWSKY, A., 2003. The Atacama Cosmology Telescope. *New Astronomy Review*, **47**, 939–943.

KRAVTSOV, A. V., NAGAI, D. & VIKHLININ, A. A., 2005. Effects of Cooling and Star Formation on the Baryon Fractions in Clusters. *ApJ*, **625**, 588–598.

LANCASTER, K., BIRKINSHAW, M., GAWROŃSKI, M. P., BROWNE, I., FEILER, R., KUS, A., LOWE, S., PAZDERSKI, E. & WILKINSON, P., 2007. Preliminary Sunyaev-Zel'dovich observations of galaxy clusters with OCRA-p. *MNRAS*, 401.

LANGE, A. E., ADE, P. A., BOCK, J. J., BOND, J. R., BORRILL, J. ET AL., 2001. Cosmological parameters from the first results of Boomerang. *PRD*, **63**(4), 042001–+.

LAROQUE, S. J., BONAMENTE, M., CARLSTROM, J. E., JOY, M. K., NAGAI, D., REESE, E. D. & DAWSON, K. S., 2006. X-Ray and Sunyaev-Zel'dovich Effect Measurements of the Gas Mass Fraction in Galaxy Clusters. *ApJ*, **652**, 917–936.

LAY, O. P. & HALVERSON, N. W., 2000. The Impact of Atmospheric Fluctuations on Degree-Scale Imaging of the Cosmic Microwave Background. *ApJ*, **543**, 787–798.

LIANG, H., HUNSTEAD, R. W., BIRKINSHAW, M. & ANDREANI, P., 2000. A Powerful Radio Halo in the Hottest Known Cluster of Galaxies 1E 0657-56. *ApJ*, **544**, 686–701.

LIDMAN, C., ROSATI, P., TANAKA, M., STRAZZULLO, V., DEMARCO, R., MULLIS, C., AGEORGES, N., KISSLER-PATIG, M., PETR-GOTZENS, M. G. & SELMAN, F., 2008. HAWK-I imaging of the X-ray luminous galaxy cluster XMMU J2235.3-2557. The red sequence at z = 1.39. *AAP*, **489**, 981–988.

LISENFELD, U. & VÖLK, H. J., 2000. On the radio spectral index of galaxies. *AAP*, **354**, 423–430.

LLOYD-DAVIES, E. J., PONMAN, T. J. & CANNON, D. B., 2000. The entropy and energy of intergalactic gas in galaxy clusters. *MNRAS*, **315**, 689–702.

LOWE, S. R., GAWROŃSKI, M. P., WILKINSON, P. N., KUS, A. J., BROWNE, I. W. A., PAZDERSKI, E., FEILER, R. & KETTLE, D., 2007. 30 GHz flux density measurements of the Caltech-Jodrell flat-spectrum sources with OCRA-p. *AAP*, **474**, 1093–1100.

MACCIÒ, A. V., DUTTON, A. A. & VAN DEN BOSCH, F. C., 2008. Concentration, spin and shape of dark matter haloes as a function of the cosmological model: WMAP1, WMAP3 and WMAP5 results. *MNRAS*, **391**, 1940–1954.

MACCIÒ, A. V., DUTTON, A. A., VAN DEN BOSCH, F. C., MOORE, B., POTTER, D. & STADEL, J., 2007. Concentration, spin and shape of dark matter haloes: scatter and the dependence on mass and environment. *MNRAS*, **378**, 55–71.

MAHDAVI, A., HOEKSTRA, H., BABUL, A., SIEVERS, J., MYERS, S. T. & HENRY, J. P., 2007. Joint Analysis of Cluster Observations. I. Mass Profile of Abell 478 from Combined X-Ray, Sunyaev-Zel'dovich, and Weak-Lensing Data. *ApJ*, **664**, 162–180.

MARKEVITCH, M., GONZALEZ, A. H., CLOWE, D., VIKHLININ, A., FORMAN, W., JONES, C., MURRAY, S. & TUCKER, W., 2004. Direct Constraints on the Dark Matter Self-Interaction Cross Section from the Merging Galaxy Cluster 1E 0657-56. *ApJ*, **606**, 819–824.

MARKEVITCH, M., GONZALEZ, A. H., DAVID, L., VIKHLININ, A., MURRAY, S., FORMAN, W., JONES, C. & TUCKER, W., 2002. A Textbook Example of a Bow Shock in the Merging Galaxy Cluster 1E 0657-56. *ApJL*, **567**, L27–L31.

MARRONE, D. P., SMITH, G. P., RICHARD, J., JOY, M., BONAMENTE, M. ET AL., 2009. LoCuSS: A Comparison of Sunyaev-Zel'dovich Effect and Gravitational-Lensing Measurements of Galaxy Clusters. *ApJL*, **701**, L114–L118.

MARSHALL, P. J., HOBSON, M. P. & SLOSAR, A., 2003. Bayesian joint analysis of cluster weak lensing and Sunyaev-Zel'dovich effect data. *MNRAS*, **346**, 489–500.

MASON, B. S., LEITCH, E. M., MYERS, S. T., CARTWRIGHT, J. K. & READHEAD, A. C. S., 1999. An Absolute Flux Density Measurement of the Supernova Remnant Cassiopeia A at 32 GHZ. *AJ*, **118**, 2908–2918.

MASON, B. S., PEARSON, T. J., READHEAD, A. C. S., SHEPHERD, M. C., SIEVERS, J. ET AL., 2003. The Anisotropy of the Microwave Background to l = 3500: Deep Field Observations with the Cosmic Background Imager. *ApJ*, **591**, 540–555.

MASON, B. S., WEINTRAUB, L., SIEVERS, J., BOND, J. R., MYERS, S. T., PEARSON, T. J., READHEAD, A. C. S. & SHEPHERD, M. C., 2009. A 31 GHz Survey of Low-Frequency Selected Radio Sources. *ApJ*, **704**, 1433–1447.

MASTROPIETRO, C. & BURKERT, A., 2008. Simulating the Bullet Cluster. *MNRAS*, **389**, 967–988.

MATEOS, S., SAXTON, R. D., READ, A. M. & SEMBAY, S., 2009. Statistical evaluation of the flux cross-calibration of the XMM-Newton EPIC cameras. *AAP*, **496**, 879–889.

MAUCH, T., MURPHY, T., BUTTERY, H. J., CURRAN, J., HUNSTEAD, R. W., PIESTRZYNSKI, B., ROBERTSON, J. G. & SADLER, E. M., 2003. SUMSS: a wide-field radio imaging survey of the southern sky - II. The source catalogue. *MNRAS*, **342**, 1117–1130.

MAUGHAN, B. J., JONES, L. R., EBELING, H. & SCHARF, C., 2006. The evolution of the cluster X-ray scaling relations in the Wide Angle ROSAT Pointed Survey sample at $0.6 < z < 1.0$. *MNRAS*, **365**, 509–529.

MILLER, A. D., CALDWELL, R., DEVLIN, M. J., DORWART, W. B., HERBIG, T., NOLTA, M. R., PAGE, L. A., PUCHALLA, J., TORBET, E. & TRAN, H. T., 1999. A Measurement of the Angular Power Spectrum of the Cosmic Microwave Background from L = 100 to 400. *ApJL*, **524**, L1–L4.

MILLER, N. A., 2005. Star Formation and Active Galactic Nuclei in the Core of the Shapley Supercluster: A Very Large Array Survey of A3556, A3558, SC 1327-312, SC 1329-313, and A3562. *AJ*, **130**, 2541–2558.

MITCHELL, N. L., MCCARTHY, I. G., BOWER, R. G., THEUNS, T. & CRAIN, R. A., 2009. On the origin of cores in simulated galaxy clusters. *MNRAS*, **395**, 180–196.

MORANDI, A. & ETTORI, S., 2007. Entropy profiles in X-ray luminous galaxy clusters at z > 0.1. *MNRAS*, **380**, 1521–1532.

MROCZKOWSKI, T., BONAMENTE, M., CARLSTROM, J. E., CULVERHOUSE, T. L., GREER, C. ET AL., 2009. Application of a Self-Similar Pressure Profile to Sunyaev-Zel'Dovich Effect Data from Galaxy Clusters. *ApJ*, **694**, 1034–1044.

MUCHOVEJ, S., MROCZKOWSKI, T., CARLSTROM, J. E., CARTWRIGHT, J., GREER, C., HENNESSY, R., LOH, M., PRYKE, C., REDDALL, B., RUNYAN, M., SHARP, M., HAWKINS, D., LAMB, J. W., WOODY, D., JOY, M., LEITCH, E. M. & MILLER, A. D., 2007. Observations of High-Redshift X-Ray Selected Clusters with the Sunyaev-Zel'dovich Array. *ApJ*, **663**, 708–716.

MULLIS, C. R., ROSATI, P., LAMER, G., BÖHRINGER, H., SCHWOPE, A., SCHUECKER, P. & FASSBENDER, R., 2005. Discovery of an X-Ray-luminous Galaxy Cluster at z=1.4. *ApJL*, **623**, L85–L88.

MURPHY, T., SADLER, E. M., EKERS, R. D., MASSARDI, M., HANCOCK, P. J. ET AL., 2010. The Australia Telescope 20 GHz Survey: the source catalogue. *MNRAS*, **402**, 2403–2423.

MYERS, S. T., CONTALDI, C. R., BOND, J. R., PEN, U.-L., POGOSYAN, D., PRUNET, S., SIEVERS, J. L., MASON, B. S., PEARSON, T. J., READHEAD, A. C. S. & SHEPHERD, M. C., 2003. A Fast Gridded Method for the Estimation of the Power Spectrum of the Cosmic Microwave Background from Interferometer Data with Application to the Cosmic Background Imager. *ApJ*, **591**, 575–598.

NAGAI, D., KRAVTSOV, A. V. & VIKHLININ, A., 2007. Effects of Galaxy Formation on Thermodynamics of the Intracluster Medium. *ApJ*, **668**, 1–14.

NAVARRO, J. F., FRENK, C. S. & WHITE, S. D. M., 1995. Simulations of X-ray clusters. *MNRAS*, **275**, 720–740.

NAVARRO, J. F., FRENK, C. S. & WHITE, S. D. M., 1996. The Structure of Cold Dark Matter Halos. *ApJ*, **462**, 563–+.

NORD, M., BASU, K., PACAUD, F., ADE, P. A. R., BENDER, A. N. ET AL., 2009. Multi-frequency imaging of the galaxy cluster Abell 2163 using the Sunyaev-Zel'dovich effect. *AAP*, **506**, 623–636.

NOZAWA, S., ITOH, N. & KOHYAMA, Y., 1998. Relativistic Corrections to the Sunyaev-Zeldovich Effect for Clusters of Galaxies. II. Inclusion of Peculiar Velocities. *ApJ*, **508**, 17–24.

NYQUIST, H., 1928. Thermal Agitation of Electric Charge in Conductors. *Physical Review*, **32**, 110–113.

PADIN, S., SHEPHERD, M. C., CARTWRIGHT, J. K., KEENEY, R. G., MASON, B. S., PEARSON, T. J., READHEAD, A. C. S., SCHAAL, W. A., SIEVERS, J., UDOMPRASERT, P. S., YAMASAKI, J. K., HOLZAPFEL, W. L., CARLSTROM, J. E., JOY, M., MYERS, S. T. & OTAROLA, A., 2002. The Cosmic Background Imager. *PASP*, **114**, 83–97.

PELLÓ, R., RUDNICK, G., DE LUCIA, G., SIMARD, L., CLOWE, D. I. ET AL., 2009. Photometric redshifts and cluster tomography in the ESO Distant Cluster Survey. *AAP*, **508**, 1173–1191.

PENZIAS, A. A. & WILSON, R. W., 1965. A Measurement of Excess Antenna Temperature at 4080 Mc/s. *ApJ*, **142**, 419–421.

PHILLIPS, P. R., 1995. Calculation of the Kinetic Sunyaev-Zeldovich Effect from the Boltzmann Equation. *ApJ*, **455**, 419.

PIFFARETTI, R., JETZER, P., KAASTRA, J. S. & TAMURA, T., 2005. Temperature and entropy profiles of nearby cooling flow clusters observed with XMM-Newton. *AAP*, **433**, 101–111.

PONMAN, T. J., CANNON, D. B. & NAVARRO, J. F., 1999. The thermal imprint of galaxy formation on X-ray clusters. *Nature*, **397**, 135–137.

PONMAN, T. J., SANDERSON, A. J. R. & FINOGUENOV, A., 2003. The Birmingham-CfA cluster scaling project - III. Entropy and similarity in galaxy systems. *MNRAS*, **343**, 331–342.

PRATT, G. W., ARNAUD, M., PIFFARETTI, R., BÖHRINGER, H., PONMAN, T. J., CROSTON, J. H., VOIT, G. M., BORGANI, S. & BOWER, R. G., 2010. Gas entropy in a representative sample of nearby X-ray galaxy clusters (REXCESS): relationship to gas mass fraction. *AAP*, **511**, A85+.

PRATT, G. W., ARNAUD, M. & POINTECOUTEAU, E., 2006. Structure and scaling of the entropy in nearby galaxy clusters. *AAP*, **446**, 429–438.

PRATT, G. W., BÖHRINGER, H., CROSTON, J. H., ARNAUD, M., BORGANI, S., FINOGUENOV, A. & TEMPLE, R. F., 2007. Temperature profiles of a representative sample of nearby X-ray galaxy clusters. *AAP*, **461**, 71–80.

PRATT, G. W., CROSTON, J. H., ARNAUD, M. & BÖHRINGER, H., 2009. Galaxy cluster X-ray luminosity scaling relations from a representative local sample (REXCESS). *AAP*, **498**, 361–378.

PRESS, W. H. & SCHECHTER, P., 1974. Formation of Galaxies and Clusters of Galaxies by Self-Similar Gravitational Condensation. *ApJ*, **187**, 425–438.

PRESS, W. H., TEUKOLSKY, S. A., VETTERLING, W. T. & FLANNERY, B. P., 1992. *Numerical recipes in C. The art of scientific computing*.

RAYMOND, J. C. & SMITH, B. W., 1977. Soft X-ray spectrum of a hot plasma. *ApJS*, **35**, 419–439.

REESE, E. D., CARLSTROM, J. E., JOY, M., MOHR, J. J., GREGO, L. & HOLZAPFEL, W. L., 2002. Determining the Cosmic Distance Scale from Interferometric Measurements of the Sunyaev-Zeldovich Effect. *ApJ*, **581**, 53–85.

REID, A. D., HUNSTEAD, R. W., LEMONON, L. & PIERRE, M. M., 1999. Radio study of X-ray clusters of galaxies – II. A1300: a post-merger cluster at z=0.31 containing a halo and a relic. *MNRAS*, **302**, 571–581.

REPHAELI, Y., NEVALAINEN, J., OHASHI, T. & BYKOV, A. M., 2008. Nonthermal Phenomena in Clusters of Galaxies. *Space Science Reviews*, **134**, 71–92.

RICE, S. O., 1945. Mathematical Analysis of Random Noise. *Bell System Technical Journal*, **24**, 46–156.

RICHARDS, P. L. & WOODY, D. P., 1980. The spectrum of the microwave background. In G. O. Abell & P. J. E. Peebles, ed., *Objects of High Redshift*, vol. 92 of *IAU Symposium*, 283–290.

ROSATI, P., TOZZI, P., GOBAT, R., SANTOS, J. S., NONINO, M., DEMARCO, R., LIDMAN, C., MULLIS, C. R., STRAZZULLO, V., BÖHRINGER, H., FASSBENDER, R., DAWSON, K., TANAKA, M., JEE, J., FORD, H., LAMER, G. & SCHWOPE, A., 2009. Multi-wavelength study of XMMU J2235.3-2557: the most massive galaxy cluster at z > 1. *AAP*, **508**, 583–591.

ROSSETTI, M., GHIZZARDI, S., MOLENDI, S. & FINOGUENOV, A., 2007. A cluster in a crowded environment: XMM-Newton and Chandra observations of A3558. *AAP*, **463**, 839–851.

RUHL, J., ADE, P. A. R., CARLSTROM, J. E., CHO, H.-M., CRAWFORD, T. ET AL., 2004. The South Pole Telescope. In C. M. Bradford, P. A. R. Ade, J. E. Aguirre, J. J. Bock, M. Dragovan, L. Duband, L. Earle, J. Glenn, H. Matsuhara, B. J. Naylor, H. T. Nguyen, M. Yun, & J. Zmuidzinas, ed., *Society of Photo-Optical Instrumentation Engineers (SPIE) Conference Series*, vol. 5498 of *Society of Photo-Optical Instrumentation Engineers (SPIE) Conference Series*, 11–29.

RYBICKI, G. B. & LIGHTMAN, A. P., 1979. *Radiative processes in astrophysics*.

SACHS, R. K. & WOLFE, A. M., 1967. Perturbations of a Cosmological Model and Angular Variations of the Microwave Background. *ApJ*, **147**, 73–+.

SCHECHTER, P., 1976. An analytic expression for the luminosity function for galaxies. *ApJ*, **203**, 297–306.

SCHWAN, D., BERTOLDI, F., CHO, S., DOBBS, M., GUESTEN, R. ET AL., 2003. APEX-SZ a Sunyaev-Zel'dovich galaxy cluster survey. *New Astronomy Review*, **47**, 933–937.

SCOTT, P. F., CARREIRA, P., CLEARY, K., DAVIES, R. D., DAVIS, R. J. ET AL., 2003. First results from the Very Small Array - III. The cosmic microwave background power spectrum. *MNRAS*, **341**, 1076–1083.

SCOTT, P. F., SAUNDERS, R., POOLEY, G., O'SULLIVAN, C., LASENBY, A. N., JONES, M., HOBSON, M. P., DUFFETT-SMITH, P. J. & BAKER, J., 1996. Measurements of Structure in the Cosmic Background Radiation with the Cambridge Cosmic Anistropy Telescope. *ApJL*, **461**, L1+.

SELJAK, U. & ZALDARRIAGA, M., 1996. A Line-of-Sight Integration Approach to Cosmic Microwave Background Anisotropies. *ApJ*, **469**, 437–+.

SHARP, M. K., MARRONE, D. P., CARLSTROM, J. E., CULVERHOUSE, T., GREER, C., HAWKINS, D., HENNESSY, R., JOY, M., LAMB, J. W., LEITCH, E. M., LOH, M., MILLER, A., MROCZKOWSKI, T., MUCHOVEJ, S., PRYKE, C. & WOODY, D., 2010. A Measurement of Arcminute Anisotropy in the Cosmic Microwave Background with the Sunyaev-Zel'dovich Array. *ApJ*, **713**, 82–89.

SIEVERS, J. L., MASON, B. S., WEINTRAUB, L., ACHERMANN, C., ALTAMIRANO, P. ET AL., 2009. Cosmological Results from Five Years of 30 GHz CMB Intensity Measurements with the Cosmic Background Imager. *ArXiv e-prints*.

SILK, J., 1968. Cosmic Black-Body Radiation and Galaxy Formation. *ApJ*, **151**, 459–+.

SKILLING, J., 2004. Bayesys and MassInf manual. *http://www.inference.phy.cam.ac.uk/bayesys/*.

SMOOT, G. F., BENNETT, C. L., KOGUT, A., WRIGHT, E. L., AYMON, J. ET AL., 1992. Structure in the COBE differential microwave radiometer first-year maps. *ApJL*, **396**, L1–L5.

SMOOT, G. F., GORENSTEIN, M. V. & MULLER, R. A., 1977. Detection of anisotropy in the cosmic blackbody radiation. *Physical Review Letters*, **39**, 898–901.

SPRINGEL, V. & FARRAR, G. R., 2007. The speed of the 'bullet' in the merging galaxy cluster 1E0657-56. *MNRAS*, **380**, 911–925.

SPRINGEL, V., WHITE, S. D. M., JENKINS, A., FRENK, C. S., YOSHIDA, N., GAO, L., NAVARRO, J., THACKER, R., CROTON, D., HELLY, J., PEACOCK, J. A., COLE, S., THOMAS, P., COUCHMAN, H., EVRARD, A., COLBERG, J. & PEARCE, F., 2005. Simulations of the formation, evolution and clustering of galaxies and quasars. *Nature*, **435**, 629–636.

STANISZEWSKI, Z., ADE, P. A. R., AIRD, K. A., BENSON, B. A., BLEEM, L. E. ET AL., 2009. Galaxy Clusters Discovered with a Sunyaev-Zel'dovich Effect Survey. *ApJ*, **701**, 32–41.

SUNYAEV, R. A. & ZEL'DOVICH, Y. B., 1970. Small-Scale Fluctuations of Relic Radiation. *Ap&SS*, **7**, 3.

SUNYAEV, R. A. & ZEL'DOVICH, Y. B., 1972. The Observations of Relic Radiation as a Test of the Nature of X-Ray Radiation from the Clusters of Galaxies. *Comments on Astrophysics and Space Physics*, **4**, 173.

TAYLOR, A. C., GRAINGE, K., JONES, M. E., POOLEY, G. G., SAUNDERS, R. D. E. & WALDRAM, E. M., 2001. The radio source counts at 15 GHz and their implications for cm-wave CMB imaging. *MNRAS*, **327**, L1–L4.

TOZZI, P. & NORMAN, C., 2001. The Evolution of X-Ray Clusters and the Entropy of the Intracluster Medium. *ApJ*, **546**, 63–84.

UDOMPRASERT, P. S., MASON, B. S., READHEAD, A. C. S. & PEARSON, T. J., 2004. An Unbiased Measurement of H_0 through Cosmic Background Imager Observations of the Sunyaev-Zel'dovich Effect in Nearby Galaxy Clusters. *ApJ*, **615**, 63–81.

USON, J. M., 1986. The Sunyaev-Zel'dovich effect - Measurements and implications. *Radio continuum processes in clusters of galaxies; Proceedings of the Workshop, Green Bank, WV, Aug. 4-8, 1986 (A88-38551 15-90). Charlottesville, VA, National Radio Astronomy Observatory, 1986, p. 255-260.*, **16**, 255–260.

VENTURI, T., BARDELLI, S., MORGANTI, R. & HUNSTEAD, R. W., 2000. Radio properties of the Shapley Concentration - III. Merging clusters in the A3558 complex. *MNRAS*, **314**, 594–610.

VENTURI, T., GIACINTUCCI, S., BRUNETTI, G., CASSANO, R., BARDELLI, S., DALLACASA, D. & SETTI, G., 2007. GMRT radio halo survey in galaxy clusters at z = 0.2-0.4. I. The REFLEX sub-sample. *AAP*, **463**, 937–947.

VIKHLININ, A., KRAVTSOV, A., FORMAN, W., JONES, C., MARKEVITCH, M., MURRAY, S. S. & VAN SPEYBROECK, L., 2006. Chandra Sample of Nearby Relaxed Galaxy Clusters: Mass, Gas Fraction, and Mass-Temperature Relation. *ApJ*, **640**, 691–709.

VOIT, G. M., KAY, S. T. & BRYAN, G. L., 2005. The baseline intracluster entropy profile from gravitational structure formation. *MNRAS*, **364**, 909–916.

WALDRAM, E. M., POOLEY, G. G., GRAINGE, K. J. B., JONES, M. E., SAUNDERS, R. D. E., SCOTT, P. F. & TAYLOR, A. C., 2003. 9C: a survey of radio sources at 15 GHz with the Ryle Telescope. *MNRAS*, **342**, 915–925.

WATERS, J. W., 1976. Absorption and emission by atmospheric gases. In *Astrophysics. Part B: Radio Telescopes*, 142–176.

WATSON, R. A., CARREIRA, P., CLEARY, K., DAVIES, R. D., DAVIS, R. J. ET AL., 2003. First results from the Very Small Array - I. Observational methods. *MNRAS*, **341**, 1057–1065.

WEYMANN, R., 1965. Diffusion Approximation for a Photon Gas Interacting with a Plasma via the Compton Effect. *Physics of Fluids*, **8**, 2112–2114.

WHITE, S. D. M., NAVARRO, J. F., EVRARD, A. E. & FRENK, C. S., 1993. The baryon content of galaxy clusters: a challenge to cosmological orthodoxy. *Nature*, **366**, 429–433.

WOLLACK, E., JAROSIK, N., NETTERFIELD, B., PAGE, L. & WILKINSON, D., 1995. A Degree-Scale Measurement of the Anisotropy in the Cosmic Microwave Background. *Astrophysical Letters Communications*, **32**, 217–+.

WROBEL, J. M. & WALKER, R. C., 1999. Sensitivity. In G. B. Taylor, C. L. Carilli, & R. A. Perley, ed., *Synthesis Imaging in Radio Astronomy II*, vol. 180 of *Astronomical Society of the Pacific Conference Series*, 171–+.

ZHANG, Y.-Y., BÖHRINGER, H., FINOGUENOV, A., IKEBE, Y., MATSUSHITA, K., SCHUECKER, P., GUZZO, L. & COLLINS, C. A., 2006. X-ray properties in massive galaxy clusters: XMM-Newton observations of the REFLEX-DXL sample. *AAP*, **456**, 55–74.

ZHANG, Y.-Y., FINOGUENOV, A., BÖHRINGER, H., KNEIB, J.-P., SMITH, G. P., KNEISSL, R., OKABE, N. & DAHLE, H., 2008. LoCuSS: comparison of observed X-ray and lensing galaxy cluster scaling relations with simulations. *AAP*, **482**, 451–472.